ATTOSECOND XUV-IR PUMP-PROBE MEASUREMENTS OF SMALL MOLECULES USING 3D MOMENTUM SPECTROSCOPY

Dissertation
zur Erlangung des Grades eines
Doktors der Naturwissenschaften

am Fachbereich Physik
der Freien Universität Berlin

vorgelegt von

MIKHAIL OSOLODKOV

Berlin, 2022

This work was performed at Max-Born-Institut für Nichtlineare Optik und Kurzzeitspektroskopie im Forschungsverbund Berlin.

1st reviewer:
Prof. Dr. Marc J. J. Vrakking

2nd reviewer:
Prof. Dr. Martin Weinelt

date of defense:
01.12.2022

To my wife Evgeniya

ACKNOWLEDGEMENTS

First off all, many thanks to the direct supervisor of my PhD project Prof. Marc J. J. Vrakking for his guidance and scientific vision, which were absolutely essential for the success of the reported effort. I would also like to thank Prof. Martin Weinelt for being a referee of the present thesis. The support of the project from the Marie Sklodowska-Curie Innovative Training Network "ASPIRE" is gratefully acknowledged.

Second, I would like to express my gratitude to the team I was working with on a daily basis: Dr. Federico J. Furch, Dr. Tobias Witting and Dr. Claus Peter Schulz. Federico has developed the NOPCPA system used for the reported experiments and was regularly performing all necessary works to keep it optimized. His expertise on laser technology was essential for creating conditions, first of all laser pulse source stability, necessary for reliable generation of attosecond pulses. Tobias has developed the pulse compression setup with the hollow core fiber and all the software that allowed automation of the performed experiments. His expertise on attosecond pulse characterization was very important for reconstruction of both attosecond pulse trains and isolated attosecond pulses performed as a part of the present work. I would like to explicitly express my gratitude to Claus Peter for sharing his expertise on the coincidence detection technique and huge support with related laboratory activities. His deep knowledge on a great variety of subjects was extremely helpful for understanding the physical mechanisms of the studied processes. Also many thanks to Claus Peter for his advice on the thesis writing. It was a great pleasure for me to work with the acknowledged team!

Then I would like to thank former PhD students who have been developing the parts of the reported beamline: Sascha Birkner, Felix Schell, Peter Šušnjar and Achut Giree, who have been working on the Reaction Microscope, the pump-probe interferometer, the XUV spectrometer and the NOPCPA system used in the present work, respectively. I also want to thank Dr. Oleg Kornilov, Dr. Arnaud Rouzee and Dr. Jochen Mikosch for informative discussions and support on technical and theoretical aspects of the performed experiments. Present work would not be possible without technical support from Roman Peslin, Ahmet Akin Ünal, Christoph Reiter, Katrin Herrmann and Armin Loudovici. I would like to explicitly acknowledge the work of Oliver Reichel on the vacuum engineering.

Finally many thanks to fellow PhD students and postdocs at Max Born Institute I had a pleasure to work with: Nicola, Peter, Evgenii,

Janina, Thomas, Ulrich, Lisa, Laura, Federico, Evaldas, Lorenz, Kasra, Meguel, Fernando, Zhuang-Yan and Camilo.

DECLARATION OF AUTHORSHIP

I declare to the Freie Universität Berlin that I have completed the submitted dissertation independently and without the use of sources and aids other than those indicated. The present thesis is free of plagiarism. I have marked as such all statements that are taken literally or in content from other writings. This dissertation has not been submitted in the same or similar form in any previous doctoral procedure.

I agree to have my thesis examined by a plagiarism examination software.

Berlin, 2022

Mikhail Osolodkov

ABSTRACT

The interaction of photons with matter can initiate complex rearrangements of the configuration of bound electrons, which in molecules, in general, is accompanied by nuclear dynamics. Photoinduced electron dynamics is much faster than that of the nuclei, and is naturally occurring on the attosecond timescale. Interrogation of these fast dynamics is possible using attosecond laser pulses. They have become routinely available a few decades ago establishing the field of attosecond spectroscopy, which allowed observation of multiple ultrafast phenomena in atoms and molecules.

Since the spectrum of an attosecond pulse is inevitably broadband, its interaction with the target induces a large number of transitions simultaneously. In order to access individual photoionization channels in molecules it is advantageous to detect all charged products in coincidence. Since coincidence detection limits the data acquisition rate down to no more than one event per five laser pulses, a high repetition rate laser pulse source is required in order to collect significant statistics.

The present thesis reports on experiments conducted at a beamline combining a high-order harmonic generation-based attosecond pulse source operating at 100 kHz with a Reaction Microscope. The beamline is driven by a noncollinear optical parametric chirped pulse amplification system, in which few-cycle near infrared pulses generated by a titanium sapphire oscillator are amplified using the picosecond laser pulses delivered by a ytterbium-YAG pump laser. The reported beamline is designed for extreme ultraviolet–near infrared pump-probe experiments either with attosecond pulse trains or isolated attosecond pulses.

A series of time-resolved measurements with attosecond pulse trains were performed in molecular nitrogen focusing on the predissociative ionic C state. The corresponding ultrafast photoelectron dynamics was accessed with vibrational resolution. The performed investigation revealed a non-trivial energy dependence of extracted photoionization delays with respect to a noble gas reference. The observed effect could be a consequence of the multi-electron character of the photoinduced process under investigation. The reported results are manifesting one more step towards the attosecond spectroscopy of large complex molecules with coincidence detection.

KURZFASSUNG

Die Wechselwirkung von Photonen mit Materie kann komplexe Umordnungen der Konfiguration gebundener Elektronen initiieren, die in Molekülen im Allgemeinen von nuklearer Dynamik begleitet ist. Die photoinduzierte Elektronendynamik ist viel schneller als die Kernbewegung und tritt natürlicherweise auf der Attosekundenzeitskala auf. Zur zeitaufgelösten Untersuchung dieser Dynamik können Attosekunden-Laserpulse dienen. Sie sind seit ca. zwei Jahrzehnten routinemäßig verfügbar und begründen das Gebiet der Attosekundenspektroskopie, das die Beobachtung einer Vielzahl von ultraschnellen Phänomenen in Atomen und Molekülen ermöglicht.

Da das Spektrum eines Attosekundenpulses zwangsläufig breitbandig ist, induziert seine Wechselwirkung mit Atomen oder Molekülen viele Übergänge gleichzeitig. Um die verschiedenen Photoinisierungskanäle zu unterscheiden, ist es vorteilhaft, alle geladenen Produkte in Koinzidenz zu detektieren. Hierzu sollte die Datenrate nicht größer als ein Ereignis pro fünf Laserpulse sein. Um Daten mit aussagekräftiger Statistik in realisierbaren Messzeiten zu erhalten, ist ein Laserpulsquelle mit hoher Wiederholrate erforderlich.

Die vorliegende Dissertation berichtet über Experimente, die an einem Aufbau durchgeführt wurden, der eine Attosekundenpulsquelle, die auf der Erzeugung hoher Harmonischer basiert und bei 100 kHz arbeitet, mit einem Reaktionsmikroskop kombiniert. Die Attosekundenpulsquelle wird von einem nicht-kollinearen optisch-parametrischen Verstärkersystem für gechirpte Pulse angetrieben, in dem von einem Titan-Saphir-Oszillator erzeugte Nahinfrarotpulse mit wenigen Zyklen durch Pikosekundenlaserpulse eines Ytterbium-YAG Pumplasers verstärkt werden. Der beschriebene Aufbau ist für Pump-Probe-Experimente mit nahinfraroten und extrem-ultravioletten Laserpulsen — entweder Attosekunden-Pulszüge oder isolierte Attosekunden-Pulse — ausgelegt.

Eine Reihe von zeitaufgelösten Messungen mit Attosekunden-Pulszügen wurde an molekularem Stickstoff durchgeführt, wobei der Fokus auf dem prädissoziativen ionischen C-Zustand lag. Die Auswertung der entsprechenden ultraschnellen Photoelektronendynamik für verschiedene Schwingungszustände ergab eine nicht triviale Energieabhängigkeit der extrahierten Photoionisationsverzögerungen in Bezug auf eine Edelgasreferenz. Der beobachtete Effekt könnte eine Folge des Mehrelektronencharakters des untersuchten photoinduzierten Prozesses sein. Die berichteten Ergebnisse zeigen einen weiteren Schritt in Richtung Attosekundenspektroskopie großer komplexer Moleküle mit Koinzidenzdetektion.

CONTENTS

LIST OF FIGURES

LIST OF TABLES

ACRONYMS

APT	Attosecond Pulse Train
BBO	β-Barium Borate
BO	Born-Oppenheimer
CCD	Charge-Coupled Device
CEP	Carrier Envelope Phase
CMOS	Complementary Metal-Oxide-Semiconductor
EWS	Eisenbud-Wigner-Smith
FFT	Fast Fourier Transform
FROG-CRAB	Frequency Resolved Optical Gating for Complete Reconstruction of Attosecond Bursts
FTPS	Fourier Transform Power Spectrum
FWHM	Full Width at Half Maximum
GD	Group Delay
GDD	Group Delay Dispersion
HHG	High-order Harmonic Generation
IAP	Isolated Attosecond Pulse
KECD	Kinetic Energy Correlation Diagram
NIR	Near InfraRed
NOPCPA	Noncollinear Optical Parametric Chirped Pulse Amplification
RABBIT	Reconstruction of Attosecond Beating by Interference of two photon Transitions
ReMi	Reaction Microscope
SAE	Single Active Electron
SEA-F SPIDER	Spatially Encoded Arrangemnt with direct spectral Filtering Spectral Phase Interferometry for Direct Electric Field Reconstruction
SFA	Strong Field Approximation

SPM	Self Phase Modulation
TDSE	Time Dependent Schrödinger Equation
TOF	Time-Of-Flight
VTGPA	Volkov-Transform Generalized Projection Algorithm
XUV	Extreme UltraViolet

Part I

INTRODUCTION AND THEORETICAL BASIS

In the first part of the present thesis, a brief discussion of physical processes experimentally studied in the present work together with theoretical models describing them is given. Chapter 1 is an introductory chapter containing an overview of recent studies of ultrafast photoinduced dynamics in small molecules. The chapter provides a context to the experiments performed as part of the present work. Chapter 2 covers theoretical concepts necessary for the description of the investigated physical processes.

1

INTRODUCTION

The interaction of light with matter resulting in electron emission has attracted researcher's attention for more than a hundred years. Originally, the electron emission from a bulk metal surface induced by incident light — the photoelectric effect was studied. Starting from the pioneering experiments on electric discharge performed by H. Hertz [1], understanding of the underlying mechanisms of the photoelectric effect raised a challenge to the scientific community. For the physicists of that time it was hard to understand why the energy of the emitted electron is depending not on the intensity of the incident light, but on the photon wavelength. The conceptual argument was so strong, that it took almost 15 years for the community to accept the quantum mechanical explanation suggested by A. Einstein [2], for which he was awarded with a Nobel Prize in Physics in 1921. This discovery revealed the quantum nature of electromagnetic radiation, which lays at the basis of our modern understanding of light–matter interactions. For a detailed overview of the history of the photoelectric effect discovery please refer to Refs. [3, 4].

The invention of the laser by T. Maiman [5] opened the era of laser photoionization spectroscopy [6, 7]. Continuous wave (cw) lasers allowed studying the photoionization of single atoms or molecules with high energy resolution, while pulsed lasers gave access to the corresponding photoinduced dynamics in the temporal domain, establishing the field of femtosecond spectroscopy [8, 9]. Allowing access to nuclear motion, the corresponding laser pulse duration was still too long for direct probing of the photoelectron dynamics.

High-order harmonic generation (HHG) with femtosecond laser pulses, first experimentally demonstrated in the end of 80's [10, 11] resulted in the generation of extreme ultraviolet (XUV) photons. The measured spectrum of the generated XUV radiation was sufficiently broad to allow an ultrashort duration in the temporal domain. In the beginning of the millennium the first temporal characterization of the generated XUV pulses was performed [12, 13]. It revealed that the typical duration of the XUV pulses achieved through HHG is on the order of a few hundreds of attoseconds. In the temporal domain such pulses can be delivered in the form of a pulse train (APT) or as an isolated pulse (IAP). The reported ultra-short duration of the XUV pulses makes them an attractive tool for studying ultrafast dynamics in different targets. Thus, approximately one year after the first reported characterization, attosecond XUV pulses were for the first time used for an experiment performed in a pump-probe configuration [14]. In this experiment the lifetime of M-shell vacancies in Kr was measured. Even though attosecond pulses were used in this experiment, the studied dynamics occurred on the femtosecond timescale.

In order to access photoinduced dynamics occurring on the attosecond timescale, interferometric techniques such as RABBIT (Reconstruction of Attosecond Beating By Interference of two-photon Transitions) or attosecond streaking, originally used for the XUV pulse characterization, were applied [15]. In such experiments the photoionization delays corresponding to photoelectron wavepackets resulting from single XUV photon ionization of different targets were accessed [16, 17]. These delays result from the photoelectron interaction with the parent ion potential. The concept of such delays was introduced and studied by E. P. Wigner [18]. Thus, they are conventionally referred to as Wigner delays. From that perspective, attosecond photoionization pump-probe experiments are to a certain extent similar to electron scattering experiments [19, 20]. In both techniques the target potential is studied by measuring the scattered electron. In that sense, electron scattering and attosecond pump-probe spectroscopy are approaching similar problems in the frequency and time domains, respectively [21].

Here a brief description of a number of attosecond pump-probe spectroscopy experiments performed on isolated atoms or molecules reported in the literature is given. The present overview mainly focuses on results that are of a certain relevance for the experimental studies performed as a part of the present work.

Relatively large photoionization cross sections in the respective XUV photon energy range and low reactivity makes noble gases an attractive target for attosecond spectroscopy. Thus, a number of pioneering time-resolved experiments were focused on them. In these experiments one of the common approaches was to compare the photoionization delays corresponding to photoelectrons emitted from two different atomic orbitals. For example, M. Schultze *et al.* performed an experiment comparing the photoionization delays corresponding to ionization from 2p and 2s orbitals in Ne [22]. The measurement was performed with isolated attosecond pulses (attosecond streaking technique) with the spectrum spanning over the 100 to 140 eV range. Due to the relatively high XUV photon energy the ionization of Ne occurred from both 2p and 2s orbitals. Comparing the phases of the two oscillating signals in the obtained streaking spectrogram a 20 as delay difference was observed. A similar method was used by K. Klünder *et al.* for investigation of the difference between the photoionization delays corresponding to 3s and 3p shells in Ar [23]. It is also possible to compare the delays corresponding to ionization of two different atoms. For example, C. Palatchi *et al.* compared photoionization delays measured in Ne, Ar and Kr with those measured in He [24].

Another method is to scan the XUV photon energy over a spectroscopic feature under investigation, for example a resonance, by tuning the central wavelength of the near infrared (NIR) pulses used for HHG. Using this technique M. Swoboda *et al.* studied resonant XUV ± NIR two-photon ionization of He with attosecond pulse trains (RABBIT technique) [25]. In this experiment a resonance with the 1s3p state was scanned revealing a $\pi/2$ phase jump. A similar principle was used by M. Kotur *et al.* and C. Alexandridi *et al.* for the investigation of photoionization delays in Ar across a Fano resonance [26] and in the vicinity of a Cooper minimum [27], respectively.

Attosecond pump-probe spectroscopy experiments performed with angular resolved photoelectron detection revealed an angular dependence of the measured photoionization delays with respect to the laser polarization. Employing angle-resolved detection techniques, photoelectron angular distributions (PADs) were accessed in different targets. For example, S. Heuser *et al.* studied angular resolved photoionization delays in He [28]. The dependence of the measured delays on the emission angle observed in this experiment was attributed to NIR photon-induced continuum transitions. Photoionization delays measured with angular resolution in Ar and Ne are reported in Refs. [29, 30]. It was shown by D. Busto *et al.* that the angular dependence of photoionization delays measured in a RABBIT experiment is a consequence of Fano's propensity rule [31].

The photoionization dynamics in molecules is richer than that in atoms due to the existence of a large number of states. Thus, the experimental study of photoionization delays even in the simplest possible molecules — diatomic molecules — raise a certain challenge. Nevertheless, modern attosecond spectroscopy is capable of accessing ultrafast photoinduced dynamics in relatively large molecules, such as phenylalanine or tryptophan [32, 33]. Due to a possible overlap of photoelectron signals corresponding to different molecular states, the photoionization delays cannot always be accessed state-selectively. Here a number of pump-probe experiments performed in small molecules with state-selectivity are discussed. A series of pioneering experiments performed using attosecond pulses or pulse trains were focusing on nuclear dynamics occurring on the femtosecond timescale. For example, F. Kelkensberg *et al.* performed a vibrational state-resolved experiment on dissociative ionization of H_2 with IAPs [34]. The H^+ fragment kinetic energy distribution was measured as a function of the pump-probe delay. The observed delay-dependence was explained by NIR field induced fragmentation of H_2^+ ions at the outer turning points of the vibrational motion, revealing the coherence between the wavepacket vibrational components. M. Lucchini *et al.* and M. Eckstein *et al.* performed studies of the photoionization dynamics corresponding to highly excited states in N_2 [35–37]. In these experiments the N^+ fragment spectra were measured as a function of the pump-probe delay in a range of a few hundreds of femtoseconds revealing the NIR field induced couplings of highly excited states in N_2.

Another series of experiments was investigating the attosecond photoinduced electron dynamics in small molecules. For example, S. Haessler *et al.* studied the vibrational state-resolved photoionization delays corresponding to the X state of the N_2^+ ion using the RABBIT technique [38]. In this experiment a 0.9π phase difference between photoelectrons corresponding to the $\nu = 1$ and $\nu = 2$ vibrational states of the X state was observed. This effect was attributed to a resonance with an autoionizing state in the continuum. G. Sansone *et al.* investigated electron localisation following the dissociation of autoionizing states in H_2 with IAPs [39]. The observed asymmetry in the H^+ fragment yield along the laser polarization was attributed to the electron–nuclear coupled dynamics. For more examples of recent ultrafast time-resolved experiments in small molecules with state-selectivity please refer to the following works: A. Trabattoni *et al.* studied dissociative ionization of N_2 with angular resolved N^+ fragments detection [40]. M. Huppert *et al.* measured photoionization delays corresponding to valence shell ionization of N_2O and H_2O molecules [41]. A. Kamalov *et al.* compared the photoionization delays corresponding to the X, A and B states of the CO_2^+ ion revealing electron correlation effects [42]. S. Nandi *et al.* and V. Loriot *et al.* performed electronic state-resolved RABBIT measurements in N_2 comparing the photoionization delays corresponding to the X and A states of the N_2^+ ion [43, 44]. S. Fukahori *et al.* studied electron-nuclear coupled dynamics in dissociative ionization of O_2 by means of XUV pump–XUV probe spectroscopy [45].

When performing photoionization spectroscopy experiments in molecules it is advantageous to measure all the resulting photoelectrons and ions or ionic fragments in coincidence. The coincidence detection allows separation of the photoelectron signals corresponding to different ion species, that could not be resolved in another way. Also, for the dissociating channels, the recoil-axis can be determined, allowing access to the photoelectron angular distributions in the molecular frame. Here a number of photoionization experiments performed in diatomic molecules with coincidence detection using synchrotron radiation are briefly discussed, illustrating the wealth of information on the photoinduced processes under investigation that can be extracted from the measured molecular frame photoelectron angular distributions (MFPADs). For example, M. Schöffler *et al.* studied core hole localization in N_2^+ by measuring the Auger electron emission in the molecular frame [46]. C. Nicolas *et al.*, T. Aoto *et al.* and T. Ayari *et al.* performed experimental studies of the dissociative ionization of N_2 around $\sim [20, 40]$ eV XUV photon energy range [47–49]. An angle-resolved study of the XUV photoionization of N_2 and CO molecules was reported in Ref. [50]. It was recently shown that with the support of theoretical simulations, time-resolved information, such as photoionization delays, can be extracted from the MFPADs. Using this approach J. Rist *et al.* investigated core electron photoionization delays in CO in the molecular frame [51]. It is worth mentioning here a recent experiment on single X-ray photon double ionization of H_2. The coincidence detection of the two resulting H^+ fragments and both photoelectrons allowed access to the photoelectron angular distributions in the molecular frame. From the photoelectron interference pattern in the molecular frame a relative photoionization delay on the order of 250 zeptoseconds (10^{-21} s) between the two photoelectrons was retrieved [52]. This result is a huge achievement on the way towards establishing the field of zeptosecond spectroscopy.

In order to study ultrafast photoionization dynamics in molecules it is advantageous to combine attosecond XUV laser pulses with coincidence detection. A number of experiments employing the combination of these two techniques for studying photoionization dynamics in diatomic molecules were reported. For example, L. Cattaneo *et al.* studied the dissociative ionization of H_2 [53]. The photoelectron distributions were accessed in the molecular frame revealing the orientation dependence of the photoionization delays together with coupled electron and nuclear dynamics. J. Vos *et al.* investigated orientation dependent, or stereo Wigner delays in the molecular frame of the CO molecule [54], theoretically predicted by P. Hockett *et al.* [55]. Approximately 20 as or up to 150 as photoionization delay difference between the photoelectrons emitted from the carbon and oxygen sides was measured for perpendicular and parallel alignment of the CO molecules with respect to the laser polarisation, respectively. Since in this experiment the photoelectron spectral lines corresponding to different electronic states were overlapping, a state-selective analysis was not possible, and the extracted delays were effectively integrated over several states.

In order to access the photoinduced dynamics with attosecond resolution in targets with increasing complexity, a number of experimental beamlines combining a high repetition rate HHG-based tabletop XUV laser pulse source with a coincidence detector have been recently reported. A 10 kHz system operating at 800 nm central wavelength and delivering 28 fs pulses was developed at the ETH Zurich, Switzerland [56, 57]. Another 10 kHz system driven with 30 fs pulses at 800 nm central wavelength is located at the Albert-Ludwigs-Universität Freiburg, Germany [58]. In this setup the pump and probe beams in the interferometer are collinear, which is advantageous for long-term stability. A 200 kHz system utilizing 5.8 fs pulses at 850 nm central wavelength is hosted in Lund, Sweden [59]. A system with tunable repetition rate operating at 1030 nm central wavelength and allowing pulse compression down to $< 8\,\mathrm{fs}$ is located in Heidelberg, Germany [60, 61]. In order to preserve sufficient pulse energy, a 49 kHz repetition rate and 40 fs pulse duration were chosen for recently reported experiments in H_2 performed using this beamline. Also several setups with similar characteristics were recently developed in China [62, 63].

In the present work a high repetition rate beamline combining an HHG-based attosecond pulse source with a Reaction Microscope developed at the Max-Born-Institut in Berlin is reported. A 100 kHz repetition rate laser pulse source operating at 800 nm central wavelength serving as a driver for the beamline is capable of delivering laser pulses with 7.2 fs or 3.3 fs durations [64]. Using these NIR pulses for HHG, few-pulse attosecond pulse trains (APTs) or isolated attosecond pulses (IAPs) can be generated, respectively. These XUV pulses can be used for time-resolved pump-probe attosecond spectroscopy experiments performed with coincidence detection.

Using the reported beamline a RABBIT experiment was performed in N_2. Due to the coincidence detection capabilities photoionization delays corresponding to the predissociative $C\,^2\Sigma_u^+$ state were measured with vibrational states resolution. The reported study complements the existing data on photoionization dynamics in N_2 covering the $C\,^2\Sigma_u^+$ state of the N_2^+ ion, to the best of our knowledge, never previously accessed in the time domain.

Over two decades after the first temporal characterization of XUV pulses, they have proven to be an excellent tool for studying ultrafast photoinduced dynamics establishing the field of attosecond science. Modern sophisticated experimental beamlines developed all over the world allow experiments in different targets with increasing complexity. For an overview of the recent advances in the field of attosecond science please refer to publications by F. Calegari *et al.* [65] and by J. Biegert *et al.* [66], and for an overview of studies on electron dynamics in molecules please refer to the publication by M. Nisoli *et al.* [67]. Despite the significant development of experimental tools in the arsenal of the attosecond community, accessing ultrafast dynamics in complex molecules state-selectively is still extremely challenging from both an experimental and theoretical perspectives. Hopefully, in the coming years novel techniques developed by a joint effort of experimentalists and theoreticians would allow approaching such problems with unprecedented resolution.

2

THEORETICAL BASIS

Chapter 2 gives a brief overview of theoretical concepts necessary for understanding not only the ultrafast photoinduced dynamics studied in the present work, but also the experimental methods allowing accessing it. The overall complexity of the performed experiments implies that a number of different topics have to be covered. In order to keep the structure clear, the present chapter is split in sections, each covering a separate problem. The sections are organized as follows:

Section 2.1 focuses on ultrashort laser pulses and their interaction with a dispersive medium. A wavepacket representation of ultrashort laser pulses is introduced in Section 2.1.1. The interaction of ultrashort laser pulses with a dispersive medium and spectral broadening by self phase modulation (SPM) are discussed in Section 2.1.2 and Section 2.1.3, respectively. The section is closed with a description of the high-order harmonic generation process in a gas medium given in Section 2.1.4.

Section 2.2 describes photoelectron wavepackets and their interaction with a potential. Starting from a classical picture of a particle travelling through a potential given in Section 2.2.1, the analysis is extended to a quantum mechanical picture of a photoelectron wavepacket travelling through a potential in Section 2.2.2. In Section 2.2.3 the concept of the Eisenbud-Wigner-Smith delay is introduced. The photoelectron wavepacket phase shifts induced by a long range Coulomb potential and by a short range potential of an ion are discussed in Section 2.2.4 and Section 2.2.5, respectively.

In Section 2.3 a brief introduction to photoionization of atomic gases is given. Section 2.3.1 contains an overview of photoionization selection rules in atoms. Since helium and argon were used as experimental targets for photoionization experiments reported in the present thesis, a brief overview of their properties is given in Section 2.3.2 and Section 2.3.3, respectively.

Since molecular nitrogen was the main experimental target studied in the present work, Section 2.4 describes properties of homonuclear diatomic molecules and their photoionization. A discussion of molecular stationary states is given in Section 2.4.1. Section 2.4.2 focuses on vibrational states in homonuclear diatomic molecules. Section 2.4.3 describes the conventional multielectron states notation and Section 2.4.4 gives an overview of photoionization selection rules in homonuclear diatomic molecules. Section 2.4.5 contains a brief description of the Franck-Condon principle. The section is closed with an overview of the properties of molecular nitrogen given in Section 2.4.6, with an emphasis on the molecular states involved in the photoinduced transitions under investigation.

Finally, Section 2.5 describes the main principles of ultrafast pump-probe spectroscopy, which is the experimental method used in the present work. Starting from basic principles of ultrafast measurements given in Section 2.5.1, the discussion is extended by a qualitative picture of a RABBIT experiment and a classical picture of an attosecond streaking experiment given in Section 2.5.2 and Section 2.5.3, respectively. In order to develop a quantum mechanical picture of an ultrafast measurement, in Section 2.5.4 the quantum mechanical problem of an atom in an external electric field is solved in the framework of first-order perturbation theory. Using a dipole transition matrix representation, briefly introduced in Section 2.5.5, the quantum mechanical description of ultrafast pump-probe spectroscopy measurements is derived in Section 2.5.6. Spectrograms acquired from ultrafast pump-probe spectroscopy measurements contain information on both the ultrafast photoinduced dynamics in a target and the properties of the laser pulses used. Thus, the pulse characterization and the phase information extraction from the measured spectrograms are discussed in Section 2.5.7 and Section 2.5.8, respectively. The chapter is concluded by Section 2.5.9 containing an analysis of the influence of the probe NIR intensity on the shape of RABBIT spectrograms and on the phase information extracted from them.

2.1 ULTRASHORT LASER PULSES

Ultrashort laser pulses in the near infrared (NIR) spectral range with typical durations on the femtosecond timescale have become a powerful tool for time-resolved spectroscopy of different photoinduced processes [8, 9]. The respective temporal resolution allows studying photoinduced nuclear dynamics, while electronic dynamics with characteristic time scales on the order of tens to hundreds of attoseconds are not accessible by the femtosecond spectroscopy. The discovery of the high-order harmonic generation (HHG) process in noble gases allowed the generation of laser pulses in the extreme ultraviolet (XUV) spectral range with durations on the order of hundreds of attoseconds [10–12]. With these attosecond pulses photoinduced electronic dynamics can be studied by time-resolved pump-probe spectroscopy involving either one XUV and one NIR pulse, or two XUV pulses.

In the present section a theoretical description of ultrashort laser pulses together with the conventional physical quantities describing their properties are discussed. Then the principles of nonlinear optical effects in a dispersive medium and their applications for manipulating the ultrashort laser pulse properties are briefly described. Finally, an overview of the physical mechanisms underlying the high-order harmonic generation process, together with the properties of the generated XUV attosecond pulses are given.

2.1.1 *Wavepacket representation*

A wavepacket representation is extremely useful for describing both ultrashort laser pulses and photoelectron wavepackets resulting from their interaction with atomic or molecular targets. In the present section a brief introduction to important concepts and quantities describing a wavepacket is given. The section opens with a description of an ultrashort laser pulse. The discussion given in the present section partially follows the textbook by J.-C. Diels and W. Rudolph [68]. In what follows real quantities, such as an electric field strength E, are written without a hat, while complex quantities, such as a complex electric field $\tilde{E}$, are written with a tilde hat.

In general, light is an electromagnetic wave, which means that it has electric and magnetic field components related by the Maxwell equations. For a laser pulse, the interaction of the electric field with matter is much stronger than that of the magnetic field. Thus, in the following discussion the magnetic field is omitted, and the real electric field strength as a function of time $E(t)$ is chosen as a suitable quantity for describing the laser pulse in the time domain. From

$E(t)$ the complex spectrum of the pulse $\tilde{E}(\omega)$ is defined through the Fourier Transform ($\mathcal{F}$):

Laser pulse complex spectrum.

$$\tilde{E}(\omega) = \mathcal{F}\{E(t)\} = |\tilde{E}(\omega)|e^{i\Phi(\omega)} \tag{1}$$

Here for each angular frequency component ω, $|\tilde{E}(\omega)|$ is the spectral amplitude and $\Phi(\omega)$ is the phase. It is convenient to separate $\tilde{E}(\omega)$ in two parts: $\tilde{E}(\omega) = \tilde{E}^{+}(\omega) + \tilde{E}^{-}(\omega)$, spanning over positive and negative angular frequencies, respectively. The corresponding $\tilde{E}^{+}(t)$ and $\tilde{E}^{-}(t)$ can be obtained through an inverse Fourier Transform ($\mathcal{F}^{-1}$). Then the real electric field is given by $E(t) = \tilde{E}^{+}(t) + \tilde{E}^{-}(t)$.

The spectral bandwidth of the laser pulse $\Delta\omega$ is defined as the angular frequency range in which the values of the spectral amplitude $|\tilde{E}(\omega)|$ are exceeding a certain threshold relative to the maximum amplitude $|\tilde{E}_{max}|$, for example a 10 dB level. The central angular frequency ω_0 is conventionally defined as the intensity-weighted mean of ω over that range. In some cases ω_0 is assigned as the carrier angular frequency at the maximum of the pulse envelope. If the spectral bandwidth of the pulse $\Delta\omega$ is much smaller than the central angular frequency ω_0, it is convenient to represent the $\tilde{E}^{+}(t)$ as the product of amplitude and phase terms:

Laser pulse in the time domain.

$$\tilde{E}^{+}(t) = \frac{1}{2}\mathcal{E}(t)e^{i\phi_0}e^{i\phi(t)}e^{i\omega_0 t} \tag{2}$$

In such a representation $\mathcal{E}(t)$ is the real field envelope and $\phi(t)$ is the time-dependent phase. The time-independent phase term ϕ_0 is relevant only for ultrashort laser pulses. It is referred to as the Carrier Envelope Phase or CEP. The CEP becomes extremely important when working with few-cycle laser pulses, because in that case it controls the maximum electric field amplitude. For example, in Fig. 1 two single-cycle Gaussian shape pulses with different CEPs are shown. In this Figure the electric field as a function of time was set as $E(t) = e^{-2\ln 2(t/\tau_{FWHM})^2}\cos(2\pi t + \phi_0)$, where the time t is measured in electric field oscillation periods, and τ_{FWHM} is the full width at half maximum (FWHM) of the intensity envelope ($I(t) \propto E(t)^2$). Inserting $\tau_{FWHM} = 1$ in the above equation a single cycle laser pulse is described. In Fig. 1 (a) such pulse with $\phi_0 = 0$ is shown. This laser pulse has a single maximum intensity peak positioned at the envelope centre. Thus, such a laser pulse is referred to as a *cosine* pulse. On the contrary, a pulse with the same envelope but with $\phi_0 = \pi/2$, shown in Fig. 1 (b), has two equivalent intensity peaks positioned symmetrically with respect to the centre of the pulse envelope. Such a laser pulse is referred to as a *sine* pulse. The two pulses shown in Fig. 1, even though they are spectrally identical, would lead to a drastically different outcome when interacting with matter. For example, when

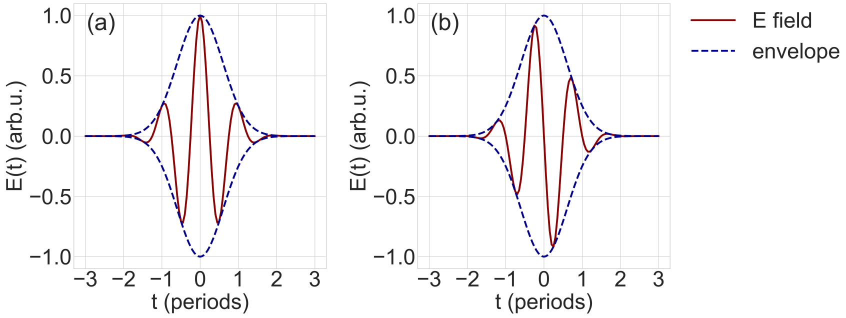

Figure 1: A schematic illustration of a cosine ($\phi_0 = 0$) *(a)* and a sine ($\phi_0 = \pi/2$) *(b)* shape single cycle laser pulse with a normalized electric field amplitude. The electric field is shown as a red solid line and the pulse envelope is shown as a blue dashed line. In both cases the pulse envelope has a Gaussian shape, and the intensity FWHM is equal to one period of the electric field oscillations. For more details please refer to the main text.

used for high-order harmonic generation, in the cut-off region of the HHG spectrum (see Section 2.1.4) these pulses would generate an isolated attosecond pulse or a pulse train consisting of two identical attosecond pulses, respectively. Because of that, the CEP should be controlled when working with few-cycle or single-cycle laser pulses.

Now let us have a closer look at the time-dependent phase $\phi(t)$ in Eq. 2. In the vicinity of $t = 0$, $\phi(t)$ can be expanded in a Taylor series as follows:

Taylor expansion of the optical phase in the time domain.

$$\phi(t) = \frac{d}{dt}\phi(t)\bigg|_0 \frac{t}{1!} + \frac{d^2}{dt^2}\phi(t)\bigg|_0 \frac{t^2}{2!} + \ldots \tag{3}$$

Here the zero-order term is not included since it was separated as the time-independent phase term ϕ_0 in Eq. 2. In this expansion the first-order term establishes the instantaneous carrier angular frequency $\omega(t) = \omega_0 + \frac{d}{dt}\phi(t)$. The second-order term $\frac{d^2}{dt^2}\phi(t)$ describing how the carrier angular frequency varies as a function of time is called Chirp. If $\frac{d^2}{dt^2}\phi(t) \gtrless 0$, the carrier frequency increases/decreases with time, and thus the laser pulse is called positively/negatively chirped.

Similar to Eq. 2 the laser pulse can be described in the frequency domain:

Laser pulse in the frequency domain.

$$\tilde{E}^+(\omega) = \frac{1}{2}\mathcal{E}(\omega)e^{i\phi_0}e^{i\phi(\omega)}e^{i\omega_0 t} \tag{4}$$

Taylor expansion of the optical phase in the frequency domain.

Expanding $\phi(\omega)$ in a Taylor series in the vicinity of the central frequency $\omega = \omega_0$ one gets:

$$\phi(\omega) = \frac{d}{d\omega}\phi(\omega)\bigg|_{\omega_0} \frac{\omega-\omega_0}{1!} + \frac{d^2}{d\omega^2}\phi(\omega)\bigg|_{\omega_0} \frac{(\omega-\omega_0)^2}{2!} + \ldots \quad (5)$$

Analogous to Eq. 3, here the zero-order term is not included since it was separated as the angular frequency-independent phase term ϕ_0 in Eq. 4. In this expansion the first-order term $\tau_{GD}(\omega) = \frac{d}{d\omega}\phi(\omega)$ conventionally called Group Delay (GD) can be interpreted as the time at which all angular frequency components in the vicinity of ω are interfering constructively. The second-order term $\frac{d^2}{d\omega^2}\phi(\omega)$ is called Group Delay Dispersion (GDD). It is conventionally used for the description of chromatic dispersion of a medium.

In both time and frequency domains the first two terms in the Taylor expansions shown in Eq. 3 and Eq. 5 are usually sufficient for describing the linear propagation of a narrowband laser pulse. For description of a broadband laser pulse higher order terms become necessary. For a given spectrum $E(\omega)$ the shortest compressed pulse possible in the time domain $E(t)$ corresponds to the Fourier Transform limited pulse. For fully compressed pulses, as a general rule, shorter pulses require broader spectrum, which can be understood as a consequence of the Fourier Transform properties.

2.1.2 *Photon wavepacket in a medium*

In the present section a brief description is given on how propagation in a medium affects the laser pulse properties. In what follows the equations are written in atomic units. The discussion given in the present section partially follows the publication by J. M. Dahlström *et al.* [69].

Fourier Transform of a wave equation.

Propagation of a photon wavepacket in a dielectric medium can be described by the Fourier Transform of a wave equation, derived from the Maxwell equations:

$$\nabla^2\vec{E}(\omega,\vec{r}) + \frac{\omega^2}{c^2}\vec{E}(\omega,\vec{r}) = -\frac{1}{\epsilon_0}\frac{\omega^2}{c^2}\vec{P}(\omega,\vec{r}) - \frac{1}{\epsilon_0}\nabla\left(\nabla\cdot\vec{P}(\omega,\vec{r})\right) \quad (6)$$

Here ϵ_0 is the vacuum dielectric permittivity, c is the speed of light in vacuum, and $\vec{E}(\omega,\vec{r})$ and $\vec{P}(\omega,\vec{r})$ are the electric field of the laser pulse and the polarization of the medium as a function of the angular frequency ω and position $\vec{r}$, respectively. For simplicity, the problem is reduced down to a two-dimensional case with corresponding Cartesian axes assigned as x and z. Let us assume that the laser pulse is propagating along the x-axis, or in other words $\vec{k} \parallel \vec{x}$, where $\vec{k}$ is the wave vector of the propagating electromagnetic field, and $\vec{x}$ is a unit vector collinear with the x-axis. The linear polarization of the laser pulse is parallel to the z-axis ($\vec{E} \parallel \vec{z}$). Then the electric field of the laser pulse can be defined as $\vec{E}(\omega, \vec{r}) = E(\omega, x) \cdot \vec{z} = \mathcal{E}(\omega) e^{i\phi(\omega,x)} \cdot \vec{z}$, where $\mathcal{E}(\omega)$ is the real positive amplitude of each angular frequency component in the wavepacket, $\phi(\omega, x)$ is the angular frequency- and position-dependent phase, and $\vec{z}$ is a unit vector collinear with the z-axis. Assuming that the laser field is relatively weak, the polarization can be approximated as depending linearly on the laser field strength: $\vec{P}(\omega, \vec{r}) = \epsilon_0 \chi^{(1)}(\omega, x)\vec{E}(\omega, \vec{r})$, where $\chi^{(1)}(\omega, x)$ is the first-order susceptibility of the medium. The first order susceptibility $\chi^{(1)}(\omega, x)$ is defined as a function of the position x since the medium could be anisotropic. Applying $\vec{E}(\omega, \vec{r})$ and $\vec{P}(\omega, \vec{r})$ as defined above into Eq. 6 it can be rewritten as follows:

One dimensional equation for a linear response.

$$\frac{\partial^2}{\partial x^2} E(\omega, x) + \frac{\omega^2}{c^2} E(\omega, x) = -\frac{\omega^2}{c^2} \chi^{(1)}(\omega, x) E(\omega, x) \tag{7}$$

The last term on the right hand side of Eq. 6 vanishes since $\nabla \cdot \vec{P}(\omega, \vec{r}) = 0$, as directly follows from the definition of $\vec{P}(\omega, \vec{r})$. Applying $E(\omega, x)$ as defined above into Eq. 7 one gets:

Equation for the optical phase.

$$i\frac{\partial^2}{\partial x^2}\phi(\omega, x) - \left(\frac{\partial}{\partial x}\phi(\omega, x)\right)^2 + \frac{\omega^2}{c^2} = -\frac{\omega^2}{c^2}\chi^{(1)}(\omega, x) \tag{8}$$

Let us assume that the optical properties of the medium vary slowly with respect to the photon wavelength λ, which implies that $\left|\frac{\partial^2}{\partial x^2}\phi(\omega, x)\right| \ll \left|\frac{\partial}{\partial x}\phi(\omega, x)\right|^2$. Then we can neglect the second-order partial derivative term in Eq. 8 and derive a differential equation for the phase $\phi(\omega, x)$ as follows:

Simplified equation for the optical phase.

$$\frac{\partial}{\partial x}\phi(\omega, x) = \frac{\omega}{c}\sqrt{\chi^{(1)}(\omega, x) + 1} = \frac{\omega}{c} n(\omega, x) \tag{9}$$

Here $n(\omega, x)$ is the position- and angular frequency-dependent refractive index of the medium. In order to calculate the phase $\delta\phi(\omega)$ acquired by the angular frequency component ω when travelling through the medium, the following integral should be calculated:

Accumulated optical phase.

$$\delta\phi(\omega) = \lim_{x\to\infty} \frac{\omega}{c} \int_{-\infty}^{x} (n(\omega, x') - 1) dx' \tag{10}$$

Here we make an assumption that the medium has a finite length, and that outside the medium the laser pulse is propagating in vacuum. Thus, the refractive index outside the medium is equal to 1. If the medium is non-dispersive, or in other words the refractive index $n(\omega, x)$ can be approximated as frequency-independent over the spectral bandwidth of the laser pulse $\Delta\omega$, the acquired phase $\delta\phi(\omega)$

depends linearly on the angular frequency ω. It means that if the laser pulse travels through the non-dispersive medium, it gets *delayed*, but the overall shape of the intensity envelope in the time domain remains unchanged. Since the intensity envelope of the laser pulse is preserved, the concept of a delay τ induced by propagation in the non-dispersive medium can be introduced. In order to define such delay let us describe a thought experiment where two initially identical laser pulses are launched simultaneously. One of the pulses, which we assign as a *free* pulse, propagates in vacuum, while another one travels through the non-dispersive medium, so we assign it as a *delayed* pulse. Then, at a randomly chosen position outside the medium the arrival times of both pulses are measured as times when the pulse intensity envelope peak in the time domain reach the measurement position. Measured this way, the resulting delays are independent of the measurement position. Then the delay τ induced by propagation in the non-dispersive medium is equal to $\tau = t_{delayed} - t_{free}$, where t_{free} and $t_{delayed}$ are the measured arrival times of the *free* and *delayed* laser pulses, respectively.

If the frequency dependence of the refractive index $n(\omega, x)$ cannot be neglected, as in the case of a broadband laser pulse propagating in a dispersive medium, the acquired phase $\delta\phi(\omega)$ (Eq. 10) is no longer linearly depending on the angular frequency ω. For example, if the angular frequency dependence of the refractive index can be approximated as linear $n(\omega, x) = n_0(x) + n_1(x) \cdot \omega$ over the spectral bandwidth of the laser pulse $\Delta\omega$, the acquired phase $\delta\phi(\omega)$ depends quadratically on the angular frequency ω. As a result, the laser pulse gets *chirped*, or in other words for $n_1 > 0$, which is true for the majority of materials in the near infrared, visible and ultraviolet spectral ranges, higher/lower angular frequencies are retarded/accelerated with respect to the central angular frequency ω_0 in the medium. Even though this affects the pulse duration, the overall shape of the intensity envelope in the time domain remains unchanged. Thus, the concept of a delay introduced above can still be applied in that case. On the other hand, if second- and higher-order terms are necessary for the description of the angular frequency dependence of the refractive index of the medium, the shape of the laser pulse intensity envelope evolves during the propagation. Thus, the concept of a delay is no longer applicable.

2.1.3 *Pulse compression using gas-filled hollow core fiber*

The shortest possible duration of a laser pulse corresponds to a Fourier Transform of its spectrum (see Section 2.1.1). Thus, in order to further compress a laser pulse it is necessary to broaden its spectrum. Among other techniques, spectral broadening can be performed using a gas-filled hollow core fiber. This method was used in the present work for the compression of laser pulses delivered by a Titanium Sapphire oscillator down to a single-cycle regime, which is necessary for the isolated attosecond pulse generation. In the present section a brief discussion of ultra short laser pulse compression using a gas-filled hollow core fiber is given. The present section partially follows the textbook by J.-C. Diels and W. Rudolph [68].

The gas-filled hollow core fiber is a capillary made of an optically transparent material, such as fused silica, with inner volume filled with gas. A laser pulse propagating through the fiber is reflected multiple times by the fiber inner surface at grazing incidence angles. Such reflections preserve the fundamental mode and significantly suppress higher-order modes. Thus, only the fundamental mode is transmitted through a long hollow core fiber. The suppression of higher-order modes provides high beam quality and spatio-temporal homogeneity. One of the important properties of hollow core fibers, is that at certain conditions they can preserve a single laser mode over large distances. Such fibers are called single-mode fibers. The core radius of a single-mode fiber R should be in agreement with the following inequality: $R < \lambda_0/(\pi\sqrt{n_g^2 - n_c^2})$, where n_c and n_g are the refractive indices of the capillary material and the gas medium, respectively, and λ_0 is the central wavelength of the laser pulse. The advantage of gas-filled hollow core fibers is that since n_g can be controlled by changing the gas medium type and pressure, it is possible to tune the nonlinearity of the medium such, that the spectral phase acquired by the laser pulse over propagation is as close as possible to a linear spectral phase. This allows easier re-compression of the laser pulses after the fiber.

The principle of the laser pulse spectral broadening in the gas-filled hollow core fiber is based on the Kerr effect — the dependence of the refractive index of the material on the applied electric field intensity of the following form: $n(I) = n_0 + n_2 I$. Here n_0 and n_2 are the linear and nonlinear refractive indices, respectively, and $I = |\vec{E}|^2$ is the intensity of the electric field. When a compressed pulse enters the fiber, the long wavelengths travel faster through the medium than the short wavelengths due to dispersion, thus introducing a chirp to the laser pulse (Eq. 10). Taking into account the intensity dependence of the refractive index, the instantaneous phase of the laser pulse $\phi_{inst}(t)$ can be described in the coordinate system defined in Section 2.1.2 as follows:

Instantaneous phase.

$$\phi_{inst}(t) = \omega_0 t - k_0 x = \omega_0 t - \frac{2\pi}{\lambda_0} \cdot n(I) \cdot L \qquad (11)$$

Here ω_0 is the central angular frequency of the laser pulse with the corresponding wave vector k_0 and central wavelength λ_0, while L is the propagation length in the medium. The instantaneous phase $\phi_{inst}(t)$ is related to the time-dependent phase $\phi(t)$ defined in Section 2.1.1 as $\phi_{\mathrm{inst}}(t) = \omega_0 t + \phi(t)$. Then the instantaneous angular frequency $\omega(t)$ can be calculated from the following equation:

Instantaneous angular frequency.

$$\omega(t) = \frac{d\phi_{\mathrm{inst}}(t)}{dt} = \omega_0 - \frac{2\pi L}{\lambda_0} \cdot \frac{dn(I)}{dt} = \omega_0 - \frac{2\pi L n_2}{\lambda_0} \cdot \frac{dI(t)}{dt} \quad (12)$$

Here $I(t)$ is the time-dependent intensity of the laser field. This effect is called Self Phase Modulation (SPM). As visible from Eq. 12, due to SPM new lower/higher frequencies are generated on the leading/tailing edge of the laser pulse envelope in the time domain, since there $\frac{dI(t)}{dt} \gtrless 0$, respectively. Generation of new frequencies results in broadening of the laser pulse spectrum. This effect is limited since stretching of the laser pulse is decreasing the instantaneous electric field intensity. A broader laser pulse spectrum allows achieving shorter pulses in the time domain after compression. The pulse compression can be performed with conventional compression tools, such as a prism pair or a set of chirped mirrors.

The first experimental demonstration of laser pulse spectral broadening in a gas-filled hollow core fiber was reported by M. Nisoli *et al.* [70]. Starting from laser pulses with 140 fs duration delivered by a Chirped Pulse Amplification system, pulse compression down to 10 fs with pulse energy on the order of 35 % of the initial pulse energy was achieved. In modern systems the gas-filled hollow core fiber technology allows achieving high energy pulses with a few optical cycles pulse durations in different spectral ranges [71–73].

In the beamline used for the experiments reported in the present thesis, a hollow core fiber was implemented with a gas medium pressure gradient. In such an arrangement the pressure gradient is parallel to the laser pulse propagation direction, i.e. lower/higher gas pressure exist at the entrance/exit of the fiber. This technique not only inhibits unwanted excessive ionization at the entrance of the fiber, such as plasma formation, but also partially compensates for the drop of the nonlinearity induced by the decrease of the peak intensity over the laser pulse propagation in the fiber [74].

2.1.4 *High-order harmonic generation*

High-order harmonic generation (HHG) is a well-established technique allowing to achieve isolated attosecond pulses (IAPs) with typical duration on the order of a couple of hundreds of attoseconds or even shorter, or trains of such pulses (APTs). The most developed technique for HHG is generation in a medium formed by a noble gas [10, 11]. HHG is also possible in liquids or solids, which is currently an actively studied research topic [75, 76]. Since for the experiments reported in the present thesis, the high-order harmonics were generated in a noble gas medium, in the following discussion only this method is covered. From the experimental point of view, in order to achieve HHG, intense NIR pulses with duration on the order of picoseconds or shorter should be focused in an atomic gas jet. The NIR field peak intensity in the focus should reach $10^{14}\,\mathrm{W/cm^2}$ or higher. Then high energy photons in the extreme ultraviolet (XUV) or soft X-ray spectral region, with energies in the range from tens of eVs up to a keV, are generated and emitted coherently. Since in the respective photon energy range any bulk material or even air is strongly absorbing, the XUV beamlines have to be built in vacuum.

The basic principle of high-order harmonic generation can be understood in the framework of a semi-classical three-step model [77, 78]. This model is established using the single active electron (SAE) approximation, which implies that an atom or molecule is approximated as a system containing a single electron and a hydrogenic potential of an ion composed of a positively charged core shielded with the remaining bound electrons. In the framework of the SAE approximation all photoinduced processes, such as photon absorption, involve only one electron and do not induce complex correlated multielectron effects. The interaction of such a simplified system with the laser pulse electric field is schematically shown in Fig. 2. The mechanism of the three-step model describing interaction is the following:

Three step model.

- *First step*, the electric field of the laser pulse is bending the Coulomb potential of the ion. Close to the peak of the electric field the potential barrier is suppressed enough for the electron to tunnel through it. In the framework of the three-step model the interaction of the continuum electron with the Coulomb potential of the parent ion after tunnelling is neglected (Strong Field Approximation, SFA).
- *Second step*, the free continuum electron is accelerated by the electric field of the laser pulse. After a quarter of a period the electric field changes sign. Thus, the electron is slowed down and driven back towards the parent ion.
- Then the final *third step*, the electron recombines with the parent ion and emits all its energy as an XUV photon. The energy of the emitted photon is equal to the energy that the electron has gained while driven by the electric field of the laser pulse, plus the ionisation potential of the ion.

The cycle-averaged energy of a free electron in the electric field of the laser pulse, also called ponderomotive energy, can be calculated as follows:

Ponderomotive energy.

$$U_p = \frac{e^2 E_0^2}{4 m \omega_0^2} = \frac{e^2 E_0^2}{16 m \pi^2 c^2} \lambda_0^2 \tag{13}$$

Here E_0 is the electric field amplitude, c is the speed of light, e and m are the electron charge and mass, and ω_0 and λ_0 are the

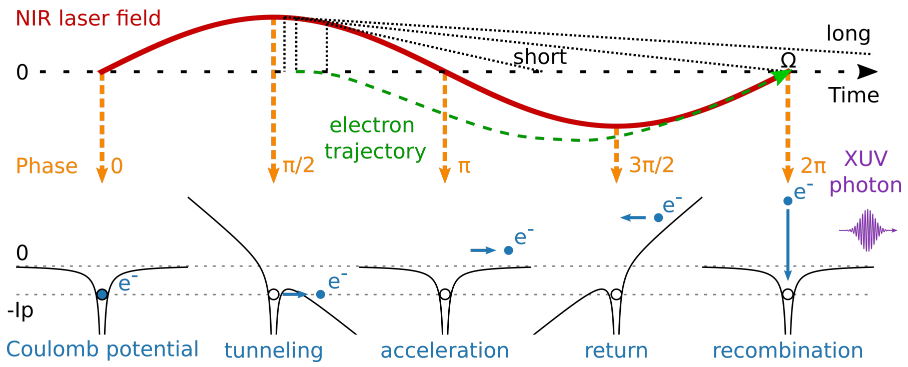

Figure 2: A schematic illustration of the three-step model: 1 — tunnelling — the electron tunnels through the bent Coulomb potential barrier of the parent ion close to the maximum of the electric field of the laser pulse; 2 — acceleration and return — the electron is driven away from the ion and accelerated by the electric field of the laser pulse until the electric field changes direction and the electron is driven back towards the ion; 3 — recombination — the electron recombines with the parent ion and all the energy it has gained in the electric field is emitted as a single high energy photon. The NIR electric field is shown as a solid red line, the corresponding sin phases are shown in orange, the electron trajectory corresponding to generation of a photon with maximum energy Ω is shown as a dashed green arrow, and the Coulomb potential of the ion is shown in black. The black dotted tangent lines to the NIR electric field illustrate the electron tunnelling and recombination times for short, long and maximum photon energy Ω trajectories, respectively.

central angular frequency and corresponding central wavelength of the laser pulse, respectively. U_p is proportional to the square of the central wavelength of the laser pulse. A typical HHG spectrum contains two distinct spectral regions: a plateau corresponding to harmonic spectral lines with approximately equal intensity, and a cutoff region corresponding to a fast decay of the harmonic intensity with XUV photon energy. The maximum photon energy generated $\Omega = Ip + 3.17U_p$, where Ip is the ionization potential of the generating medium gas. This means that if the harmonics are generated with a longer/shorter central wavelength laser pulse, the maximum photon energy generated Ω is higher/lower, since the ejected electron acquires more/less energy while travelling in the electric field (see Eq. 13). For all generated photon energies smaller than Ω two distinct electron trajectories exist: a short and a long trajectory, carrying positive and negative chirp, respectively [79]. Tangential lines to the NIR electric field curve can be used as a simple illustration of the electron tunnelling and recombination times as shown in Fig. 2. For such tangential lines the tunnelling and recombination times correspond to the tangent and crossing with the time axis points, respectively. In Fig. 2 such tangential lines illustrating tunnelling and recombination

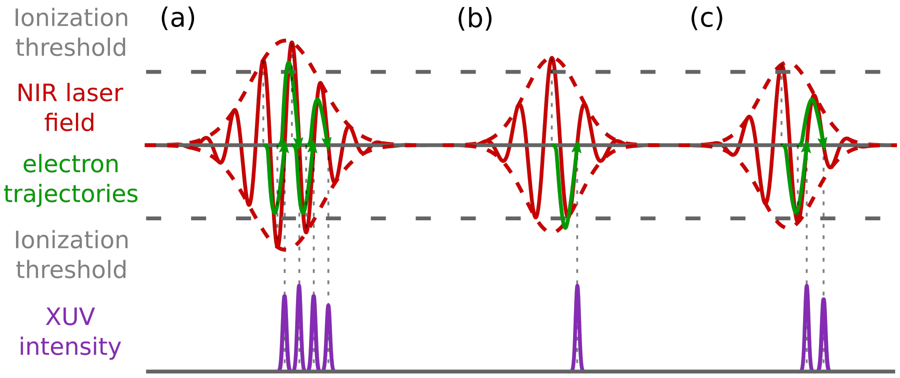

Figure 3: Schematic illustration of the temporal profiles of XUV pulses generated using different NIR laser pulses. *(a)* an attosecond pulse train generated using a few-cycle NIR pulse, *(b)* an isolated attosecond pulse generated with a cosine shape single cycle NIR pulse, *(c)* a pulse train consisting of two attosecond pulses generated with a sine shape single cycle NIR pulse. The NIR pulses in *(b)* and *(c)* have the same envelope but different CEPs. The electric fields of the NIR laser pulses are shown as a solid red lines, the corresponding pulse envelopes are shown as dashed red lines, the electron trajectories are shown as green arrows, and the XUV pulse intensity envelopes are shown in violet.

times for the short, long and maximum photon energy Ω trajectories are shown.

The group delay of the generated XUV pulses or pulse trains depends on the NIR field peak intensity. In general, XUV pulses generated at lower/higher NIR intensities have bigger/smaller group delays in the range from tens to hundreds of attoseconds [80].

Since for experimental applications a big number of XUV photons should be emitted in phase from a whole generation volume, phase-matching becomes crucial. Phase-matching can be optimized by changing the generating medium density or the intensity of the NIR field, for example by changing the focusing conditions. Changing the position of the NIR laser focus with respect to the generating medium one can favour phase-matching for short or long trajectories. For the experiments short electron trajectories are conventionally preferred.

The temporal profile of generated XUV pulses depends on the properties of the NIR pulses used for generation. Bursts of XUV photons are generated every half cycle of the NIR pulse as long as the strength of the NIR pulse electric field exceeds the ionization threshold of the generating medium. Thus, as shown in Fig. 3 (a), with a few-cycle NIR pulse an XUV attosecond pulse train is generated. The spectrum of the attosecond pulse train has the form of a series of discrete spectral lines centred at photon energies corresponding to odd harmonics of the central angular frequency of the NIR pulse used for generation. Since for a system with spherical symmetry the polarization $P(E) = -P(-E)$, even harmonics are cancelled out. The harmonic spectrum can be understood as the result of an interference of individual pulses in the attosecond pulse train. In general, generating APTs with long/short NIR laser pulses (with FWHM on the order of tens/a few laser periods) the resulting XUV spectrum consists of narrow/broad harmonic spectral lines.

The spectrum of an isolated attosecond pulse is smooth and spanning over several eV. In order to generate an IAP, the electric field strength of the NIR pulse used for generation should exceed the ionization threshold only once. This condition is met by few-cycle laser pulses with a controlled CEP. An example of such a pulse, conventionally called a *cosine* pulse, is shown in Fig. 3 (b). Changing the CEP of this pulse by $\pi/2$ results in a *sine* pulse with two equivalent intensity peaks, as shown in Fig. 3 (c). Thus, using the sine pulse for HHG results in a short XUV pulse train consisting of a pair of pulses. Using few-cycle laser pulses with identical envelopes but different CEPs for HHG results in drastically different temporal profiles of the generated XUV pulses. Thus, for the generation of IAPs the CEP stability of the few-cycle NIR laser pulses used becomes crucial.

2.2 PHOTOELECTRON IN A POTENTIAL

In ultrafast pump-probe photoionization experiments, such as the experiments performed in the scope of the present work, one of the main observables are photoelectrons resulting from the ionization of the target. The properties of the measured photoelectrons (such as photoelectron delays) contain information on the ultrafast photoinduced dynamics under investigation. After photoionization, the interaction of an emitted photoelectron with the potential of the parent ion modifies the photoelectron properties. Thus, in the present section the interaction of a photoelectron with a potential is discussed. Starting from a classical picture the analysis is extended to a quantum mechanical description. Then the concept of the Eisenbud-Wigner-Smith delay is introduced. The section is closed with a brief discussion of the photoelectron interaction with the long range Coulomb and short range multielectron potentials of the parent ion.

2.2.1 *Classical particle travelling through a potential*

The time delays acquired by photoelectrons emitted from atomic or molecular targets after photoionization is the physical quantity the present work is mainly focusing on. Before starting a detailed discussion of the origin of these delays a simple classical picture of the photoionization process is introduced first. In this simplistic picture a photon is absorbed by a target, and then a photoelectron is instantaneously emitted. This photoelectron has an asymptotic kinetic energy E_{kin} equal to the difference between the energy of the absorbed photon $\hbar\omega$ and the ionization potential Ip of the respective state: $E_{kin} = \hbar\omega - Ip$. During emission, the photoelectron travels through the potential of the parent ion, which is assumed to have a finite length. From this perspective, the photoionization is equivalent to half of the scattering of electron on the corresponding ionic potential. Exploiting this similarity, the discussion is started with an illustration of a scattering process and then extended to a half-scattering, which is to some extent equivalent to photoionization.

In order to qualitatively illustrate the delay acquired by the photoelectron scattered on the potential of the parent ion a classical picture of a particle travelling through a potential is introduced. Let us reduce the problem to a one-dimensional case (the corresponding coordinate is assigned as x) and keep it fully qualitative for the sake of simplicity, at the price of mathematical and physical accuracy.

Let us define a classical particle with mass m moving at a constant velocity V (V is non-relativistic). Since no dissipation forces are present, the energy of the particle outside the potential is constant and equal to its kinetic energy $E_{kin} = mV^2/2$. Now let us introduce a potential $U(x)$ with finite range L. For simplicity we assume that

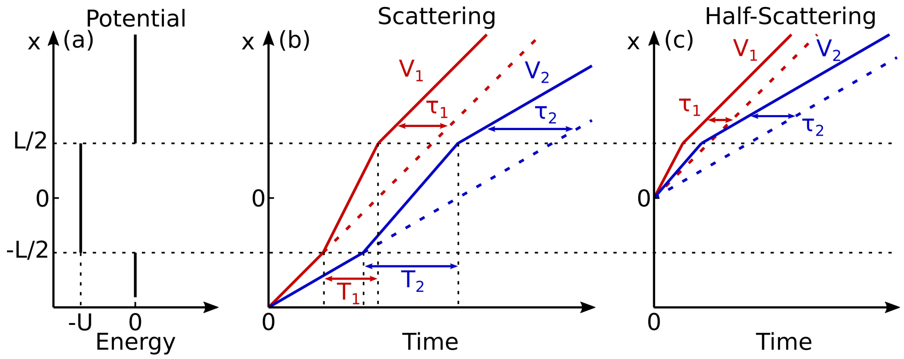

Figure 4: Schematic illustration of a particle travelling through a one dimensional attractive potential. *(a)* the potential energy function $U(x)$ (Eq. 14), *(b)* trajectories of two particles with different initial velocities V_1 and V_2 ($V_1 > V_2$) scattered on the potential $U(x)$, shown as solid lines in red and blue, respectively; dashed lines show the trajectories of free propagating particles with the same initial energies. $T_{1,2}$ is the time spent by each particle in the potential and $\tau_{1,2}$ is the acquired delay with respect to a free propagating particle with the same initial energy. *(c)* trajectories of two particles with different initial energies ejected inside the potential $U(x)$ at $x = 0$ are shown as solid lines, while the dashed lines show the trajectories of free particles with the same final energies outside the potential ($x > L/2$), which correspond to velocities V_1 and V_2 from *(b)* (red and blue, respectively). $\tau_{1,2}$ shows the acquired delay with respect to a free propagating particle with the same final energy. The acquired delays $\tau_{1,2}$ in *(c)* are half the corresponding delays in *(b)*.

this potential is attractive and has a square form, as shown in Eq. 14 and Fig. 4 (a). For the present discussion we neglect the consequences of a non-smooth (and non-differentiable) potential energy function at boundaries $U(\pm L/2)$, which, in principle, results in an infinite potential energy gradients and, as a consequence, infinite instantaneous forces acting on the particle at the potential boundaries.

Model potential.

$$\begin{cases} U(x) &= 0;\ x < -L/2 \ \vee \ x > L/2 \\ U(x) &= -U < 0;\ -L/2 < x < L/2 \end{cases} \tag{14}$$

When the particle travels through the potential $U(x)$ ($-L/2 < x < L/2$), the velocity of the particle V' due to the energy conservation law becomes:

Particle velocity in the potential.

$$V' = \sqrt{V^2 - \frac{2U(x)}{m}} = \sqrt{V^2 + \frac{2U}{m}} \tag{15}$$

As visible from Eq. 15 the particle inside the attractive potential ($U(x) < 0$) moves faster than a free particle with the same initial energy. After leaving the potential ($x > L/2$) the velocity of the particle becomes equal to it's initial velocity. The corresponding trajectories are schematically shown in Fig. 4 (b) as solid lines. In order to determine the time delay acquired by the particle in the potential, its trajectory is compared with the trajectory of a similar particle with the same *initial* energy that propagates without scattering — a *free* particle. The trajectories of such particles are shown as dashed lines in Fig. 4 (b). The acquired delays $\tau_{1,2}$ are then measured as time differences between the *scattered* and *free* particles outside the potential ($x > L/2$) as shown in Fig. 4 (b). These delays are negative for an attractive potential, when the scattered particle is effectively accelerated, and are independent of the position x where they are measured. The delay τ_2 acquired by a particle with lower initial energy is bigger than the delay τ_1 acquired by a particle with higher initial energy. Also the time spent in the potential $T = L/V' = L/\sqrt{V^2 - 2U(x)/m}$ is longer for a particle with lower initial energy.

For a repulsive potential ($U(x) > 0$, not shown here) the situation is inverted. The scattered particle is retarded with respect to a free particle with the same initial energy. A limiting case is a particle with the initial energy $mV^2/2 = U$ that has a zero velocity $V' = 0$ inside the potential, and thus stops right at its edge.

Using this simplistic picture, the photoionization process can be described as an ejection of a particle in the centre of the potential $U(x)$, at $x = 0$, with sequential propagation through the half of its range ($0 < x < L/2$), as shown in Fig. 4 (c). In that case, a good reference for measuring the delay acquired by a particle travelling through a potential is a free propagating particle with the same *final* energy, in order to keep the measured delay τ independent of the position x outside the potential, as in the scattering case. The measured delays $\tau_{1,2}$ are then equal to one half of the full scattering delays shown in Fig. 4 (b).

It is worth mentioning here that the suggested model fundamentally differs from a real ion potential. The Coulomb potential has infinite range and, as a consequence, its integral is diverging (for more details please refer to Section 2.2.4). Thus, in ultrafast photoionization experiments a particle with the same energy propagating in the same Coulomb potential serves as a reference.

2.2.2 *Photoelectron wavepacket travelling through a potential*

In the present section a photoelectron wavepacket propagating in a potential is described. This is compared with laser pulse propagating in a medium (please refer to Section 2.1.2). The given discussion partially follows the publication by J. M. Dahlström *et al.* [69]. All the equations are written in atomic units.

In order to derive the equation describing time evolution of a photoelectron the Time-Dependent Schrödinger Equation (TDSE) in three dimensional space should be solved:

Time-dependent Schrödinger equation.

$$i\frac{\partial}{\partial t}\left|\Psi(\vec{r},t)\right\rangle = \hat{H}\left|\Psi(\vec{r},t)\right\rangle \tag{16}$$

Here a single active electron approximation (SAE) which implies that the problem can be approximated by a single electron interacting with the time-independent potential of the parent ion is used. The time-independent Hamiltonian $\hat{H} = -\frac{1}{2}\boldsymbol{\nabla}^2 + \hat{U}(\vec{r})$, where the former term is a kinetic energy operator and $\hat{U}(\vec{r})$ is the potential energy operator corresponding to the interaction of the photoelectron with the parent ion. In order to solve Eq. 16 first we need to find solutions to the time-independent Schrödinger equation:

Time-independent Schrödinger equation.

$$\hat{H}\left|\Psi_{n,l,m}(\vec{r})\right\rangle = E_{n,l,m}\left|\Psi_{n,l,m}(\vec{r})\right\rangle \tag{17}$$

Here $\left|\Psi_{n,l,m}(\vec{r})\right\rangle$ are the eigenstates and $E_{n,l,m}$ are the eigenvalues of the time-independent Schrödinger equation. The quantum numbers n, l, m are the principal quantum number, angular momentum quantum number and magnetic quantum number, respectively (the spin quantum number is neglected). The set of eigenstates $\left|\Psi_{n,l,m}(\vec{r})\right\rangle$ form a complete basis on which the solution of the TDSE $\left|\Psi(\vec{r},t)\right\rangle$ is spanned. Since the potential $\hat{U}(\vec{r})$ is spherically symmetric, each eigenstate of the time-independent Schrödinger equation $\left|\Psi_{n,l,m}(\vec{r})\right\rangle$ can be written as the product of a radial wavefunction $\left|R_{n,l}(r)\right\rangle$ and a spherical harmonic $\left|Y_l^m(\theta,\phi)\right\rangle$ with corresponding quantum numbers:

Photoelectron wavefunction in radial and spherical harmonic representation.

$$\left|\Psi_{n,l,m}(\vec{r})\right\rangle = \left|R_{n,l}(r)\right\rangle\left|Y_l^m(\theta,\phi)\right\rangle \tag{18}$$

In order to reduce the problem down to a one-dimensional case and compare it with the laser pulse propagation in a dispersive medium, we are going to use effective radial electron wavefunctions $\left|u_{n,l}(r)\right\rangle = r\left|R_{n,l}(r)\right\rangle$. Then the one dimensional Schrödinger equation along the radial axis r has the form:

One dimensional Schrödinger equation.

$$\left(-\frac{1}{2}\frac{\partial^2}{\partial r^2} + \hat{U}(r)\right)\left|u_{n,l}(r)\right\rangle = E_{n,l}\left|u_{n,l}(r)\right\rangle \tag{19}$$

Since the potential of the parent ion $\hat{U}(r)$ equals zero at infinity ($\lim_{r\to\infty}\hat{U}(r) = 0$), the effective radial photoelectron wavefunction is proportional to a complex exponential: $\left|u_{n,l}(r)\right\rangle \propto e^{i\phi(E_{n,l},r)}$, where

$\phi(E_{n,l}, r)$ is the phase of the photoelectron wavepacket angular frequency component. Inserting the effective radial photoelectron wavefunction in the form shown above into Eq. 19 one gets a differential equation for the phase $\phi(E_{n,l}, r)$ in the following form:

Equation for the angular frequency component phase.

$$-i\frac{1}{2}\frac{\partial^2}{\partial r^2}\phi(E_{n,l}, r) + \frac{1}{2}\left(\frac{\partial}{\partial r}\phi(E_{n,l}, r)\right)^2 = E_{n,l} - U(r) \tag{20}$$

Here the $e^{i\phi(E_{n,l},r)}$ term cancels on both sides of the equation. In analogy to a photon wavepacket we assume that the phases of angular frequency components in the photoelectron wavepacket vary slowly with respect to the photoelectron de Brogile wavelength $\lambda = 1/p$, or in other words $\left|\frac{\partial^2}{\partial r^2}\phi(E_{n,l}, r)\right| \ll \left|\frac{\partial}{\partial r}\phi(E_{n,l}, r)\right|^2$. This is equivalent to the assumption that the local photoelectron momentum $p(r) \equiv \frac{\partial}{\partial r}\phi(E_{n,l}, r)$ varies slowly with respect to λ. Thus, we can neglect the second-order partial derivative term in Eq. 20 and derive a simplified differential equation for the phase $\phi(E_{n,l}, r)$:

Simplified equation for the frequency component phase.

$$\frac{\partial}{\partial r}\phi(E_{n,l}, r) = \sqrt{2(E_{n,l} - U(r))} = p(r) \tag{21}$$

Then, in analogy to a photon wavepacket, the phase $\delta\phi(E, r_0, r)$ accumulated by the angular frequency component of the photoelectron wavepacket travelling trough a potential $U(r)$ can be calculated as follows:

Accumulated phase.

$$\delta\phi(E) = \lim_{r\to\infty}\int_{-\infty}^{r}(\sqrt{2(E - U(r'))} - p_0)dr' = \lim_{r\to\infty}\int_{-\infty}^{r}(p(r') - p_0)dr' \tag{22}$$

Here E is the asymptotic photoelectron energy and $p_0 = \sqrt{2E}$ is the corresponding asymptotic momentum. The phases acquired by the photoelectron during the interaction with the potential are conventionally called 'phase shifts' [81]. Comparing the equation for the phases accumulated by the angular frequency component of the photon wavepacket travelling through a medium (Eq. 10) with the equation for the phase shifts acquired by the angular frequency component of the photoelectron wavepacket travelling trough a potential (Eq. 22), it becomes clearly visible that these two processes are to some extent similar. In the case of a non-dispersive medium, for which $n(\omega)$ can be approximated as constant over the photon wavepacket bandwidth, the photon wavepacket angular frequency component phase is linearly proportional to the photon momentum $p = \omega/c$, where c is the speed of light in vacuum. The phase shift accumulated by the photoelectron wavepacket angular frequency component is also linearly proportional to the photoelectron momentum for positions in space where the potential is negligible ($U(r) \ll E$). On the other hand, the phase accumulated by the photon wavepacket angular frequency component is linearly proportional to the photon energy, while the phase shift accumulated by a photoelectron wavepacket is proportional to the square root of the photoelectron energy. In other words, in contrast to photons, electrons with different energies travel at different velocities. The latter implies that the envelope of a photoelectron wavepacket evolves even travelling outside a potential. As a consequence, the concept of a delay between the two photoelectron wavepackets is unambiguous only if both wavepackets were launched simultaneously and measured at the same position in space. Technically this means that the delay between two photoelectrons with the same asymptotic momenta measured in the experiment is meaningful only if the distance between the photoelectron ejection and detection positions (namely the interaction region and the detector) was the same for both photoelectrons. This can be achieved, for example, by measuring both photoelectrons simultaneously.

It is worth mentioning here that Eq. 22 is applicable only to potentials varying slowly with respect to the photoelectron de Brogile wavelength $\lambda = 1/p$, such as the long range Coulomb potential of an ion (see Section 2.2.4). For short range potentials the uncertainty principle implies that at a precisely defined position r the photoelectron momentum $p(r)$ is fundamentally uncertain. Thus, the corresponding phase shifts $\delta\phi(E)$ could not be accessed using Eq. 22 [20].

2.2.3 *Eisenbud-Wigner-Smith delay*

Now let us extend the discussion of the delays acquired by a photoelectron travelling through a potential to a quantum mechanical picture of a photoelectron wavepacket scattered on a potential, and investigate the resulting phase shifts. The discussion given in the present section partially follows the original publication by E. P. Wigner [18].

For simplicity the problem is reduced down to one dimension, assigned as the x-axis, with the centre of the scattering potential positioned at the origin of the coordinate system. As in the classical case discussed in Section 2.2.1, a good reference for the scattered photoelectron wavepacket is a free photoelectron wavepacket with the same spectrum and initial spectral phases. It is worth mentioning that there is a qualitative difference between a classical particle, a laser pulse and a photoelectron wavepacket. If for a classical particle the concept of its position is clear, for a laser pulse or photoelectron wavepacket it corresponds to the position of the peak of its envelope. As discussed in Section 2.2.2 the photoelectron wavepacket envelope is different at different positions in space even in the absence of a potential. Hence, for a photoelectron wavepacket scattered on a potential a good reference is a photoelectron wavepacket with the same spectrum and initial spectral phases emitted at the same position and time. Then the envelopes of the scattered and free photoelectron wavepackets are similar at any position and thus can be directly compared.

Here we consider the simple case of an incident plane wave scattered on a potential in order to illustrate the origin of the Eisenbud-Wigner-Smith delays. Let us assume that an incident wavepacket $|\Psi_i\rangle$ consists of two frequency components $\omega + \delta\omega$ and $\omega - \delta\omega$. The corresponding wavevectors are $k + \delta k$ and $k - \delta k$. Both $\delta\omega$ and δk are infinitesimally small. Then the wavepacket $|\Psi_i\rangle$ has a form:

Incident wavepacket.

$$|\Psi_i\rangle = e^{-i(k+\delta k)|x| - i(\omega+\delta\omega)t} + e^{-i(k-\delta k)|x| - i(\omega-\delta\omega)t} \tag{23}$$

Here $|x|$ is the absolute value of the coordinate x, or, in other words, the distance from the centre of the scattering potential. The centre of the wavepacket $|\Psi_i\rangle$ corresponds to the situation where both frequency components are in phase, which is equivalent to:

Centre of the incident wavepacket.

$$\delta k \cdot |x| + \delta\omega \cdot t = 0 \tag{24}$$

Now let us consider a wavepacket with similar spectrum scattered on a potential and assign it as $|\Psi_s\rangle$. For $|\Psi_s\rangle$ the position-dependent term changes sign with respect to $|\Psi_i\rangle$, assuming that the incident and scattered wavepackets are moving towards or away from the potential, respectively. Let us assign the resulting phase shifts as $2(\phi + \delta\phi)$ and $2(\phi - \delta\phi)$ for the $\omega + \delta\omega$ and $\omega - \delta\omega$ angular frequency components, respectively. These phase shifts are conventionally defined as $2\delta\phi$ due to the potential symmetry. Then $\delta\phi$ is the phase shift corresponding to half-scattering. The wavepacket $|\Psi_s\rangle$ has the form:

Scattered wavepacket.

$$|\Psi_s\rangle = e^{i(k+\delta k)|x| - i(\omega+\delta\omega)t + 2i(\phi+\delta\phi)} + e^{i(k-\delta k)|x| - i(\omega-\delta\omega)t + 2i(\phi-\delta\phi)} \tag{25}$$

The centre of the wavepacket $|\Psi_s\rangle$ corresponds to the following condition:

Centre of the scattered wavepacket.

$$\delta k \cdot |x| - \delta\omega \cdot t + 2\delta\phi = 0 \tag{26}$$

Rewriting Eq. 26 one gets:

Wavepacket position.

$$|x| = \frac{\delta\omega}{\delta k} t - 2\frac{\delta\phi}{\delta k} = \left(t - 2\frac{\delta\phi}{\delta\omega}\right)\frac{\delta\omega}{\delta k} \tag{27}$$

Here the term $2\frac{\delta\phi}{\delta\omega}$ corresponds to a time shift of the photoelectron wavepacket. In other words, the scattered photoelectron wavepacket

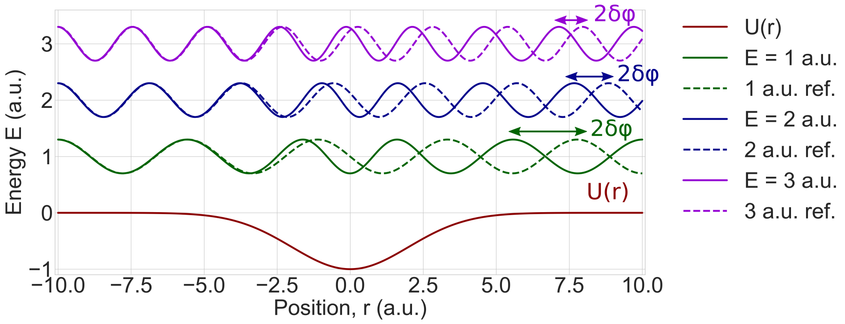

Figure 5: A schematic picture of the $2\delta\phi$ phase shifts acquired by photoelectron wavepacket angular frequency components with asymptotic energies 1, 2 and 3 a.u. shown in green, blue and violet, respectively, travelling through an attractive potential $U(r)$ (shown in red). The potential $U(r)$ has a Gaussian shape: $U(r) = -e^{-r^2/2\sigma^2}$, with $\sigma = 2\,\text{a.u.}$ Photoelectrons travelling through the potential and free photoelectrons with the same asymptotic energy, which are used as a phase reference, are shown as solid and dashed lines, respectively. The figure is adapted from [69].

reaches the position x later than the reference free wavepacket by $\Delta t = 2\frac{\delta\phi}{\delta\omega}$ (or faster if the $\frac{\delta\phi}{\delta\omega} < 0$). Since $\delta\phi$ and $\delta\omega$ are infinitesimally small, their ratio can be replaced by a partial derivative.

In a more general formulation the Eisenbud-Wigner-Smith delay $\tau_{EWS}(\omega)$ is a function the photoelectron energy, and is equal to the energy derivative of the spectral phase difference between the scattered $\phi_{scatt}(\omega)$ and the reference $\phi_{ref}(\omega)$ (free) photoelectron wavepackets:

Eisenbud-Wigner-Smith delay.

$$\tau_{EWS}(\omega) = \frac{\partial(\phi_{scatt}(\omega) - \phi_{ref}(\omega))}{\partial\omega} \tag{28}$$

In Fig. 5 a schematic picture of the phase shifts $2\delta\phi$ acquired by photoelectron wavepacket frequency components with asymptotic energies 1, 2 and 3 a.u. travelling through an attractive potential $U(r)$ is shown. The photoelectron phase shifts were calculated according to Eq. 21. Free photoelectrons with the same asymptotic energies, which are used as a reference, are shown as dashed lines. A photoelectron travelling through an attractive potential is accelerated with respect to a free photoelectron with the same asymptotic energy, thus in that case $2\delta\phi(\omega) > 0$. As visible from the figure, the absolute value of the phase shift $|2\delta\phi(\omega)|$ is smaller for photoelectrons with higher asymptotic energies. In other words, the phase difference $\phi_{scatt}(\omega) - \phi_{ref}(\omega)$ has a positive sign and decreases in amplitude as a function of the photoelectron energy, which corresponds to negative Eisenbud-Wigner-Smith delays $\tau_{EWS}(\omega)$ defined in Eq. 28.

In analogy to the classical case discussed in Section 2.2.1, photoionization is equivalent to half-scattering. Thus, for photoionization the resulting phase shifts are equal to $\delta\phi$ as defined in the Eq 25. A suitable reference for measuring photoionization phase shifts is a free photoelectron emitted from the centre of the potential (close to the position of the ion core) with the momentum equal to the asymptotic momentum of the scattered photoelectron.

The schematic picture of the potential-induced phase shifts shown in Fig. 5 can be used for a qualitative description of the phase shifts induced by the long range Coulomb potential of the ion in the photoionization process. Except for $r \to 0$ and $r \to \pm\infty$, the Coulomb potential $U_C(r) \propto -1/r$ can be approximated as similar to the Gaussian shape potential shown in Fig. 5. A detailed discussion of the phase shifts induced by a Coulomb potential is given in Section 2.2.4.

2.2.4 *Phase shifts induced by a long range Coulomb potential*

After photoionization an emitted photoelectron is travelling through the Coulomb potential of the parent ion, which in atomic units has the form $U_C(r) = -Z/r$, where Z is the ion charge and r is the distance towards the potential centre. According to Eq. 21, the local photoelectron momentum $p(r) = \sqrt{2(E + Z/r)}$, where E is the asymptotic photoelectron energy with the corresponding asymptotic photoelectron momentum $p_0 = \sqrt{2E}$. For r at which $E \gg Z/r$ the equation for the local photoelectron momentum can be simplified as follows: $p(r) = p_0 + Z/(2Er) + \mathcal{O}((Z/r)^2)$. Then the phase $\phi(E, r)$ of the photoelectron ejected at position r_0 and detected at position r (for simplicity we assume that the initial phase of the photoelectron is zero) can be calculated as follows:

Phase shifts induced by a Coulomb potential.

$$\begin{aligned}\phi(E,r) &= \int_{r_0}^{r} p(r')dr' = \int_{r_0}^{r} \left(p_0 + \frac{Z}{2Er'}\right) dr' \\ &= p_0 r + \frac{Z}{2E}\ln(r) - p_0 r_0 - \frac{Z}{2E}\ln(r_0)\end{aligned} \tag{29}$$

The equation for the photoelectron phase $\phi(E,r)$ (Eq. 29) contains a diverging logarithmic term. Applying the photoelectron phase $\phi(E,r)$ in the form shown in Eq. 29 as $\phi_{scatt}(\omega)$ into Eq. 28 and using the free photoelectron phase $\phi_{ref}(E) = \int_{r_0}^{r} p_0 dr' = p_0(r - r_0)$ as a reference, the equation for the delay induced by the long range Coulomb potential τ_C is derived:

EWS delays induced by a Coulomb potential.

$$\tau_C(E,r) = \frac{\partial}{\partial E}\left(\frac{Z}{2E}\ln\left(\frac{r}{r_0}\right)\right) = -\frac{Z}{2E^2}\ln\left(\frac{r}{r_0}\right) \tag{30}$$

Since $r > r_0$, the delay induced by a Coulomb potential has a negative sign (the photoelectron in the potential is accelerated) and depends logarithmically on the measurement position. Since the logarithmic function diverges, there is no well-defined value of the

Coulomb potential-induced delays τ_C. The logarithmic term in the equation for the photoelectron delays (Eq. 30) can be cancelled out by measuring the difference between the delays of photoelectrons with similar asymptotic energies. In that case both delays should be measured at the same distance from the photoelectron ejection position — interaction region in the experiment. This can be achieved, for example, performing a photoionization experiment simultaneously in two different targets with similar ionization potentials, and comparing the delays of the emitted photoelectrons. Then, if both targets were singly ionized, since the long range Coulomb potential can be approximated as independent of the bound electron configuration, the diverging logarithmic term cancels, and the measured delay difference reveals the difference between the short range potential-induced Wigner delays in the two targets (see Section 2.2.5).

2.2.5 *Phase shifts induced by a short range potential*

The short range potential photoionization (scattering) phase shifts with corresponding Wigner delays are determined by the configuration of the remaining bound electrons in the ion, and thus are complicated to calculate. For the special case of atomic hydrogen, which has a pure Coulomb potential, the equation for the scattering phase $\sigma_l^H(p)$ can be obtained analytically [82]:

Atomic hydrogen ion short range potential scattering phase shifts.

$$\sigma_l^H(p) = \arg(\Gamma(l + 1 - i/(pa_0))) \tag{31}$$

Here p is the asymptotic momentum and l is the angular momentum quantum number of the scattered photoelectron, respectively, a_0 is the Bohr radius and $\Gamma(z) = \int_0^\infty t^{z-1} e^{-t} dt$ is a complex Gamma function. For heavier atomic ions the direct analytical solution for the scattering phase shifts is not possible due to the effect of the remaining electrons. In the framework of quantum defect theory for such ions the short range potential scattering phase shifts can be approximated as scattering phase shifts of the atomic hydrogen ion $\sigma_l^H(p)$ (Eq. 31) with an additional correction phase term $\delta_l(p)$ [82]:

Scattering phase shifts in heavier atoms.

$$\sigma_l(p) = \sigma_l^H(p) + \delta_l(p) \tag{32}$$

The correction term $\delta_l(p)$ is determined by the multielectron configuration of a particular ion state. It is compensating for deviations of the ion potential from a pure Coulomb potential-induced by the remaining bound electrons. In general, in ultrafast photoionization experiments only the difference between the correction phase terms $\Delta\delta_l(p)$ corresponding to the potentials of two distinct states or targets can be accessed.

The measured quantities in attosecond pump-probe experiments are delays τ. These delays correspond to the energy derivatives of the scattering phase shits $\sigma_l(p)$ (for more details please refer to Section 2.5.8). The difference between the Wigner delays measured for the potentials of selected states are an observable of interest in the experiments reported in the present thesis. It is worth mentioning here that the Wigner delays depend on the angular momentum of the scattered photoelectron [69]. Thus, it is advantageous to compare the Wigner delays of photoelectrons with equal angular momenta in order to cancel the atomic hydrogen ion phase $\sigma_l^H(p)$.

In case of a hydrogen-like system the corresponding Wigner delays have positive signs, or in other words, the photoelectrons scattered on the short range potential are retarded with respect to the reference free photoelectrons with the same asymptotic momenta. In general, the short range potential-induced Wigner delays can have both negative or positive signs.

2.3 PHOTOIONIZATION OF ATOMS

Due to low reactivity noble gases are convenient experimental targets to work with. Thus, their properties are extensively studied with different experimental methods and, as a result, a significant amount of information on them is available. Because of that, noble gases became popular targets for ultrafast photoionization pump-probe spectroscopy. Relatively simple photoionization dynamics (comparing to molecules) allows using photoionization of noble gases for the characterization of XUV attosecond pulses (see Section 2.5). That is why for the experiments reported in the present thesis photoelectrons ionized from noble gases were chosen as a reference. Thus, in the present section a brief introduction to photoionization of atoms is given. Since helium and argon were used in the experiments reported in the present thesis, their properties are described. A brief overview of Fano's propensity rule and its relevance for time-resolved pump-probe spectroscopy experiments is closing the present section. The given discussion partially follows the textbook by I. V. Hertel and C. P. Schulz [83]. All the spectroscopic data, such as ionization potentials and the energy separation between the ion states, was taken from the National Institute of Standards and Technology database [84].

2.3.1 *Photoionization selection rules in atoms*

In the present section photoionization of atoms by a linearly polarized laser field is discussed. All the equations are written in atomic units. In atoms a unique set of quantum numbers (n, l, m, s) describes each bound electron state. These quantum numbers are:

Quantum numbers describing states in atoms.

- $n \in [1, 2, ..., \infty)$ is a *principal quantum number*
- $l \in [0, 1, ..., n-1]$ is the *orbital angular momentum quantum number*. The orbital angular momentum operator $\hat{L} = \hbar\sqrt{l(l+1)}$ and the conventional notation for the corresponding states is: $s, p, d, f, ...$.
- $m \in [-l, -l+1, ..., l-1, l]$ is the *orbital angular momentum projection quantum number*. The orbital angular momentum projected on the z-axis operator $\hat{L}_z = \hbar m$.
- $s = \pm 1/2$ is a *spin quantum number*. The spin angular momentum operator $\hat{S} = \hbar\sqrt{|s|(|s|+1)}$.

Since electrons are fermions (particles with half integer spin), the Pauli exclusion principle implies that each state can be occupied by no more than a single electron.

The principal quantum number n indicates the number of the *electron shell*, which is conventionally denoted as $K, L, M, ...$ shell. The total number of states in the electron shell is equal to n^2. Going from light to heavy atoms, the ground state configuration corresponds to electron shells sequentially filled in the following order: $1s^2, 2s^2, 2p^6, 3s^2, 3p^6, \dots$. Noble gases have their outer shells completely filled in the ground state, which explains their low reactivity. For example, for He and Ar used for the experiments reported in the present thesis the outer shells are $1s^2$ and $3p^6$, respectively.

Since atoms are spherically symmetric systems (belong to the R_3 point group) the multielectron states in atoms are conventionally labelled with term symbols of the following form:

Atomic multielectron state term symbol.

$$^{2S+1}L_J \tag{33}$$

Here S is a total spin angular momentum (thus $2S+1$ is the multiplicity of the state), L is the total orbital angular momentum conventionally labelled with capital Latin letters $S, P, D, \dots$ for $L = 0, 1, 2, \dots$, respectively (in analogy to electron states), and $J = L + S$ is a total angular momentum. In this notation the ground states of He and Ar are written as $^1S_0$.

Ionization of an atom by a single linearly polarized photon can be described by the following equation:

Single photon ionization of an atom.

$$A(L, M) + \gamma = A^+(L', M') + e^-(l) \tag{34}$$

Here $A(L, M)$ is the neutral atom prior to ionization, γ is a photon (with spin angular momentum equal $s_{ph} = \pm 1$ for circular polarization; a linear polarized photon is in a superposition of the two circular polarization states), $A^+(L', M')$ is an ion and $e^-(l)$ is a photoelectron with corresponding angular momentum quantum numbers. Single photon ionization selection rules follow from the conservation of the total angular momentum J and the angular momentum projection onto a particular axis M. For the simple picture of a single photon ionization shown in Eq. 34 this implies that $L \pm 1 = L' + l$, or in other words, that the change of the orbital angular momentum quantum number of the whole system $\Delta L = \pm 1$. For example, in case of a single XUV photon ionization of Ar from the initial p bound state the final photoelectron state can be either s or d continuum states (Fig. 6). For linearly polarized light the photon spin projection quantum number onto the z-axis parallel to $\vec{E}$, $s_{ph,z} = 0$. This implies that during the photoionization of atoms with linearly polarized light the orbital angular momentum projection quantum number is conserved: $\Delta m = 0$.

2.3.2 *Helium*

Helium is the second element in the periodic system with a 4.003 Da atomic weight. The electron configuration of He contains two electrons, which in the ground state occupy the $1s^2$ orbital. The relatively simple atomic structure (one ion core and two electrons) simplifies the theoretical analysis of photoinduced processes in He.

The ionization potential of the ground state of He is 24.58 eV. Single photon ionization of He from the $1s^2$ orbital results in emission of a *p* photoelectron (Fig. 6). Then the He^+ ion is left in the $^2S_{\frac{1}{2}}$ state. The ionization of He does not contain resonances in the XUV photon energy range used in the present work (from 15 up to 50 eV). This makes He a good experimental target for XUV pulse characterization using pump-probe time-resolved spectroscopy techniques. On the other hand, the relatively small photoionization cross section of He in the 10 to 50 eV XUV photon energy range (from 8 down to 2 Mb [85]) implies certain limitations on either XUV photon flux or target gas density in the interaction region required for the experiments.

2.3.3 *Argon*

Argon is the element with number 18 of the periodic system with 39.95 Da atomic weight. The electron configuration of Ar contains eighteen electrons, with the $3s^2 3p^6$ as the highest occupied orbital in the ground state.

The ionization potential of the ground state of Ar is 15.76 eV. In the XUV photon energy range used in the present work (from 15 up to 40 eV) the photoionization of Ar dominantly occurs from the $3p^6$ orbital with *s* or *d* photoelectrons emitted (Fig. 6). Then the Ar^+ ion is left in either the $^2P_{3/2}$ or $^2P_{1/2}$ state. The energy difference between these two states is on the order of 0.2 eV [84]. Due to a relatively big photoionization cross section in the 10 to 50 eV XUV photon energy range (from 35 down to 1 Mb due to vicinity of a Cooper minimum around 50 eV [85]) Ar is one of the most well studied objects in the field of attosecond science. In this XUV photon energy range, photoionization of Ar contains a $3s^{-1}4p$ resonance around 26.63 eV XUV photon energy, significantly modifying the measured photoelectron delays [26]. The presence of the resonance adds extra complexity to XUV pulse characterization from RABBIT spectrograms measured in Ar.

2.3.4 *Fano's propensity rule*

The strict rules of single photon ionization of atoms listed in Section 2.3.1 are called selection rules, while rules that are not universal are called propensity rules. In the present section one such rule — Fano's propensity rule is discussed, since it has a certain relevance for the experiments reported in the present thesis. Fano's propensity rule states that the absorption/emission of a photon accompanied by an increase/decrease of the angular momentum of the system

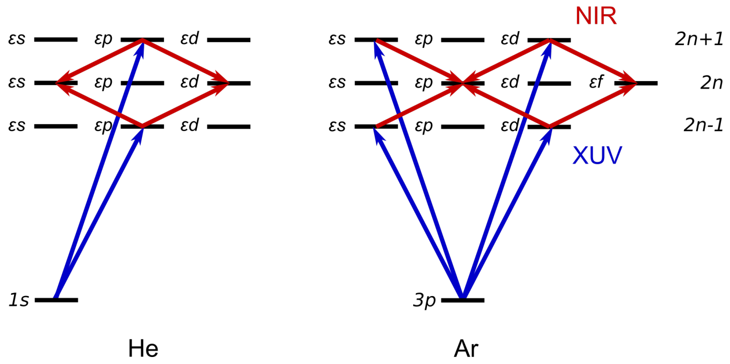

Figure 6: Scheme of the photoinduced transitions involved in a RABBIT measurement in He and Ar shown in the left and right subplots, respectively. The photoionization of He and Ar occurs from the $1s^2$ and $3p^6$ shells, respectively. The continuum states are denoted as ϵl, where l is the angular momentum quantum number. The transitions induced by the XUV and NIR photons are shown as blue and red arrows, respectively. The XUV photon energies correspond to the adjacent high-order harmonics $2n \pm 1$, where n is an integer. The NIR photon-induced transitions lead to the sideband $2n$.

$(\Delta l = \pm 1)$ has a higher probability than that accompanied by a decrease/increase [86].

This effect has a certain influence on the results of RABBIT measurements in atoms (see Section 2.5.2). Let us use the transitions involved in a RABBIT measurement in Ar as an illustration (Fig. 6). Due to Fano's propensity rule, the NIR photon-induced continuum–continuum transitions shown as red arrows are not equally probable. For example, the transition $\epsilon_{2n+1}d \rightarrow \epsilon_{2n}p$ has a higher probability than the transition $\epsilon_{2n+1}s \rightarrow \epsilon_{2n}p$. On the other hand the transition $\epsilon_{2n-1}d \rightarrow \epsilon_{2n}p$ has a lower probability than the transition $\epsilon_{2n-1}s \rightarrow \epsilon_{2n}p$. In the recent publication by David Busto *et al.* [31] it was shown that this asymmetry results in an angular dependence (with respect to the laser polarization) of the photoelectron delays acquired when performing a RABBIT experiment in Ar.

2.4 PHOTOIONIZATION OF DIATOMIC MOLECULES

The photoionization dynamics in diatomic molecules, studied in the present work, is way more complex than that in the atomic targets. Due to a big number of photoionization channels, including photodissociation channels, the separation of the corresponding signals becomes a non-trivial task. In order to develop a better understanding of the photoinduced dynamics in diatomic molecules a short overview of their properties is given in the present section. Starting from a description of multielectron states in diatomic molecules and their conventional notation, the discussion is extended by a brief summary of photoionization mechanisms and corresponding selection rules. Since studying the photoinduced dynamics in molecular nitrogen was the main goal of the present work, the section is closed with an overview of the properties of molecular nitrogen with an emphasis on the states involved in the photoinduced processes under investigation. The discussion given in the present section partially follows the textbook by I. V. Hertel and C. P. Schulz [83].

2.4.1 *Molecular stationary states*

In the present section we are going to discuss the Schrödinger equation describing the stationary states of a molecule, and the conventional approximations, such as Born-Oppenheimer approximation, used to find the solutions of this equation. Here we focus on homonuclear diatomic molecules, since they were studied in the present work, but a significant part of the following discussion is universal and can be applied to molecules with much more complex structure.

The motion of a molecule can be separated into three different parts: rotation of the whole system, relative movement of the nuclei with respect to each other, or vibrational motion, and electronic configuration rearrangements. The translational movement of the molecule can be neglected by choosing a coordinate system fixed to the centre of mass of the system. The three types of motion listed above are occurring on different time scales: the rotational motion has a typical period in the range from 0.1 to 10 ps, while the vibrational and electronic motion have typical periods on the order of tens of femtoseconds and hundreds of attoseconds, respectively. As a result, the wavefunction Ψ_n describing a stationary state of a molecule can be approximated as a product of the following form:

Stationary state wavefunction.

$$\Psi_n = \psi_e(\vec{q}_i)\psi_\nu(\vec{Q}_\alpha)\psi_r(\theta) \tag{35}$$

Here $\psi_e(\vec{q}_i)$ is an electronic wavefunction of N electrons labelled with index $i = 1, ..., N$ with corresponding coordinates $\vec{q}_i$, $\psi_\nu(\vec{Q}_\alpha)$ is a vibrational wavefunction of K nuclei labelled with index $\alpha = 1, ..., K$

with corresponding coordinates $\vec{Q}_\alpha$, and $\psi_r(\theta)$ is a rotational wavefunction where θ is the set of Euler angles. The corresponding eigenvalues E_e, $E\nu$, Er are electronic, vibrational and rotational energies, respectively. The total energy of the stationary state of a molecule E_n is then equal to their sum: $E_n = E_e + E\nu + Er$.

We assign the position, charge and mass of the nuclei with index α as $\vec{Q}_\alpha$, Z_α and M_α, respectively, while the position of the electron with index i is assigned as $\vec{q}_i$ (the electron mass is not included in the equations since atomic units are used). Then the Hamiltonian of the molecule $\hat{H}(\vec{Q}_\alpha, \vec{q}_i)$ has the form:

Molecular Hamiltonian.

$$\hat{H}(\vec{Q}_\alpha, \vec{q}_i) = \hat{T}_{nucl} + \hat{T}_e + \hat{V}(\vec{Q}_\alpha, \vec{q}_i) \tag{36}$$

Here $\hat{T}_{nucl}$ and $\hat{T}_e$ are the kinetic energy operators corresponding to motion of the nuclei and the electrons, respectively, and $\hat{V}(\vec{Q}_\alpha, \vec{q}_i)$ is the potential energy operator. The time-independent Schrödinger equation describing the stationary states of the molecule is:

Time-independent Schrödinger equation.

$$\hat{H}(\vec{Q}_\alpha, \vec{q}_i)\Psi_n(\vec{Q}_\alpha, \vec{q}_i) = E_n\Psi_n(\vec{Q}_\alpha, \vec{q}_i) \tag{37}$$

In order to simplify this equation the Born-Oppenheimer (BO) approximation is used. The BO approximation is based on the assumption that due to the huge mass difference, the motion of the nuclei is significantly slower than the motion of the electrons, so the electron configuration can be approximated as immediately responding to the nuclear rearrangement. Thus, the electronic and nuclear wavefunctions can be separated and the wavefunction $\Psi_n(\vec{Q}_\alpha, \vec{q}_i)$ describing the molecular stationary state can be written as:

Separability of the stationary state wavefunctions.

$$\Psi_n(\vec{Q}_\alpha, \vec{q}_i) = \psi_m^{(n)}(\vec{Q}_\alpha)\psi_n(\vec{Q}_\alpha, \vec{q}_i) \tag{38}$$

Here $\psi_n(\vec{Q}_\alpha, \vec{q}_i)$ is an electronic wavefunction with n labelling different electronic states, and $\psi_m^{(n)}(\vec{Q}_\alpha)$ is the nuclear wavefunction corresponding to the electronic state with index n, where m is labelling different nuclear states.

In order to solve Eq. 37 in the framework of the BO approximation, the solution to the simplified equation for a fixed arrangement of the nuclei has to be found first. We assign all coordinates describing the arrangement of all K nuclei in the molecule as $\vec{R}_K$. At this step the $\vec{R}_K$ are treated as a parameter, and thus $\hat{T}_{nucl}\Psi_n(\vec{R}_K, \vec{q}_i) = 0$ in Eq. 36, and $\psi_m^{(n)}(\vec{R}_K)$ is simply a multiplier on both sides of Eq. 37. Then the equation for the electronic states $\psi_n(\vec{R}_K, \vec{q}_i)$ has a form:

Equation for electronic wavefunctions.

$$\left(\hat{T}_e + \hat{V}(\vec{R}_K, \vec{q}_i)\right)\psi_n(\vec{R}_K, \vec{q}_i) = U_n(\vec{R}_K)\psi_n(\vec{R}_K, \vec{q}_i) \tag{39}$$

Here $U_n(\vec{R}_K)$ is the energy of the electronic state with index n. For diatomic molecules R is the internuclear distance and thus $U_n(R)$

is a one-dimensional potential energy curve, while for polyatomic molecules $U_n(\vec{R}_K)$ is a multi-dimensional surface. Solving Eq. 39, the potential energy surfaces $U_n(\vec{Q}_\alpha)$ and corresponding electronic wavefunctions $\psi_n(\vec{Q}_\alpha, \vec{q}_i)$ are obtained.

Equation for nuclear wavefunctions.

The next step is to find the nuclear wavefunctions $\psi_m^{(n)}(\vec{Q}_\alpha)$. They can be obtained by inserting $U_n(\vec{Q}_\alpha)$ and $\psi_n(\vec{Q}_\alpha, \vec{q}_i)$, calculated in the previous step, into Eq. 37 as follows:

$$\left(\hat{T}_{nucl} + U_n(\vec{Q}_\alpha)\right)\psi_n(\vec{Q}_\alpha, \vec{q}_i)\psi_m^{(n)}(\vec{Q}_\alpha) = E_n^{(m)}\psi_n(\vec{Q}_\alpha, \vec{q}_i)\psi_m^{(n)}(\vec{Q}_\alpha) \tag{40}$$

Solving this equation, the nuclear wavefunctions $\psi_m^{(n)}(\vec{Q}_\alpha)$ for the $n = 0, 1, \ldots$ electronic states and for the $m = 0, 1, \ldots$ nuclear states, with corresponding total energies $E_n^{(m)}$ are obtained.

2.4.2 *Vibrational states*

In the following discussion we are going to focus on the vibrational structure of homonuclear diatomic molecules, since it is important for understanding the photoinduced processes studied in the present work. We can neglect the rotational wavefunctions since the corresponding energies E_r are much lower than the vibrational energies E_ν. Thus, we can find a solution of the problem in coordinate system fixed to the molecular frame. We assign the mass of each nucleus as M, and the internuclear distance as R. Then Eq. 40 for a homonuclear diatomic molecule has the form (using atomic units):

Equation for vibrational wavefunctions in homonuclear diatomic molecule.

$$\left(-\frac{1}{M}\frac{\partial^2}{\partial R^2} + U_n(R)\right)\psi_m^{(n)}(R) = E_n^{(m)}\psi_m^{(n)}(R) \tag{41}$$

For long living vibrational states to exist, the potential energy curve $U_n(R)$ should have a local minimum. Let us assign the internuclear distance corresponding to the local minimum of $U_n(R)$ as R_{eq}, or in other words:

Potential energy curve minimum.

$$\left(\frac{\partial U_n(R)}{\partial R}\right)_{R_{eq}} = 0. \tag{42}$$

Then let us introduce a new variable $\rho = R - R_{eq}$. We assume that the internuclear distance varies slightly over the vibrational motion of the molecule, which implies that $\rho \ll R_{eq}$. This means that we can expand $U_n(\rho)$ in the vicinity of $\rho = 0$ in a Taylor series, which is equivalent to the expansion of $U_n(R)$ in the vicinity of R_{eq}:

Taylor expansion of the potential energy function.

$$U_n(\rho) = U_n(R_{eq}) + \left(\frac{\partial U_n(R)}{\partial R}\right)_{R_{eq}} \rho + \left(\frac{\partial^2 U_n(R)}{\partial R^2}\right)_{R_{eq}} \frac{\rho^2}{2} + \cdots \tag{43}$$

In this expansion, the linear term $(\partial U_n(R)/\partial R)_{R_{eq}} = 0$, since $U_n(R)$ has a local minimum at R_{eq} (Eq. 42). Applying $U_n(\rho)$ in the form shown in Eq. 43 (here third- and higher-order terms are assumed to be negligible) into Eq. 41, and performing a change of the coordinate system $R \to \rho$, one acquires an equation for the vibrational state wavefunctions:

Simplified equation for vibrational wavefunctions.

$$\left(-\frac{1}{2\mu}\frac{\partial^2}{\partial \rho^2} + \frac{1}{2}\left(\frac{\partial^2 U_n(R)}{\partial R^2}\right)_{R_{eq}} \rho^2\right) \psi_m^{(n)}(\rho) = (E_n^{(m)} - U_n(R_{eq}))\psi_m^{(n)}(\rho) \tag{44}$$

Here the mass of the nucleus M was replaced by the mass of a virtual particle $\mu = M/2$. As visible from the form of Eq. 44, it is equivalent to a Schrödinger equation describing a harmonic oscillator:

Schrödinger equation for a harmonic oscillator.

$$\left(-\frac{1}{2\mu}\frac{\partial^2}{\partial \rho^2} + \frac{1}{2}k\rho^2\right) \psi_\nu(\rho) = E_\nu \psi_\nu(\rho) \tag{45}$$

Thus, the vibrational motion of a homonuclear diatomic molecule is equivalent to the motion of a virtual particle with mass $\mu = M/2$ in the potential $U_n(\rho)$. The eigenvalues E_ν of the harmonic oscillator can be calculated using the following equation:

Eigenenergies of the harmonic oscillator.

$$E_\nu = (\nu + 1/2)\sqrt{\frac{k}{\mu}} = (\nu + 1/2)\omega_{osc} \tag{46}$$

Here $\nu = 0, 1, ...$ are the vibrational quantum numbers, and ω_{osc} is the angular frequency of the harmonic oscillator. Using the analogy between the equation describing a harmonic oscillator (Eq. 45) and the equation for the vibrational states of a homonuclear diatomic molecule (Eq. 44, here $k = \left(\partial^2 U_n(R)/\partial R^2\right)_{R_{eq}}$), the total energy of the molecular state $E_n^{(m)}$ can be approximated as:

Total energy of the vibrational states.

$$E_n^{(m)} = U_n(R_{eq}) + (\nu + 1/2)\omega_{osc} \tag{47}$$

The Taylor expansion of $U_n(\rho)$ up to a quadratic term (Eq. 43) is a good approximation of the real molecular potential $U_n(R)$ only in the vicinity of the R_{eq}. For ρ comparable with R_{eq}, higher-order terms have to be taken into account. This results in an anharmonicity of the resulting potential $U_n(\rho)$, which can be approximated as a *Morse* potential of the following form:

Morse potential.

$$U_{Morse}(\rho) = U_{asymp}\left(1 - e^{-\beta\rho}\right)^2 \tag{48}$$

Here β and U_{asymp} are constants. The Morse potential equals zero at $\rho = 0$ ($U_{Morse}(0) = 0$), and converges to an asymptotic value U_{asymp} at $\rho \to \infty$. The eigenenergies of the Morse potential are:

Eigenenergies of the Morse potential.

$$E_v^{Morse} = (v + 1/2)\omega_{osc} - x_e\omega_e(v + 1/2)^2 \tag{49}$$

Here $x_e\omega_e$ is a constant ($x_e\omega_e > 0$). Eq. 49 is conventionally used for calculating the energies of the vibrational states of different electronic states in diatomic molecules. For these calculations the values of $x_e\omega_e$ and ω_{osc} are determined experimentally. The energy spacing between adjacent eigenstates of the Morse potential is equal to:

Energy spacing between the eigenstates of the Morse potential.

$$\Delta E_v^{Morse} = E_{v+1}^{Morse} - E_v^{Morse} = \omega_{osc} - 2x_e\omega_e(v + 1) \tag{50}$$

As visible from Eq. 50, the energy spacing between the adjacent vibrational states is linearly decreasing with the quantum number v (Fig. 7). This implies that at a certain maximal quantum number v_{max}, corresponding to $\Delta E_{v_{max}}^{Morse} = 0$, the vibrational spectrum of a molecule becomes continuous, which means that at v_{max} the molecule dissociates. As follows from Eq. 50, v_{max} is related to the ω_{osc} and $x_e\omega_e$ as follows:

Maximal vibrational quantum number.

$$v_{max} = \frac{\omega_{osc} - 2x_e\omega_e}{2x_e\omega_e} \tag{51}$$

The comparison of Harmonic and Morse potentials approximating the same system is shown in Fig. 7. For the calculation of the shown potentials, the parameter k entering the equation of the harmonic potential (Eq. 45) is related to the parameters U_{asymp} and β describing the Morse potential (Eq. 48) by the following consideration:

$$k = \left(\frac{\partial^2 U_{Morse}(\rho)}{\partial\rho^2}\right)_0 = 2U_{asymp}\beta^2 \tag{52}$$

Since $E_{v_{max}}^{Morse} = U_{asymp}$, applying v_{max} into Eq. 49 the following relation between U_{asymp}, ω_{osc} and $x_e\omega_e$ is derived:

Asymptotic energy.

$$U_{asymp} = \frac{\omega_{osc}^2 - x_e\omega_e^2}{4x_e\omega_e} \tag{53}$$

For potential energy curves corresponding to different electronic states of homonuclear diatomic molecules, the asymptotic energy

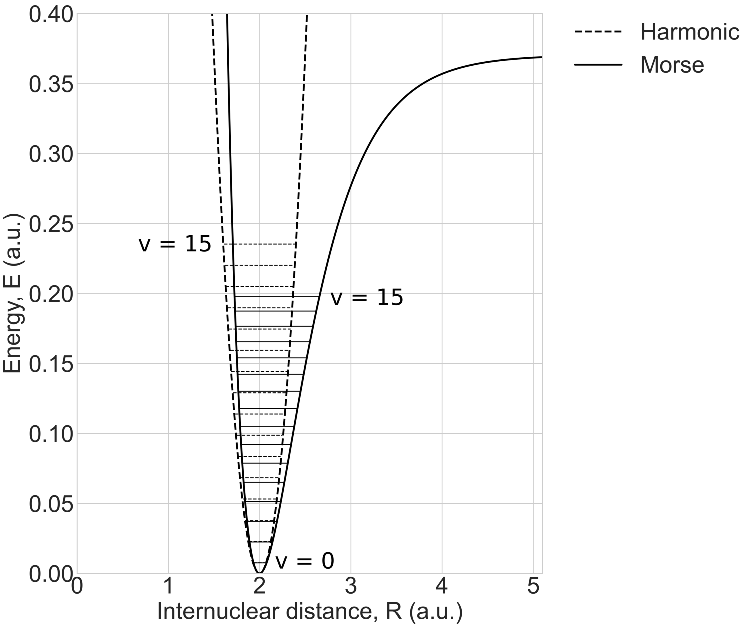

Figure 7: Comparison of a harmonic potential (dashed line) with a Morse potential (solid line), corresponding to an approximate model of the ground state $X\,^1\Sigma_g^+$ of the N_2 molecule. For the calculation of both potentials $R_{eq} = 2.0\,\text{a.u.}$ and $\mu = 12.9 \cdot 10^3\,\text{a.u.}$ (1/2 of the atomic nitrogen mass) were chosen. The Morse potential was calculated according to Eq. 48 with the following parameters applied: $\beta = 2$ and $U_{asymp} = 0.37\,\text{a.u.}$ (corresponds to the first dissociation limit of the N_2 molecule), $k = 3\,\text{a.u.}$ and $\omega_{osc} = 0.015\,\text{a.u.}$, which is equivalent to an oscillation period $T = 414\,\text{a.u.} \approx 10\,\text{fs}$. The vibrational states with vibrational quantum numbers $\nu = 0, ..., 15$ for both potentials are shown as horizontal lines (for the Morse potential the parameter $x_e\omega_e$ was calculated according to Eq. 53, in the present case $x_e\omega_e = 1.5 \cdot 10^{-4}$).

U_{asymp} equals the sum of the energies of the two infinitely far separated fragments in the respective electronic states (the two fragments do not interact). These asymptotic energies are called the dissociation limits. The potential energy curves of different electronic states at infinitely long internuclear distances converge to one of the dissociation limits, depending on the electronic configuration. If the energy of an excited molecular state exceeds the corresponding dissociation limit, the molecule will dissociate with the exceeding energy released as kinetic energy of the fragments.

2.4.3 *Multielectron states notation*

In the present section we are going to discuss the conventional notation of the electronic states of homonuclear diatomic molecules. Homonuclear diatomic molecules, such as N_2 or H_2, are cylindrically symmetric with respect to the internuclear axis (i.e. belong to $D_{\infty h}$ point group). In contrast to atoms, for homonuclear diatomic molecules the total orbital angular momentum quantum number L is not a good quantum number. Thus another quantum number Λ — the total orbital angular momentum projection onto the internuclear axis is introduced.

The electronic states in diatomic molecules are historically labelled with capital Latin letters in the order they were observed for the first time. The electronic ground state is labelled as X, while the electronically excited states with increasing energy are sequentially labelled as $A, B, C, \ldots$. The same notation is used for the electronic states of the ion.

In analogy to atoms, the molecular orbitals of homonuclear diatomic molecules are labelled with Greek letters $\sigma^{+}_{g/u}, \pi^{+/-}_{g/u}, \delta^{+/-}_{g/u}, \ldots$, corresponding to the orbital angular momentum projection on the internuclear axis quantum number $\lambda = 0, 1, \ldots$, respectively. Here g/u stands for gerade/ungerade and indicates the inversion symmetry/asymmetry with respect to the molecular centre of mass. In the coordinate system with the origin fixed to the molecular centre of mass: $\Psi_g(x) = \Psi_g(-x)$ and $\Psi_u(x) = -\Psi_u(-x)$. The $+/-$ indicates the reflection symmetry/asymmetry with respect to an arbitrary plane containing the internuclear axis (thus a σ^- orbital does not exist).

The term symbols for the multielectron states of homonuclear diatomic molecules are conventionally written in the following form:

Multielectron states term symbol.

$$^{2S+1}\Lambda^{+/-}_{g/u} \tag{54}$$

In analogy to atoms, here S is the total spin angular momentum (thus $2S + 1$ is the multiplicity of the state), Λ is the projection of the total orbital angular momentum onto the internuclear axis conventionally written as capital Greek letters $\Sigma, \Pi, \Delta, \ldots$ for $\Lambda = 0, 1, 2, \ldots$, respectively, and g/u and $+/-$ are assigned similarly to the assignment of the molecular orbitals.

2.4.4 *Photoionization selection rules in homonuclear diatomic molecules*

In the present section the selection rules governing the single photon-induced transitions in homonuclear diatomic molecules are discussed. Let us assign the total initial and final states wavefunctions as Ψ_i and Ψ_f, respectively. As discussed in Section 2.4.1, in the framework of the Born-Oppenheimer approximation, both of these wavefunctions can be written as a product of an electronic ψ_e and vibrational ψ_ν wavefunctions (here we neglect the rotational wavefunctions): $\Psi_{i/f} = \psi_{e,i/f}\psi_{\nu,i/f}$.

First, let us focus on the transitions between the two vibrational states of the same electronic state. In that case the electronic wavefunction remains unchanged over the transition ($\psi_{e,i} = \psi_{e,f}$). Then the intensity of the transition I_ν is proportional to $I_\nu \propto |\langle\psi_{\nu,f}|\,\mu(R)\,|\psi_{\nu,i}\rangle|^2$, where $\mu(R)$ is the dipole moment as a function of the internuclear distance R. For the electronic ground state of a homonuclear diatomic molecule $\mu(R) = 0$, which implies that single linearly polarized photon-induced transitions between vibrational states of the electronic ground state in homonuclear diatomic molecules are not possible. Such transitions may only occur if the dipole moment of the system is non-zero. In case of a non-zero dipole moment, the transition between the two vibrational states should be accompanied by a change of the total angular momentum of the system $\Delta J = \pm 1$ for Σ electronic states, and $\Delta J = 0, \pm 1$ for electronic states with higher Λ quantum number.

Now let us discuss the transitions between two electronic states. The selection rules for electronic transitions induced by linearly polarized light in homonuclear diatomic molecules depend on the transition dipole moment orientation with respect to the internuclear axis (for more details please refer to Section 2.5.5). In case the transition dipole moment is parallel to the internuclear axis, such a transition is called a *parallel* transition, and the difference in the projection of the total orbital angular momentum onto the internuclear axis for initial and final states $\Delta\Lambda = 0$. In case the transition dipole moment and the internuclear axis are orthogonal the transition is called *perpendicular* and $\Delta\Lambda = \pm 1$. For both parallel and perpendicular electronic transitions not accompanied by an electron emission induced by linearly polarized light in homonuclear diatomic molecules, the inversion symmetry has to change. In other words, in excitation process, transitions from a u state are only allowed to a g state and vice versa.

In general, the following transitions between electronic states in homonuclear diatomic molecules are allowed: [87]:

Selection rules in homonuclear diatomic molecules.

- $\Delta\Lambda = 0/\pm 1$ for *parallel*/*perpendicular* transitions
- $g \longleftrightarrow u$ for molecular excitation
- $\Delta S = 0$ for molecules consisting of light atoms
- $\Sigma^+ \longleftrightarrow \Sigma^+$ or $\Sigma^- \longleftrightarrow \Sigma^-$ but not $\Sigma^+ \longleftrightarrow \Sigma^-$

2.4.5 *Franck-Condon principle*

In the present section the photoinduced transitions occurring between different electronic and vibrational states of a diatomic molecule — vibronic transitions — are discussed. For a qualitative picture of vibronic transitions we again make use of the fact that the electronic motion in the molecule is substantially faster than the nuclear motion. This implies that in a simplistic picture of a vibronic transition, the internuclear distance remains unchanged during the electronic transition. In other words, the vibronic transitions preferably occur along

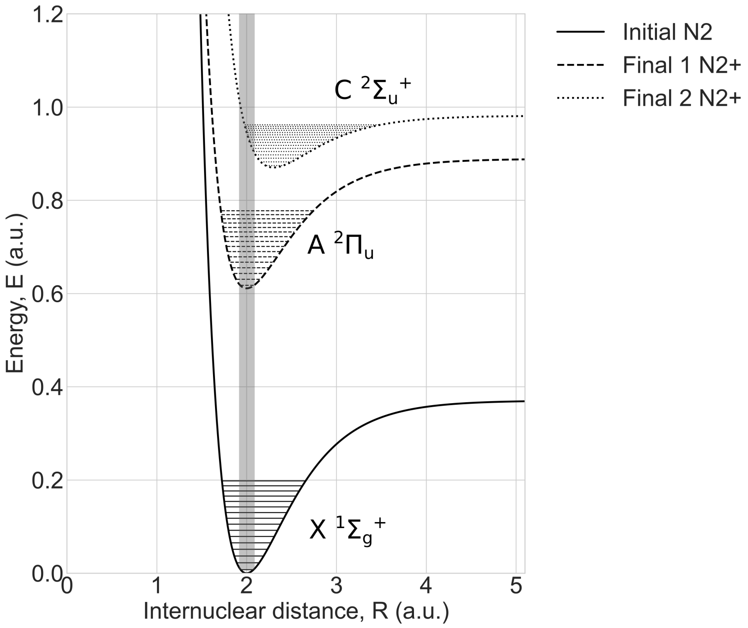

Figure 8: An illustration of the Franck-Condon principle. The potential energy curves of all three states shown in the figure are approximated by Morse potentials with different parameters R_{eq} and U_{asymp} applied (calculated according to Eq. 48, similar to Morse potential shown in Figure 7). These three electronic states are approximate models of the $X\,^1\Sigma_g^+$ electronic ground state of the N_2 molecule (shown as a solid line), and the $A\,^2\Pi_u$ and $C\,^2\Sigma_u^+$ states of the N_2^+ ion (shown as dashed and dotted lines, respectively). The vibrational states corresponding to $v = 0, ..., 15$ for all three potentials are shown as horizontal lines. For the initial $v = 0$ vibrational state of the $X\,^1\Sigma_g^+$ electronic state the internuclear distance region where the initial vibrational wavefunction has a non-zero amplitude is shown as a shaded area (Franck-Condon region).

the vertical energy axis in Fig. 8 (inside the shaded area), while the internuclear distance R remains constant. This is called the Franck-Condon principle.

Now let us give a brief quantum mechanical description of the Franck-Condon principle. In analogy to the previous section we assign the total initial and final states wavefunctions as Ψ_i and Ψ_f, respectively. As discussed above, using the separability of the electronic and vibrational states of a molecule, one can write both the initial and final state wavefunctions as a product of the corresponding electronic ψ_e and vibrational ψ_v wavefunctions: $\Psi_{i/f} = \psi_{e,i/f}\psi_{v,i/f}$. We neglect the dependence of the dipole moment μ on the internuclear distance R, so the intensity of the transition is proportional to $|\langle\psi_{e,f}|\,\mu\,|\psi_{e,i}\rangle\,\langle\psi_{v,f}|\psi_{v,i}\rangle|^2$. Here the second term $|\langle\psi_{v,f}|\psi_{v,i}\rangle|^2$ is called the Franck-Condon factor. The Franck-Condon factor is equal to the overlap between the initial and final states vibrational wavefunctions. It shows how the intensity of the vibronic transition is distributed among different vibrational states of the final electronic state.

Let us discuss two different vibronic transitions illustrated in Fig. 8. First, let us have a look at the $X\,^1\Sigma_g^+ \rightarrow A\,^2\Pi_u$ state transition. In this simplistic model, the potential energy curves of the $X\,^1\Sigma_g^+$ and $A\,^2\Pi_u$ states can be approximated as almost equivalent (up to a constant energy shift). Thus, as a first-order approximation, the set of the vibrational wavefunctions of these two electronic states can be estimated as similar. Then, taking into account the orthogonality of the vibrational states, the Franck-Condon factor $|\langle\psi_{\nu',f}|\psi_{\nu,i}\rangle|^2 = \delta_{\nu,\nu'}$, where ν and ν' are the vibrational quantum numbers of the initial and final states, respectively. This implies, that if the potential energy curves of the initial and final states are similar, the vibronic transitions occur only between vibrational states with the same vibrational quantum numbers. In case of a single photon-induced vibronic transition from the initial $\nu = 0$ vibrational state of the $X\,^1\Sigma_g^+$ electronic state to the final $A\,^2\Pi_u$ electronic state, as discussed above, only the $\nu' = 0$ final vibrational state is occupied. As a result, the photoelectron spectrum corresponding to such a vibronic transition, measured with a monochromatic photon source, would contain a single dominant spectral line.

On the other hand, if the potential energy curves of the initial and final electronic states are substantially different, as for example in case of the vibronic transition $X\,^1\Sigma_g^+ \rightarrow C\,^2\Sigma_u^+$, the Franck-Condon factors $|\langle\psi_{\nu',f}|\psi_{\nu,i}\rangle|^2$ show how the population is distributed between vibrational states of the final electronic state (here ν and ν' are the vibrational quantum numbers of the initial and final vibrational states, respectively). As a result, the photoelectron spectrum corresponding to such vibronic transitions, measured with a narrowband photon source, would consist of multiple spectral lines (plus a continuous part corresponding to the transitions to dissociating states).

2.4.6 *Molecular nitrogen*

Atomic nitrogen is the element with number 7 in the periodic system. The atomic weight of a nitrogen atom is 14.007 Da. In the N_2 molecule two nitrogen atoms are bound with a triple bond, one of the strongest in diatomic molecules. This results in a low reactivity of molecular nitrogen. The energies of the electronic orbitals in N_2 and also in the singly charged N_2^+ ion form the following sequence (the antibonding states are labelled with asterisk):

Electronic orbitals energy sequence.

$$1\sigma_g < 1\sigma_u^* < 2\sigma_g < 2\sigma_u^* < 1\pi_u < 3\sigma_g < 1\pi_g^* < 3\sigma_u^* \qquad (55)$$

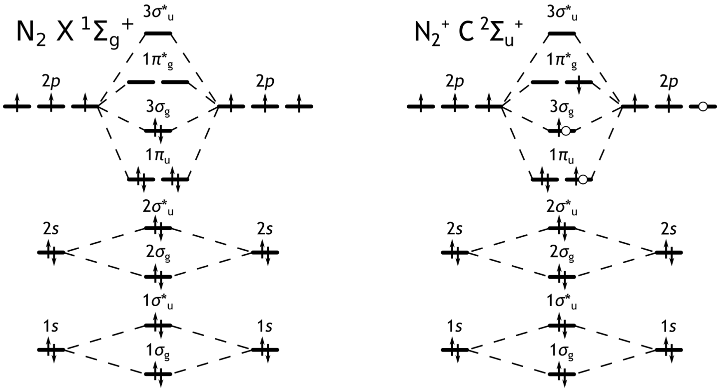

Figure 9: Molecular orbital diagrams of the ground state of the N_2 molecule $X\,^1\Sigma_g^+$ (left) and the N_2^+ $C\,^2\Sigma_u^+$ ion state (right). The number of horizontal lines represents the degeneracy of a state. The antibonding states are labelled with an asterisk.

We are going to focus on two particular states: the $X\,^1\Sigma_g^+$ ground state of the N_2 molecule, and the $C\,^2\Sigma_u^+$ state of N_2^+ ion, since single XUV photon-induced transitions between these two states are studied in the present work. The ground state of the N_2 molecule $X\,^1\Sigma_g^+$ has the following electronic configuration:

$X\,^1\Sigma_g^+$ *state electronic configuration.*

$$(1\sigma_g)^2(1\sigma_u^*)^2(2\sigma_g)^2(2\sigma_u^*)^2(1\pi_u)^4(3\sigma_g)^2 \tag{56}$$

The molecular orbital diagram and the potential energy curve of the $X\,^1\Sigma_g^+$ state are shown schematically in Fig. 9 and Fig. 10, respectively. The equilibrium internuclear distance of the $X\,^1\Sigma_g^+$ state $R_{eq} = 1.1$ Å.

The $C\,^2\Sigma_u^+$ state of the N_2^+ ion is a predissociative state for $\nu \geqslant 3$ vibrational states with energies above the first dissociation limit L1 of the N_2^+ ion at 24.31 eV ($N(^4S^0) + N^+(^3P)$ [91]). The molecular orbital diagram and the potential energy curve of the $C\,^2\Sigma_u^+$ state are schematically shown in Fig. 9 and Fig. 10, respectively. The equilibrium internuclear distance of the $C\,^2\Sigma_u^+$ state $R_{eq} = 1.3$ Å. The $C\,^2\Sigma_u^+$ state has the following electronic configuration (see Fig. 9):

$C\,^2\Sigma_u^+$ *state electronic configuration.*

$$(1\sigma_g)^2(1\sigma_u^*)^2(2\sigma_g)^2(2\sigma_u^*)^2(1\pi_u)^3(3\sigma_g)^1(1\pi_g^*)^1 \tag{57}$$

This means that in the single XUV photon-induced $X\,^1\Sigma_g^+ \rightarrow C\,^2\Sigma_u^+$ transition two electrons from the $1\pi_u$ and $3\sigma_g$ orbitals are involved: one is emitted into the continuum, and simultaneously another is excited to the $1\pi_g^*$ orbital. Multiple electronic transitions involved increase the overall complexity of the numerical simulation of the $X\,^1\Sigma_g^+ \rightarrow C\,^2\Sigma_u^+$ transition. Due to the population of the antibonding $1\pi_g^*$ orbital the bond strength of the $C\,^2\Sigma_u^+$ state is substantially weakened and thus it predissociates. The radiative lifetime of the $C\,^2\Sigma_u^+$

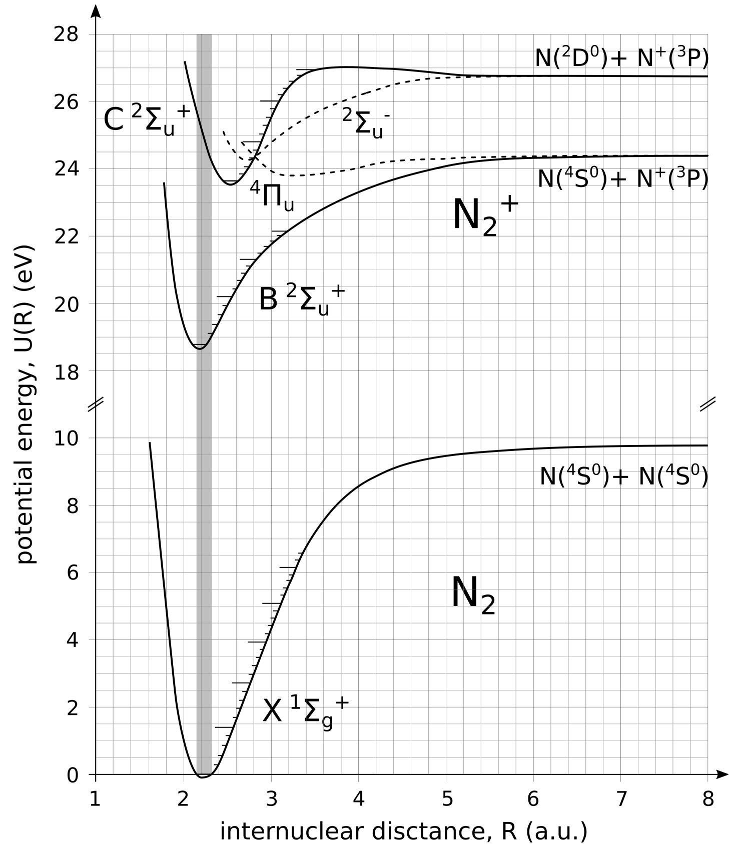

Figure 10: Potential energy curves of the molecular nitrogen states relevant for the photoinduced processes studied in the present work. The initial and final states of the single XUV photon-induced transitions: $X\,^1\Sigma_g^+$ state of the neutral N_2 molecule and $C\,^2\Sigma_u^+$ state of the N_2^+ ion, respectively, together with the $B\,^2\Sigma_u^+$ state the predissociation decay of the $C\,^2\Sigma_u^+$ state occurs through [88, 89] are shown as thick solid lines. The Franck-Condon region of the respective single XUV photon-induced transition is shown as a shaded area. Thin horizontal marks indicate energies of the corresponding vibrational states. The $^2\Sigma_u^-$ and $^4\Pi_u$ states of the N_2^+ ion involved in the alternative dissociation pathway suggested by S. Langhoff and C. Bauschlicher [90] are shown as dashed lines. The potential energy curves are adapted from [83].

state of the N_2^+ ion has been estimated to exceed 60 ns [90, 92]. The radiative decay is accompanied by transitions to the $X\,^2\Sigma_g^+$ ground state of the N_2^+ ion [49]. The predissociative lifetime for the vibrational states $v \geqslant 3$ with energies exceeding the first dissociation limit L1 has been determined to be on the order of 5 ns [92, 93]. S. Langhoff and C. Bauschlicher suggested the following dissociation path: $C\,^2\Sigma_u^+ \rightarrow\, ^2\Sigma_u^- \rightarrow\, ^4\Pi_u$ [90]. The corresponding potential energy curves are shown in Fig. 10 as dashed lines. An alternative mechanism was suggested by A. Roche and J. Tellinghuisen and later confirmed by B. Paulus *et al.* implying that the predissociation decay occurs through the $B\,^2\Sigma_u^+$ state [88, 89] (see Fig. 10). In the recent study by T. Ayari *et al.* it was shown that both suggested mechanisms are contributing to the predissociation of the $C\,^2\Sigma_u^+$ state [49]. The predissociative lifetimes calculated in this work vary from a few nanoseconds for $\nu = 3$ to a few hundreds of picoseconds for $\nu = 14$ vibrational states.

Due to the corresponding Franck-Condon factors, as shown in Fig 10, absorption of a single XUV photon induces transitions from the $\nu = 0$ vibrational state of the $X\,^1\Sigma_g^+$ ground state of the N_2 molecule to a set of vibrational states of the $C\,^2\Sigma_u^+$ state of N_2^+ ion. These transitions are accompanied by the emission of *s* or *d* photoelectrons. The vibrational states with $\nu \geqslant 3$ predissociate and corresponding signal appears in the N^+ fragment spectrum. For a detailed overview of the studies performed on the $C\,^2\Sigma_u^+$ state of N_2^+ ion please refer to the publication by T. Ayari *et al.* [49].

2.5 ULTRAFAST PUMP-PROBE SPECTROSCOPY

The ultrafast pump-probe spectroscopy is an experimental technique allowing studying of physical processes occurring on ultrashort time scales, such as the photoinduced nuclear or electronic dynamics in different targets. The temporal resolution on the attosecond (10^{-18} s) timescale became accessible after the discovery of the high-order harmonic generation process allowing generation of XUV pulses with typical duration on the order of a hundred of attoseconds. The first characterization of XUV attosecond pulse trains generated was done using a pump-probe technique called the Reconstruction of Attosecond Beating By Interference of two-photon Transitions or RABBIT [12, 15]. This technique was later implemented not only for XUV pulse characterization, but also for the investigation of different ultrafast photoinduced processes in atoms or molecules. Since ultrafast XUV–NIR pump-probe spectroscopy is the main experimental method used in the experiments reported in the present thesis, in the following section the principles of this technique are discussed. Starting from a classical qualitative picture of a pump-probe spectroscopy measurement, explaining the shape of the acquired spectrograms, the discussion is extended by a quantum mechanical description. Then the extraction of the photoelectron delays from a RABBIT spectrogram is explicitly described. Finally, the section is closed with the analysis of the influence of the NIR probe intensity on the shape of the measured spectrograms and the photoelectron delays extraction.

2.5.1 *Principles of ultrafast measurements*

The basic principles of ultrafast pump-probe spectroscopy using attosecond pulse trains or isolated attosecond pulses (in what follows both called XUV pulses for simplicity), called RABBIT and attosecond streaking, respectively, are similar and relying on the measurement of a cross correlation between the XUV and NIR pulses [94]. Since the NIR pulse used as a probe in the experiment is usually a copy of the NIR pulse used for the high-order harmonic generation, the XUV and NIR pulses delivered to the experiment are inherently synchronized. The two pulses with a controlled delay between them are focused into an atomic gas target. For the XUV pulse characterization it is advantageous to use a target that does not have resonances in the corresponding XUV photon spectral range. Since the XUV photon energy is usually sufficient for single photon ionization of the target, the temporal profile of the photoelectron wavepacket emitted after the absorption of an XUV photon represents the intensity profile $|E(t)|^2$ of the XUV pulse modified by the ionization probability of the target. The synchronized NIR field interacts with the emitted photoelectrons further altering their measured momentum distribution. In this picture the NIR pulse serves as a phase gate acting on the photoelectron wavepacket. From the measured photoelectron momentum or energy distribution as a function of the XUV–NIR delay, called RABBIT or streaking spectrogram, both the XUV and NIR pulses can be reconstructed, or properties of the target can be investigated.

Before introducing a quantum mechanical description of the ultrafast pump-probe spectroscopy technique, a qualitative classical pictures of both the RABBIT (Section 2.5.2) and attosecond streaking (Section 2.5.3) techniques are briefly discussed, in order to give a simple explanation of the features observed in the measured spectrograms.

2.5.2 *Qualitative picture of a RABBIT measurement*

The Reconstruction of Attosecond Beating By Interference of two-photon Transitions (RABBIT) is an XUV–NIR pump-probe photoelectron spectroscopy technique with XUV attosecond pulse trains (APTs) and short NIR pulses used. As shown in Section 2.1.4, the spectrum of an XUV attosecond pulse train consists of a set of discrete spectral lines with central energies corresponding to odd harmonics of the central angular frequency of the NIR pulse. Let us assume that the RABBIT experiment is performed on an atomic target, and photoionization is occurring from its ground state. Then the spectrum of a photoelectron wavepacket ionized form the target by an XUV APT also consists of a set of discrete spectral lines with the energies described by the following equation:

Energies of photoelectrons ionized with an APT.

$$E_{e^-} = \hbar\omega_{2n+1} - Ip \tag{58}$$

Here ω_{2n+1} is the central angular frequency of the high-order harmonic $2n+1$ (n is an integer) and Ip is the ionization potential of the initial bound state. As visible from Eq. 58, the energy separation between the two adjacent photoelectron spectral lines ΔE_{e^-} is twice the fundamental NIR photon energy: $\Delta E_{e^-} = 2\omega_0$.

If the XUV photon-induced ionization occurs in the presence of a synchronized NIR field with up to $10^{12}\,\mathrm{W/cm^2}$ peak intensity, the NIR field induces a continuum–continuum photoelectron state coupling. The NIR field peak intensity has to be limited in order to keep the number of transitions involving two or more NIR photons negligibly small. Absorption or stimulated emission of an NIR photon by a photoelectron in a continuum state transfers the photoelectron population to a set of continuum states with energies $E_{e^-} = \hbar\omega_{2n} - Ip$ corresponding to even high-order harmonics of the fundamental NIR photon. The photoelectron spectral lines corresponding to these continuum states are called *sidebands*. A schematic picture of the XUV and NIR photon-induced transitions is shown in Fig. 11. There are

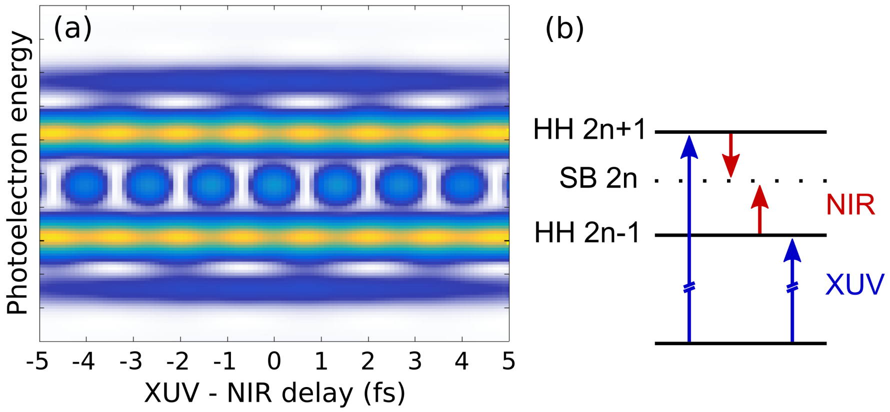

Figure 11: Schematic picture of a RABBIT measurement: *(a)* calculated RABBIT spectrogram for two adjacent high-order harmonics and *(b)* schematic view of the XUV and NIR photon-induced transitions involved (shown as blue and red arrows, respectively). The interference appears between the two indistinguishable quantum paths leading to the same final continuum photoelectron state ($2n$ sideband) through the absorption of the XUV photons corresponding to lower/higher neighbouring harmonics ($2n \pm 1$, where n is an integer) followed by an absorption/emission of a fundamental frequency NIR photon.

two competing quantum paths leading to the same final continuum state with energy $E_{e^-} = \hbar\omega_{2n} - Ip$: one involving absorption of an XUV photon with energy $\hbar\omega_{2n-1}$ accompanied by absorption of an additional NIR photon, and another involving absorption of an XUV photon with energy $\hbar\omega_{2n+1}$ accompanied by emission of an NIR photon. Therefore an interference occurs. The sideband signal oscillates as a function of the delay between the XUV and NIR pulses at twice the fundamental NIR photon frequency. This can be understood taking into account that the probability of the NIR photon-induced transitions is proportional to the intensity of the NIR field, which oscillates with twice the frequency of the electric field oscillations.

Extraction of the sideband phases from the measured RABBIT spectrogram allows either characterization of the XUV attosecond pulse train (retrieving the properties of the XUV APTs such as temporal profile and spectral phases) in case the measurement was performed in a target with known photoionization dynamics, or the other way around, studying the properties of the experimental target, if the characteristics of the XUV pulse train are known. The simple picture of a RABBIT experiment given in the present section is useful for qualitative understanding of the features observed in a measured RABBIT spectrogram.

2.5.3 *Classical picture of attosecond streaking*

An XUV–NIR pump-probe photoelectron spectroscopy experiment with isolated attosecond XUV and synchronized few-cycle NIR pulses is called attosecond streaking. Even though the quantum mechanical description of RABBIT and attosecond streaking experiments is similar, the classical description is different. Thus, in the present section a simple classical picture of an attosecond streaking experiment illustrating the features observed in the measured spectrogram is introduced.

In case of photoionization with isolated attosecond pulses, assuming that the photoionization dominantly occurs from a single initial bound state, the resulting photoelectron spectrum is smooth. It replicates the XUV photon spectrum shifted by the ionization potential of the initial state: $E_{e^-} = \hbar\omega_{XUV} - Ip$. Let us assume that the Coulomb interaction of the continuum photoelectron with the parent ion can be neglected, or in other words, after emission the photoelectron is considered as a free electron. This is called a *Strong Field Approximation* (SFA). The synchronized NIR field is linearly polarized with polarization parallel to the x-axis. Then, in the electric field of the synchronized NIR few-cycle pulse the classical equation of motion of the free electron has the form:

Equation describing photoelectron motion.

$$\ddot{x}(t) = -\frac{|e^-|}{m_e}E(t) \tag{59}$$

Here $|e^-|$ is the absolute electron charge and m_e is the electron mass. For simplicity, let us assume that at the time of photoelectron ejection t the initial momentum of the photoelectron $\vec{p}_i \upuparrows \vec{x}$, where $\vec{x}$ is a unity vector corresponding to the x-axis. Then, integrating Eq. 59 over t one gets:

Photoelectron momentum change induced by a vector potential.

$$\frac{|\vec{p}_f(t_\infty)| - |\vec{p}_i(t)|}{m_e} = -\frac{|e^-|}{m_e}A(t) \tag{60}$$

Here $\vec{p}_f(t_\infty)$ is the measured photoelectron momentum, and $A(t)$ is the vector potential of the NIR field, which is related to the electric field strength as $A(t) = \int_t^\infty E(t')dt'$, since $E(t) = -\frac{dA(t)}{dt}$. As visible from Eq. 60, the measured photoelectron momentum is modulated by the instantaneous vector potential of the NIR field at the photoelectron ejection time t, which is correlated to the XUV pulse shape. Varying the delay between the isolated XUV pulse and the dressing NIR pulse the photoelectron momentum modulation along the laser polarization can be measured as a function of the delay, forming an attosecond streaking spectrogram. From that spectrogram, similar to the RABBIT experiment, either the isolated attosecond XUV pulse can be characterized, or the properties of the target can be investigated.

It is worth showing here a simple derivation of the classical Hamiltonian H of a free electron in the external electric field, because it is going to be used in the following discussion. Since the electron is free, the Hamiltonian H contains only the kinetic energy term, while the potential energy term vanishes. Using Eq. 60 the following form of the Hamiltonian H can be derived:

Hamiltonian of an electron in the external electric field.

$$H = \frac{|\vec{p}_f|^2}{2m_e} = \frac{||\vec{p}_i| - |e^-| \cdot A|^2}{2m_e} = \frac{|\vec{p}_i|^2}{2m_e} + \frac{-2|e^-||\vec{p}_i|A + (|e^-| \cdot A)^2}{2m_e} \tag{61}$$

On the right hand side of Eq. 61 the first term corresponds to the Hamiltonian of a free electron with the initial momentum $\vec{p}_i$, while the second term describes the energy modulation induced by the external electric field.

2.5.4 *Perturbation induced by an electric field*

In the present section a simple picture of an atom in an external electric field is discussed. All the equations given in this section are written in atomic units. The given discussion partially follows the textbook by R. Zimmermann and L. Hanley [95]. In the following a *Single Active Electron* (SAE) approximation is used, meaning that the atom is approximated by a single electron in the Coulomb potential of the ion U_C. For simplicity the problem is reduced down to one dimension with the corresponding axis assigned as x-axis. Then the unperturbed Hamiltonian of the system $\hat{H}_0$ has the following form:

Unperturbed Hamiltonian.

$$\hat{H}_0 = -\frac{1}{2}\frac{\partial^2}{\partial x^2} + \hat{U}_C \tag{62}$$

The time-dependent perturbation induced by an external electric field $\hat{V}$ can be obtained from a classical Hamiltonian shown in Eq. 61 by substituting the quantum mechanical operator $\hat{p} = -i\frac{\partial}{\partial x}$ instead of a classical momentum. Then the operator $\hat{V}$ has the following form:

External electric field operator.

$$\hat{V} = iA\frac{\partial}{\partial x} + \frac{1}{2}A^2 \tag{63}$$

Since in the type of experiments discussed in the present section the electric field strength is relatively low, the corresponding vector potential is small comparing with the initial photoelectron energy $|\vec{p}_i|/2$. Thus, the second-order term in Eq. 63 can be neglected. Then the total Hamiltonian of the system $\hat{H}$ has the form:

Perturbed Hamiltonian.

$$\hat{H} = \hat{H}_0 + iA\frac{\partial}{\partial x} = -\frac{1}{2}\frac{\partial^2}{\partial x^2} + \hat{U}_C + iA\frac{\partial}{\partial x} \tag{64}$$

Let us assign the eigenvectors of the unperturbed Hamiltonian $\hat{H}_0$ as $\{|\Psi_n(x)\rangle\}$ with corresponding eigenvalues E_n: $\hat{H}_0 |\Psi_n(x)\rangle =$

$E_n |\Psi_n(x)\rangle$. Here we assume that the $\{|\Psi_n(x)\rangle\}$ set is complete and orthonormal. According to first-order perturbation theory, the eigenvector $|\Psi(x,t)\rangle$ of the perturbed Hamiltonian $\hat{H}$ can be expressed as a linear combination of eigenvectors of the unperturbed Hamiltonian $\{|\Psi_n(x)\rangle\}$ with corresponding coefficients $c_n(t)$ as follows:

Perturbed wavefunction representation in the unperturbed eigenfunctions basis.

$$|\Psi(x,t)\rangle = \sum_n c_n(t) e^{-iE_n t} |\Psi_n(x)\rangle \tag{65}$$

Inserting $|\Psi(x,t)\rangle$ in the form shown in Eq. 65 into the time-dependent Schrödinger equation: $i\frac{\partial}{\partial t} |\Psi(x,t)\rangle = \hat{H} |\Psi(x,t)\rangle$, where Hamiltonian $\hat{H}$ is shown in Eq. 64, and taking into account that the E_n are eigenvalues of $\hat{H}_0$, one gets:

Time-dependent Schrödinger equation.

$$\sum_n (i\frac{d}{dt}c_n(t) + E_n) e^{-iE_n t} |\Psi_n(x)\rangle = \sum_k (E_k + \hat{V}) c_k(t) e^{-iE_k t} |\Psi_k(x)\rangle \tag{66}$$

Since the basis $\{|\Psi_n(x)\rangle\}$ is orthonormal, multiplying both sides of Eq. 66 by $\langle\Psi_n|$ one derives a set of coupled equations for the $c_n(t)$ of the form:

Equation for the expansion coefficients.

$$\frac{d}{dt}c_n(t) = -i\sum_k \langle\Psi_n(x)| \hat{V} |\Psi_k(x)\rangle c_k(t) e^{i(E_n - E_k)t} \tag{67}$$

Here the term $E_n e^{-iE_n t}$ cancels on both sides of the equation. Now let us consider a system with two states $|\Psi_a(x)\rangle$ and $|\Psi_b(x)\rangle$. The system is initially in the state $|\Psi_a(x)\rangle$ and the external electric field induces coupling between the states $|\Psi_a(x)\rangle$ and $|\Psi_b(x)\rangle$. Then, using the linear term in Eq. 63 as an operator $\hat{V}$ describing the interaction, the equation for the coefficient $c_b(t)$ is derived:

Expansion coefficients for a two state system.

$$\begin{aligned} c_b(t) &= -i\int_0^t \langle\Psi_b(x)| \hat{V} |\Psi_a(x)\rangle e^{i(E_b - E_a)t'} dt' \\ &= \int_0^t \langle\Psi_b(x)| A\frac{\partial}{\partial x} |\Psi_a(x)\rangle e^{i(E_b - E_a)t'} dt' \end{aligned} \tag{68}$$

It is convenient to assign an angular frequency ω_{ba} corresponding to the energy difference between the eigenenergies of the $|\Psi_a(x)\rangle$ and $|\Psi_b(x)\rangle$ states: $\omega_{ba} = E_b - E_a$.

The vector potential $A(x,t)$ can be written in the following form:

Vector potential.

$$A(x,t) = A\cos(kx - \omega t + \phi) = \frac{1}{2}A(e^{i(kx-\omega t+\phi)} + e^{-i(kx-\omega t+\phi)}) \tag{69}$$

Here k and ω are the photon wavevector and angular frequency, respectively and A is an amplitude. Applying Eq. 69 into Eq. 68 for $c_b(t)$ one gets:

Absorption and emission of a photon.

$$\begin{aligned} c_b(t) = &\frac{1}{2}Ae^{i\phi}\langle\Psi_b(x)|\, e^{ikx}\frac{\partial}{\partial x}\,|\Psi_a(x)\rangle \int_0^t e^{i(\omega_{ba}-\omega)t'}dt' \\ &+ \frac{1}{2}Ae^{-i\phi}\langle\Psi_b(x)|\, e^{-ikx}\frac{\partial}{\partial x}\,|\Psi_a(x)\rangle \int_0^t e^{i(\omega_{ba}+\omega)t'}dt' \end{aligned} \tag{70}$$

Here the first term corresponds to the photon absorption. It is non-zero only for $E_b = E_a + \omega$ due to the periodicity of the complex exponent. Symmetrically, the second term corresponding to photon emission is non-zero only for $E_b = E_a - \omega$. If the system was initially in the state $|\Psi_a(x)\rangle$, then the $c_b(t)$ is a complex time-dependent amplitude of the transition from $|\Psi_a(x)\rangle$ to $|\Psi_b(x)\rangle$ induced by the interaction with a photon.

2.5.5 *Dipole transition matrix representation*

The term $\langle\Psi_b(x)|\, e^{ikx}\frac{\partial}{\partial x}\,|\Psi_a(x)\rangle$ in Eq. 70 is often referred to as the transition matrix element $\tilde{M}_{ba}$ for the transition from $|\Psi_a(x)\rangle$ to $|\Psi_b(x)\rangle$ induced by the interaction with a photon (here complex quantities, such as the transition matrix element $\tilde{M}_{ba}$, are written with a tilde hat). In other words, $\tilde{M}_{ba}$ describes the strength of the system interaction with the incident light. The term e^{ikx} defines the dependency of $\tilde{M}_{ba}$ on the photon wavevector k (equivalent to photon momentum $p = k$, here atomic units are used). If photon wavelength $\lambda = \frac{2\pi}{k}$ is substantially larger than the spatial dimensions of the system, a valid approximation is: $e^{ikx} \approx 1$. This approximation is applicable to XUV photon ionization of atomic or molecular targets, for which 10 to 100 nm is a typical wavelength range, while the typical target size is below one nanometer. Then the system interaction with an electric field can be approximated as a dipole interaction with corresponding operator $\hat{D} = -\hat{x}$. Thus, the transition matrix element $\tilde{M}_{ba}$ can be replaced by a dipole transition matrix element $\tilde{D}_{ba} = \langle\Psi_b(x)|\,\hat{x}_{ba}\,|\Psi_a(x)\rangle$, where $\hat{x}_{ba}$ is the position operator. This approximation is called the dipole approximation. In the framework of the dipole approximation the first term in Eq. 70 corresponding to the absorption of a photon becomes:

Expansion coefficients in dipole transition representation.

$$\begin{aligned} c_b(t) &= \frac{1}{2} A e^{i\phi} \langle \Psi_b(x) | \hat{x}_{ba} | \Psi_a(x) \rangle \int_0^t e^{i(\omega_{ba}-\omega)t'} dt' \\ &= \frac{1}{2} A e^{i\phi} \tilde{D}_{ba} \int_0^t e^{i(\omega_{ba}-\omega)t'} dt' \end{aligned} \tag{71}$$

2.5.6 *Quantum mechanical description*

As already mentioned above, the quantum mechanical description of RABBIT and attosecond streaking experiments is similar. It basically describes the photoionization of a target induced by a single XUV photon absorption in the presence of an external laser field. In the present section the equations conventionally used for the description of XUV–NIR pump-probe photoelectron spectroscopy experiments are derived and discussed. All the equations are given in atomic units, and all complex quantities, such as for example the dipole transition matrix element $\tilde{D}$, are written with a tilde hat.

Let us assume that the XUV and dressing NIR laser pulses are linearly polarized with polarization parallel to the x-axis. The target system is initially in the bound state $|\Psi_0\rangle$. After interaction of the system with an XUV photon, a photoelectron wavepacket $|\Psi(t)\rangle$ is emitted into the continuum. A suitable basis for the description of continuum states $\{|p_f\rangle\}$ with asymptotic momentum values $\vec{p}_f$ is the set of Coulomb-Volkov states corresponding to a basis of continuum eigenstates of the unperturbed system Hamiltonian H_0 [96]. In this basis the interaction of the ejected photoelectron with the parent ion is taken into account.

For simplicity, we reduce the problem down to one dimension, or, in other words, we assume that all the detected photoelectrons have the asymptotic momentum $\vec{p}_f$ parallel to the x-axis. Experimentally this would correspond to the detection of photoelectrons emitted along the laser polarization. Thus, in what follows we can use scalar momentum values p_f instead of vectors. The measured photoelectron spectrum $S(p_f)$, which is equivalent to the probability density of detecting a photoelectron with asymptotic momentum p_f, is then:

Photoelectron spectrum.

$$S(p_f) = |\langle p_f | \Psi(t) \rangle|^2 = |\tilde{a}(p_f)|^2 \tag{72}$$

Here $\tilde{a}(p_f)$ is a complex amplitude of the transition from the initial state $|\Psi_0\rangle$ to the continuum state $|p_f\rangle$ with asymptotic momentum p_f. A slightly different notation is used in the present section since it is conventional in the field of attosecond physics (comparing with the one used in Section 2.5.4). According to first-order perturbation theory (Eq. 68) in combination with the dipole approximation (Eq. 71), in the absence of the dressing NIR field the amplitude $\tilde{a}(p_f)$ of the transition from the initial state $|\Psi_0\rangle$ to the continuum state $|p_f\rangle$ with the asymptotic momentum p_f is equal to:

Complex transition amplitude.

$$\tilde{a}(p_f) = -i\int_{-\infty}^{\infty} \tilde{E}(t)\tilde{D}(p_f)e^{i(p_f^2/2+Ip)t}dt \tag{73}$$

Here $\tilde{E}(t)$ is the electric field of the XUV pulse in the temporal domain and $\tilde{D}(p_f)$ is the dipole transition matrix element for the transition from the initial state $|\Psi_0\rangle$ to the continuum state $|p_f\rangle$ with the asymptotic momentum p_f. The energy difference between these two states is equal to the sum of the final energy of the continuum photoelectron $p_f^2/2$ and Ip — the ionization potential of the initial state $|\Psi_0\rangle$. The integration is performed over the whole laser pulse duration.

Inserting Eq. 73 into Eq. 72, the photoelectron spectrum $S(p_f)$ resulting from single XUV photon ionization in the absence of the dressing NIR field is acquired:

Photoelectron spectrum resulting from single XUV photon ionization.

$$S(p_f) = \left|\int_{-\infty}^{\infty} \tilde{E}(t)\tilde{D}(p_f)e^{i(Ip+p_f^2/2)t}dt\right|^2 \tag{74}$$

Now, let us apply a synchronized NIR field with vector potential $A(t)$ to the system. The NIR pulse is delayed with respect to the XUV pulse by τ. Then, according to Eq. 60, due to the photoelectron momentum modulation by the NIR field vector potential, the detected photoelectron with measured asymptotic momentum p_f right after the ionization has had initial momentum $p_i = p_f + A(t)$. So the dipole transition matrix element in Eq. 74 in the presence of the NIR field becomes $\tilde{D}(p_f + A(t))$. Following the same logic, in the presence of the synchronized NIR field the exponential term in Eq. 74 becomes:

Phase term.

$$\begin{aligned} e^{i\left(Ip+\frac{(p_f+A(t))^2}{2}\right)t} &= e^{i\left(Ip+\frac{p_f^2}{2}+p_fA(t)+\frac{A(t)^2}{2}\right)t} \\ &= e^{i\left(Ip+\frac{p_f^2}{2}\right)t}\cdot e^{i\left(p_fA(t)+\frac{A(t)^2}{2}\right)t} \end{aligned} \tag{75}$$

It is convenient to separate the terms as shown in Eq. 75, where the first term is similar to Eq. 74, while the second term corresponds to the continuum photoelectron phase modulation induced by the NIR field vector potential $A(t)$. Then the photoelectron spectrum $S(p_f, \tau)$

corresponding to single XUV photon ionization in the presence of the NIR field delayed with respect to the XUV pulse by τ is equal to:

Photoelectron spectrum resulting from two photon transition.

$$S(p_f, \tau) = \left| \int_{-\infty}^{\infty} \tilde{E}(t-\tau)\tilde{D}(p_f + A(t)) e^{i\Phi(p_f,t)} e^{i(Ip + p_f^2/2)t} dt \right|^2 \quad (76)$$

The phase term $\Phi(p_f, t)$ is called the Volkov phase. It is equal to the phase acquired by a free electron with momentum p_f in an external electric field with vector potential $A(t)$:

Volkov phase.

$$\Phi(p_f, t) = -\int_{t}^{\infty} \left(p_f A(t') + \frac{1}{2} A^2(t') \right) dt' \quad (77)$$

Here t is the time of the photoelectron ejection.

2.5.7 *Attosecond pulse characterization*

A well-established technique for characterization of femtosecond duration laser pulses is Frequency Resolved Optical Gating (FROG) [97]. The basic principle of this technique is the following: the laser pulse under investigation $E(t)$ is overlapped with a gate pulse $G(t)$, and the resulting spectrum $S(\omega)$ is recorded. Varying the delay between the pulse and the gate τ, a two-dimensional map or spectrogram $S(\omega, \tau)$ is recorded. Both the laser pulse $E(t)$ and the gate $G(t)$ can be reconstructed from the measured spectrogram using different iterative algorithms, such as for example different versions of the Generalized Projection Algorithm (GPA) [98]. The measured trace $S(\omega, \tau)$ is described by the following equation:

Frequency Resolved Optical Gating.

$$S(\omega, \tau) = \left| \int_{-\infty}^{\infty} G(t) E(t-\tau) e^{i\omega t} dt \right|^2 \quad (78)$$

Comparing Eq. 76 describing a streaking spectrogram recorded during an attosecond streaking experiment with Eq. 78 describing a conventional FROG, it becomes clearly visible that these two measurements are to some extent similar. In the attosecond streaking experiment the term $e^{i\Phi(p_f,t)}$ in Eq. 76, where $\Phi(p_f, t)$ is the Volkov phase (Eq. 77), acts as a phase gate. Thus, the spectrogram acquired during an attosecond streaking experiment (or a RABBIT experiment for attosecond pulse trains) can be used for the characterization of both XUV and NIR pulses used. This technique is called Frequency Resolved Optical Gating for Complete Reconstruction of Attosecond Bursts (FROG CRAB) [99].

2.5.8 *Measured delays in RABBIT experiment*

In the present section the relation between the delays measured in a RABBIT experiment and different potential-induced photoelectron wavepacket phase shifts described in Section 2.2 is discussed. The given discussion partially follows the publication by J. M. Dahlström *et al.* [69]. As described in Section 2.5.2, in a RABBIT experiment the time-resolved information is extracted from the phases of the sideband oscillations as a function of the the XUV–NIR pump-probe delay. Two quantum paths contribute to the sideband spectral line in a RABBIT spectrogram: involving absorption of one XUV photon from lower/higher adjacent harmonics and absorption/emission of a fundamental frequency NIR photon. The two quantum paths are interfering constructively, and thus the sideband signal reaches maximum, when the complex amplitudes of these two transitions are in phase:

Constructive interference at sideband spectral line.

$$\phi_{\Omega_<} + \omega_0\tau + \sigma_l(p_<) + \phi_{cc}(p_<, p_0) = \phi_{\Omega_>} - \omega_0\tau + \sigma_l(p_>) + \phi_{cc}(p_>, p_0) \tag{79}$$

The left hand side of Eq. 79 corresponds to the quantum path involving NIR photon absorption, while the right hand side corresponds to the quantum path involving NIR photon emission. They include a $\pm\omega_0\tau$ term, respectively, where ω_0 is the angular frequency of the fundamental NIR photon and τ is the delay between the XUV and NIR pulses corresponding to the maximum of the sideband signal. $\phi_{\Omega_<}$ and $\phi_{\Omega_>}$ are the phases of the single XUV photon-induced transitions from the initial bound electron state to the continuum photoelectron states by XUV photons with energies $\Omega_<$ and $\Omega_>$, corresponding to lower and higher adjacent harmonics, respectively. $\phi_{cc}(p_<, p_0)$ and $\phi_{cc}(p_>, p_0)$ are the phases of the NIR photon-induced transitions between the continuum photoelectron states, from the initial states with asymptotic momentum $p_>$ and $p_<$, reached by absorption of XUV photons with energies $\Omega_<$ and $\Omega_>$, respectively, to final state with asymptotic momentum p_0 corresponding to the sideband spectral line in the photoelectron spectrum. Finally, the phases $\sigma_l(p_<)$ and $\sigma_l(p_>)$ are the scattering phase shifts of photoelectrons with asymptotic momenta $p_>$ and $p_<$ and angular momentum l on the short range potential of the ion (Eisenbud-Wigner-Smith delays). Rearranging the terms in Eq. 79, the following equation for the delay τ between the XUV and NIR pulses corresponding to the maximum of the sideband signal is derived:

Measured delay.

$$\begin{aligned}\tau &= \frac{\phi_{\Omega_>} - \phi_{\Omega_<}}{2\omega_0} + \frac{\sigma_l(p_>) - \sigma_l(p_<)}{2\omega_0} + \frac{\phi_{cc}(p_>, p_0) - \phi_{cc}(p_<, p_0)}{2\omega_0} \\ &= \tau_{GD} + \tau_W + \tau_{cc}\end{aligned} \tag{80}$$

Here we assume that all three phase terms in Eq. 79 vary slowly, so the finite differences in Eq. 80 can be approximated as equal to the corresponding partial derivatives. Then the measured delay τ is equal to the sum of three different delays as shown in Eq. 80. The first term τ_{GD} corresponds to the group delay of the XUV pulse. In the RABBIT measurements performed for the XUV pulse characterization this term is the quantity of interest. The second term τ_W is the Wigner delay corresponding to the scattering phase shifts on the short range potential of the parent ion of a photoelectron ionized by a single XUV photon. This delay contains information on the bound state electron dynamics during the photoionization, and thus is the quantity of interest in ultrafast photoionization experiments. As discussed in Section 2.2.2, due to the evolution of the photoelectron wavepacket while travelling through the potential, τ_W is a meaningful quantity only in comparison to a delay acquired by a reference photoelectron scattered on a known potential. Finally, the third term τ_{cc} is the measurement-induced delay corresponding to the NIR photon-induced continuum–continuum photoelectron transitions. As a first-order approximation this term can be assumed universal for different ions with the same charge Z. In a number of publications the latter two terms are merged together and their sum is called the atomic delay $\tau_{at} = \tau_W + \tau_{cc}$. For a hydrogen-like system τ_W and τ_{cc} have positive and negative signs, respectively. Since the absolute value of τ_{cc} exceeds the absolute value of τ_W, the resulting τ_{at} is negative [100].

As visible from Eq. 80, in order to access information on the short range potential scattering phase shifts, namely extract τ_W from the measured delay τ, the group delay of the XUV pulse τ_{GD} has to be known, or vice versa (the τ_{cc} term can be calculated). One of the ways to overcome this circular argument is to perform a measurement simultaneously in two targets with similar ionization potentials of the initial bound states. As a result, the photoelectrons ionized from both targets with XUV photons corresponding to the same high-order harmonics have similar asymptotic energies. Then, as discussed in Section 2.2.4, the delays of photoelectrons ionized from the two targets can be compared, since the delays induced by the photoelectron propagation in the long range Coulomb potential τ_{cc} are the same, and thus cancel out. Moreover, the τ_{GD} term also cancels since the quantum paths leading to the sideband spectral lines in the two spectrograms involve the absorption of XUV photons from the same harmonics. Then the difference between the measured delays $\Delta\tau$ is equal to the difference between the Wigner delays $\Delta\tau_W$, which in turn corresponds to the energy derivative of the difference between the quantum defect $\Delta\delta_l(p)$ for the two potentials (for more details please refer to Section 2.2.5):

Measured delay difference.

$$\begin{aligned}\Delta\tau(\omega) = \Delta\tau_W(\omega) &= \frac{\partial(\sigma_l^H(p) + \delta_l(p))}{\partial\omega} - \frac{\partial(\sigma_l^H(p) + \delta_l'(p))}{\partial\omega} \\ &= \frac{\partial(\Delta\delta_l(p))}{\partial\omega}\end{aligned} \tag{81}$$

Here $\sigma_l^H(p)$ is the scattering phase shift on the potential of the atomic hydrogen ion and $\delta_l(p)$, and $\delta_l'(p)$ are the quantum defects for the two potentials, respectively. Thus, the measured delay difference $\Delta\tau(\omega)$ reveals the difference between the short range potentials of the two targets.

2.5.9 *RABBIT measurements at different probe NIR intensities*

In the present section the effect of the NIR probe intensity applied during a RABBIT measurement on the shape of the resulting spectrogram and the delay information extracted from it is discussed. The spectrograms presented in this section were calculated by solving the Time-Dependent Schrödinger Equation (TDSE) for XUV single photon ionization of argon in the presence of a synchronized NIR field with different intensities. Since the process under investigation involves only one XUV photon, the strength of the XUV field is not affecting the resulting photoelectron spectrograms up to a certain limit, above which the fraction of processes involving double or higher number of XUV photons is no longer negligible. The calculations presented here were performed by Dr. Marc J. J. Vrakking.

The normalized temporal profiles of the NIR and XUV pulses used for the calculations are shown in Fig. 12. These pulses were reconstructed from RABBIT spectrogram measured in Ar [101]. The CEP of the XUV pulse is not accessible with the FROG CRAB method, and thus was chosen randomly.

Knowing the peak electric field strength $|E_{max}|$, the peak intensity I_{max} of the NIR pulse can be calculated using the following formula:

Peak NIR field intensity.

$$I_{max} = \frac{\epsilon_0 c |E_{max}|^2}{2} \tag{82}$$

Here ϵ_0 is the vacuum dielectric permittivity and c is the speed of light.

First, let us have a look at the RABBIT spectrogram calculated for a conventional $8.1 \cdot 10^{10}\,\mathrm{W/cm^2}$ NIR probe intensity shown in Fig. 13 (a). The present spectrogram was constructed from photoelectrons emitted along the laser polarization. In Fig. 13 (b) the square root of the Fourier Transform Power Spectrum (FTPS) of the calculated RABBIT spectrogram is shown. The transformation was per-

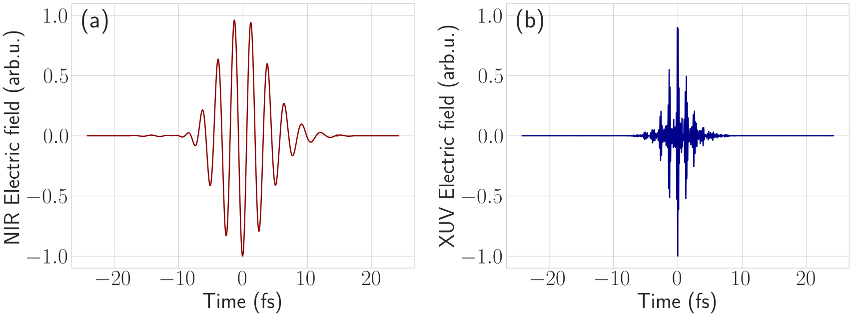

Figure 12: Normalized electric fields of the pulses used for the TDSE calculations: *(a)* NIR pulse, *(b)* XUV pulse. These pulses were reconstructed from the RABBIT trace measured in Ar as a part of the experiment reported in [101].

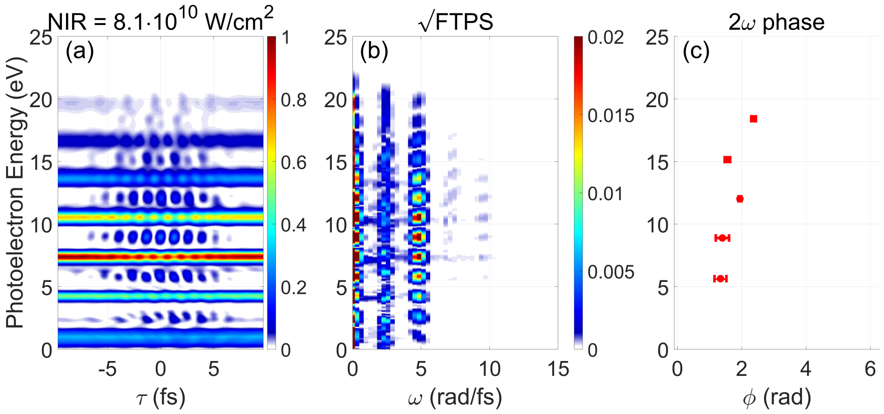

Figure 13: Calculation of a RABBIT experiment in Ar at $8.1 \cdot 10^{10}\,\mathrm{W/cm^2}$ NIR peak intensity. *(a)* RABBIT spectrogram (normalized) constructed from photoelectrons emitted along the laser polarization, *(b)* the square root of the Fourier Transform Power Spectrum, and *(c)* the extracted $2\omega_0$ frequency component phases for sidebands 14–22.

formed using a Fast Fourier Transform (FFT) algorithm. The dominant angular frequency component in the FTPS is the $2\omega_0$, where $\omega_0 = 2.36\,\mathrm{rad/fs}$ is the central angular frequency of the NIR laser pulse (corresponds to $\lambda = 800\,\mathrm{nm}$ central wavelength). As discussed in Section 2.5.2, the $2\omega_0$ frequency component in the FTPS corresponds to the NIR photon-induced continuum–continuum photoelectron transitions. They occur every half cycle of the NIR pulse, since the probability of the continuum–continuum transitions depends on the NIR probe intensity ($\propto |E|^2$).

The frequency components in the FTPS of the RABBIT spectrogram can also be interpreted from another point of view. Each $n\omega_0$ frequency component, where n is an integer and ω_0 is the central angular frequency of the NIR pulse, corresponds to multi NIR photon-induced transitions creating interfering quantum paths between continuum photoelectron states with energy separation equal $n\omega_0$. These two interpretations are in agreement with each other, since the $2\omega_0$ component corresponds to quantum paths involving XUV photons from two adjacent harmonics with $2\omega_0$ energy difference. In this picture the $1\omega_0$ frequency component corresponds to interference between two quantum paths involving one XUV and one XUV ± one NIR photon, respectively. It is present in all three spectrograms shown in Figs. 13–15 since the XUV pulse trains used for the TDSE calculations were relatively short as shown in Fig. 12 (b), which results in broad spectral lines for each individual harmonic. Thus, single XUV photon-induced transitions may lead to the sideband photoelectron spectral lines in the RABBIT spectrogram.

The sideband phases determine the delays of the detected photoelectrons, which in turn allow access to time-resolved information on photoionization process, for example to the Eisenbud-Wigner-Smith delays. The pump-probe delay axis in all RABBIT spectrograms shown in the present work is the delay between the XUV and NIR pulses. In other words, positive delays correspond to XUV pulses arriving first. The sideband oscillation phases can be extracted as phases of the $2\omega_0$ angular frequency component in the Fourier Transform of the RABBIT spectrogram, or by performing a fitting with a cosine function of the form $\cos(2\omega_0\tau - \phi)$, where τ is the delay between the XUV and NIR pulses and ϕ is the linear phase term. It is a convention to use $-\phi$ for the transformation from time to frequency domain [83]. Symmetrically, for the inverse transformation a $+\phi$ phase term is used. The $2\omega_0$ phases ϕ extracted with any of these two methods correspond to the measured delays τ as follows:

Relation between the delays and the 2ω phases.

$$\tau = \frac{\phi}{2\omega_0} \tag{83}$$

In the present case the sideband oscillation phases were extracted from the Fourier Transform of the calculated RABBIT spectrograms as complex phases of the $2\omega_0$ angular frequency component for each photoelectron energy. Then the extracted phases were integrated along each individual sideband spectral line, which are approximately 1.3 eV broad for the XUV pulses used. The resulting phases are shown in Fig. 13 (c). The corresponding delays reveal that the original XUV pulse train had a positive group delay. The shift of the measured phases for sidebands 18 and 20 is induced by the presence of a $3s^{-1}4p$ resonance in Ar at XUV photon energies around 26.63 eV [26] (see Section 2.3.3). These resonance-induced phase shifts were not taken into account during the pulse characterization from the experimentally acquired RABBIT spectrograms. Thus, the corresponding delays were effectively imprinted onto the XUV pulse train phases. As a result, using these XUV phases for the TDSE calculations, the resonance induced delays appeared in the calculated spectrograms.

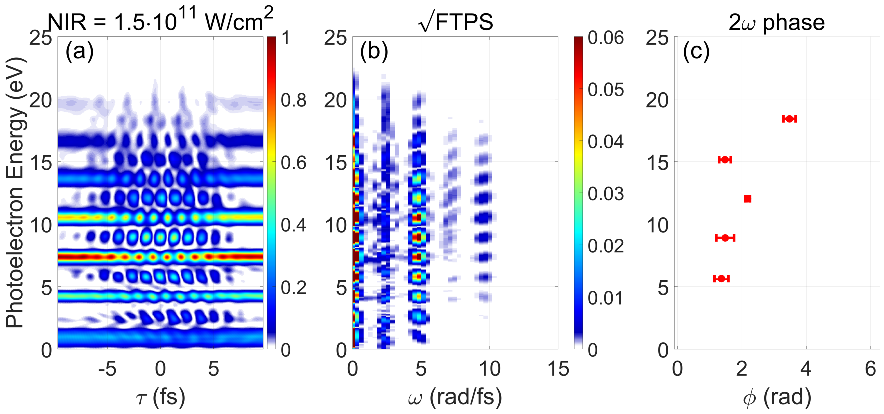

Figure 14: Calculation of a RABBIT experiment in Ar at $1.5 \cdot 10^{11}$ W/cm^2 NIR peak intensity. *(a)* RABBIT spectrogram (normalized) constructed from photoelectrons emitted along the laser polarization, *(b)* the square root of the Fourier Transform Power Spectrum, and *(c)* the extracted $2\omega_0$ frequency component phases for sidebands 14–22.

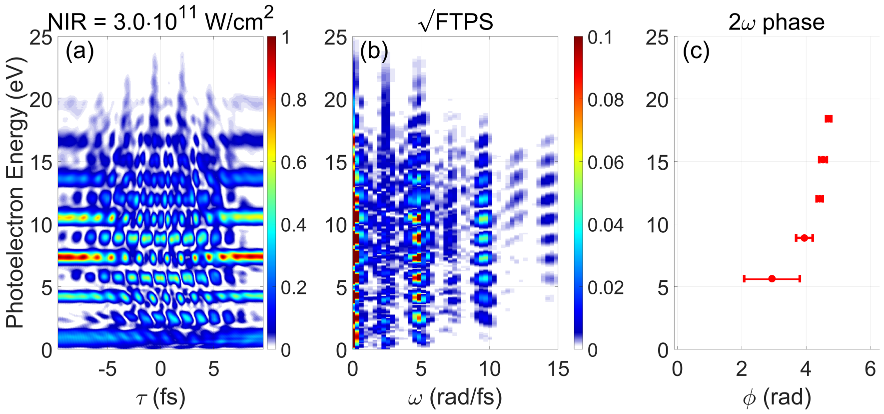

Figure 15: Calculation of a RABBIT experiment in Ar at $3.0 \cdot 10^{11}$ W/cm^2 NIR peak intensity. *(a)* RABBIT spectrogram (normalized) constructed from photoelectrons emitted along the laser polarization, *(b)* the square root of the Fourier Transform Power Spectrum, and *(c)* the extracted $2\omega_0$ frequency component phases for sidebands 14–22.

A RABBIT spectrogram calculated for approximately twice higher NIR probe intensity $1.5 \cdot 10^{11}$ W/cm^2 with corresponding Fourier Transform Power Spectrum is shown in Fig. 14. Higher-order angular frequency components, such as $3\omega_0$ and $4\omega_0$, appear in the FTPS. They correspond to transitions involving one or two additional NIR photons, respectively. The presence of these high number of NIR photon transitions affects the shape of the RABBIT spectrogram. In Fig. 14 (a), the sideband signal peaks are slightly extended along the pump-probe delay axis compared with the conventional RABBIT spectrogram shown in Fig. 13 (a).

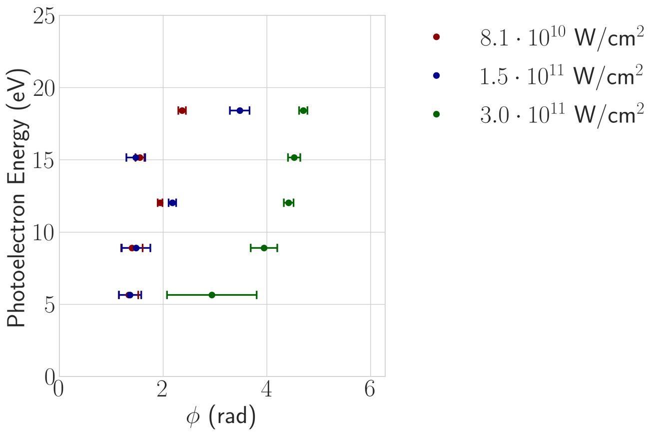

Figure 16: Comparison of the sidebands 14–22 oscillation phases extracted from RABBIT spectrograms calculated for different NIR probe intensities (shown in figures 13–15).

Increasing the NIR probe peak intensity further to $3.0 \cdot 10^{11}$ W/cm^2 the acquired RABBIT spectrogram shown in Fig. 15 (a) gets significantly distorted. In that case not only $3\omega_0$ and $4\omega_0$ angular frequency components became much more prominent than at lower NIR probe peak intensities, but also higher-order components such as $5\omega_0$ and $6\omega_0$ appear in the FTPS shown in Fig. 15 (b). This indicates a higher probability of transitions involving multiple NIR photon.

In Fig. 16 the $2\omega_0$ angular frequency component sideband phases extracted from the RABBIT spectrograms calculated for the three different NIR probe peak intensities are shown together. Since the zero delay was assigned for all three calculations similarly, a direct comparison of the extracted phases is possible. The phases extracted from the RABBIT spectrograms calculated for $8.1 \cdot 10^{10}$ W/cm^2 and $1.5 \cdot 10^{11}$ W/cm^2 NIR peak intensities are in agreement with each other. The discrepancy in the extracted sideband phases from the two spectrograms is most prominent for the high energy photoelectrons — sideband 22. This means that the distortions observed in the RABBIT spectrogram shown in Fig. 14 (a) do not significantly affect the extracted sideband phases. This result shows that for a certain range of the NIR probe peak intensities the extracted sideband phases are the same, even though the shape of the corresponding RABBIT spectrograms could be slightly distorted, which is indicated by the presence of higher-order angular frequency components in the Fourier domain.

Increasing the NIR field intensity further, the situation changes dramatically. The sideband phases extracted from the RABBIT spectrogram calculated for $3.0 \cdot 10^{11}$ W/cm^2 NIR peak intensity are up to π rad different from the phases acquired for lower NIR probe peak intensities as shown in Fig. 15 (c). Since the Ar dipole transition matrix elements and the XUV and NIR pulses used for all three calculations were the same, this result shows that applying a NIR probe with peak intensity exceeding approximately $2.0 \cdot 10^{11}\,\mathrm{W/cm^2}$ during a RABBIT measurement, the delay information can no longer be reliably extracted from the experimentally acquired RABBIT spectrograms using conventional methods.

From the results of the calculations reported in the present section one could conclude that below a certain threshold for the NIR probe intensity applied during a RABBIT experiment the delay information can be reliably extracted as $2\omega_0$ angular frequency component phases in the Fourier Transform of the measured RABBIT spectrograms or by any other equivalent method. We estimate this threshold to be on the order of $2.0 \cdot 10^{11}\,\mathrm{W/cm^2}$. Approaching it the discrepancies are stronger for the high energy photoelectrons. If angular frequency components higher than $4\omega_0$ are present in the FTPS of a measured RABBIT spectrogram the delay evaluation using conventional methods is no longer possible.

Part II

ATTOSECOND BEAMLINE

In the second part of this thesis a description of the attosecond beamline used for the experiments performed as a part of the present work is given. In Chapter 3 the design and characteristics of the laser system and the pump-probe interferometer are discussed. Chapter 4 covers a description of the charged particle detection techniques used in the present work.

3

ATTOSECOND BEAMLINE

In Chapter 3 the laser system serving as a driver for the experiments reported in the present thesis is discussed. Since ultrashort NIR laser pulses were used, the chapter starts with a brief description of general principles of generation and amplification of such pulses. The main part of the chapter is focused on the design and characteristics of the laser system and the pump-probe interferometer. The chapter closes with a description of XUV attosecond pulse trains or isolated attosecond pulses available for the experiments. The content of the chapter is organized in sections as follows:

The chapter opens with a brief introduction to the basic principles of laser pulse technology given in Section 3.1. Starting from laser technology in general briefly described in Section 3.1.1, the discussion later focuses on the generation and amplification of ultrashort laser pulses covered in Section 3.1.2 and Section 3.1.3, respectively.

In Section 3.2 a Noncollinear Optical Parametric Chirped Pulse Amplification (NOPCPA) system serving as the laser source for the attosecond beamline, and the attosecond pump-probe interferometer are discussed. Section 3.2.1 gives a short description of the design and characteristics of the NOPCPA system accompanied by properties of the delivered NIR laser pulses. For a certain class of applications isolated attosecond pulses are required instead of attosecond pulse trains. In order to generate them the NIR laser pulses delivered by the NOPCPA system have to be further compressed towards the single cycle regime. This can be achieved by spectral broadening in a gas-filled hollow core fiber. The properties of the resulting pulses after compression are given in Section 3.2.2.

In Section 3.2.3 the design and characteristics of the attosecond pump-probe interferometer are described. In order to be able to perform attosecond pump-probe photoionization experiments with coincidence detection a number of modifications improving the stability were applied as part of the present work. One of the major modifications was the installation of an active delay stabilization system. The basic working principles and implementation of that system are described in Section 3.2.4. Since the requirements for the vacuum conditions of the setup containing simultaneously an HHG cell and a Reaction Microscope are to some extent challenging, the vacuum system is discussed in Section 3.2.5.

The chapter is concluded with Section 3.3 describing the properties of the XUV pulses available for the experiments in the reported beamline. In Section 3.3.1 the properties of the attosecond pulse trains generated with the NIR laser pulses directly from the NOPCPA system are given. Section 3.3.2 describes the properties of the isolated attosecond pulses generated with NIR laser pulses after spectral broadening in a gas-filled hollow core fiber.

3.1 LASER PULSE TECHNOLOGY

Bright photon sources with coherent emission are advantageous for a broad range of spectroscopic applications. As examples of such photon sources can serve either a continuous wave (*cw*) or a pulsed laser. These sources emit a large number of photons either continuously with a narrow spectral bandwidth, or in short temporally separated sequential bursts with a broadband spectrum, respectively. The availability of *cw* lasers opened the prospects for high resolution spectroscopy, which allowed studying complex molecules down to their rotational structure [7]. On the other hand, a well-defined ultrashort temporal structure makes laser pulses an extremely attractive tool for studying the dynamics of different processes. In case the laser pulse duration is on the order of a few tens of femtoseconds it reaches the typical timescale of molecular vibrational periods. Thus, using such femtosecond laser pulses in a pump-probe configuration the nuclear dynamics in different molecules can be studied revealing the intrinsic mechanisms of a wide range of photoinduced processes [8]. The discovery of the high-order harmonic generation process in turn provided the availability of XUV laser pulses or pulse trains with attosecond duration for the experiments [12]. With these XUV attosecond pulses photoinduced electron dynamics in different targets can be accessed. The HHG process requires laser peak intensities exceeding $10^{14}\,\mathrm{W/cm^2}$. In order to reach such intensities ultrashort laser pulses delivered by a typical oscillator have to be further amplified.

In the present section the basic principles of the laser pulse generation and amplification are described. Since Noncollinear Optical Parametric Chirped Pulse Amplification was used in the present work the basic principles of that technique are briefly discussed. The present section partially follows the textbooks by J.-C. Diels and W. Rudolph [68] and by I. V. Hertel and C. P. Schulz [83].

3.1.1 *Fundamentals of laser technology*

LASER is an acronym for: Light Amplification by Stimulated Emission of Radiation [5]. On the most basic level a laser is an electromagnetic field generator which consists of an optical cavity and an amplification medium. The optical cavity serves simultaneously as a resonator and as a feedback mechanism. In the most simple case the cavity is confined by two mirrors, one of which — the output mirror has a certain non-zero transmissivity and thus serves as an output of the generator. Inside the cavity a set of standing waves — longitudinal modes are formed, while other non-resonant frequencies are suppressed. As a first-order approximation the longitudinal mode frequencies $\nu(z)$ can be described by the following equation:

Frequencies of the longitudinal modes.

$$\nu(z) = z\frac{\nu_g}{2L} = \frac{z}{T_r} \tag{84}$$

Here z is a positive integer which is called the index of the mode, ν_g is the group velocity and L is the cavity length. The frequency gap between two adjacent modes $\Delta\nu$ is equal to the inverse turnaround time T_r — the time needed for a photon to make a complete round trip through the resonator.

The amplification medium of a laser is pumped with energy from an external source. Let us imagine for simplicity that the amplification medium is a two-level system: a ground state and an excited state. The external pump up converts the population from the ground to the excited state. The down conversion accompanied by emission of a photon can happen either as spontaneous or as stimulated emission. The stimulated emission is triggered by an interaction of the medium with a photon with energy equal to the energy gap between the two levels. This process is fundamental for laser technology, since it allows the generation of a big number of photons with the same energy emitted coherently. In order to achieve that, the probability of stimulated emission should exceed the probability of absorption of a photon with resonant energy. This condition is fulfilled in case the population of the excited state is larger than the population of the ground state in the amplification medium, which is called population inversion. Technically it is not possible to induce a population inversion in a two-level system. Thus, in real applications the amplification medium is a three-, four- or many-level system. The energy corresponding to nonradiative transitions between the levels dissipates as heat.

In addition to the desired output a real resonator has non-zero losses. This implies that for a laser to operate, the overall gain should exceed the total losses. Technically this is achieved by creating a positive feedback by sending the radiation multiple times through the amplification medium. Then each turnaround a fraction of the radiation is emitted through the output mirror keeping the amount of energy inside the cavity constant.

3.1.2 *Generation of ultrashort laser pulses*

In general, the gain of the amplification medium is not constant over the whole spectral range covered by the longitudinal modes of the resonator (see Eq. 84). The spectral range over which the gain is higher than the losses is called the gain bandwidth. As a result, only a fraction of all possible longitudinal modes of the resonator are amplified — those that overlap with the gain bandwidth of the amplification medium. Thus, only frequencies corresponding to these modes are present in the output spectrum of the laser. If the relative phases of the different modes are fixed, mode-locking is achieved. For a mode-locked laser at a certain phase relation between the modes the temporal profile of the output radiation is forming a short pulse.

The simplified principle of mode-locking can be described as follows: since the amplification efficiency is higher at high field intensities, after the laser pulse structure is formed inside the resonator it is going to remain self-sustaining and getting shorter every amplification cycle. In order to form a laser pulse structure inside the resonator in the first place the system should be disturbed. This disturbance can be for example mechanical, such as movement of one of the cavity mirrors.

The angular frequency of the mode with index z can be written using the same notation as in Eq. 84 as follows:

Angular frequencies of the modes.

$$\omega(z) = (z + z_0) \cdot 2\pi \cdot \frac{\nu_g}{2L} + \omega_{off} \tag{85}$$

Here index z_0 corresponds to the central angular frequency $\omega_0 = z_0 \cdot 2\pi \cdot \frac{\nu_g}{2L} + \omega_{off}$ (in this notation z is either a positive or a negative integer), $\nu_g/2L = f_{rep}$ is the repetition rate of the laser pulse source, and ω_{off} is an angular frequency offset. In case the group and phase velocities of the laser pulse in the resonator are not equal, the angular frequency offset ω_{off} is non-zero. Then a small phase shift $\phi_{slip} = \omega_{off} \cdot T_r$, which is called a phase slip, is accumulated by the laser pulse each full round trip in the resonator (here T_r is the turnaround time). This results in a constant CEP drift of the output pulses, which can be crucial for practical applications. The frequency offset ω_{off} can be measured for laser pulses with octave spanning spectra using an f-to-2f interferometer. This technique is based on the spectral interference between the second harmonic of the low angular frequency component in the laser pulse spectrum and the corresponding high angular frequency component it overlaps with [102]. In order to illustrate the basic working principle of the f-to-2f interferometer let us assign the indexes of the low and high angular frequency components involved in the process as n and $m = 2n$, respectively. The frequency difference between the two is described by the following equation:

CEP measurement principle

$$2\omega(n) - \omega(m) = (2\pi \cdot 2n \cdot f_{rep} + 2\omega_{off}) - (2\pi \cdot m \cdot f_{rep} + \omega_{off}) = \omega_{off} \tag{86}$$

One of the techniques for CEP stabilization is to make the phase slip ϕ_{slip} equal to a rational fraction of the 2π, and then use only the pulses with the same CEP. For example, setting $\phi_{slip} = \pi/2$ and

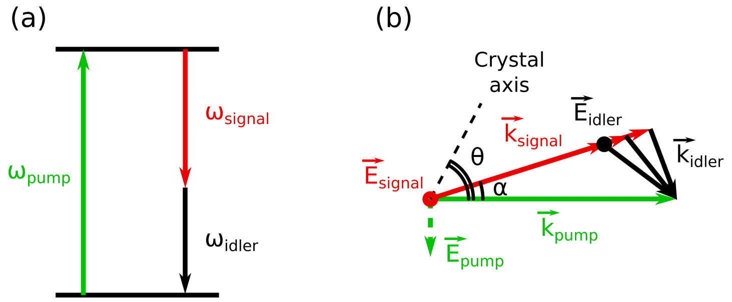

Figure 17: Schematic view of the Noncollinear Optical Parametric Amplification principle. In *(a)* and *(b)* the energy and momentum conservation diagrams are shown, respectively. In *(b)* α is a non-collinear angle and θ is an angle between the crystal optical axis and the $\vec{k}_{pump}$. The polarization of the *pump* beam, and *seed* and *idler* beams is parallel or perpendicular to the plane of the scheme, respectively. The scheme is adapted from [106]

picking up each forth pulse generated one acquires a train of pulses with constant CEP. In case such pulses are amplified in the NOPCPA system (see Section 3.1.3) the repetition rate of the pumping laser can be chosen equal to the divisor of one quarter of the repetition rate of the oscillator. In this configuration all amplified laser pulses carry constant CEP.

3.1.3 *Noncollinear Optical Parametric Chirped Pulse Amplification*

Noncollinear Optical Parametric Chirped Pulse Amplification (NOPCPA) is a technique for the amplification of ultrashort (broadband) laser pulses. It effectively combines two methods: Noncollinear Optical Parametric Amplification (NOPA) [103, 104] and a Chirped Pulse Amplification (CPA) [105]. The inventors of the latter G. Mourou and D. Strickland were honoured with a Nobel Prize in Physics in 2018. In NOPCPA two laser pulses, a seed and a pump, are temporally and spatially overlapped in a non-linear medium. The amplification of the seed pulse results from the energy transfer from the pump pulse due to non-linear interactions in the medium.

The NOPA is a particular case of a difference frequency generation process. The NOPA principle is schematically shown in Fig. 17. Two laser pulses with central angular frequencies ω_1 and ω_2 are spatially and temporally overlapped in a non-linear medium. Let us assume that $\omega_2 > \omega_1$. Then in what follows photons with energies corresponding to central angular frequencies ω_1 and ω_2 are called *signal* and *pump*, respectively.

The polarization of a non-linear medium $P(t)$ can be described as follows:

Polarization of a non-linear medium.

$$P(t) = \epsilon_0 \chi^{(1)} E(t) + \epsilon_0 \chi^{(2)} E(t)^2 + \mathcal{O}(E(t)^3) \tag{87}$$

Here ϵ_0 is the vacuum dielectric permittivity, $\chi^{(n)}$ is the n^{th}-order susceptibility and $E(t)$ is the electric field. Since the total electric field at the laser pulse overlap is equal $E(t) = E_1 \cos(\omega_1 t) + E_2 \cos(\omega_2 t)$, the square term $E(t)^2$ in Eq. 87 contains four angular frequency components: $2\omega_1$, $2\omega_2$, $\omega_2 + \omega_1$ and $\omega_2 - \omega_1$. We are particularly interested in the latter one: $\omega_2 - \omega_1$. A photon with corresponding energy is called *idler*. In order to generate an *idler* photon both energy and momentum conservation laws have to be fulfilled as schematically illustrated in Fig. 17 (a) and (b), respectively:

Energy and momentum conservation.

$$\begin{aligned} \hbar\omega_{pump} &= \hbar\omega_{signal} + \hbar\omega_{idler} \\ \vec{k}_{pump} &= \vec{k}_{signal} + \vec{k}_{idler} \end{aligned} \tag{88}$$

This is called the phase-matching condition. The absolute value of the wave vector depends on the refractive index of the medium $n(\omega)$ as follows: $|\vec{k}| = n(\omega) \cdot \omega/c$. Here ω is the angular frequency and c is the speed of light in vacuum. In order to achieve phase-matching, $\vec{k}_{pump}$ and $\vec{k}_{signal}$ have to be adjusted such that Eq. 88 is fulfilled using an amplification medium with the corresponding refractive indices n_{pump} and n_{signal}. A birefringent crystal — a crystal with the refractive index depending on the polarization direction with respect to the plane containing the crystal optical axis and the wave vector, can serve as such medium. In the birefringent crystal the beam with polarization perpendicular/parallel to such plane is called an *ordinary/extra-ordinary* beam. For an *ordinary* beam the refractive index is independent of the propagation direction, while for an *extra-ordinary* beam the refractive index depends on the angle θ between the optical axis and the wave vector. In the OPA the crystal optical axis is oriented such that the *seed* and *pump* beams are an *ordinary* and *extra-ordinary* beams, respectively, as shown in Fig. 17 (b). Then, by changing the angle θ the refractive index for the *pump* can be adjusted without affecting the refractive index for the *seed*, and thus the phase-matching can be achieved.

Optical parametric amplification can be performed in either collinear or noncollinear geometries, for which $\vec{k}_{signal}$ and $\vec{k}_{pump}$ are collinear or at a non-collinear angle α, respectively. A noncollinear configuration allows phase-matching for a broad spectral range. Thus, it is preferable for amplification of ultrashort laser pulses. For example, in the present system at a non-collinear angle $\alpha = 2.5°$ and $\theta = 24.45°$ the phase-matching can be achieved for a 700 to 1000 nm spectral range [106]. In a noncollinear configuration the *idler* has an angular dispersion, as shown in Fig. 17 (b).

One of the advantages of the NOPA is that the pumping energy is not stored in a medium, in contrast to a laser oscillator. This allows operating at high average pulse power. The maximum power for the NOPA is limited only by the peak intensity damage threshold of the amplification medium. To overcome this limitation a CPA technique is used. The basic principle of CPA is the following: prior to amplification the laser pulses are stretched (or *chirped*), which limits the peak intensity in the amplification medium. After the amplification the pulses are compressed back. The pulse stretching can be performed introducing either positive or negative chirp. Then after the amplification the chirp with opposite sign is induced for pulse compression. The positive chirp can be achieved using any dispersive medium such as air or fused silica. On the other hand, in order to induce negative chirp special artificial optical elements, such as chirped mirrors, are required. It is worth mentioning here that the pulse compression is challenging for ultra broadband laser pulses. In general, chirped mirrors have a limited spectral bandwidth for which they introduce a linear phase. In case a part of the spectrum of the ultrashort laser pulse is exceeding the chirped mirrors bandwidth, these spectral components are not compressed. This results in an increase of the pulse duration after compression comparing to a Fourier Transform limited pulse with corresponding spectrum. The energy losses during the pulse compression depend on the particular system design. In the NOPCPA system reported in the present thesis the losses during the pulse compression after the amplification are on the order of 10 % of the initial pulse energy.

An important parameter for the NOPCPA process that strongly affects the properties of the amplified pulses is the timing between the seed and pump pulses. Since the seed pulse is chirped and the amplification is more efficient at high pump pulse intensities, the spectrum of the amplified pulse can be controlled by changing the delay between the seed and pump pulses in the NOPCPA system. For amplification of ultrashort pulses the seed pulse usually has a shorter duration than the pump pulse in order to have all spectral components of the seed pulse equally amplified, and thus avoid spectral narrowing.

In recent years NOPCPA systems operating in different spectral ranges have become a popular tool for amplification of CEP stable ultrashort laser pulses at high repetition rate. For examples of high repetition rate NOPCPA systems developed for scientific applications operating at 800 nm central wavelength or in the mid infra red spectral range please refer to [107–109] and [110, 111], respectively. For more details on the OPCPA technology please refer to the publications by G. Cerullo and S. De Silvestri, and by I. N. Ross [112, 113].

3.2 LASER BEAMLINE

For the experiments reported in the present thesis an attosecond beamline developed at the Max-Born-Institut in Berlin was used. In this beamline a Noncollinear Optical Parametric Chirped Pulse Amplification (NOPCPA) system operating at 800 nm central wavelength serves as the laser pulse source [64]. Then the generated ultrashort NIR laser pulses are delivered to an actively stabilized attosecond pump-probe interferometer where attosecond pulses are generated [101]. After the pump-probe interferometer, pairs of XUV and NIR pulses with controlled delay are delivered to the experiment.

A detailed description of the NOPCPA system and the pump-probe interferometer are given in Section 3.2.1 and Section 3.2.3, respectively. For a detailed description of the two different experimental end stations used in the present work: a VMI and a Reaction Microscope please refer to Chapter 4.

3.2.1 *Laser pulse source*

The NOPCPA system serving as the laser pulse source for the attosecond beamline is capable of delivering 7 fs FWHM laser pulses with 800 nm central wavelength and up to 190 μJ pulse energy at 100 kHz repetition rate [64]. A schematic top view of the NOPCPA system is shown in Fig. 18. A Titanium Sapphire (Ti:Sapphire) oscillator (Venteon Pulse:One, Venteon Femtosecond Technologies GmbH) generates broadband CEP-stabilized laser pulses at approximately 800 nm central wavelength with a spectral bandwidth exceeding 300 nm, at 80 MHz repetition rate. The FWHM duration of the Fourier Transform Limited (FTL) pulses with corresponding broadband spectrum is shorter than 5.5 fs. The average power delivered by the oscillator is more than 240 mW (more than 3 nJ pulse energy) with residual power fluctuations below 0.1 % rms. The oscillator is actively Carrier-Envelope Offset frequency stabilized with a phase slip of $\pi/2$ at 80 MHz by controlling the pump power with an acusto-optic modulator (driven by XPS800-E system, Menlo Systems GmbH) [114].

A 10 nm bandwidth fraction of the oscillator spectrum centred at 1030 nm is filtered out using a dichroic mirror. Through a polarization maintaining fiber the radiation at 1030 nm is delivered to a Chirped Pulse Amplification (CPA) system, which is used as the pump laser for the NOPCPA system. In the CPA laser system (Dira 200-100, TRUMPF Scientific) the incoming laser pulses are first stretched with a fiber Bragg grating stretcher and amplified in a set of three Ytterbium doped (Yb-doped) fiber pre-amplifiers. Then the pulses are further amplified in a thin-disk regenerative Ytterbium Yttrium Aluminium Garnet (Yb:YAG) amplifier and compressed with a grating compressor. As a result, laser pulses with more than 1.9 mJ pulse

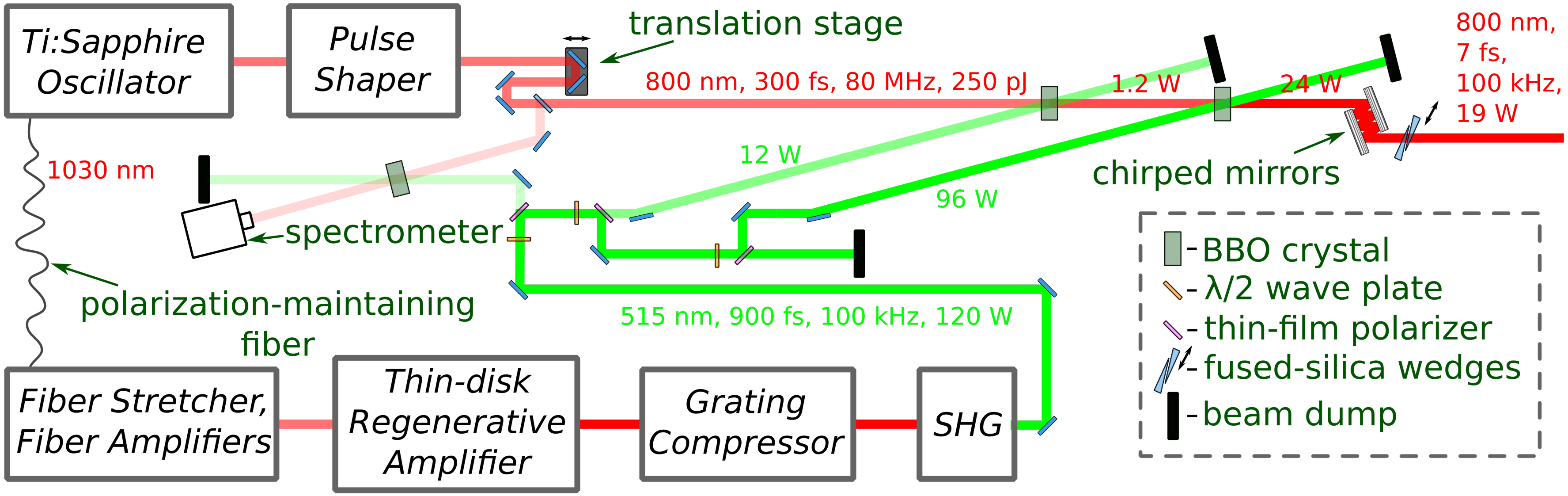

Figure 18: Schematic view of the Noncollinear Optical Parametric Chirped Pulse Amplification system. 800 ± 30 nm central wavelength broadband laser pulses generated by a Ti:Sapphire oscillator (shown in red) are amplified in noncollinear geometry in two stages using the second harmonic of the Yb:YAG pumping laser (shown in green). For a detailed description please refer to the main text.

energy at 100 kHz repetition rate (more than 190 W average power) at 1030 nm central wavelength are generated. In order to use these pulses for amplification of the laser pulses delivered by the Ti:Sapphire oscillator, the second harmonic is generated (with generation efficiency on the order of 60 %). The resulting pulses with 515 nm central wavelength and more than 1.2 mJ pulse energy at 100 kHz repetition rate (more than 120 W average power) are utilized as pump pulses for the NOPCPA system. The duration of the pump pulses delivered to the NOPCPA system is on the order of 900 fs.

Prior to amplification, the laser pulses from the oscillator are sent to a Spatial Light Modulator (SLM) pulse shaper (MIIPS Box 640 P, Biophotonics Solutions). This configuration allows control of the spectral phase of the laser pulses prior to amplification. Further propagation towards the NOPCPA amplification stages in air stretches the pulses up to approximately 300 fs FWHM duration. The duration of the seed pulses delivered to the NOPCPA system is shorter than that of the pump pulses, since the seed pulses get further stretched propagating in the β-Barium Borate (BBO) crystals in the amplification stages. Due to losses, laser pulses with approximately 250 pJ pulse energy (20 mW) are delivered to the first amplification stage of the NOPCPA system.

In the configuration described above the seed and pump pulses of the NOPCPA system are intrinsically synchronized. In order to temporally overlap them in the amplification stages, the temperature induced fluctuations in the optical path difference between the seed and pump pulses should be compensated for. In order to do that an active delay stabilization system is installed in the seed pulse arm of the system (shown in Fig. 18). The delay stabilization system consists of two translation stages with different working ranges and step sizes for slow and fast loops installed in series. In order to measure the delay between the pulses a small fraction of the radiation (approximately 3 %) is filtered out and overlapped in an auxiliary NOPCPA stage (see Fig. 18). Prior to amplification in the auxiliary stage, the seed pulses are substantially chirped. Then measuring the spectrum of the amplified pulses a feedback signal for the delay stages is generated. With this delay stabilization system the temporal overlap between the seed and pump pulses at the main stages of the NOPCPA system is actively controlled.

The laser pulse amplification is performed in two NOPCPA stages in BBO crystals. The pump power is divided between the stages utilizing $\lambda/2$ wave plate and thin-film polariser sets. The first stage is pumped with 120 μJ pump pulses (average power 12 W). The energy of the pulses pumping the second stage can be tuned up to 960 μJ (maximum average power 96 W). In the first NOPCPA stage the 300 fs FWHM duration seed pulses are amplified from 3 nJ to 12 μJ. The resulting approximately 700 fs FWHM duration pulses are further am-

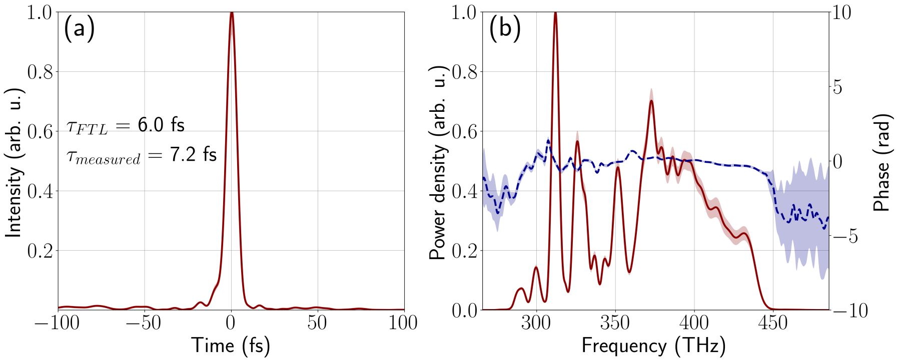

Figure 19: Typical temporal profile *(a)* and spectrum *(b)* of the NIR laser pulses after compression delivered by the Noncollinear Optical Parametric Chirped Pulse Amplification system. In *(b)* the laser pulse spectrum is shown in red with the corresponding spectral phases shown in blue. The measurement was performed using the SEA-F-SPIDER technique [115]. The mean values and the $\pm 1\sigma$ ranges over the distribution of a series of 5 sequential measurements are shown as bright lines and shaded areas, respectively.

plified in the second stage up to 240 µJ (maximum average power 24 W). Since the efficiency of the NOPCPA process is very sensitive not only to temporal, but also to spatial overlap of the seed and pump pulses, the beam pointing into the amplification stages is actively stabilized (Aligna, TEM-Messtechnik GmbH and Kinesis, Thorlabs Inc. for seed and pump beams, respectively).

After the amplification, the laser pulses are compressed using a set of chirped mirrors (Laser Quantum DCM11). The introduced negative chirp is balanced by a pair of thin fused silica wedges. Higher-order phase terms can be compensated for by applying a phase mask to the SLM pulse shaper. After compression laser pulses with 190 µJ maximum pulse energy (19 W maximum average power) and approximately 7.2 ± 0.1 fs FWHM duration are delivered to the attosecond pump-probe setup. Fourier Transform limited pulses with a corresponding spectrum would have approximately 6 fs FWHM duration. The typical temporal profile and spectrum of the NIR laser pulses after compression are shown in Fig 19 (a) and (b), respectively. The pulse duration and spectral phases were measured using the SEA-F-SPIDER technique [115]. The bright lines and shaded areas in the figure represent mean values and $\pm 1\sigma$ ranges over the distribution of a series of 5 sequential measurements, respectively. These measurements were performed over 1 minute and thus show the short term stability of the laser pulse source. The acquired NIR laser pulse spectrum shown in Fig 19 (b) is broader than 280 to 450 THz, or approximately 700 to 1050 nm. Applying a phase mask to the SLM pulse shaper the spectral phases are flattened over the full broadband spectrum. In the temporal domain this results in a compressed laser pulse with a duration approximately 20 % longer than that of a Fourier Transform limited pulse with the corresponding spectrum.

3.2.2 *Operation with a hollow core fiber*

When generating high-order harmonics with approximately 7 fs FWHM duration NIR laser pulses at 800 nm central wavelength (the corresponding laser period is approximately 2.7 fs) delivered by the NOPCPA system one obtains short XUV attosecond pulse trains consisting of approximately seven XUV pulses (see Section 3.3.1). Such APTs could be used for a big variety of attosecond pump-probe spectroscopy experiments implementing the RABBIT technique (for a detailed description please refer to Section 2.5.2). In a RABBIT experiment due to the temporal structure of the XUV pulse train, the XUV photon interaction with a target occurs every half cycle of the fundamental NIR laser field. This regime is not suitable for a certain type of experiments, for which a single instant of the XUV photon ionization of a target is necessary in order to access the photoinduced dynamics. For this type of experiment isolated attosecond pulses (IAPs) are required.

In order to generate IAPs through high-order harmonic generation, NIR laser pulses with durations approaching a single cycle should be used. Then, by controlling the CEP an intensity profile with a single maximum required for IAP generation can be achieved (for a detailed description please refer to Section 2.1.4). In order to acquire NIR laser pulses approaching single cycle duration in the present setup, the spectrum of the pulses delivered by the NOPCPA system has to be broadened.

In the present setup the spectral broadening of the NIR laser pulses is performed using a 1 m long 340 µm inner diameter differential pressure gas filled hollow core fiber (for more details please refer to Section 2.1.3). During the operation approximately 2.5 bar of neon is applied to the output port of the fiber, while the pressure at the input port is kept on the order of a few mbar. Using this technique the spectrum of the NIR laser pulses delivered by the NOPCPA system shown in Fig. 19 (b) is broadened up to 330 to 1100 nm wavelength range with up to 70 % efficiency. Unfortunately, there are no chirped mirrors available on the market fully covering such a broadband spectrum. In the present setup a set of broadband chirped mirrors with a 500 to 1050 nm working range (PC70, Ultrafast Innovation) is used for pulse compression, which results in effective narrowing of the pulse spectrum. After compression broadband laser pulses with 95 µJ maximum pulse energy (9.5 W maximum average power) and approximately 3.3 ± 0.1 fs FWHM duration were achieved. The Fourier Transform limited pulses have approximately 3.1 fs FWHM duration.

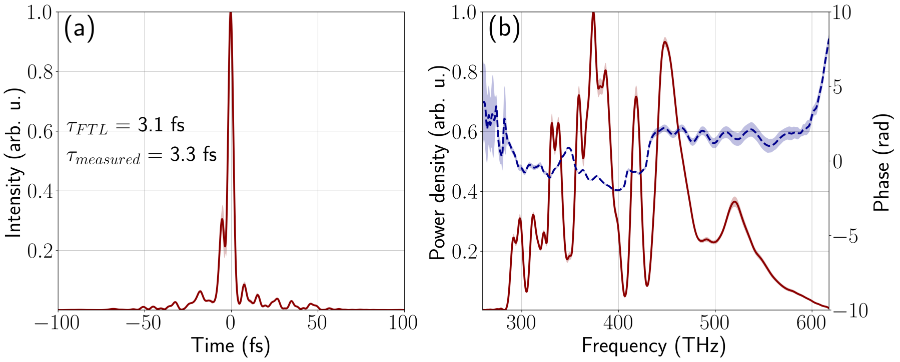

Figure 20: Typical temporal profile *(a)* and spectrum *(b)* of the NIR laser pulses after spectral broadening in a gas filled hollow core fiber and compression. In *(b)* the laser pulse spectrum is shown in red with the corresponding spectral phases shown in blue. The measurement was performed using the SEA-F-SPIDER technique [115]. The mean values and the $\pm 1\sigma$ ranges over the distribution of a series of 5 sequential measurements are shown as bright lines and shaded areas, respectively.

The typical temporal profile and spectrum of the NIR laser pulses after spectral broadening in the gas filled hollow core fiber and compression are shown in Fig 20 (a) and (b), respectively. The pulse duration and spectral phases were measured using the SEA-F-SPIDER technique [115]. The bright lines and shaded areas in the figure represent mean values and $\pm 1\sigma$ ranges over the distribution of a series of 5 sequential measurements, respectively. These measurements were performed over 1 minute and thus show the short term stability of the laser pulse source. The acquired NIR laser pulse spectrum shown in Fig 20 (b) is broader than 280 to 610 THz, or approximately 500 to 1100 nm.

Generation of IAPs using these NIR laser pulses is possible only if the CEP is stabilized. In order to do that, the NIR laser pulses are sampled right before the pump-probe interferometer by catching a reflection from one of the thin fused silica wedges. The CEP is measured using a custom made f-to-2f interferometer based on a fast USB3 spectrometer (FX series, Ocean Optics) [114]. Based on that measurement, the CEP of the laser pulses delivered by the Ti:Sapphire oscillator is actively controlled. Using the CEP stabilized approximately 1.5 cycle NIR laser pulses for HHG, isolated attosecond pulses are obtained (for more details please see Section 3.3.2).

3.2.3 *Pump-probe interferometer*

The XUV–NIR pump-probe interferometer used in the present work was originally designed by F. Schell [116]. A number of modifications were implemented to the original design allowing to use this pump-probe interferometer for coincidence detection experiments. The performed modifications were targeting two separate issues: the long term stability and the vacuum properties of the setup.

First, the modifications performed in order to improve the long term stability of the pump-probe interferometer are described. It was shown by V. Stert *et al.* and by A. Boguslavskiy *et al.* that the optimal detection rate for photoelectron and photoion coincidence detection is on the order of 20 % of the repetition rate of the laser pulse source [117, 118]. Thus, for the reported 100 kHz NOPCPA system the corresponding optimal detection rate is on the order of 20 kHz. At such a detection rate, the attosecond pump-probe experiments similar to those reported in the present thesis require 50 or more hours of unperturbed operation. Thus, the long term stability of the pump-probe interferometer is crucial to obtain high temporal resolution. One of the major upgrades of the setup performed as part of the present work was the development of an active pump-probe delay stabilization system. For a detailed description of the delay stabilization system working principle and implementation please refer to Section 3.2.4. The thermal expansion-induced deformations of the mirror mounts and the optical breadboard are main limiting factors for the stability of an optical beamline positioned in vacuum and operated at relatively high average laser power. In order to reduce the thermal expansion-induced disturbances a passive cooling system was installed. The technical implementation of that system is described in the present section.

Requirements for the vacuum properties of the pump-probe interferometer raise another challenge. Since the ionization of background in the Reaction Microscope contaminates the measured data and could possibly lead to false coincidences, pressures on the order of 10^{-9} mbar or lower in the apparatus are required. On the other hand, in the vacuum chamber where the high-order harmonics are generated the pressure could reach the 10^{-3} mbar range. Due to strong absorption of XUV photons by any material no windows could be used to separate these two chambers. The distance between the laser foci in the HHG unit and the interaction region of the Reaction Microscope is dictated by the properties of the XUV optics. In the present setup this distance is 2.5 m long, which corresponds to a 1250 mm object distance toroidal mirror. In order to reach 6 orders of magnitude pressure difference over that distance multiple techniques were used. A detailed description of the vacuum system of the pump-probe interferometer is given in Section 3.2.5.

A schematic top view of the attosecond pump-probe interferometer is shown in Fig. 21. The interferometer is constructed in a Mach-Zehnder configuration with approximately 2.5 m arm length. The NIR laser pulses delivered by the NOPCPA system are linearly polarized with polarization perpendicular to the plane of the scheme. The arriving NIR pulses are split in 80/20 ratio using a beam split-

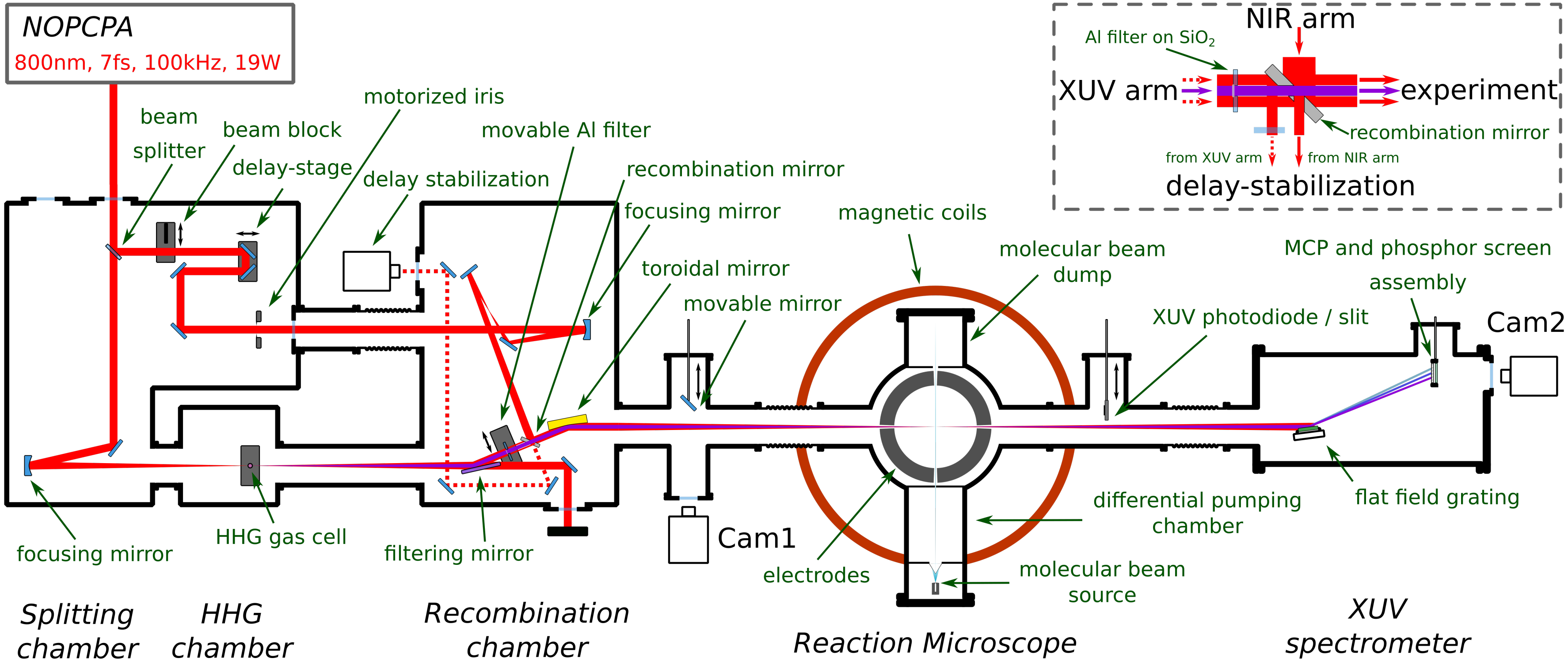

Figure 21: Schematic top view of the attosecond pump-probe interferometer and the experimental endstation. The incoming NIR beam (shown in red) is split in two interferometer arms. In one arm XUV light is generated in a gas cell. Then the XUV (shown in violet) and NIR beams are recombined and focused into the interaction region of the Reaction Microscope. The inset shows the beam overlay at the recombination mirror. For a detailed description please refer to the main text.

ter (s-polarization) with a flat response over a 500 to 1100 nm spectral range. The high power arm of the interferometer is used for the generation of the XUV pulses through HHG in a noble gas. The low power arm is delivering NIR probe pulses to the experiment with a controlled delay with respect to the XUV pulses. Thus, in what follows the high and low power arms of the interferometer are referred to as the *XUV arm* and the *NIR arm*, respectively. The laser beams from the two arms of the interferometer are recombined using a custom made *recombination* mirror. The *recombination* mirror has two perpendicular 5 mm diameter drilled holes oriented at 45 degree with respect to the mirror surface. The *recombination* mirror is positioned in such a way, that these holes are parallel to the plane of the scheme shown in Fig. 21. This design allows collecting a fraction of the laser radiation from both arms of the interferometer at both output ports of the *recombination* mirror: towards the experiment and towards the active delay stabilization system, respectively. The laser beam overlay at the *recombination* mirror is shown in the inset of Fig. 21. More details on the recombination of the XUV and NIR laser beams are given in the following discussion.

The high-order harmonics are generated in a 2 mm long gas cell in a noble gas medium. The NIR laser pulses are focused into the gas cell by a spherical silver mirror with 50 cm focal distance. The backing pressure in the gas cell is kept below 100 mbar using an electrical needle valve with a pressure control unit (Type 250E, MKS). In order to reduce the generation medium gas load on the vacuum system the output ports of the gas cell are covered with an aluminium tape with approximately 200 µm diameter holes for the laser beam to get through. These holes are drilled in the aluminium tape outside the vacuum setup prior to installation. The drilling is performed using the high power 515 nm pump laser of the NOPCPA. The gas cell is mounted on a three-dimensional stage equipped with piezo actuators (SLC-1750-HV for the two horizontal axes and SLC-1730-W-D-HV for the vertical axis, SmarAct). The stage allows precise positioning of the gas cell with respect to the laser focus in order to optimize the phase-matching conditions in the HHG process.

Prior to being used for the experiments, the XUV pulses have to be separated from the co-propagating NIR laser pulses used for the high-order harmonic generation. A conventional filtering technique utilizing a single thin metal filter is not applicable in the present case, since such a filter would be immediately melted due to the average NIR laser power exceeding 10 W. In order to perform NIR light filtering at high power in the present setup a specially designed dichroic *filtering* mirror is used in combination with a 200 nm thick Al filter (see Fig. 21). The *filtering* mirror has a broadband dielectric multilayer anti-reflection coating for NIR radiation. A 200 nm thick top layer of $\mathrm{SiO_2}$ functions as bulk reflection for the XUV radiation. In the present setup the *filtering* mirror is positioned at a grazing incidence angle of 75 degree with respect to the combined XUV plus NIR beam. At these conditions the *filtering* mirror has a 20 % reflectivity for the NIR radiation and 45 % average reflectivity for the 20 to 60 eV XUV photon spectral range. The NIR radiation transmitted through the *filtering* mirror is sent to an external beam dump, while the remaining reflected part of the NIR beam is blocked by a 5 mm diameter 200 nm thick Al filter. The Al filter is mounted on a drilled 1 mm thick SiO_2 plate. Such a configuration allows transmission of the NIR beam part from the *XUV arm* of the interferometer through the SiO_2 plate around the Al filter. Then the transmitted NIR radiation is reflected by the back side of the *recombination* mirror towards the active delay stabilization system (see inset of Fig. 21). The Al filter is installed on a motorized translation stage (X-LSM025A-SV1, Zaber) which allows adjustment of the filter position with respect to the laser beam. The XUV beam transmitted through the Al filter passes through a 5 mm diameter hole in the *recombination* mirror (see inset of Fig. 21). After that it is focused into the interaction region of the Reaction Microscope with a gold coated toroidal mirror (1250 mm object distance). In the interaction region of the Reaction Microscope the toroidal mirror creates a 1 : 1 image of the generation volume in the HHG cell.

In the *NIR arm* of the interferometer a nanometer precision translation stage is installed (SLC-1750-S-HV, SmarAct). This stage controls the delay between the XUV and NIR laser pulses delivered to the experiment. It is also incorporated into the active delay stabilization system (for more details please refer to Section 3.2.4). Apart from the delay stage, a motorized iris (SID-5714, SmarAct) is installed in the *NIR arm* of the interferometer. It allows controlling the NIR probe intensity during the experiment. The laser beam from the *NIR arm* is reflected by the front side of the *recombination* mirror around the 5 mm diameter hole creating an annular beam (see inset of Fig. 21). This annular NIR beam is then focused into the interaction region of the Reaction Microscope by the toroidal mirror. In order to increase the power of the annular beam and thus the NIR probe power in the experiment it is advantageous to make the size of the laser beam from the *NIR arm* at the *recombination* mirror as large a possible. In the present setup this is achieved by generating a laser focus by a spherical silver mirror ($f = 50$ cm) in the *NIR arm* in the equivalent plane to the focus in the HHG cell. In such a configuration both the XUV pump and NIR probe beams are focused into the interaction region of the Reaction Microscope using the same toroidal mirror. The remaining central part of the laser beam from the *NIR arm* of the interferometer is transmitted through the second 5 mm diameter hole in the *recombination* mirror and sent towards the active delay stabilization system.

The *recombination* mirror is installed on a mirror mount equipped with picomotor actuators (8823-UHV, Newport). A 3 inch version of the mirror mount was chosen in order to allow propagation of both output beams of the *recombination* mirror as shown in the inset of Fig. 21. The 1 inch *recombination* mirror is then mounted using a custom made 1 inch to 3 inch adapter. The motorized mirror mount is used for controlling the overlap of the probe laser focus within the interaction region in the Reaction Microscope. In order to improve the stability of the pump-probe interferometer the parity of the number of reflections in both arms is kept equal. From that perspective, the auxiliary focus in the *NIR arm* is needed to make the number of foci in both arms equal. In this configuration both output beams of the Mach-Zehnder type interferometer are translated together.

Between the pump-probe interferometer and the Reaction Microscope an additional vacuum chamber is installed. It serves simultaneously as a differential pumping stage for the vacuum system and as a station for sampling the XUV and NIR laser pulses spatial and temporal overlap at the focus. In order to sample the foci overlap the Al filter in the *XUV arm* is taken out and after substantial filtering the NIR beams from both arms of the interferometer are sent to a USB 3 CCD camera (acA2040-90umNIR, Basler) positioned at the focal plane. The temporal overlap between the two NIR laser pulses is then found by searching for spatial interference in the focus.

As mentioned above, thermal expansion-induced deformations of the mirror mounts and the optical breadboard are one of the main sources of instability of the pump-probe interferometer operated at relatively high laser power in vacuum. In the absence of thermal conduction through air, heat from the laser beam is dissipating through the mirror mounts and the optical breadboard, which results in a thermal expansion. This affects both the spatial and temporal overlap of the pump and probe laser beams in the interaction region of the Reaction Microscope. In order to limit this effect, in the present setup a passive cooling system is installed. The basic principle of this cooling system is to conduct the heat in a controlled way into the vacuum chamber walls. In order to do that, all mirror mounts in the pump-probe interferometer are wrapped with thick copper wires connected to the chamber walls using aluminium or Kapton (polyimide) tape, depending on the vacuum requirements in the respective chamber. In order to reduce the amount of heat deposited on the mirror mounts in the first place, the outer part of the NIR laser beam, not used for the experiments, is blocked by a couple of orifices directly installed on the vacuum chamber walls. For the mirrors installed at grazing incidence angle, such as the *filtering* mirror, additional rectangular shape mirrors block the part of the laser beam exceeding the mirror size. The NIR power reflected by these mirrors is sent to external beam dumps.

In order to perform real time measurements of the XUV spectrum during the photoionization experiments, an XUV spectrometer is positioned in the beamline after the Reaction Microscope. The XUV spectrometer was designed and assembled by S. Birkner, P. Šušnjar and F. Schell [101]. In this device the XUV laser pulse spectrum is spatially resolved with a flat field aberration-corrected XUV grating with 20 to 113 eV energy range (001-0640, Hitachi, 1200 grooves per mm, 85.3 degree incidence angle). The signal is detected with an MCP and phosphor screen assembly (Hamamatsu) and a CCD camera (scA1400-17gm, Basler). Between the Reaction Microscope and the XUV spectrometer at the focal distance of the flat field grating a slit is installed on a movable mount. Together with the slit an XUV photodiode (AXUV100G, Optodiode) is installed on the same movable mount. It allows measurement of the XUV photon flux on target.

3.2.4 *Active delay stabilization system*

In ultrafast pump-probe spectroscopy experiments the acquired temporal resolution is restricted not only by the duration of the laser pulses used, but also by the stability of the delay between the pump and probe pulses. The latter becomes especially important in the attosecond regime since then the optical path difference between the two arms should be defined with nanometer precision. The experimental techniques used for controlling this delay can be divided in two major groups: passive and active. Passive stabilization is based on the mechanical and thermal stability of the setup [119], while active stabilization requires an automated feedback system compensating for changes in the optical path difference [120]. The main advantage of passive delay stabilization is that it is robust and does not rely on any complicated hardware or software. That reduces the overall complexity of the experimental setup making it easier to operate. Passive delay stabilization is sufficient for interferometers with collinear arms [121]. The present beamline could not be designed in a collinear geometry since the additional *filtering* mirror is required for the NIR radiation filtering due to the high average power (see Section 3.2.3). In the noncollinear configuration where the two arms of the pump-probe interferometer are geometrically separated, as in the present case, it is not possible to achieve the required pump-probe delay stability with passive delay stabilization only, especially operating at high laser power. The situation becomes even more complicated in case laser pulses in the XUV spectral range are used. Then the pump-probe setup has to be positioned in vacuum, which makes the heat dissipation a significant source of pump-probe delay instability. Thus, for such setups active delay stabilization is required.

The basic principle of active delay stabilization can be described as follows: the intended pump-probe delay is compared with a measured optical path difference between the two arms of the pump-probe interferometer. A signal compensating for the difference between the intended and measured delays is created and sent to the delay stage, installed in one of the interferometer arms. Incorporating these two steps in a feedback loop the pump-probe delay can be stabilized and controlled. Then the interferometer is 'locked'.

In general, in order to lock an interferometer it is sufficient to track only the relative changes in the difference between the optical path length in the two arms and compensate for them. In that case the initial temporal overlap of the laser pulses from the two arms, or 'time zero', has to be determined with another method. After the 'time zero' is found the interferometer can be locked by controlling the relative changes in the optical path difference. One of the conventional ways of measuring such relative changes is based on spatial interference of a *cw* laser [120]. A *cw* laser beam is sent through both arms of the pump-probe interferometer collinear with the pulsed laser beams. At the point where the laser beams are recombined, the *cw* beams are separated from the pulsed laser beams and focused into a camera with overlapping foci. Utilizing spatial interference fringes in the focus recorded by a camera, relative changes in the optical path length difference between the two arms of the pump-probe interferometer can be measured. Based on that measurement, the signal controlling the delay stage is created. For more details on active delay stabilization technique employing a *cw* laser please refer to publications by M. Chini *et al.* and by M. Sabbar *et al.* [56, 120].

The configuration with a *cw* laser has a number of constraints. First of all, in order to be able to filter out the *cw* laser radiation from the pulse laser radiation, which, in general, has a much higher power, the *cw* laser wavelength λ should be distinct from the pulsed laser spectrum as much as possible. This condition is not easy to fulfil working with ultrashort laser pulses, especially in the case of pulse spectra broader than one octave. Alternatively, the *cw* and pulsed laser beams can be spatially separated. In a setup incorporating a high-order harmonic source this approach can be challenging to implement due to the pinholes on the HHG cell (see Section 3.2.3). Another drawback of this technique is that it is not capable of resolving changes in the optical path difference equal to $n \cdot \lambda/2$, where n is an integer and λ is the *cw* laser wavelength. Also, an additional laser increases the overall complexity of the experimental setup.

In order to overcome the limitations related to using a *cw* laser for measuring the optical path length difference between the two arms of the interferometer, as a part of the present work a modification to this active delay stabilization technique was introduced. In this method the residual NIR laser pulse radiation that is not used for the experiment is utilized for measuring the optical path length difference. In order to do that, a fraction of the NIR laser pulse radiation from both arms of the interferometer is collected at the *recombination* mirror. Utilizing the spectral interference fringes at the spatial overlap of these two beams, not only changes in the relative difference between the optical path of the two arms can be tracked, but also the absolute difference can be measured. The availability of information on the absolute optical path length difference allows the detection of changes exceeding $\lambda/2$ of the central wavelength of the laser pulses. Another advantage of this method is that it utilizes the residual NIR laser pulse radiation and thus does not require any additional light source to operate.

In the present section the basic principles of the developed active delay stabilization technique are discussed. Then the implementation of this technique in our attosecond pump-probe setup is described. In the following discussion complex quantities, such as the complex electric field $\tilde{E}$, are written with a tilde hat.

Electric field of the laser pulse.

In the frequency domain the electric field of a laser pulse $\tilde{E}(\omega)$ can be expressed as follows:

$$\tilde{E}(\omega) = |\tilde{E}(\omega)| e^{i\phi(\omega)} \tag{89}$$

Electric field of the delayed laser pulse.

Here $|\tilde{E}(\omega)|$ and $\phi(\omega)$ are the spectral amplitude and phase of different angular frequency components, respectively (for more details please refer to Section 2.1.1). The same laser pulse with a relative delay τ in the frequency domain can be expressed as:

$$\tilde{E}_{del}(\omega) = \tilde{E}(\omega) \cdot e^{i\phi_{shift}(\omega)} = \tilde{E}(\omega) \cdot e^{i(\phi_0 + \omega\tau)} \tag{90}$$

Spectrum of the combined two laser pulses.

Here $\phi_{shift}(\omega)$ is a linear phase shift. Then the spectrum $S(\omega)$ of the combined two pulses $\tilde{E}(\omega)$ and $\tilde{E}_{del}(\omega)$ can be expressed as:

$$\begin{aligned} S(\omega) &= |\tilde{E}(\omega) + \tilde{E}_{del}(\omega)|^2 \\ &= 2|\tilde{E}(\omega)|^2 + 2|\tilde{E}(\omega)|^2 \operatorname{Re}(e^{i(\phi_0 + \omega\tau)}) \\ &= 2I(\omega) + 2I(\omega) \cdot \cos(\omega\tau + \mathrm{const}) \end{aligned} \tag{91}$$

Here $I(\omega)$ is the laser pulse intensity. The measured spectrum corresponds to a sum of two contributions: a delay-independent and a delay-dependent term. The latter is related to the delay τ as $\cos(\omega\tau + \mathrm{const})$. Performing a Fourier Transform of $S(\omega)$ these two contributions can be separated. Then from the delay-dependent term, the delay τ between the two pulses can be extracted.

As an illustration of this delay extraction method a simple numerical simulation was performed. In this simulation two Gaussian shape pulses were considered with the spectral amplitude $\tilde{E}(\omega)$ described by the following equation:

Gaussin shape laser pulse.

$$\tilde{E}(\omega) = \exp\left(-\frac{(\omega-\omega_0)^2}{2\sigma^2}\right) \tag{92}$$

The following parameters were chosen for the description of the laser pulse: the central angular frequency $\omega_0 = 2.36\,\mathrm{rad/fs}$ (corresponding to 800 nm central wavelength) and $\sigma = 0.1\,\mathrm{rad/fs}$. The delay between the two laser pulses $\tau = 290.0\,\mathrm{fs}$ was chosen. The resulting spectrum $S(\omega)$ of the two laser pulses combined calculated according to Eq. 91 is shown in Fig. 22 (a).

A Fourier Transform of the obtained spectrum $S(\omega)$ was performed numerically using Fast Fourier Transform algorithm (FFT). The square root of the Fourier Transform Power Spectrum (FTPS) of $S(\omega)$ is shown in Fig. 22 (b). It consists of two peaks at $+\tau$ and $-\tau$, respectively. These two peaks carry the same information on the delay between the two laser pulses. Applying a Gaussian shape filter to the FTPS of $S(\omega)$ centred close to the maximum of the peak at $+\tau$, the delay-dependent signal is separated. By measuring the phase of the complex value of the Fourier Transform of $S(\omega)$ at a particular delay $\tau_{measure}$ close to the maximum of the filtered peak fast changes in the delay between the two pulses can be tracked. The change of this phase is then used as an error signal for the feedback loop controlling the relative delay between the two pulses. This approach was chosen for the active delay stabilization due to low computational costs and, as a consequence, high repetition rate capabilities.

In order to measure the absolute delay between the two laser pulses the inverse Fourier Transform of the filtered peak should be performed as shown in Fig. 22 (c). Retrieving the phases of the complex values of the inverse Fourier Transform of the filtered peak as a function of angular frequency and applying a linear fit to them, as shown in Fig. 22 (d), the absolute delay between the two laser pulses can be measured. If the dispersion in both interferometer arms is balanced, the absolute delay τ is then equal to the first-order coefficient of the linear fit. This method allows measuring the absolute delay between the two NIR laser pulses, though computationally it is more expensive than tracking relative delays as described above. The measurement of the absolute delay between the two NIR pulses allows avoiding the previously described ambiguity appearing when tracking changes in the optical path difference that are proportional to $\lambda/2$ of the central wavelength of the laser pulses (800 nm in the present case). It is also useful for determination of the temporal overlap or 'time zero' between the laser pulses delivered to the experiment.

The attosecond pump-probe interferometer used in the present work was designed to perform measurements with XUV–NIR delays in a

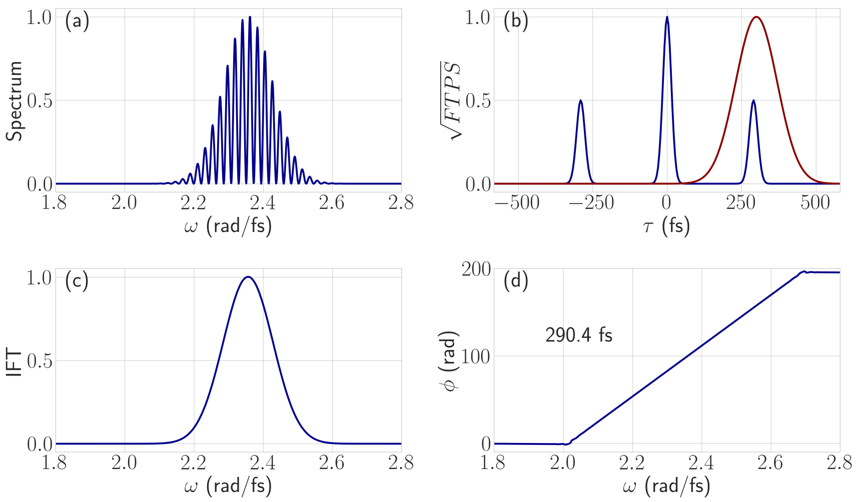

Figure 22: Numerical simulation illustrating the principle of the active delay stabilization technique: *(a)* normalized spectrum of the two Gaussian shape pulses recombined with a relative delay $\tau = 290$ fs; *(b)* normalized square root of the Fourier Transform Power Spectrum of the recombined spectrum (blue) with the Gaussian shape filter (red); *(c)* normalized absolute value of the inverse Fourier Transform of the filtered peak; *(d)* the retrieved phases of the complex values of the inverse Fourier Transform of the filtered peak. The first-order coefficient of the linear fit to the extracted phases is 290.4 fs.

range smaller than 100 fs. In the active delay stabilization system described above the angular frequency peak in the FTPS of the measured spectrum $S(\omega)$ should stay in range of a fixed Gaussian shape filter over the whole scan as shown in Fig. 22 (b). In order to achieve that a delay on the order of 0.5 ps between the NIR pulses from the two arms of the interferometer is introduced using a fused silica plate. In this configuration a 0.5 ps delay between the laser pulses arriving to the delay stabilization spectrometer corresponds to temporal overlap of the XUV and NIR pulses in the interaction region of the Reaction Microscope. This way high frequency spectral modulations are obtained in the recorded spectra over a 100 fs delay range around the time zero, which is beneficial for the phase evaluation.

In the present experimental setup NIR laser beams from both arms of the interferometer are sampled from the second output of the *recombination* mirror. The inner part of the laser beam from the *NIR arm* is transmitted through the hole in the *recombination* mirror, while the outer part of the NIR beam from the *XUV arm* transmitted around the Al filter through the SiO_2 mount is reflected by the back side of the *recombination* mirror (see Fig. 21). The spectrum of the combined NIR pulses is measured by overlapping their foci onto the slit of a spectrometer positioned outside the vacuum chamber. In order to measure the combined NIR pulses spectrum at high repetition rate a custom made spectrometer based on a fast USB3 camera (acA2040-90umNIR, Basler) was constructed. It consists of a 5 µm slit (S5RD, ThorLabs), two plano-convex lenses with 100.0 mm focal length (LA4380-B-ML, ThorLabs) and a visible transmission grating with 830 grooves/mm and 29.87 ° groove angle (GT25-08, ThorLabs). This spectrometer is operating at 720 to 850 nm spectral range. The calibration of the spectrometer is performed using krypton spectral lines (6031 Spectral Calibration Lamp, Newport). Using a small region of interest on the chip of the camera up to 1 kHz acquisition rate can be achieved. The relative phase-shift evaluation is performed using a Fast Fourier Transform (FFT) algorithm. The evaluation of the absolute delay between the pulses is much more computationally expensive than the phase-shift retrieval. Thus the absolute delay is measured every 100th frame in order to avoid a reduction of the overall acquisition rate. In the present setup a translation stage with nanometer precision (SLC-1750-S-HV, SmarAct) installed in the *NIR arm* of the interferometer is incorporated into the active delay stabilization feedback loop. The piezo actuator controlling the delay stage is not capable of responding to the feedback signal at 1 kHz. Thus, we intentionally restrict the feedback loop repetition rate down to < 500 Hz.

The results of a one hour long pump-probe delay stability measurement are shown in Fig. 23. Over the measurement the pump-probe interferometer was locked using the NIR–NIR spectral interference. The measured delay between the NIR pulses used in the feedback loop controlling the delay stage is shown in Fig. 23 (b). Over the measurement the feedback loop was operating at approximately 430 Hz. The standard deviation of the distribution of the recorded temporal offsets over the whole inloop measurement is equal to approximately 70 as as shown in Fig. 23 (a) and (c).

Additionally, a *cw* monochromatic blue laser (473 nm) was sent through both arms of the pump-probe interferometer collinear with the NIR laser beams. The *cw* beams from both arms were collected at the second output of the *recombination* mirror and their foci were overlapped. The spatial interference fringes in the focus were recorded using a fast USB3 camera (acA2040-90umNIR, Basler), and the relative difference in optical path length of the two interferometer arms was measured. Using a small area on the camera chip a 2 kHz acquisition rate was achieved. From the results of the delay measurement with a *cw* laser shown in Fig. 23 (d)–(f) a linear drift on the order of 100 as per hour was observed. The standard deviation of the measured delay distribution is on the order of 100 as.

Another independent measurement of the pump-probe delay stability was performed using the spectral interference of the NIR pulses from both arms of the interferometer at the detector. The recombined

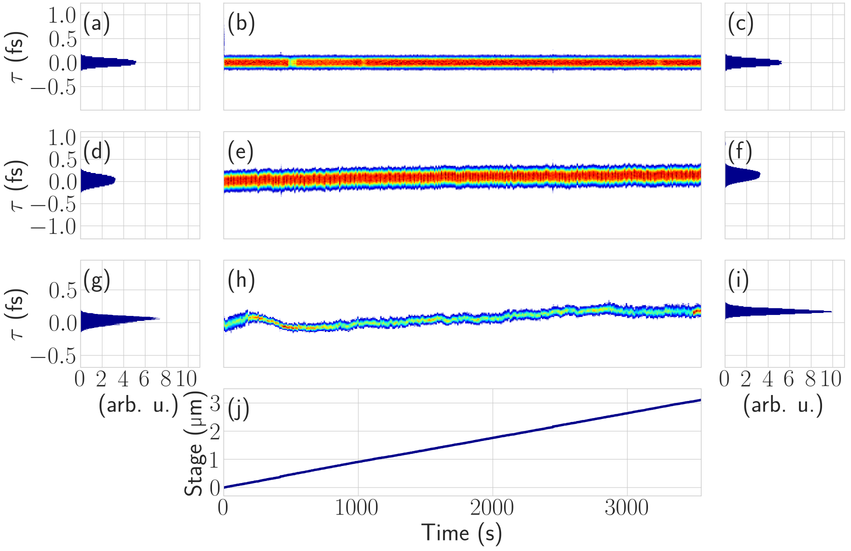

Figure 23: Active pump-probe delay stabilization system performance. The temporal offset between the two interferometer arms was measured for 3600 s using three different signals: *(a)–(c)* the NIR–NIR laser pulse spectral interference also used in the feedback loop controlling the delay stage; *(d)–(f)* the monochromatic blue laser (473 nm) spatial interference in the focus; *(g)–(i)* the NIR–NIR spectral interference in the focus. *(a)*, *(d)*, *(g)* and the *(c)*, *(f)*, *(i)* show normalized histograms (with the integral equal to 1) of the measured delays for the first and the last 360 s of each measurement, respectively. In *(j)* the delay stage position is shown.

laser beam was sent out of the vacuum chamber using a mirror installed on a movable mount at the differential pumping stage between the pump-probe interferometer and the Reaction Microscope (Fig. 21). The spectrum of the overlapped NIR beams was measured in the focus. In order to do that, the position of the Al filter in the *XUV arm* of the interferometer was shifted with respect to the laser beam. As a result, the central part of the NIR beam was no longer blocked by the filter, while the outer part used for the active delay stabilization was still propagating through the SiO_2 mount. In order to achieve easily detectable spectral fringes the delay between the two NIR pulses was intentionally kept on the order of one picosecond. The delay between the NIR pulses was calculated from the complex phase of the spectral modulation frequency component in the FTPS of the measured spectrum, similar to the active delay stabilization principle. During the measurement the spectrometer acquisition rate was around 50 Hz. From the measured delays shown in Fig. 23 (g)–(i) a linear drift on the order of 100 as per hour was observed. The standard deviation of the measured delay distribution is below 100 as.

Finally, in Fig. 23 (j) the delay stage position is shown. The delay stage was continuously moving over the whole measurement. The

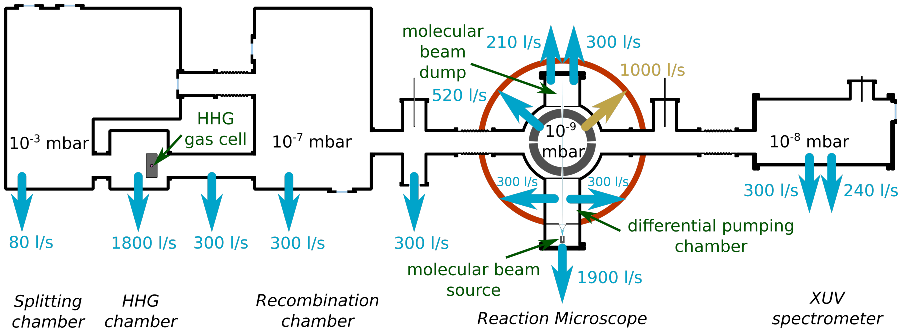

Figure 24: Schematic top view of the pump-probe interferometer vacuum system. Turbo molecular pumps are shown as blue arrows and a non-evaporative chemical getter pump is shown in yellow.

total delay stage movement over one hour is on the order of 3 µm, which corresponds to a 6 µm drift of the optical path length difference since the NIR beam path is folded at the delay stage. We assume that the main source of the observed drift is thermal expansion.

The results of the pump-probe delay stability measurement shown in Fig. 23 prove that the implemented active delay stabilization system is capable of locking the pump-probe interferometer compensating for substantial instabilities. The observed drift of the pump-probe delay is smaller than 100 as per hour, which is comparable with the duration of the XUV pulses used for the experiments. Thus, the active delay stabilization system precision is sufficient for time-resolved pump-probe spectroscopy experiments.

3.2.5 *Pump-probe interferometer vacuum system*

Meeting the requirements for the vacuum system of an XUV attosecond beamline with a Reaction Microscope as a detector is challenging due to up to six orders of magnitude pressure difference between distinct parts of the beamline. In order to achieve that, in the present setup the pump-probe interferometer is positioned in three separate vacuum chambers. The schematic view of the pump-probe interferometer vacuum system is shown in Fig. 24. In the following discussion these three chambers are called: *Splitting*, *HHG* and *Recombination* referring to optical elements located inside.

During normal operation a substantial amount of the generation medium gas has to be evacuated from the *HHG* chamber. In order to do that a 1800 l/s turbo molecular pump is used (STP-iXR1606, Edwards). This pump allows keeping the pressure at approximately $1 \cdot 10^{-3}$ mbar in the *HHG* chamber. Since there are no strict requirements for the pressure in the *Splitting* chamber it is equipped with a single 80 l/s turbo molecular pump (EXT75DX, Edwards). On the other hand, in the *Recombination* chamber the pressure should be kept on the order of $1 \cdot 10^{-7}$ mbar or lower in order to avoid a pressure increase in the Reaction Microscope. In order to achieve a three orders of magnitude pressure difference between *HHG* and *Recombination* chambers a differential pumping stage equipped with a 300 l/s turbo molecular pump is installed between them (STP-301, Edwards). To further increase the vacuum impedance between the two chambers a half inch diameter tube and an orifice with the size adjusted to the laser beam diameter are installed at the vacuum connections of the differential pumping stage towards the *HHG* and the *Recombination* chambers, respectively. The orifice is made from a drilled blank copper gasket. Apart from improving the vacuum conditions it is simultaneously blocking the outer part of the NIR laser beam after the high-order harmonic generation. The heat is dumped into the chamber walls reducing the thermal expansion induced instabilities of the optical setup. The *Recombination* chamber is equipped with a 300 l/s turbo molecular pump (STP-301, Edwards) allowing to keep the pressure on the order of $1 \cdot 10^{-7}$ mbar at operation.

In the present setup the *NIR arm* of the pump-probe interferometer is positioned in vacuum in order to avoid unbalanced dispersion in air with respect to the *XUV arm*. This configuration not only allows operating with ultrashort NIR laser pulses with down to a single cycle duration, but also prevents instabilities induced by air turbulences. In the *NIR arm* of the interferometer a 0.5 mm thick fused silica window separating the *Splitting* and *Recombination* chambers is installed. It not only decouples the two chambers, but also partially balances the dispersion induced by the beam splitter to the NIR pulses in the *XUV arm*.

In order to achieve two orders of magnitude pressure difference between the *Recombination* chamber and the Reaction Microscope an additional differential pumping stage equipped with a 300 l/s turbo molecular pump (STP-301, Edwards) is installed. This differential pumping stage is simultaneously used as a station for sampling the foci of the laser beams from the two arms of the interferometer (see Section 3.2.3). On the vacuum connection towards the Reaction Microscope a drilled blank copper gasket is installed in order to increase the vacuum impedance, similar to the differential pumping stage between *HHG* and *Recombination* chambers.

Operating turbo molecular pumps produce vibrations, which could potentially affect the temporal resolution of the performed experiments. In order to minimise this effect, in the present setup all three vacuum chambers with mounted turbo pumps are mechanically decoupled from the optical table by vibrational dumps (M-ND series, Newport). On the other hand, optical breadboards inside the chambers are directly installed on the optical table. In this configuration the optical setup is vibrationally decoupled from the turbo molecular pumps.

The vacuum system of the Reaction Microscope is described in Section 4.2.2. During operation, the output port of the Reaction Microscope could not be blocked due to back reflection of XUV photons resulting in strong ionization of the background gas. Thus, in order to reduce the gas flow from the XUV spectrometer to the Reaction Microscope, the pressure in the spectrometer is kept below $2 \cdot 10^{-8}$ mbar using two turbo molecular pumps with $300\,\mathrm{l/s}$ and $240\,\mathrm{l/s}$ pumping speeds (nEXT series, Edwards).

The described vacuum system prevents the generation medium gas flow into the Reaction Microscope, and thus allows performing XUV–NIR pump-probe experiments with coincidence detection.

3.3 XUV PULSES

In the present section the properties of XUV attosecond pulse trains (see Section 3.3.1) and the isolated attosecond pulses (see Section 3.3.2) available for experiments in the reported beamline are described. The XUV pulse trains and isolated pulses were reconstructed from experimentally acquired RABBIT and streaking spectrograms, respectively. For a detailed description of these two methods please refer to Section 2.5.

3.3.1 *Attosecond pulse trains*

In the present section the properties of the XUV APTs generated with approximately 7 fs FWHM NIR laser pulses delivered by the NOPCPA system (see Section 3.2.1) are described. The given discussion partially follows the original publication by M. Osolodkov *et al.* [101].

The cutoff photon energy Ω in the HHG spectrum depends on the ionization potential of the generation medium gas Ip as follows: $\Omega = \mathrm{Ip} + 3.17U_p$, where U_p is the ponderomotive potential (see Section 2.1.4). For the experiments reported in the present thesis XUV photons with energies up to 40 eV are required. Thus, Kr with Ip = 13.99 eV was chosen as a generation medium. The high-order harmonics were generated in the HHG cell at approximately 70 mbar with the NIR intensity on the order of $2 \cdot 10^{14}$ W/cm^2. The resulting XUV photon flux on target was measured using an XUV photodiode installed right after the Reaction Microscope (see Section 3.2.3). The XUV photon flux on target was estimated to exceed $2 \cdot 10^6$ photons per laser pulse. At 100 kHz repetition rate this corresponds to $2 \cdot 10^{11}$ XUV photons per second. Such an XUV photon flux is sufficient for photoionization experiments in different targets. In the pump-probe interferometer the XUV beam path contains three optical elements: the *filtering* mirror, the Al filter and the gold coated toroidal mirror (see Section 3.2.3). In the 15 to 50 eV XUV photon energy range the reflectivity of the *filtering* and the toroidal mirrors is on the order of 45 % and 60 %, respectively, while the transmissivity of the Al filter is on the order of 60 % [84]. Taking into account the losses the generated XUV photon flux was estimated to exceed $1 \cdot 10^{12}$ XUV photons per second.

In order to characterize the generated APTs, a RABBIT experiment was performed in Ar (Ip = 15.76 eV) using a VMI as a detecting system (see Section 4.1). The NIR probe peak intensity during the RABBIT measurement was kept on the order of $5 \cdot 10^{10}$ W/cm^2. The photoelectron momentum distributions were measured for a 20 fs long pump-probe delay range with 100 as steps. The inversion of the mea-

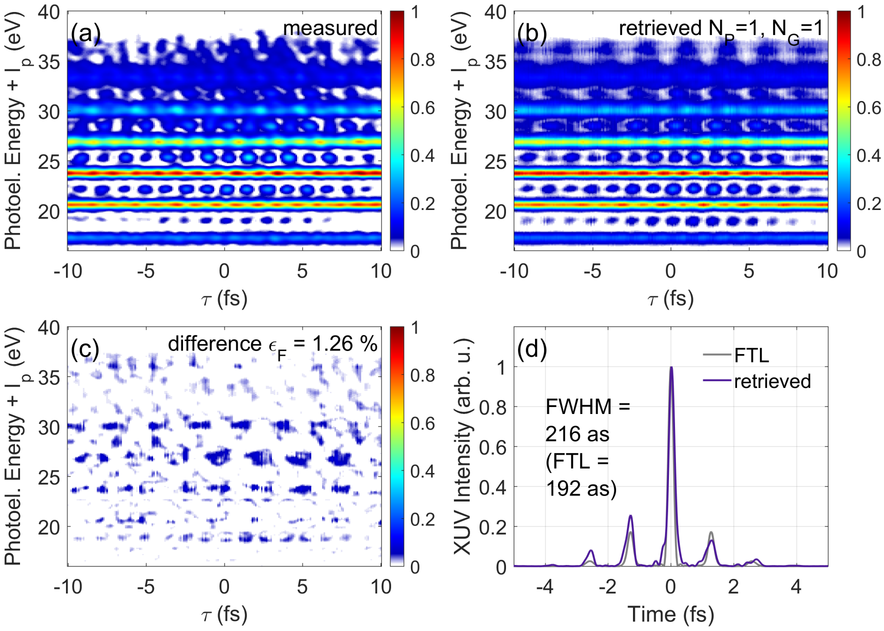

Figure 25: Reconstruction of attosecond pulse trains from the measured RABBIT spectrogram using a single pair of an XUV pulse and NIR gate. The measured and retrieved spectrograms are shown in *(a)* and *(b)*, respectively. *(c)* Difference between the measured and the reconstructed spectrograms. *(d)* Temporal profiles of the reconstructed APT and the Fourier Transform limited pulse train corresponding to the reconstructed XUV spectrum shown in violet and grey, respectively. The figure is reproduced from [101].

sured experimental images was performed with the BASEX algorithm [122].

From the reconstructed photoelectron momentum distributions RABBIT spectrograms were constructed for different angles with respect to the laser polarization by integrating corresponding angular ranges. For the APT reconstruction a RABBIT spectrogram constructed by integrating a 0 to 10 degree angular range with respect to the laser polarization was used. The resulting RABBIT spectrogram is shown in Fig. 25 (a). The photoelectrons emitted along the laser polarization were chosen for the APT reconstruction due to strong angle dependence of photoionization delays observed in Ar [26].

From the measured RABBIT spectrogram both XUV APTs and dressing NIR pulses were reconstructed using the time domain extended ptychographic iterative engine (td-ePIE) algorithm [123–125]. The temporal profile of the reconstructed attosecond pulse train is shown in Fig 25 (d). The calculated RABBIT spectrogram corresponding to the reconstructed APTs and NIR laser pulses is shown in Fig 25 (b). The difference between the calculated and measured spectrograms shown in Fig 25 (c) is indicating the precision of the pulse reconstruction. For the present reconstruction the calculated RABBIT spectrogram is not in complete agreement with the experimentally measured one. The difference between the two spectrograms has a prominent periodic pattern. Another reason to suspect that the reconstructed laser pulses do not exactly describe the laser pulses used in the experiment is that the temporal profile of the reconstructed APT has almost the same duration as the Fourier Transform limited pulse train, which is rather unrealistic.

The observed effect is a the result of the CEP jitter of the NIR laser pulses used for the HHG. The spectrum of 7 fs duration NIR laser pulses delivered by the NOPCPA system is narrower than one octave. Thus, a CEP measurement of these pulses could not be performed directly using an f-to-2f interferometer and requires additional spectral broadening, which is strongly susceptible to the laser stability. Even though the NOPCPA system output power fluctuations are below 1 % the reliability of this CEP stabilization method for the present setup is questionable [64]. Thus, for the experiments with 7 fs duration NIR laser pulses only the Ti:Saph oscillator seeding the NOPCPA system was actively CEP stabilized, while the CEP of the amplified pulses was not controlled [114]. As a result, the RABBIT experiment in Ar was effectively performed with an ensemble of XUV APTs and NIR laser pulses with different CEPs rather than with a single pair of them. The measured RABBIT spectrogram is then an incoherent sum of the spectrograms corresponding to XUV and NIR pulse pairs from the ensemble.

In order to take the CEP jitter into account and reconstruct the full ensemble of APTs delivered to the experiment a time domain ensemble extended ptychographic iterative engine algorithm (td-e^{2}PIE) was developed. The td-e^{2}PIE algorithm is capable of reconstructing the full ensemble of XUV APTs and probe NIR pulses from the measured RABBIT spectrogram. For a detailed description of the td-e^{2}PIE algorithm please refer to the original publication by T. Witting *et al.* [126].

The td-e^{2}PIE algorithm was applied to the RABBIT spectrogram measured in Ar. The reconstruction was performed for an ensemble of 20 APTs and 20 NIR probe pulses. In Fig. 26 (b) the resulting spectrogram calculated for this ensemble of pulses is shown. As visible from the difference plot shown in Fig. 26 (c), the calculated spectrogram for an ensemble of XUV pulse trains and NIR pulses is in better agreement with the experimentally measured one than that calculated for a single pair of XUV and NIR pulses. Also the reconstructed mean temporal profile over the ensemble of 20 APTs shown in Fig. 26 (d) is approximately 30 % exceeding the Fourier Transform limited pulse with the corresponding XUV spectrum, which is a more realistic result than that given by the reconstruction assuming a single pair of pulses.

The reconstructed ensembles of APTs and probe NIR pulses are shown in Fig. 27. In Fig. 27 (a) the mean temporal profile over the en-

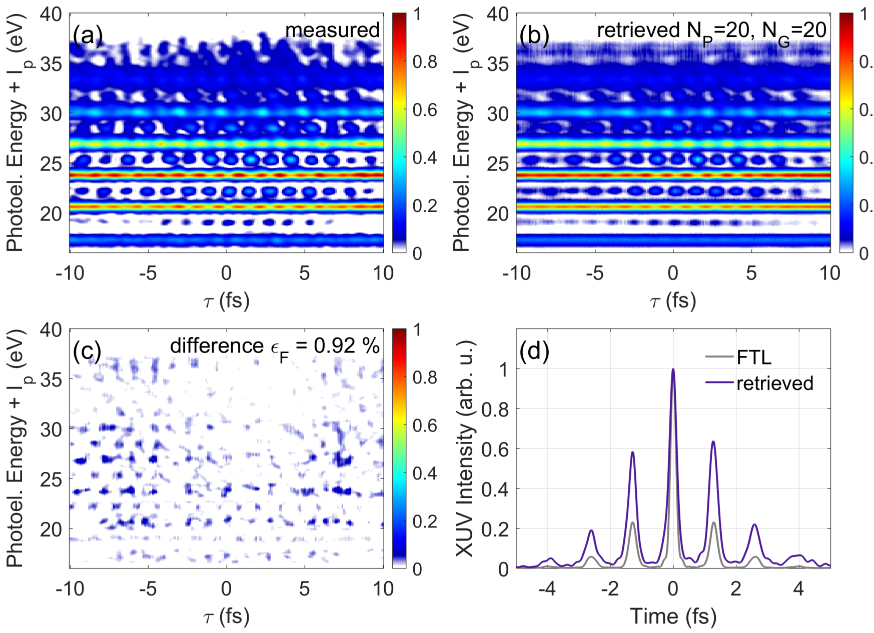

Figure 26: Reconstruction of attosecond pulse trains from the measured RABBIT spectrogram using an ensemble of 20 XUV pulses and 20 NIR gates. The measured and retrieved spectrograms are shown in *(a)* and *(b)*, respectively. *(c)* Difference between the measured and the reconstructed spectrograms. *(d)* Mean temporal profile over the ensemble of the reconstructed APT and the Fourier Transform limited pulse train corresponding to the mean reconstructed XUV spectrum shown in violet and grey, respectively. The figure is reproduced from [101].

semble of 20 reconstructed APTs is shown with a $\pm 1\sigma$ confidence range. The attosecond pulse trains delivered to the experiment in the present beamline consist of approximately 7 pulses with FWHM duration on the order of 300 ± 100 as each. In Fig. 27 (b) the mean electric field over the ensemble of 20 retrieved NIR probe pulses is shown. The NIR probe pulse delivered to the experiment has approximately 7 ± 3 fs duration.

In order to access the phases of the XUV APTs the dipole transition phases corresponding to photoionization of Ar were taken into account [127]. In Fig. 27 (c) an average Gabor distribution (a time-resolved spectrogram obtained using the time-windowed Fourier Transform — the Gabor Transform) over the retrieved ensemble of XUV APTs is shown. The attosecond pulse train has a positive chirp. The spectrum of the central pulse in the pulse train is broader than that of the pulses at the edges. Thus, at photon energies around 40 eV the pulse train is effectively shorter than at lower energies. This is manifested in a 'streaking like' photoelectron energy modulations observed at photoelectron energies above 25 eV in the measured RABBIT spectrogram (see Fig. 25 and 26).

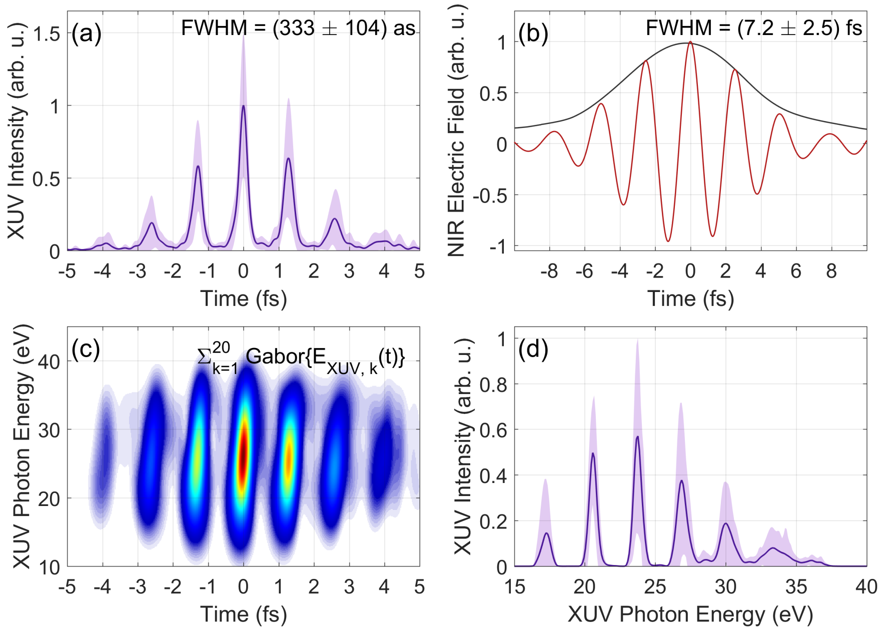

Figure 27: *(a)* Retrieved average temporal profile of the APTs delivered to the experiment. The solid line and the shaded area are representing the mean and the ±1σ of the distribution of 20 retrieved XUV pulses, respectively. *(b)* Mean electric field of the ensemble of 20 retrieved NIR probe pulses. *(c)* Sum of the Gabor plots over the ensemble of retrieved XUV pulses. *(d)* Average spectrum of the retrieved XUV APTs. The solid line and the shaded area are representing the mean and the ±1σ of the distribution of the 20 retrieved XUV pulses, respectively. The figure is reproduced from [101].

In Fig. 27 (d) the mean spectrum over the ensemble of 20 reconstructed APTs is shown with a ±1σ confidence range. It is spanning over 15 to 40 eV photon energy range. The low energy cutoff is induced by the Al filter absorbance. The high energy cutoff of the spectrum is underestimated in the reconstruction due to a Cooper minimum around 50 eV in the photoionization cross section of Ar [85].

The properties of XUV attosecond pulse trains and NIR probe pulses available for the experiments in the present beamline could slightly vary from those reported in the present section. This is a result of small differences in the performance of the NOPCPA system, since it is very sensitive to fluctuations of the seed and pump power. In general, using Kr as generation medium gas, one could expect to achieve APTs with very similar properties to those shown in Fig. 27. In order to acquire precise properties of APTs used for a particular experiment, a complementary RABBIT measurement in an atomic target with known dipole transition phases is necessary. Performing photoionization experiments in the gas phase with a Reaction Microscope such reference measurement can be done simultaneously using a mixture of a target an atomic reference gases (see Section 4.2.2).

3.3.2 *Isolated attosecond pulses*

In the present section the properties of IAPs generated with approximately 3.3 fs FWHM NIR laser pulses acquired after spectral broadening of the laser pulses delivered by the NOPCPA system in a gas filled hollow core fiber are described (see Section 3.2.2). The given discussion partially follows the original publication by T. Witting *et al.* [128].

Similar to attosecond pulse trains (see Section 3.3.1) isolated attosecond pulses were generated in Kr at approximately 70 mbar pressure in the HHG cell. Actively CEP stabilized 3.3 fs FWHM NIR laser pulses (see Section 3.2.2) were focused into the cell reaching peak intensity on the order of $2 \cdot 10^{14}\,\mathrm{W/cm^2}$. In order to optimize the HHG process for the generation of isolated attosecond pulses the CEP of the NIR laser pulses was tuned using thin fused silica wedges. The shortest available XUV pulse generated with the 0 rad CEP — a cosine NIR pulse, would correspond to the XUV photon spectrum with the highest cutoff energy. The achieved XUV photon flux on target was estimated to be on the order of $1 \cdot 10^6$ XUV photons per laser pulse ($1 \cdot 10^{11}$ XUV photons per second). Since such an XUV photon flux is sufficient for photoionization spectroscopy experiments, a streaking measurement was performed in Ne ($Ip = 21.56\,\mathrm{eV}$) using a VMI as the detecting system in order to characterize the generated IAPs (for more details on the attosecond streaking technique please refer to Section 2.5.3). Ne was chosen as the target for the attosecond streaking experiment due to its relatively big photoionization cross section and the absence of resonances in the corresponding XUV photon energy range [85]. During the measurement the NIR probe intensity was kept on the order of $5 \cdot 10^{12}\,\mathrm{W/cm^2}$. The resulting photoelectron momentum distributions were measured for a 30 fs pump-probe delay range with 200 as steps.

The photoelectron momentum distributions were obtained in a Legendre polynomial expansion in polar coordinates using the rBASEX algorithm [129]. Legendre polynomial basis up to the 14^{th}-order was used in order to describe multi NIR photon processes. From the inverted photoelectron momentum distributions streaking spectrograms were constructed for 0, $\pi/12$, $\pi/6$, $\pi/4$, $3\pi/4$, $5\pi/6$, $11\pi/12$ and π rad angles with respect to the laser polarization. In Fig. 28 (a) the resulting streaking spectrogram constructed from photoelectrons emitted along the laser polarization is shown. In the photoelectron energy range below approximately 20 eV "harmonic like" structures are observed. Such features in the photoelectron spectrum are conventionally observed in RABBIT spectrograms acquired with attosecond pulse trains. In the present case they hint to the presence of a weak satellite pulse. On the other hand, in the photoelectron energy range above 20 eV the spectrum is smooth indicating an isolated attosecond pulse.

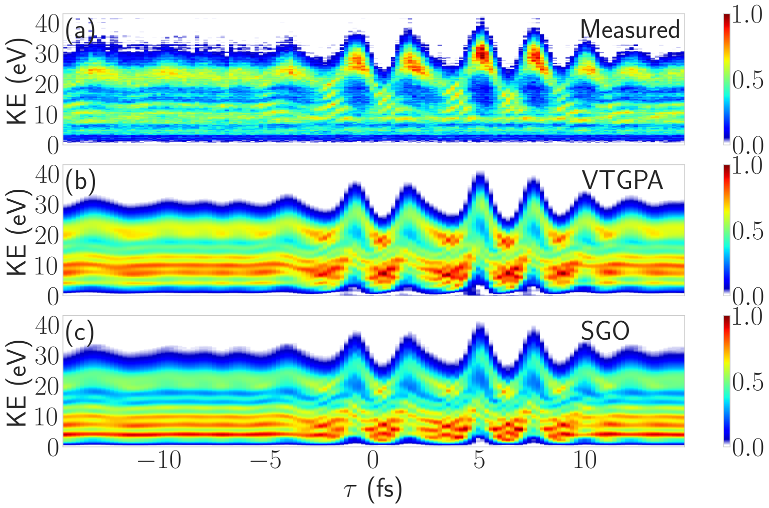

Figure 28: *(a)* Measured streaking spectrogram along the laser polarization. In *(b)* and *(c)* reconstructed streaking spectrograms using VTGPA and SGO algorithms are shown, respectively. The figure is reproduced from [128].

Conventional methods for IAPs reconstruction from measured streaking spectrograms rely on the central momentum approximation (CMA). It implies that the measured photoelectron momentum p_f can be replaced in the equation describing a Volkov phase (Eq. 77) by the central momentum of the measured photoelectron wavepacket (see Section 2.5.6). The CMA can be used as long as the central momentum of the wavepacket is much larger than its bandwidth, which is obviously not true in the present case as shown in Fig. 28 (a). The low energy cutoff of the XUV photon spectrum delivered to the experiment around 15.5 eV is induced by the Al filter absorption. Performing an attosecond streaking experiment in Ne (Ip = 21.56 eV) with such IAPs information on the XUV photon spectral range below the ionization potential is lost, since it is not imprinted in the measured photoelectron wavepacket. Thus, the XUV pulse reconstructed from the measured streaking spectrogram represents only a part of the initial pulse with photon energies above the ionization potential of Ne.

Since the CMA could not be used for the IAPs reconstruction in the present case, the Volkov-transform generalized projection algorithm (VTGPA) was chosen as an alternative [130]. The streaking spectrogram reconstructed using the VTGPA algorithm is shown in Fig. 28 (b). A complementary reconstruction was performed with the streaking global optimization (SGO) routine (for more details please refer to [128]). The streaking spectrogram reconstructed using the SGO algorithm is shown in Fig. 28 (c). The applicability of both the VTGPA and SGO algorithms to streaking spectrograms that could not be approached using CMA, as in the present case, was insured by

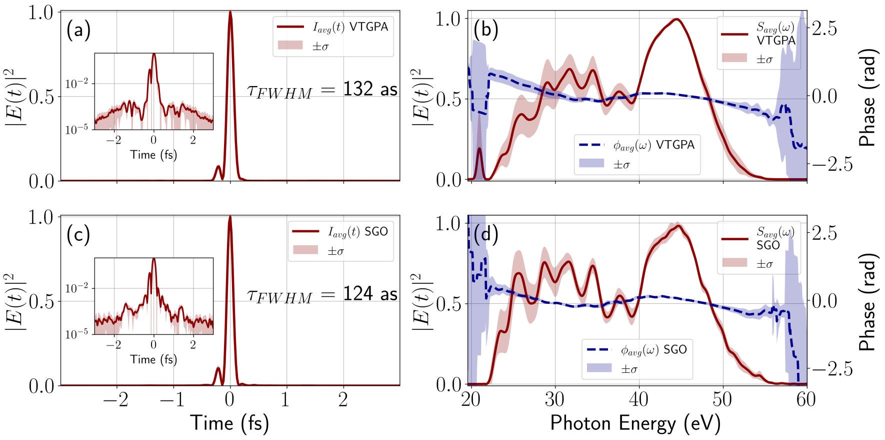

Figure 29: Reconstructed temporal profile and spectrum of the isolated attosecond pulses. In *(a)* and *(b)* the results given by the VTGPA algorithm are shown. In *(c)* and *(d)* the results given by the SGO algorithm are shown. Inset in *(a)* and *(c)* shows the temporal profile of the IAP in logarithmic scale. In *(b)*, *(d)* the spectra are shown as red solid lines with corresponding spectral phases shown as blue dashed lines. In all plots the mean values and the $\pm 1\sigma$ ranges over the distribution of 32 reconstructed IAP are shown as bright lines and shaded areas, respectively. The figure is reproduced from [128].

a series of calculations. For these calculations streaking spectrograms were simulated by solving the time-dependent Schrödinger equation. The XUV pulses were reconstructed from calculated spectrograms and compared with the initial pulses used for the TDSE calculations. For both retrieval algorithms it was shown that the root-mean-square field (RMFS) error [131] is on the order of 0.1, thus proving that the pulse reconstruction precision is sufficient [128].

For the data processing three different techniques were used: background subtraction (BS), correction on the total electron yield (TEY) and Fast Fourier Transform filtering (FFTf). For each of the eight observation angles listed above four different combinations of these techniques were applied: BS, BS + TEY, BS + FFTf and BS + TEY + FFTf. In total 32 streaking spectrograms were constructed from the measured photoelectron momentum distributions. From each of these spectrograms the initial IAPs were reconstructed with both VTGPA and SGO algorithms. The mean temporal profile with the $\pm 1\sigma$ range over the distribution of IAPs reconstructed with the VTGPA and SGO algorithms are shown in Fig. 29 (a) and (c), respectively. The results given by the two algorithms are in a good agreement. The FWHM of the main pulse is on the order of 130 ± 10 as. Satellite pre- and post-pulses with relative intensities below 0.1 % were retrieved by both algorithms. The XUV spectra and spectral phases retrieved with the VTGPA and SGO algorithms are shown in Fig. 29 (b) and (d), respectively.

The results given in the present section show that not only attosecond pulse trains, but also isolated attosecond pulses are available for experiments in the present beamline. As in the APT case (see Section 3.3.1), the IAPs delivered to the experiments can be slightly different from those shown in Fig. 29 due to small differences in the NOPCPA performance. The properties of the IAPs used for a particular experiment can be accessed performing a measurement with the Reaction Microscope in a gas mixture as discussed in Section 3.3.1.

4

CHARGED PARTICLE DETECTION

In the experiments reported in the present thesis the momenta of photoelectrons and photoions resulting from photoionization of atomic or molecular targets were measured. Thus, in Chapter 4 the charged particle detection techniques used in the present work are discussed. For the reported experiments two different charged particle detectors were used: a Velocity Map Imaging spectrometer (VMI) and a Reaction Microscope (ReMi). The VMI was used as a photoelectron detector for RABBIT and attosecond streaking experiments performed in noble gases for XUV pulse characterisation (see Section 3.3.1 and Section 3.3.2, respectively). For RABBIT experiments performed in molecular nitrogen a ReMi was used in order to access photoelectron dynamics corresponding to predissociative ion states (see Section 2.4.6). The present chapter is organised in sections as follows:

Section 4.1 describes the basic principles of a Velocity Map Imaging spectrometer. Conventional routines for initial photoelectron momentum distribution reconstruction from measured 2D projections are briefly discussed. The section is closed with a description of the VMI spectrometer used for the XUV pulse characterization experiments.

Studying photoionization of molecules it is advantageous to detect photoelectrons and photoions in coincidence. This method allows resolving photoelectrons corresponding to photoinduced transitions to dissociating ion states, which is not possible otherwise since, in general, they are overlapping with photoelectrons emitted during transitions to non-dissociating ion states. Thus, for time-resolved photoionization experiments in molecular nitrogen performed as a part of the present work a Reaction Microscope was used as detecting system. Thus, the remaining part of the present chapter is devoted to coincidence detection technique.

Section 4.2 opens with a discussion of coincidence detection measurements from a quantum mechanical perspective given in Section 4.2.1. The design of the Reaction Microscope used for the reported experiments is described in Section 4.2.2. After a brief overview of the basic principles of the charged particle detection and electric signal processing in the ReMi given in Section 4.2.3, Section 4.2.4 and Section 4.2.5, the section is closed with a description of the triggering scheme used (see Section 4.2.6).

In the Reaction Microscope used in the present work a gas target is created in the form of a supersonic molecular beam. Thus, Section 4.3 covers the working principles and implementation of this technique in the reported setup. In Section 4.3.1 and Section 4.3.2 the basic principles of a supersonic molecular beam are discussed. In order to be able to perform XUV–NIR pump-probe spectroscopy measurements using the ReMi a high density molecular beam source was developed as a part of the present work. A description of the design and characteristics of the developed source is given in Section 4.3.3.

In the Reaction Microscope after photoionization charged particles are guided towards their respective detectors by homogeneous electric and magnetic fields. In Section 4.4 the resulting trajectories of the charged particles in the ReMi are discussed. From the equations describing these trajectories equations for the initial charged particle momentum reconstruction are derived in Section 4.4.2. The special case of ions is discussed in Section 4.4.3.

The chapter is closed with a discussion of different factors limiting the obtained photoelectron momentum resolution given in Section 4.5. The effect of unprecisely defined parameters entering the photoelectron momentum reconstruction routine on the resulting momentum distribution is described in Section 4.5.1. In Section 4.5.2 the influence of noncollinearity of the electric and magnetic fields applied during the measurement on the obtained photoelectron momentum resolution is discussed. The section is closed by a brief description of the calibration routines for the main and compensatory magnetic fields in the ReMi given in Section 4.5.3 and Section 4.5.4, respectively.

4.1 VELOCITY MAP IMAGING SPECTROMETER

A Velocity Map Imaging (VMI) spectrometer is a two-dimensional (2D) charged particle momentum detector. In a VMI the three-dimensional (3D) momentum distribution of photoelectrons or photoions resulting from photoionization of a target under investigation is projected onto a 2D detector by an electrostatic lens. In photoionization experiments with linearly polarized light, the axis of cylindrical symmetry of the resulting charged particle 3D momentum distribution is parallel to the laser polarization. Thus, this momentum distribution can be unambiguously reconstructed from a 2D projection on the plane parallel to the axis of symmetry using an Abel inversion. In order to allow the initial charged particle 3D momentum distribution reconstruction, a position-sensitive detector has to be oriented parallel to the laser polarization during the experiment.

The concept of such a detecting system was first introduced by D. W. Chandler and P. L. Houston in 1987 [132]. In the first implementation a flat electric field was guiding charged particles towards the detector. Ten years later in 1997 the concept was further developed by A. T. Eppink and D. H. Parker [133], who shifted to an electrostatic lens configuration, which has substantially improved the acquired momentum resolution. Some of the recent VMI designs include a couple of electrostatic lenses creating an imaging system [134]. Controlling the voltages applied to the electrodes, the imaging system can be adapted for a particular experiment.

In VMI spectrometers micro channel plate (MCP)–phosphor screen assemblies are conventionally used as position-sensitive detectors. In such an assembly the MCP serves as an amplifier (see Section 4.2.3), while the phosphor screen allows recording the resulting signal with a camera operating in the visible range. Applying a temporal gate to the MCP, charged particles (usually ions) arriving during a chosen time-of-flight window can be selected. This can be advantageous for studying photodissociation processes. Another advantage of an MCP–phosphor screen assembly is the high multi-hit detection capability. In a VMI spectrometer equipped with such a detector the multi-hit detection capability is limited mainly by space-charge effects in the interaction region resulting in spectral line broadening. In the present setup this effect starts playing a role at detection rates higher than 10^3 counts per laser pulse.

Another option for a charged particle position-sensitive detector for a VMI spectrometer is an MCP–delay line anode detector (Section 4.2.4). It provides a good time-of-flight and impact position resolution, at the expense of the multi-hit detection capability, which is limited to a few charged particles detected simultaneously. Thus, an MCP–delay line anode detector is preferable for single event detection, as in the coincidence detection experiments.

In some recent setups a TimePix camera is used as the detector in a VMI spectrometer [135]. A TimePix camera provides information on the time-of-flight of a charged particle for each pixel individually. This allows splitting the initial charged particle 3D momentum distribution into "slices" parallel to the detector plane. The slice imaging technique allows direct access to the initial 3D momentum distribution of the charged particles instead of its 2D projection. Slice imaging works better for heavy particles, like ions or ionic fragments, since they have relatively long times-of-flight. Due to the significant difference in masses and as a consequence the times-of-flight of photoelectrons and photoions, a VMI spectrometer equipped with a TimePix camera can be used in the coincidence detection regime. In this regime the extraction electric field in the interaction region of the VMI is first guiding photoelectrons towards the detector, and then flips the sign in order to project photoions on the same detector. The multi-hit detection capability of a TimePix camera is limited to a few detected events per laser pulse.

The conventional technique for gas target creation in a VMI spectrometer is a supersonic molecular beam (see Section 4.3.2). It allows to achieve target gas densities in the interaction region of the VMI on the order of 10^{13} particles per cubic centimetre. Such target gas densities are not sufficient for photoionization experiments with XUV pulses generated through HHG, due to the typical relatively low XUV photon fluxes. Taking into account the high multi-hit detection capability of an MCP–phosphor screen assembly detector, it is advantageous to increase the target gas density in such experiments, in order to reduce data acquisition times. One of the ways to do that is to have a gas nozzle incorporated into the repeller electrode, as suggested in [136, 137]. This method allows to increase the target gas density in the interaction region of the VMI up to 10^{15} particles per cubic centimetre. In this configuration the interaction region could not be positioned closer than approximately 0.5 mm to the repeller electrode in order to avoid XUV photon-induced emission of electrons from the electrode surface. Since the pressure in a VMI should not exceed 10^{-5} mbar to operate MCPs, the target gas density is limited by the pumping capacity of the vacuum system. The overall gas load can be reduced using a pulsed nozzle instead of a continuous gas source. A pulsed nozzle can be used only at relatively low repetition rates up to a few kHz. For experiments performed at high repetition rate, such as those reported in the present thesis, a continuous gas source is required.

In Fig. 30 (a) a schematic view of the VMI spectrometer used for the experiments reported in the present thesis is shown. This VMI was constructed at AMOLF in the Netherlands in 2009 [138]. The imaging system of the VMI consists of two open electrodes (extractor and the flight tube) and a repeller electrode with a 50 μm diameter nozzle

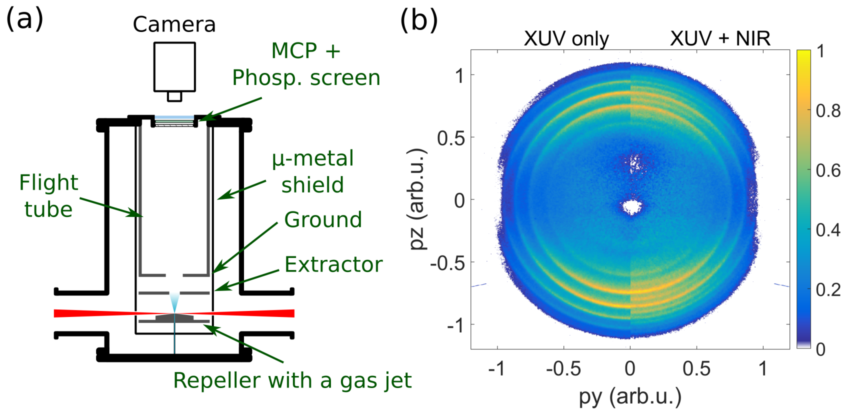

Figure 30: *(a)* Schematic view of the Velocity Map Imaging spectrometer used for the experiments reported in the present thesis, and *(b)* an example of a slice through the measured photoelectron momentum distribution after inversion with the BASEX algorithm [122]. Subplot *(b)* is reproduced from [101]. The shown data was measured in Ar as part of the RABBIT experiment described in Section 3.3.1. The left/right half of the image shows a photoelectron distribution resulting from single XUV/XUV ± NIR photon ionization of the target.

incorporated into it. The shape of the repeller electrode is specially designed in order to obtain a smooth extraction electric field in the interaction region. The whole imaging system is positioned inside a μ-metal shielding in order to prevent deformation of the photoelectron trajectories induced by an external magnetic field. Applying voltages to the three electrodes described above an electrostatic lens is created. It images the charged particle momentum distribution on the MCP–phosphor screen assembly detector plane. The ground electrode is separating a field free flight tube. In the present setup an 80 mm diameter MCP–phosphor screen detector is used. The signal is recorded using a CMOS (Complementary Metal-Oxide-Semiconductor) camera (BASLER acA2040-90umNIR) positioned outside the vacuum chamber. The energy resolution $\Delta E/E$ of the present VMI is on the order of a few percent. For a detailed description of the VMI spectrometer please refer to Ref. [138].

In Fig. 30 (b) an example of a slice through the initial 3D photoelectron momentum distributions measured in Ar as a part of a RABBIT experiment is shown. For more details please refer to Section 3.3.1. On the left/right hand side of Fig. 30 (b) the photoelectron distribution resulting from single XUV/XUV ± NIR photon ionization of Ar is shown. Sidebands are clearly visible in the photoelectron spectrum resulting from XUV ± NIR two photon processes.

The initial 3D momentum distribution can be reconstructed from the measured 2D projection using different numerical algorithms. These algorithms are based on a similar principle: the measured 2D projection of the charged particles momentum distribution is expanded in a basis of functions that can be analytically Abel transformed. Then the transformation is performed in the chosen basis. One of the conventional algorithms for initial momentum distribution reconstruction is BASEX (BAsis Set EXpansion), which uses a basis set of Gaussian functions [122]. Another class of algorithms including rBASEX and pBASEX uses a basis of Legendre polynomials in polar coordinates [129, 139]. The latter approach is advantageous for the reconstruction of charged particle momentum distributions measured in photoionization experiments, since polynomials in the Legendre series can be directly connected to physically meaningful partial waves.

Velocity Map Imaging spectrometers have been used for a big number of ultrafast photoionization experiments. The relative simplicity of the design, good multi-hit detection capability when equipped with an MCP–phosphor screen assembly detector, and access to angle resolved information makes a VMI an attractive tool for studying a large variety of photoinduced processes. One of the disadvantages of a VMI spectrometer is the requirement for cylindrical symmetry of the initial charged particle momentum distribution necessary to be able to perform an Abel inversion on the measured 2D projection. This requirement limits the potential applications of VMI spectrometers making them incompatible with experiments with elliptically polarized light. Even though at certain conditions a VMI spectrometer can be used in coincidence detection regime, in general, for this type of measurements it is advantageous to use a detecting systems equipped with two independent detectors for photoelectrons and photoions, such as a Reaction Microscope (see Section 4.2.2).

4.2 COINCIDENCE DETECTION

Coincidence detection of all charged fragments resulting from a photoinduced process is advantageous for studying the photoionization of molecules. Even the simplest molecules — homonuclear diatomic molecules such as H_2 or N_2 have a manifold of states and, as a consequence, a rich and complex photoionization dynamics. In order to study the dynamics corresponding to photoinduced transitions to dissociative states, which in general have a significantly lower probability than transitions to non-dissociative states, coincidence detection becomes necessary. In the present section the basic principles of coincidence detection are discussed. Then characteristics of the Reaction Microscope used for the experiments reported in the present thesis are described. A brief overview of the charged particle detection techniques used and the resulting electric signal evaluation is closing the present chapter.

4.2.1 *Coincidence detection measurements from quantum mechanical perspective*

In photoionization experiments among the possible observables are the momenta of charged particles: negatively charged photoelectrons and positively charged ions or ionic fragments resulting from the interaction of a target with single or multiple photons. In charged particle detection techniques such as Time-Of-Flight spectroscopy (TOF) or Velocity Map Imaging spectroscopy (VMI, see Section 4.1) in general only particles with the same electric charge sign can be detected simultaneously. This approach allows simultaneous detection of up to several thousands particles. Then the measured values are effectively integrated over the whole ensemble. In contrast, a Reaction Microscope allows coincidence detection of particles with both positive and negative charges. This capability comes at a certain price: no more than a single event should be detected simultaneously in order to avoid false coincidences.

The discussion given in the present section focuses on the difference between "ensemble-integrated" detection techniques and the coincidence detection technique from a quantum mechanical perspective. Let us consider the Hilbert space of photoelectron momentum eigenstates after photoionization as H_{e^-}. Similarly a Hilbert space of photoion momentum eigenstates is defined as H_{i^+}. For simplicity here we assume that the ion is singly ionized and does not dissociate. Generally speaking, the Hilbert space of photoelectron eigenstates H_{e^-} is infinite dimensional if continuum states are taken into account. The Hilbert space of the complete system after photoionization H_{complete} is the tensor product of Hilbert spaces H_{e^-} and H_{i^+}:

Hilbert space of the complete system.

$$H_{\mathrm{complete}} = H_{e^-} \otimes H_{i^+} \tag{93}$$

This is also applicable to the density matrix of the final state of the complete system ρ_{complete} after photoionization:

Density matrix of the complete system.

$$\rho_{\mathrm{complete}} = \rho_{e^-} \otimes \rho_{i^+} \tag{94}$$

Here ρ_{e^-} and ρ_{i^+} are the density matrices of the photoelectron and photoion final states, respectively. The expectation value of an observable $<A>$ with corresponding operator $\hat{A}$ can be calculated as $<A> = \mathrm{Tr}(\hat{A}\rho_{\mathrm{complete}})$. Performing a measurement only on one of the species of charged particles one effectively performs a measurement on the reduced density matrix, which is assigned as ρ_{measure}. The reduced density matrix can be acquired taking a partial trace of the complete density matrix ρ_{complete} with respect to the Hilbert space of eigenstates of particles that are not measured. For example, if the measurement is performed only on photoelectrons, the resulting reduced density matrix ρ_{measure} has a form:

Measured density matrix.

$$\rho_{\mathrm{measure}} = \mathrm{Tr}_{H_{i^+}}(\rho_{e^-} \otimes \rho_{i^+}) = \mathrm{Tr}(\rho_{i^+})\rho_{e^-} = \rho_{e^-} \tag{95}$$

The latter step in Eq. 95 is due to the property of any density matrix ρ: $\mathrm{Tr}(\rho) = 1$. This property can be understood from the probability interpretation of the density matrix diagonal elements. Even though Eq. 95 is trivial, it illustrates the reduction of available information on the final state of the system in case only one species of charged particles is detected. Detection of both photoelectrons and ions simultaneously but not in coincidence results in two measurements performed on ρ_{e^-} and ρ_{i^+} independently. The available information in that case is equivalent to information obtained performing a measurement on photoelectrons and ions sequentially. Then only the diagonal elements of ρ_{e^-} and ρ_{i^+} can be accessed, while the information on the diagonal elements of their tensor product $\rho_{e^-} \otimes \rho_{i^+}$ is lost.

The only way to experimentally access the diagonal elements of the complete density matrix of the final state ρ_{complete} (Eq. 94) is to detect all particles resulting from photoionization in coincidence, as it is done in a Reaction Microscope. Since, generally speaking, in the experiment there is no way to unambiguously assign the products of two similar but not fully equivalent events, only products of a single ionization event should be detected simultaneously. This condition is called *the single ionization event restriction*. It crucially limits the available experimental statistics. The approach to overcome this limitation realized in the present work relies on an increase of the laser pulse source repetition rate. Then the number of simultaneously detected events can be kept as low as required, while the overall data acquisition rate is significantly increased.

4.2.2 *Reaction Microscope*

A Reaction Microscope (ReMi) is a combined electron and ion spectrometer with coincidence detection capability. In a ReMi a homogeneous electric field is guiding both positively and negatively charged particles towards two time- and position-sensitive detectors. The basic principle of the ReMi is up to certain extent similar to a Recoil Ion Momentum Spectrometer (RIMS) developed for ion coincident detection [140]. The main advantage of a ReMi compared to RIMS is that it incorporates an additional magnetic field, originally introduced by R. Moshammer *et al.* [141], allowing detection of the full 3D photoelectron momentum distribution. For a detailed overview of charged particle detection with a ReMi please refer to the publication by J. Ullrich *et al.* [142].

The Reaction Microscope used for the experiments reported in the present thesis was designed and constructed at the Max-Born-Institut by S. Birkner [143]. The original design was optimized for strong field ionization experiments [144, 145], in which the required target gas density in the interaction region is typically smaller than that for XUV–NIR time-resolved pump-probe spectroscopy. This is due to typical relatively low XUV photon flux on the order of 10^6 XUV photons per pulse. Using the reported Reaction Microscope for attosecond spectroscopy, the data acquisition rate was limited by the relatively low target gas density delivered by the molecular beam. The single XUV photon ionization probability can be approximated by a Poisson distribution. Thus, in order to keep the amount of double and higher number of photoionization events per laser pulse low, the optimal detection rate for coincidence detection experiments should not exceed approximately 20 % of the repetition rate of the laser pulse source [117, 118]. For the experiments reported in the present thesis the Reaction Microscope was modified with a new molecular beam source allowing to reach an optimal target gas density in the interaction region. With this new molecular beam source the data acquisition was performed at 20 kHz in the XUV–NIR time-resolved pump-probe spectroscopy experiments. A detailed description of the new molecular beam source is given in Section 4.3.

In the Reaction Microscope the applied homogeneous magnetic field allows to project the full three-dimensional photoelectron momentum distribution on the detector plane. The effect of the magnetic field on the ion trajectories is negligible. For a detailed discussion of

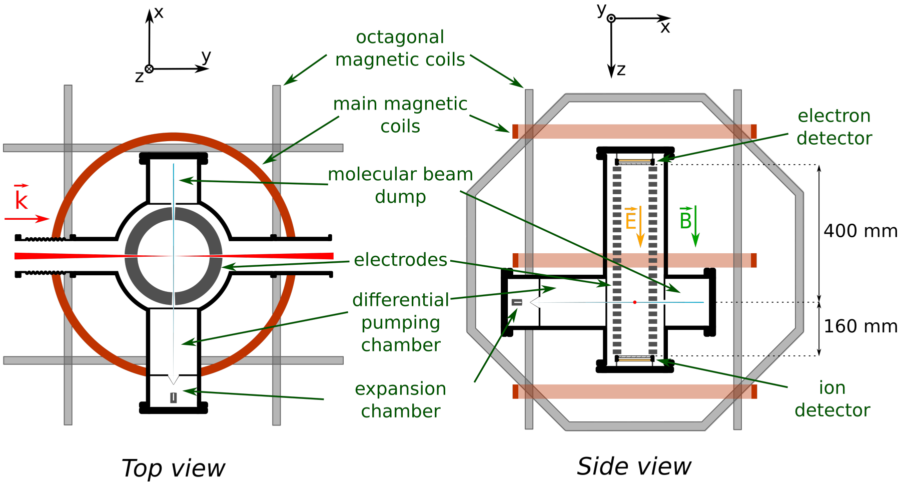

Figure 31: Schematic top and side views of the Reaction Microscope used in the present work. The orientation of the laboratory coordinate system is shown on top of the scheme.

charged particles trajectories in the Reaction Microscope please refer to Section 4.4.

In Fig. 31 a schematic view of the Reaction Microscope used in the present work is shown. The laboratory Cartesian coordinate system O used in the following discussion is illustrated on top of Fig. 31. It is oriented with respect to the Reaction Microscope as follows:

Laboratory coordinate system.

- x-axis: molecular beam direction,
- y-axis: laser beam direction ($\vec{k}$),
- z-axis: spectrometer axis towards the ion detector ($\vec{E}$ and $\vec{B}$).

The electrode stack producing an electric field and the laser polarization are both parallel to the z-axis (for a detailed description of the laser system please refer to Section 3.2.1). The electrode stack has a full length of 560 mm and consists of 25 electrodes with 80 mm diameter. These electrodes are connected in series with 50 kΩ resistors separating them. The electron/ion detector is positioned at the top/bottom of the electrode stack. The distances from the interaction region towards the ion and electron detectors are 160 mm and 400 mm, respectively. This configuration with a short ion arm was chosen in order to keep the ion times-of-flight relatively short, which is advantageous when working with a high repetition rate laser pulse source. In the experiments reported in the present thesis an electric field with 300 V/m strength was applied. Such a relatively low electric field strength was chosen in order to increase the photoelectron times-of-flight, and, as a consequence, to improve the obtained photoelectron momentum resolution (for more details please refer to Section 4.4).

The magnetic field is collinear with the electric field (parallel to the vertical z-axis). It is created by a set of three copper wire coils connected in series with equal 500 mm diameter and 380 mm distance between them. In order to create a homogeneous magnetic field in this geometry, the centre coil contains 13 windings, while the top and the bottom coils both contain 25 windings. For the experiments reported in the present thesis a magnetic field with 580 µT strength was applied, which corresponds to approximately 11 A current in the coils. This magnetic field strength was chosen in order to position magnetic nodes — the times-of-flight at which all the photoelectron trajectories overlap, symmetrically with respect to the measured photoelectron momentum distribution (for more details please refer to Section 4.4).

Octagonal coils for an auxiliary magnetic field with 1.75 m and 1.6 m diameters are installed on the Reaction Microscope in order to be able to compensate for the x and y components of external magnetic field. The dominant contribution to the external magnetic field is the tangential component of the magnetic field of the Earth. For more details on the effect of non-compensated x and y components of the external magnetic field on the obtained photoelectron momentum resolution please refer to Section 4.5.2.

Considering XUV–NIR pump-probe spectroscopy experiments, it should be taken into account that the energy of XUV photons used is sufficient for single-photon ionization of almost any atom or molecule they interact with. This leads to photoionization not only in the interaction region — the volume defined by the overlap of the molecular and laser beams, but also of background gas along the XUV laser beam propagation. Together with the single ionization event restriction this effect results in a demand for a high vacuum on the order of 10^{-9} mbar or lower in the Reaction Microscope during the experiment. Taking into account the large surface of the electrode stack and the detectors, meeting this requirement is particularly challenging. In order to reach the required pressure, the Reaction Microscope is equipped with six turbo molecular pumps with different capacities and a non-evaporative chemical getter pump.

A schematic view of the Reaction Microscope vacuum system is shown in Fig. 32. The Reaction Microscope can be separated in two parts: a *main* chamber containing the electrode stack and the detectors, and a molecular beam source consisting of three vacuum chambers — an *expansion* chamber, a *differential pumping* chamber and a *beam dump*. For more details on the design of the molecular beam source please refer to Section 4.3.3. The *main* chamber is equipped with one 520 l/s turbo molecular pump (TMU 521 P, Pfeiffer) and a 1000 l/s non-evaporative chemical getter pump (MK5 series, CapaciTorr). The turbo pump installed on the *main* chamber is connected in series with a 60 l/s "booster" turbo pump (TMH 071 P, Pfeiffer). In this configuration the base pressure in the *main* chamber is kept on the order of

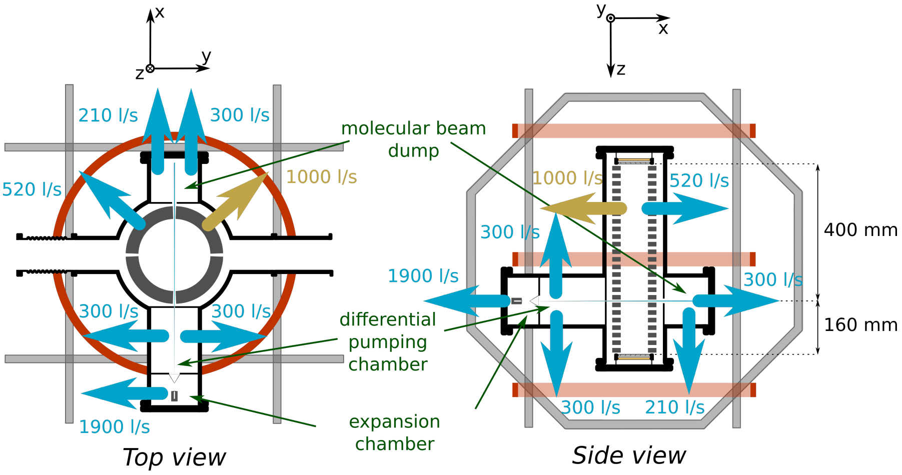

Figure 32: Schematic top and side views of the vacuum system of the Reaction Microscope used in the present work. Turbo molecular pumps are shown in blue and a non-evaporative chemical getter pump is shown in yellow.

10^{-10} mbar. With operating molecular beam the pressure in the *main* chamber could reach up to the 10^{-9} mbar range due to back scattering from the *beam dump* chamber.

Due to the high load, the *expansion* chamber of the molecular beam source is equipped with a 1900 l/s turbo molecular pump (TC 1200, Pfeiffer). Such a large pumping capacity is required in order to allow formation of a supersonic molecular beam (see Section 4.3.2). With an operating molecular beam, the pressure in the *expansion* chamber reaches up to the 10^{-4} mbar range. The *differential pumping* chamber is equipped with two 300 l/s turbo molecular pumps (HiPace 300, Pfeiffer and nEXT series, Edwards). The total pumping capacity is sufficient to keep the pressure in the *differential pumping* chamber in the 10^{-6} mbar range with the molecular beam operating, which prevents an increase of the background pressure in the *main* chamber of the Reaction Microscope. Finally, after the interaction region, the molecular beam is dumped into the *beam dump* chamber. The *beam dump* chamber is equipped with two turbo molecular pumps with 300 l/s and 210 l/s pumping capacities (nEXT series, Edwards and TMU 261, Pfeiffer). The two turbo pumps installed on the *beam dump* chamber are connected in series with the same "booster" turbo pump as the turbo pump installed on the *main* chamber. With the molecular beam operating the pressure in the *beam dump* chamber is in the 10^{-9} mbar range. For more details on the molecular beam please refer to Section 4.3.

Both the electron and ion detectors in the Reaction Microscope are MCP stack–delay line anode assemblies. In both detectors the MCP stacks consist of two MCPs — a chevron stack. The delay line anode for the ion detector has two layers — a quad-anode. Since multiple photoelectrons could result from a photoionization process under investigation, the delay line anode for the electron detector has three layers — a hex-anode. It was chosen in order to enhance the multi-hit detection capability. For a description of the MCP stack–delay line anode assembly detector please refer to Section 4.2.3 and Section 4.2.4, respectively, while for more information on the design and characteristics of the Reaction Microscope please refer to [116, 143].

4.2.3 *Micro channel plates*

Micro Channel Plates (MCPs) are high gain signal amplifiers preserving the spatial position of a detected charged particle or high energy photon. MCPs are approximately 1 mm thick plates made of dielectric material, for example glass, with multiple small channels with typical diameter on the order of 10 µm. The inner surface of these channels is coated with a thin semiconductor layer, which has a high secondary electron emission efficiency. The basic principle of charged particle or high energy photon (XUV or X-ray spectral range) signal amplification in the MCPs is the following: a detected charged particle or high energy photon interacts with the semiconductor layer on the inner surface of a channel and creates an avalanche of secondary electrons. An accelerating voltage on the order of 1 kV is applied between front and back surfaces of the MCP in order to guide the secondary electrons through the channel. The MCP surfaces are coated with a thin conducting layer. The electrical resistance between the two MCP surfaces is typically on the order of tens of MΩ. Every time a secondary electron hits the channel wall it again produces another bunch of secondary electrons. The overall amplification factor, or gain, can reach up to 10^6. It is advantageous to operate the MCP at saturation. Then the resulting signal is independent of the detected particles initial energy.

In order to increase the interaction probability of a detected particle with the channel inner surface, in an MCP the channels are oriented at a small angle to the surface normal. MCPs can be used in a set of two — a V-stack or chevron stack, or three — a Z-stack in order to reach an amplification factor up to 10^7. In some configurations thin conducting spacers are installed between the MCPs in the stack. The orientation of the channel plates in the stack is chosen so that the channels of the adjacent plates are not collinear. The advantage of this configuration is that it prevents the detected electrons or photons from passing through a channel without interacting with its inner surface. Thus, homogeneous amplification can be achieved for particles arriving at different angles with respect to the detector surface.

When a particle hits an MCP and creates an avalanche of secondary electrons a significant charge is removed from it over a short time period. This results in a rapid increase of current in the MCP accompanied by a voltage pulse that can be detected. In this detection regime an MCP on its own can be used as a time-of-impact detector. The temporal resolution of the MCPs used in the present setup is below 100 ps. Due to charge removal from individual channels after the interaction with a particle, each channel has a dead time on the order of a few microseconds. This time is needed for the charge distribution to recover.

Since the signal amplification occurs in each channel individually and the channel size is small, the information on the detected particle impact position is preserved. This allows to use MCPs in combination with position-sensitive detectors, such as a phosphor screen with a CCD or CMOS camera, as in the VMI used in the present work (see Section 4.1), or a delay line anode (see Section 4.2.4).

During operation the residual pressure in the vacuum chamber with an MCP detector installed should not exceed 10^{-6} mbar in order to avoid sparking. Even operated at optimal conditions the lifetime of an MCP detector is limited. Degradation of the semiconductor layer on the channel inner surface results in inhomogeneity of the gain over the MCP's surface. This effect is especially prominent for the detection of ions. In case the semiconductor layer is significantly damaged in a particular channel, this position would appear as a blind spot in the detected particle's distribution.

In the present setup 80 mm diameter MCPs are used (Hamamatsu). Voltages on the order of 3.1 kV and 2.5 kV are applied to the MCP stacks on the electron and ion detectors, respectively.

4.2.4 *Delay line anode*

A delay line anode is a position-sensitive electron detector. It consists of two/three layers of wire pairs wrapped around a rectangular/hexagonal plate. Such detectors are called a quad-anode or a hex-anode, respectively. The wires are electrically insulated from the plate. The distance between the wires is usually on the order of 0.5 mm. Two wires in a pair are called signal and reference. A higher positive voltage on the order of 50 V is applied to the signal wire with respect to the reference. Thus, all arriving electrons are collected by the signal wire. As a result, an electric pulse propagates to both ends of the wire where it can be detected. Knowing the difference between the arrival times of the electric signals on the two ends of the signal wires from all layers, the electron cloud impact position can be reconstructed.

Since a significant electron cloud is required, delay lines are commonly used with MCPs for signal amplification. In such an assembly delay lines are positioned a couple of millimetres behind the MCP stack. A positive extraction voltage on the order of 500 V with respect to the back surface of the MCP stack is applied to the delay lines. The large number of electrons in the cloud allows for a centre-of-mass averaging of the detected signal. As a result, distances between the two impact positions smaller than the spacing between the wires can be resolved. For the detectors used in the reported setup the spatial resolution is below 50 µm.

The quad-anode delay line multi-hit detection capability is limited. Detection of a charged particle results in the creation of a "dead" region on the detector surface [146]. If another particle arrives to the "dead" region during the delay line dead time, the two signals could not be resolved. The dead time of the delay line anodes used in the present setup is on the order of 50 ns. On the other hand, a hex-anode provides redundant information on the charged particle impact position, which can be used to overcome the "dead" region issue. Thus, with a hex-anode better multi-hit detection capability is achieved. In the present setup it is especially important for photoelectron detection, since in the reported experiments the full measured photoelectron time-of-flight distribution is narrower than 100 ns. For the ion detection a quad-anode is used since in the reported experiments the full measured ion time-of-flight spectrum covers approximately 25 µs range. Thus, the demand for a multi-hit detection capability for the ion detector is not as high as for the electron detector. The delay line anodes for both the electron and ion detectors are produced by RoentDek.

4.2.5 *Signal detection*

The output signals of both the MCPs and delay line anodes are electric pulses with a certain distribution of heights depending on the amplification factor, which can be slightly inhomogeneous across the detector plane. In the experiment measurement of the arrival times of these electric pulses with as high as possible resolution is important. A simple way of doing that is to set a threshold and detect times when the electric signal exceeds it. That method leads to inaccuracies in the arrival time detection for electric pulses with non-constant heights. In order to measure the arrival times of electric pulses more precisely a Constant Fraction Discriminator (CFD) is used in the present setup. The basic principle of a CFD is to measure the time at which an electric pulse signal is equal to a certain fraction of the maximum signal over the pulse. In order to do that, for each arriving electric pulse a copy is produced. Then this copy is inverted and superimposed with the original pulse at a certain fixed delay. The arrival time is measured as the time when the combined electric pulse signal changes sign. This way the detection occurs equally for pulses with different heights.

All electronics for the electric signal detection used in the present setup were produced by RoentDek. For the ion detector an ATR19 unit is used. It incorporates both an electric signal amplifier and a

CFD. For the electron detector signal amplification was performed with a FAMP8 unit with sequential discrimination with a CFD8c unit. After the discriminators, the resulting NIM-signals are delivered to a Time-to-Digital Converter (TDC). In the present design the TDC unit consists of a pair of 8 channel PCI cards with synchronized clock. The time resolution of the TDC unit is on the order of 25 ps.

The electron/ion detector has 7/5 output channels: 1 for the MCP and 2 for each layer of the hex-anode/quad-anode. In the present configuration an additional TDC channel is connected to a photo diode (DET210, ThorLabs) picking up the NIR laser pulses. This allows synchronization of the TDC common clock with the laser. One more channel is used for encoding the pump-probe delay into the measured data. For this channel a signal is generated with a digital delay pulse generator (Quantum Composers 9200) using the photo diode signal as a trigger. The delay between the signals from the photodiode and the digital delay pulse generator is used for distinguishing events corresponding to different pump-probe delays. The temporal resolution of the delay pulse generator is 10 ns. Thus, a 40 ns delay step was chosen in order to ensure an unambiguous decoding. For a 10 µs time window between the consequent laser pulses (corresponds to 100 kHz repetition rate source) this method allows encoding up to 250 pump-probe delays. Application of delays between the photo diode and digital delay generator signals exceeding 10 µs may possibly lead to an overlap of the latter with the data acquisition time window opened by the consequent ionization event, which results in wrong delay encoding. In case the number of pump-probe delays needed for the experiment exceeds 250, two channels of the digital delay pulse generator can be used simultaneously.

4.2.6 *Triggering scheme*

In the experiments reported in the present thesis an electron detector MCP signal was used as a trigger for the data acquisition. The electron MCP signal was chosen instead of a photo diode signal (triggering on the laser pulses) since in coincidence detection experiments the conditions are adjusted such that about 80 % of the laser pulses do not result in photoionization of the target (see Section 4.2.2). Thus, when triggering on laser pulses only every fifth recorded event would contain meaningful information and the rest would be empty. The triggering scheme used allows to substantially reduce the size of the experimentally acquired datasets without any information losses.

The schematic view of the triggering scheme used in the present work is shown in Fig. 33. Since the repetition rate of the laser pulse source used is 100 kHz, a laser pulse is arriving at the experiment every 10 µs. If photoionization occurs, in the present spectrometer geometry with an extraction electric field strength on the order of

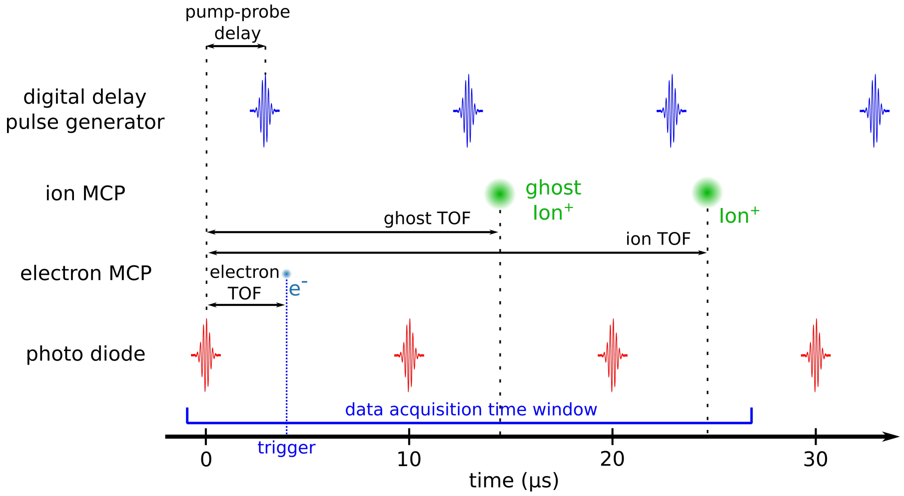

Figure 33: Schematic view of the triggering scheme of the Reaction Microscope used for the experiments reported in the present work. For a detailed description please refer to the main text.

300 V/m applied, the typical photoelectron time-of-flight is on the order of 100 ns. The signal from the electron detector MCP serves as the trigger and an event is recorded. For measuring the detected photoelectron time-of-flight, the signal from the photo diode serves as a time reference. At the respective conditions the typical time-of-flight of a heavy singly charged ion could exceed 20 µs. Thus, such an ion would arrive to the detector after two consequent laser pulses, as shown in Fig. 33. In order to detect all ions corresponding to a photoionization event and measure their times-of-flight with respect to the photodiode signal, a [−0.5, 25.0] µs data acquisition time window was set. On top of that, the charged particle detection has approximately 50 % probability for both detectors. Thus, the following situation may occur: from a photoionization event the photoelectron is either not detected or counted as a sequential electron since it has arrived into the open data acquisition time window. Then let us assume that the corresponding ion was detected and a photoelectron ionized with the following laser pulse is opening a new data acquisition time window. As a result, the ion ionized with the previous laser pulse is incorrectly assigned to the following photoionization event. The corresponding ion signal appears in the measured TOF spectrum as a "ghost" peak shifted by 10 or 20 µs with respect to their real times-of-flight, as shown in Fig. 33.

A sequence of two or three pulses from the digital delay pulse generator appear in the data acquisition time window depending on the applied delay. In order to avoid ambiguity the first pulse in the sequence is used for encoding the information on the applied pump-probe delay in the measured dataset.

Due to different cable lengths and the beam path of the laser pulse, the photo diode signal arrives at the TDC with a time offset on the order of a few nanoseconds with respect to the arrival time of the respective laser pulse at the experiment. Thus, using this triggering scheme the acquired photoelectron and ion TOF spectra have a linear shift on the order of a few nanoseconds. This time shift can be determined from peaks in the photoelectron and ion TOF spectra corresponding to XUV photon scattering on the gas target. Using this information the measured TOF spectra could be corrected prior to momentum reconstruction.

4.3 MOLECULAR BEAM

A supersonic molecular beam is a well-established technique for gas sample delivery to the experiment. Due to the supersonic expansion the temperature along the molecular beam axis can be reduced down to the 10^{-2} K range [147]. Such a cold target significantly improves the acquired momentum resolution in photoionization experiments.

In the present section the basic principles of a supersonic molecular beam are discussed. Since an upgrade of the molecular beam source in the Reaction Microscope performed as a part of the present work was necessary for the reported experiments, the section is closed with a description of the new source design and characteristics.

4.3.1 *Basic principles*

For XUV photoionization experiments performed with coincidence detection a high density gas target is needed, since a high XUV photon flux at a high repetition rate is challenging to achieve. On the other hand, the pressure in the *main* chamber of the ReMi during the measurement has to be on the order of 10^{-9} mbar or lower. Since the XUV photon energy is in general sufficient for single photon ionization of the majority of gases, XUV photons would ionize any atom or molecule they interact with. This results in a strong background gas ionization contaminating the measured data.

In order to illustrate this effect let us make a calculation. For simplicity, let us assume that the XUV photon spectrum consists of a single spectral line with photon energy ω. Here we approximate the XUV photon flux F [photons/s] as isotropic over a beam profile with cross section S. We also approximate the target gas as an ideal gas. Let us now consider a volume $V = S \cdot \delta l$, where δl is an infinitesimally small length. Then the number of particles N in the volume V due to the ideal gas law is equal to:

Ideal gas law.

$$N = \frac{p \cdot S\delta l}{kT} \tag{96}$$

Here p is the gas pressure, k is Boltzmann's constant and T is the temperature. Let us assign the density of gas particles in the target as $\rho = \frac{N}{S\delta l}$. Then the probability of interaction of an XUV photon with a target gas atom or molecule R is equal to:

Probability of interaction with an XUV photon.

$$R = \rho \cdot \sigma \cdot L = \frac{N \cdot \sigma}{S\delta l} \cdot L = \frac{p \cdot \sigma}{kT} \cdot L \tag{97}$$

Here σ is a photoionization cross section of the target gas at the respective XUV photon energy ω, and L is the total length of the gas sample. Thus, at constant temperature, the ionization rate is growing linearly with pressure.

Maxwell-Boltzmann distribution.

Another requirement for obtaining a high momentum resolution in the experiment, is a narrow initial momentum distribution of the particles in the target. In the following discussion the velocities of the particles are defined with respect to the centre of mass of the ensemble. The distribution of the absolute velocity of gas particles in an ensemble is described by the Maxwell-Boltzmann distribution:

$$f(v') = \frac{4}{\sqrt{\pi}} \left(\frac{m}{2kT}\right)^{3/2} v'^2 e^{-\frac{m}{2kT}v'^2} \tag{98}$$

Equation for the most probable velocity.

Here m and v' are the particle's mass and velocity, respectively. The most probable velocity v_p can be calculated from Eq. 98 as the position of the distribution maximum, which is equivalent to finding a solution to the following equation:

$$\frac{df(v')}{dv'} = \frac{8}{\sqrt{\pi}} \left(\frac{m}{2kT}\right)^{3/2} v' \left(1 - \frac{m}{2kT}v'^2\right) e^{-\frac{m}{2kT}v'^2} = 0 \tag{99}$$

Maxwell-Boltzmann distribution.

Then the most probable velocity $v_p = \sqrt{\frac{2kT}{m}}$. It is convenient to rewrite Eq. 98 using v_p as follows:

$$f(v') = \frac{4}{\sqrt{\pi}} \frac{v'^2}{v_p^3} e^{-\frac{v'^2}{v_p^2}} \tag{100}$$

Mean velocity.

The mean velocity over the ensemble $\langle v' \rangle$ can be calculated as:

$$\begin{aligned} \langle v' \rangle &= \int_0^\infty v' f(v') dv' = \frac{2v_p}{\sqrt{\pi}} \int_0^\infty \frac{v'^2}{v_p^2} e^{-\frac{v'^2}{v_p^2}} d\frac{v^2}{v_p^2} \\ &= -\frac{2v_p}{\sqrt{\pi}} \left(\frac{v'^2}{v_p^2} e^{-\frac{v'^2}{v_p^2}} \Big|_0^\infty - \int_0^\infty e^{-\frac{v'^2}{v_p^2}} d\frac{v'^2}{v_p^2} \right) = \frac{2v_p}{\sqrt{\pi}} \end{aligned} \tag{101}$$

Mean velocity square.

The mean velocity square $\langle v'^2 \rangle$ can be calculated as:

$$\begin{aligned} \langle v'^2 \rangle &= \int_0^\infty v'^2 f(v) dv' = \frac{4}{\sqrt{\pi} v_p^3} \int_0^\infty v'^4 e^{-\frac{v'^2}{v_p^2}} dv' \\ &= \frac{4}{\sqrt{\pi} v_p^3} \int_0^\infty \frac{\partial^2}{\partial \left(\frac{1}{v_p^2}\right)^2} e^{-\frac{v'^2}{v_p^2}} dv' = \frac{4}{\sqrt{\pi} v_p^3} \frac{\sqrt{\pi}}{2} \frac{\partial^2}{\partial \left(\frac{1}{v_p^2}\right)^2} \left(\frac{1}{v_p^2}\right)^{-\frac{1}{2}} \\ &= \frac{2}{v_p^3} \frac{3v_p^5}{4} = \frac{3}{2} v_p^2 \end{aligned} \tag{102}$$

Then the standard deviation of the velocity distribution σ_b is equal to:

Standard deviation of the velocity distribution.

$$\sigma_b = \sqrt{\langle v'^2 \rangle - \langle v' \rangle^2} = \sqrt{\frac{3}{2} - \frac{4}{\pi}} \cdot v_p \tag{103}$$

Applying the most probable velocity v_p into Eq. 103, it becomes clearly visible that the standard deviation of the velocity distribution σ_b is proportional to square root of the gas temperature. In other words, in order to obtain a narrow momentum distribution of particles in a target, it has to be cooled down.

It is worth mentioning here that the velocity distribution of gas particles in the ensemble along a particular axis can be described by a Gaussian distribution:

Velocity distribution along x-axis.

$$f(v'_x) = \sqrt{\frac{m}{2\pi kT}} e^{-\frac{m}{2kT} v'^2_x} \tag{104}$$

Here v'_x is the projection of the particle's velocity on the x-axis. The standard deviation of $f(v'_x)$ is $\sigma_x = \sqrt{\frac{kT}{m}}$. For the Gaussian distribution the FWHM is related to the standard deviation as follows:

Gaussian distribution FWHM.

$$\mathrm{FMHM} = 2\sqrt{2 \ln 2}\sigma_x \tag{105}$$

Using this relation the temperature of the molecular beam can be estimated from the FWHM of the velocity distribution along a particular direction.

A supersonic molecular beam meets all the requirements described above, allowing the creation of a cold dense gas target. The basic principle of this technique is the following: a reservoir with gas at relatively high pressure, on the order of a few bar, is connected to a vacuum chamber with relatively low pressure, on the order of 10^{-3} mbar or lower, through an orifice with a few tens of µm diameter. A supersonic regime is achieved if the mean free path of the gas particles in a reservoir is smaller than the orifice size. If the mean free path is exceeding the orifice size, an effusive beam is created.

Let us assume that the expansion of gas leaving a reservoir through the nozzle is isentropic, or in other words, both reversible and adiabatic. Such a process occurs without energy transfer between the system and the surroundings. Then the enthalpy of the system $H = U + pV$ is conserved. Here U is the internal energy, and pV is the work corresponding to a change in volume V at constant pressure p.

During the expansion, the enthalpy is transformed into kinetic energy of the gas particles in the beam:

Enthalpy conservation.

$$H_0 = H_1 + N\frac{m\langle v\rangle^2}{2} \tag{106}$$

Here H_0 and H_1 are the enthalpy of the system before and after the expansion, respectively, N is the number of particles in the beam, and $\langle v\rangle$ is the velocity of the centre of mass of the particle ensemble in the beam (not equal to the particle's mean velocity with respect to the centre of mass shown in Eq. 101). The total change of the system enthalpy $\Delta H = H_0 - H_1$ is related to the temperature difference between the reservoir T_0 and the expanded beam T_1 as follows:

Change of the enthalpy of the system.

$$\Delta H = \frac{N}{N_A} C_p (T_0 - T_1) \tag{107}$$

Here C_p is the isobaric (constant pressure) molar (per one mole of gas) heat capacity, and N_A is the Avogadro constant. For simplicity we assume that C_p is constant over the whole temperature range, which is not true for real gases. The isobaric molar heat capacity C_p can be written in the following form:

Isobaric molar heat capacity.

$$C_p = \frac{\gamma}{\gamma - 1} k N_A \tag{108}$$

Here k is the Boltzmann's constant, N_A is the Avogadro constant, and γ is a Poisson coefficient. The Poisson coefficient is equal to $\gamma = (f+2)/f$, where f is the number of degrees of freedom of the particles in the gas. For example, for an atomic gas, such as He or Ar, $\gamma = 5/3$. For diatomic molecules, such as H_2 or N_2 $\gamma = 7/5$. The Poisson coefficient gets smaller for more complex molecules converging to 1.

Combining Eq. 106, 107 and 108 an equation for the velocity of the centre of mass of particles in the beam $\langle v\rangle$ is derived:

Centre of mass velocity in the molecular beam.

$$\langle v\rangle = \sqrt{\frac{2\gamma}{\gamma - 1}\frac{k(T_0 - T_1)}{m}} \tag{109}$$

Then the maximum velocity of the centre of mass of the particles in the beam $\langle v\rangle_{max}$ can be calculated as:

Centre of mass maximum velocity.

$$\langle v\rangle_{max} = \lim_{T_1 \to 0} \langle v\rangle = \sqrt{\frac{2\gamma}{\gamma - 1}\frac{kT_0}{m}} \tag{110}$$

The mean value of the velocity distribution of particles in the beam is equal to the velocity of the centre of mass $\langle v\rangle$, while the standard deviation of the distribution is equal to standard deviation of the Maxwell – Boltzmann distribution at the beam temperature T_1 (see Eq. 103). In the limit of $T_1 \to 0\,K$ the velocity distribution is equivalent to a delta function $\delta(\langle v \rangle_{max})$.

For real gases the difference in the enthalpy of the system due to expansion ΔH can not be completely transformed into kinetic energy of particles in the beam. This results in a slight deviation of the centre of mass velocity in the beam $\langle v \rangle$ achieved in experiments from the values calculated according to Eq. 110.

As visible from Eq. 109, the centre of mass velocity in a molecular beam $\langle v \rangle$ depends on the square root of the particle mass. This effect can be used for controlling $\langle v \rangle$ by using a mixture of gases with different masses. Then the centre of mass velocity $\langle v \rangle$ can be calculated applying an average mass $m_{ave} = \frac{m_1 n_1 + m_2 n_2}{n_1 + n_2}$ instead of m in Eq. 109. Here $m_{1,2}$ and $n_{1,2}$ are the masses and numbers of particles of the two gases in the mixture, respectively. For example, adding light gases, such as He, in a mixture would increase the centre of mass velocity $\langle v \rangle$ and vice versa.

4.3.2 *Supersonic molecular beam*

In the present section the technical implementation of a supersonic molecular beam is described. The given discussion partially follows the textbook by G. Scoles [148]. In Fig. 34 a schematic view of the molecular beam source is shown. It consists of a gas reservoir and four separate vacuum chambers: an *expansion* chamber, a *differential pumping* chamber, a *main* chamber, and a *beam dump* chamber.

Gas filling the reservoir at initial temperature T_0 and pressure p_{jet} is expanding through a small orifice into the first vacuum chamber — the *expansion* chamber. The pumping capacity of the vacuum pumps installed on the *expansion* chamber should be sufficient for compensating for the gas inlet from the reservoir, since only a small fraction of it is forming the molecular beam delivered to the experiment.

In the *expansion* chamber a *zone of silence* is formed. It is a region where the velocity of gas particles exceeds the local speed of sound $v_{sound} = \sqrt{\gamma k T / m}$. During further expansion the pressure of the gas decreases, until it becomes comparable with the background pressure p_{back} in the chamber. Then the number of interactions between particles from the expanding beam and the background is significantly increasing, which results in a disturbance of the velocity distribution of the particles in the beam. The surface confining the *zone of silence* can be separated in two parts: a cylindrically symmetric surface with axis of symmetry parallel to the molecular beam axis called *barrel shock*, and a plane perpendicular to the molecular beam called *Mach*

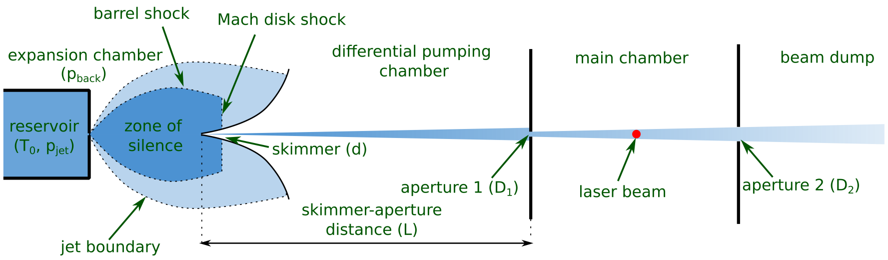

Figure 34: Schematic view of a supersonic molecular beam along the molecular beam axis. A detailed description is given in the main text. The scheme is partially adapted from [148].

Mach disk distance.

disk. The distance form the orifice to the *Mach disk* x_{Md} is described by the following formula:

$$x_{Md} = 0.67 d_{res} \sqrt{\frac{p_{res}}{p_{back}}} \tag{111}$$

Here d_{res} is the diameter of the orifice on the reservoir, and p_{res} and p_{back} are pressures in the reservoir and the *expansion chamber*, respectively. In real applications the Mach disk distance x_{Md} is in a range from a few to a few tens of mm.

In order to preserve conditions similar to the *zone of silence* at distances exceeding the Mach disk distance a skimmer is used. A skimmer is a "funnel" shape piece with a small orifice on the tip with typical diameter on the order of a few hundreds of µm. The skimmer shape is specially designed such that the gas particles scattered on a skimmer surface are not reflected backwards, so they do not disturb the incoming molecular beam. The skimmer is positioned so that it penetrates the *Mach disk shock* and enters the *zone of silence*. A fraction of the expanding gas is transmitted through the orifice on the skimmer tip and enters the second vacuum chamber — the *differential pumping* chamber. The vacuum conductance of an orifice C [l/s] is defined as $C = \frac{q}{\Delta p}$, where q [bar · l/s] is the amount of gas transmitted trough the orifice per unit of time, and Δp [bar] is the pressure difference between the two sides of the orifice. In the molecular flow regime — conditions at which the probability of a particle collision is substantially lower than that of a particle interaction with the chamber walls, the vacuum conductance of an orifice can be calculated according to the following formula:

Vacuum conductance of an orifice.

$$C = \frac{\pi d^2 \langle v \rangle}{16 \cdot 10^8} \tag{112}$$

Here d is the diameter of the orifice [µm], and $\langle v \rangle$ [m/s] is the mean particle velocity. For a skimmer penetrating into the *zone of silence* $\langle v \rangle$ is equal to the velocity of the centre of mass in the beam, that can be calculated according to Eq. 109.

Due to relatively low gas input, the pressure in the *differential pumping* chamber can be kept multiple orders of magnitude lower than in the *expansion* chamber. Then the mean free path of gas particles in the *differential pumping* chamber is comparable with the chamber size. This results in a relatively low number of interactions between the particles in the molecular beam and the background gas. Thus, the velocity distribution in the beam is not disturbed.

The pressure in the *differential pumping* chamber is typically still too high for experiments. Due to that, the *main* chamber containing the interaction region is separated from the *differential pumping* chamber by an *aperture 1* (see Fig. 34) with diameter D_1 on the order of one mm. This aperture not only allows reaching multiple orders of magnitude lower pressure in the *main* chamber than in the *differential pumping* chamber, but also limits the maximum perpendicular velocity with respect to the beam axis $v_{max\perp}$. For a simple geometrical reason $v_{max\perp}$ can be approximated as:

Maximum velocity perpendicular to the beam axis.

$$v_{max\perp} = \frac{D_1 \langle v \rangle}{L} \tag{113}$$

Here L is the distance between the skimmer orifice and *aperture 1* (see Fig. 34), and $\langle v \rangle$ is the velocity of the centre of mass in the beam. The velocity distribution of gas particles in the interaction region in the *main* chamber is described by Eq. 109 and 113. In some setups a second *differential pumping* chamber is required in order to reach the required vacuum conditions in the *main* chamber.

After the *main* chamber the molecular beam is transmitted into the last vacuum chamber — the *beam dump* chamber. The diameter of *aperture 2* D_2 separating the *main* chamber and the *beam dump* should be slightly bigger than the cross section of the molecular beam in order to avoid back scattering of gas particles into the *main* chamber.

The molecular beam source described in the present section allows the creation of a supersonic molecular beam providing a dense gas target with a narrow particle momentum distribution for the experiments.

4.3.3 *Molecular beam source design*

In the present section the new molecular beam source developed as a part of the present work is described. It was used for the experiments reported in the present thesis. The setup is a redesign of the original molecular beam source developed by S. Birkner described in [143].

A slice through a CAD model of the new molecular beam source is shown in Fig. 35. The aim of the new design was to increase the target gas density in the interaction region of the ReMi. This was achieved by implementing two independent modifications: the distance between the jet and the interaction region was reduced almost

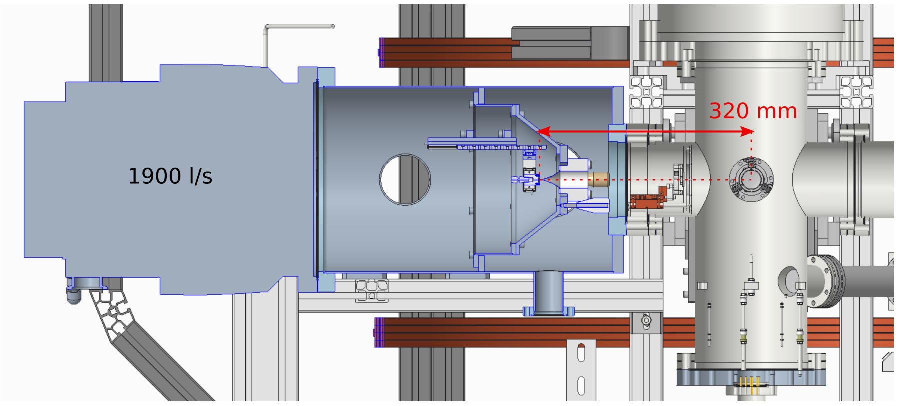

Figure 35: A slice through a CAD model of the new molecular beam source along the molecular beam axis. The CAD model was developed by Oliver Reichel.

to half, 320 mm, and the pumping speed of the turbo pump installed on the *expansion* chamber was increased up to 1900 l/s (HiPace 2300, Pfeiffer). The latter allows using relatively big nozzle diameters and applying pressures up to a few bar in the jet. In the present setup the nozzle diameter is 50 μm.

In the setup a skimmer with a 300 μm diameter aperture is installed on a cone shaped wall separating the *expansion* and the *differential pumping* chambers (see Fig. 35). This configuration allows positioning the nozzle closer to the interaction region without reducing the effective pumping speed of the turbo pumps installed on the *differential pumping* chamber. Also, this cone shape reduces the probability of back scattering of gas particles from the molecular beam.

The gas jet is installed on a three-dimensional manipulator (custom made assembly based on the SLC24-S-HV linear stage, SmarAct). It allows changing the position of the nozzle with respect to the skimmer during the operation. As discussed in Section 4.3.2, in order to form a supersonic molecular beam, the skimmer has to penetrate into the *zone of silence* (see Fig. 34). The optimal conditions are achieved when the nozzle–skimmer distance is a fraction of the corresponding Mach disk distance (see Eq. 111).

In order to define the optimum nozzle–skimmer distance for the molecular beam source a measurement was performed in N_2 with attosecond pulse trains. Separation of the signals corresponding to the molecular beam and the background gas ionization was performed based on the ion impact position on the detector as shown in Fig. 36. Ions originating from the molecular beam arrive at the detector in a confined area with a size dictated by the velocity distribution of the particles in the molecular beam. This area is shifted with respect to the laser beam (parallel to the y-axis) along the molecular beam axis x by $x_{beam} = \langle v \rangle \cdot t_{TOF}$, where $\langle v \rangle$ is the centre of mass velocity in the molecular beam and t_{TOF} is the ion time-of-flight. Thus, from

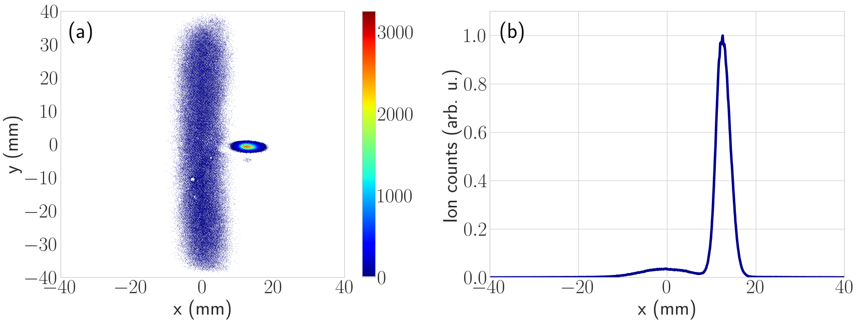

Figure 36: *(a)* The ion impact position distribution on the ion detector. The bright area shifted along the x-axis (molecular beam axis) by approximately 12 mm corresponds to ions originating from the molecular beam, while the broad line parallel to the y-axis (laser beam) corresponds to background gas ionization. *(b)* The ion signal shown in *(a)* integrated over $y \in [-4, 4]$ mm range. The peaks centred at 0 and 12.6 mm correspond to the background and molecular beam ionization, respectively.

the absolute value of the shift x_{beam} and the ion time-of-flight t_{TOF}, $\langle v \rangle = x_{beam}/t_{TOF}$ can be approximated. For the dataset shown in Fig. 36 x_{beam} = 12.6 mm and t_{TOF} = 17 µs, which corresponds to $\langle v \rangle$ = 741 m/s. According to Eq. 109, this centre of mass velocity corresponds to a temperature in the molecular beam T_1 = 28 K ($\gamma = 7/5$ and the molar mass is 28 g/mol for a nitrogen molecule, the initial temperature of the gas in the reservoir is approximated as 293 K). An alternative estimation of the molecular beam temperature can be performed from the width of the peak corresponding to the impact of ions originating from the molecular beam along the x-axis Δx using Eq. 105. In the present case Δx = 4.0 mm, which corresponds to a FWHM of the velocity distribution $FWHM = 236$ m/s and T_1 = 34 K. Ions originating from the background appear in Fig. 36 (a) as a line parallel to the laser beam. A "checker board" pattern on the ion impact distribution is due to electrostatic micro lensing induced by the mesh installed on the ion detector.

In Fig. 37 (a) the number of ions originating from the molecular beam and background ionization detected over a 10 min long measurements are plotted as a function of nozzle–skimmer distance for 0.6 bar and 2.0 bar pressures in the jet. Assuming that the XUV photon flux was constant over all measurements, the number of counts corresponding to the molecular beam is proportional to the gas density in the interaction region, while the number of background counts is proportional to the pressure in the *main* chamber (Eq. 97). The number of molecular beam counts depends linearly on the distance for both pressures in the reservoir. For nozzle–skimmer distances exceeding 20 mm, the number of background counts also shows a linear dependence. The trend is changing for nozzle–skimmer distances below

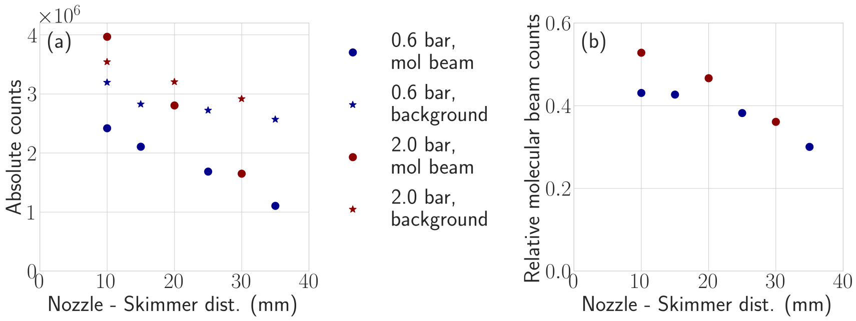

Figure 37: *(a)* Absolute number of ion counts corresponding to the molecular beam ionization (dots) and the background gas ionization (stars) as a function of the nozzle-skimmer distance at two different pressures in the jet: 0.6 bar and 2.0 bar shown in blue and red, respectively; *(b)* fraction of the total number of counts corresponding to the molecular beam ionization. The signal was integrated over a 10 min measurement.

20 mm as shown in Fig. 37 (a) from a curve corresponding to 0.6 bar in the jet. This effect is a result of a pressure growth in the *main* chamber of the Reaction Microscope.

In Fig. 37 (b) the molecular beam to total count ratio as a function of nozzle–skimmer distance is shown. Decreasing the nozzle–skimmer distance the relative amount of counts corresponding to the molecular beam ionization is increasing reaching saturation around 10 mm as visible from the measurement performed at 0.6 bar in the reservoir. The saturation is not reached in the measurement performed at 2.0 bar in the reservoir, since at that pressure it occurs at a shorter nozzle–skimmer distance. The shift of the distance corresponding to the molecular beam to background count ratio saturation as a function of the pressure in the reservoir can be explained by the pressure dependence of the Mach disk distance (see Eq. 111). The pressures in the *expansion* chamber are equal $8.5 \cdot 10^{-5}$ mbar and $3.2 \cdot 10^{-4}$ mbar at 0.6 bar and 2.0 bar pressures in the reservoir, respectively. For a 50 µm diameter orifice that corresponds to 89 mm and 81 mm Mach disk distances respectively. Since, in general, the saturation is reached at a nozzle–skimmer distance proportional to the corresponding Mach disk distance, this distance is shorter at 2.0 bar in the reservoir than at 0.6 bar, which is in agreement with the experimental results shown in Fig. 37 (b).

At optimal conditions the gas target density obtained with the present molecular beam source was estimated to be on the order of 10^{11} particles/cm^3. This is up to two orders of magnitude higher density in comparison with the old molecular beam source [143].

4.4 CHARGED PARTICLE TRAJECTORIES

In photoionization experiments performed using a Reaction Microscope as a detecting system, charged particles resulting from the interaction of the atomic or molecular target with ionizing radiation are propagating in homogeneous collinear static electric and magnetic fields. In what follows these two fields are referred to as E and B fields, respectively. The E field is guiding charged particles along the $\vec{E}$ vector towards the two respective detectors. The B field is required in order to collect photoelectrons with large momentum components perpendicular to the E field. Using an MCP–delay line anode assembly detector, for each detected charged particle the following quantities are measured:

Experimentally measured quantities.

- a time-of-flight assigned in what follows as T,
- a 2D impact coordinate on the detector assigned in what follows as $x_T = x(T)$ and $y_T = y(T)$.

The initial momentum of a particle after ionization can be unambiguously reconstructed from this set of quantities.

Let us define a Cartesian coordinate system O with respect to the Reaction Microscope as follows (see Fig. 31):

Cartesian coordinate system.

- x-axis: molecular beam axis parallel to $\langle\vec{v}\rangle$,
- y-axis: laser beam axis parallel to laser photon $\vec{k}$,
- z-axis: spectrometer axis towards the ion detector parallel to $\vec{E}$ and $\vec{B}$.

The coordinate system O is a laboratory frame coordinate system used in the coincidence detection experiments reported in the present thesis.

In the present section the initial momentum reconstruction routines are discussed. Starting from a description of charged particle trajectories in the Reaction Microscope given in Section 4.4.1, the initial momentum reconstruction equations are derived in Section 4.4.2. Since the effect of the B field on the ion trajectories is negligible, a set of simplified equations for the initial ion momentum reconstruction is given in Section 4.4.3.

4.4.1 *Motion of a particle in cylindrical coordinate system*

In order to illustrate the charged particle trajectories in the Reaction Microscope it is advantageous to describe them in cylindrical coordinate system. Such a description gives a simple explanation to the mechanisms determining different features, such as magnetic nodes, observed in the measured data. In the present section a set of equations describing the motion of a charged particle in collinear homogeneous E and B fields in a cylindrical coordinate system O_{cyl} is derived. The cylindrical coordinate system O_{cyl} can be obtained from the laboratory Cartesian coordinate system O defined in Section 4.4 as follows:

Cylindrical coordinate system.

- z-axis: spectrometer axis towards the ion detector parallel to $\vec{E}$ and $\vec{B}$,
- $\vec{r} = x \cdot \vec{e_x} + y \cdot \vec{e_y}$: radial coordinate of a particle in the detector plane with $r = 0$ corresponding to the projection of the interaction region on the detector along the z-axis (here $\overrightarrow{e_{x,y}}$ are the Cartesian basis vectors),
- the origin $(0, 0)$ is fixed to the interaction region.

As a first-order approximation, we assume that the E and B fields are exactly collinear and perpendicular to the detector plane. Then, for $\vec{r}$ and z components in the coordinate system O_{cyl}, the equation of motion of a particle with charge q and mass m has the form (here $\times$ stands for vector multiplication):

Equation of motion.

$$\begin{cases} m\ddot{z}(t) & = q \cdot E \\ m\ddot{\vec{r}}(t) & = q \cdot \dot{\vec{r}}(t) \times \vec{B} \end{cases} \tag{114}$$

A schematic view of the corresponding particle trajectory in the detector plane is shown in Fig. 38. Since $\vec{B}$ is perpendicular to the detector plane, $|\dot{\vec{r}}(t) \times \vec{B}| = |\dot{\vec{r}}(t)| \cdot |B|$ at any t. Also, since $\ddot{\vec{r}}(t) \perp \dot{\vec{r}}(t)$ at any t, $|\dot{\vec{r}}(t)| = const(t)$. In the detector plane a charged particle is moving along a circular orbit with constant velocity and period equal to a cyclotron period T_{cycl} defined as:

Cyclotron period.

$$T_{cycl} = 2\pi \frac{m}{|qB|} \tag{115}$$

The complete equation describing the charged particle trajectory in the coordinate system O_{cyl} has the following form (for an explicit derivation please refer to Section A.1.1):

Charged particle motion in cylindrical coordinate system.

$$\begin{cases} z(t) & = \frac{qE}{2m} \cdot t^2 + \frac{p_{0\,z}}{m} \cdot t \\ |\vec{r}(t)| & = \sqrt{2 \cdot \frac{|\vec{p}_{0\,\vec{r}}|}{|qB|} \cdot \left(1 - \cos\left(\frac{|qB| \cdot t}{m}\right)\right)} \end{cases} \tag{116}$$

Here $p_{0\,z}$ and $\vec{p}_{0\,\vec{r}}$ are the charged particle z and $\vec{r}$ initial momentum components, respectively.

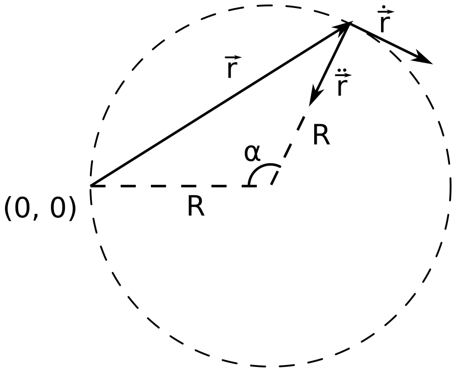

Figure 38: Schematic view of a charged particle motion in the detector plane. The origin of the coordinate system O_{cyl} is fixed to an interaction region labelled as $(0, 0)$. R represents a radius of the charged particle circular trajectory. Charged particle position, velocity and acceleration are shown on the scheme as $\vec{r}$, $\dot{\vec{r}}$ and $\ddot{\vec{r}}$, respectively.

For heavy particles with relatively low charge to mass ratio, such as ions or ionic fragments, the cyclotron period T_{cycl} is big comparing with the T_{cycl} of photoelectrons (Eq. 115). If the cyclotron period T_{cycl} of a charged particle substantially exceeds its time-of-flight T ($T \ll T_{cycl}$), the particle trajectory in the detector plane can be approximated as a linear motion with velocity $\dot{\vec{r}} = \frac{\vec{p}_{0\vec{r}}}{m}$. Then the equation describing the approximate trajectories of ions or ionic fragments in the Reaction Microscope has the following form:

Ion motion in cylindrical coordinate system.

$$\begin{cases} z(t) & = \frac{qE}{2m} \cdot t^2 + \frac{p_{0z}}{m} \cdot t \\ \vec{r}(t) & = \frac{\vec{p}_{0\vec{r}}}{m} \cdot t \end{cases} \tag{117}$$

This equation corresponds to a simple ballistic parabolic trajectory in the plane containing both $\vec{p}_{0\vec{r}}$ and the z-axis.

In order to illustrate the electron trajectories in the Reaction Microscope, a simple calculation modelling the detection of photoelectrons resulting from single XUV photon ionization of Ar was performed. For this calculation the distance between the interaction region and the photoelectron detector $z_{det} = 400\,\text{mm}$ and the detector diameter $D_{det} = 80\,\text{mm}$ were applied. These parameters correspond to the Reaction Microscope used for the experiments reported in the present thesis. The XUV photon spectrum used for the calculation consists of odd high-order harmonics of the 800 nm fundamental wavelength (corresponding to 1.55 eV photon energy) from 11^{th} up to 23^{d}. For simplicity, the harmonic spectral lines were approximated as monoenergetic spectral lines, which corresponds to an ideal case of an infinitely long pulse train. Photoelectrons are ionized from the $3p^6$ orbital of Ar with ionization potential Ip = 15.76 eV (see Section 2.3.3). For each resulting photoelectron energy a spherical angular momentum distribution was created and projected onto the coordinate sys-

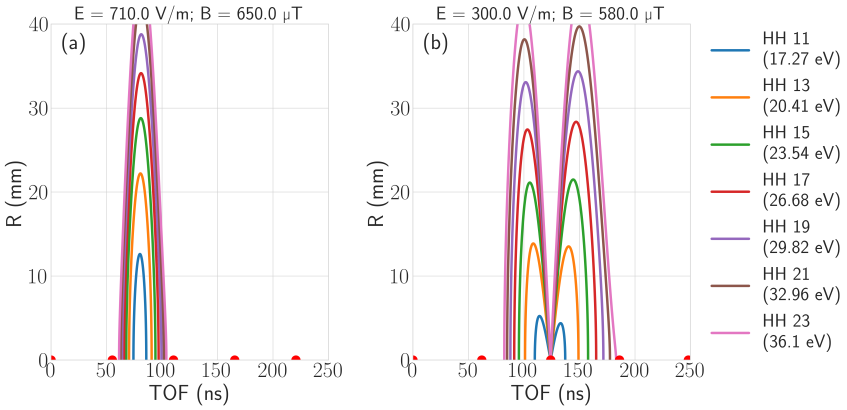

Figure 39: The radial position of impact as a function of time-of-flight for photoelectrons ionized from the $3p^6$ orbital of Ar (Ip = 15.76 eV) with high-order harmonics of 800 nm fundamental wavelength propagating in E and B fields with 710 V/m and 650 µT, and 300 V/m and 580 µT strengths shown in *(a)* and *(b)*, respectively. Red dots represent the magnetic nodes.

tem O_{cyl}. For the resulting z and $\vec{r}$ initial momentum components $p_{0\,z}$ and $|\vec{p}_{0\,\vec{r}}|$, photoelectron trajectories were calculated according to Eq. 116. The photoelectron radial position of impact on the detector $R(|\vec{p}_{0\,\vec{r}}|)$ together with the time-of-flight T were calculated according to the following consideration:

Photoelectron impact position.

$$\begin{cases} z(p_{0\,z}, T) & = z_{det} \\ R(|\vec{p}_{0\,\vec{r}}|) & = |\vec{r}(|\vec{p}_{0\,\vec{r}}|, T)| \end{cases} \tag{118}$$

In Fig. 39 the calculated dependence of the radial position of the photoelectron impact on the detector $R(|\vec{p}_{0\,\vec{r}}|)$ on the time-of-flight T is shown for two different E and B fields. Applying 710 V/m and 650 µT the full photoelectron distribution fits in between the adjacent nodes depicted in Fig. 39 (a) as red dots (corresponding T_{cycl} = 55 ns). On the other hand, in that case photoelectrons ionized with high-order harmonics 21 and 23 with dominant $|\vec{p}_{0\,\vec{r}}|$ momentum component are not detected since for them $R(|\vec{p}_{0\,\vec{r}}|)$ exceeds the MCP radius.

The reconstructed momentum resolution is defined by the time-of-flight and the impact position measurement resolution. For the detectors and fast electronics used in the present setup, the time-of-flight and impact position measurement resolution is on the order of 0.1 ns and 0.1 mm, respectively. Since the initial momentum reconstruction equations (see Eq. 121 and 122) are mapping the time-of-flight and impact position space $\{T, R(|\vec{p}_{0\,\vec{r}}|)\}$ onto the initial momentum space $\{\vec{p}_0\}$, it is advantageous to adjust the E and B fields such that the measured photoelectron distribution spans the whole detector surface and has as long as possible time-of-flight range. In Fig. 39 (b) the same photoelectron distribution as in Fig. 39 (a) detected with 300 V/m and 580 μT is shown. At lower fields it is spanning over an approximately twice broader time-of-flight range, which increases the $p_{0\,z}$ initial momentum component resolution almost twice. This momentum resolution enhancement comes at the expense of information on the part of the photoelectron distribution overlapping with a node, which is inevitable since in that case T_{cycl} is smaller than the full TOF distribution range.

In the experiment the applied E and B fields are defining the time-of-flight range the measured photoelectron distribution spans and the cyclotron period T_{cycl} corresponding to separation between two adjacent nodes, respectively. Thus, they can be adjusted for each particular experiment based on the properties of the photoelectron distribution under investigation. For the measurements reported in the present thesis approximately 300 V/m and 580 μT were applied in order to increase the obtained $p_{0\,z}$ initial momentum component resolution. The photoelectron distribution detected with these fields contains one node as shown in Fig. 39 (b).

4.4.2 *Motion of a particle in Cartesian coordinate system*

In order to derive an equation for the charged particle initial momentum reconstruction from the measured time-of-flight and impact position $\{T,\ x_T,\ y_T\}$, one needs to use the equation of motion of a charged particle in homogeneous collinear E and B fields in a Cartesian coordinate system as a starting point. The charged particle initial momentum reconstruction routine is based on the assumption that the applied E and B fields are exactly collinear and perpendicular to the detector plane. The effect of E and B field noncollinearity on the reconstructed momentum resolution in the Reaction Microscope is discussed in Section 4.5.2.

The equation of motion of a charged particle with charge q and mass m in the Reaction Microscope in the laboratory Cartesian coordinate system O defined in Section 4.4 has the form (for an explicit derivation please refer to Section A.1.2):

Motion of a charged particle in Cartesian coordinate system.

$$\vec{x}(t) = \begin{pmatrix} x(t) \\ y(t) \\ z(t) \end{pmatrix} = \begin{pmatrix} \frac{1}{m\omega_c}(p_{0\,x}\cdot\sin\omega_c t - p_{0\,y}\cdot\cos\omega_c t + p_{0\,y}) + x_0 \\ \frac{1}{m\omega_c}(p_{0\,y}\cdot\sin\omega_c t + p_{0\,x}\cdot\cos\omega_c t - p_{0\,x}) + y_0 \\ \frac{q}{2m}E\cdot t^2 + \frac{1}{m}p_{0\,z}\cdot t + z_0 \end{pmatrix} \tag{119}$$

Here x_0, y_0 and z_0 are the coordinates of the interaction region, and $\omega_c = 2\pi/T$ is the cyclotron frequency. The initial momentum components $p_{0\,x}$, $p_{0\,y}$ and $p_{0\,z}$ can be reconstructed from the measured time-of-flight T and the impact position on the detector $x_T = x(T)$ and $y_T = y(T)$, while $z_T = z(T)$ corresponds to the detector coordinate along the z-axis. Let us have a look at a special case of a charged particle with zero initial momentum $\vec{p_0} = \vec{0}$. The equation of motion of a zero initial momentum particle has a form:

Zero initial momentum particle trajectory.

$$\begin{cases} x(t) & = x_0 \\ y(t) & = y_0 \\ z(t) & = \frac{q}{2m} E \cdot t^2 + z_0 \end{cases} \tag{120}$$

The time-of-flight of a zero initial momentum particle is assigned as T_0. Since $z(T) - z_0 = L$ — the distance from the interaction region to the detector plane, it is universal for all particles. Exploiting this universality and combining Eq. 119 with Eq. 120, an equation for the initial momentum z component $p_{0\,z}$ reconstruction can be derived:

$p_{0\,z}$ initial momentum component reconstruction.

$$p_{0\,z} = \frac{qE}{2} \frac{T_0^2 - T^2}{T} \tag{121}$$

The equation for the initial momentum x and y components $p_{0\,x}$ and $p_{0\,y}$ reconstruction has the form:

$p_{0\,x}$ and $p_{0\,y}$ initial momentum component reconstruction.

$$\begin{pmatrix} p_{0\,x} \\ p_{0\,y} \end{pmatrix} = \frac{m\omega_c}{2 \sin \frac{\omega_c T}{2}} \begin{bmatrix} \cos \frac{\omega_c T}{2} & -\sin \frac{\omega_c T}{2} \\ \sin \frac{\omega_c T}{2} & \cos \frac{\omega_c T}{2} \end{bmatrix} \times \begin{pmatrix} (x(T) - x_0) \\ (y(T) - y_0) \end{pmatrix} \tag{122}$$

For the initial momentum reconstruction the impact position of a zero initial momentum particle is applied as x_0 and y_0 into Eq. 122. In the experiments the time-of-flight T_0 and the impact position x_0, y_0 of a zero initial momentum particle are determined as the median of a measured particle distribution.

4.4.3 *Momentum reconstruction for ions*

For particles with small charge to mass ratio, such as ions or ionic fragments, the initial momentum reconstruction equations can be simplified. The kinetic energy of a particle with initial momentum p_0 equals $W_{init} = \frac{p_0^2}{2m}$. For ions W_{init} is small in comparison with the $W_{acq} = qEd_z$ — the energy acquired in the E field during the propagation from the interaction region towards the detector. Here d_z is the particle path along the z-axis. Then the difference between the times-of-flight of particles with zero and non-zero initial momenta is negligible, or in other words $T_0 \approx T$. Thus, the initial momentum z component reconstruction equation Eq. 121 can be rewritten as:

$p_{0\,z}$ initial ion momentum component reconstruction.

$$p_{0\,z} = \frac{qE}{2}\frac{(T_0+T)(T_0-T)}{T} \approx \frac{qE}{2}\frac{2T(T_0-T)}{T} = qE(T_0-T) \quad (123)$$

For ions the cyclotron period T_{cycl} defined in Eq. 115 can be approximated as ∞, and thus the corresponding cyclotron frequency $\omega_c \to 0$. Then the following limits are valid:

Negligibly small cyclotron frequency limit.

$$\begin{aligned} &\lim_{\omega_c T\to 0} \sin\frac{\omega_c T}{2} = \frac{\omega_c T}{2} \to 0 \\ &\lim_{\omega_c T\to 0} \cos\frac{\omega_c T}{2} = 1 \end{aligned} \quad (124)$$

Using these limits, the initial momentum x and y component reconstruction equation (see Eq. 122) can be simplified as follows, where I is the identity matrix:

$p_{0\,x}$ and $p_{0\,y}$ initial ion momentum component reconstruction.

$$\begin{pmatrix} p_{0\,x} \\ p_{0\,y} \end{pmatrix} = \frac{2m\omega_c}{2\omega_c T} \cdot I \times \begin{pmatrix} (x(T)-x_0) \\ (y(T)-y_0) \end{pmatrix} = \frac{m}{T}\begin{pmatrix} (x(T)-x_0) \\ (y(T)-y_0) \end{pmatrix} \quad (125)$$

4.5 FACTORS LIMITING THE PHOTOELECTRON MOMENTUM RESOLUTION

The photoelectron momentum resolution acquired with a Reaction Microscope is limited not only by the time-of-flight and position resolution of the respective detector, but also by errors induced by the initial momentum reconstruction routine. Since the time-of-flight and impact position of a zero initial momentum photoelectron applied into the momentum reconstruction equations as parameters are determined from the measured photoelectron distribution, they could slightly differ from their actual values. As a result, the reconstructed photoelectron momentum distribution is distorted. In Section 4.5.1 the effect of errors in the parameters applied in the initial photoelectron momentum reconstruction routine on the obtained momentum resolution is investigated.

The initial photoelectron momentum reconstruction equations (Eq. 121 and 122) are derived assuming that the E and B fields applied during the experiment are exactly collinear. In order to achieve that in real experiments, the tangential component of the magnetic field of the Earth should be compensated for. If the compensatory fields are not optimized, and thus the applied E and B fields are not collinear, the photoelectron trajectories in the Reaction Microscope are no longer described by Eq. 119. Application of conventional initial momentum reconstruction equations in that case results in distortions of the reconstructed photoelectron momentum distribution. In Section 4.5.2 the effect of noncollinear E and B fields on the obtained momentum resolution are discussed. The chapter is closed with a description of the compensatory and main B fields calibration routines given in Section 4.5.3 and Section 4.5.4, respectively.

4.5.1 *Distortions in the photoelectron momentum reconstruction*

The initial photoelectron momentum $\{p_{0x}, p_{0y}, p_{0z}\}$ can be reconstructed from the measured time-of-flight and impact position $\{T, x(T), y(T)\}$ using Eq. 121 and 122. The time-of-flight and impact position $\{T_0, x_0, y_0\}$ of a photoelectron with zero initial momentum enter the momentum reconstruction equations as parameters. They are defined from the measured time-of-flight and impact position distributions as their medians. Another two parameters entering the momentum reconstruction equations are encoding the E and B fields strengths. In the routine used for the reported experiments the E field strength [V/m] is directly applied into the momentum reconstruction equations. On the other hand, instead of the B field strength a cyclotron period T_{cycl} [ns] is applied into the equations. It is directly related to the B field strength as shown in Eq. 115. Since a set of five parameters $\{x_0, y_0, T_0, E, T_{cycl}\}$ is obtained from the mea-

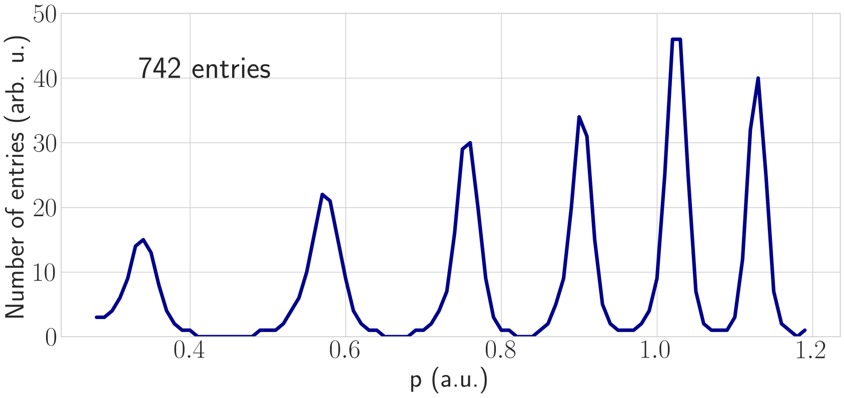

Figure 40: Momentum spectrum of the ensemble of photoelectrons used for the calculation. Contains 742 entries total.

sured distribution and applied fields, they can slightly deviate from their actual values. Thus, there is a non-zero difference between the 'exact' parameter value and the one used for the momentum reconstruction. In the present section these differences are assigned as $\{dx_0, dy_0, dT_0, dE, dT_{cycl}\}$. The difference da for a parameter a is defined as $da = a_{applied} - a_{'exact'}$.

In the present section the effect of non-zero $\{dx_0, dy_0, dT_0, dE, dT_{cycl}\}$ on the initial photoelectron momentum reconstruction is discussed. Photoelectron momentum distribution distortions corresponding to each of the parameters in the set are illustrated. In order to do that, a simulation of photoelectron propagation from the interaction region towards the detector in the Reaction Microscope was performed. Then, from the calculated $\{T, x(T), y(T)\}$ the initial momenta were reconstructed. Photoionization from the $3p^6$ orbital of Ar (Ip = 15.76 eV) with high-order harmonics from 11^{th} up to 21^{st} of the 800 nm fundamental wavelength was modelled. The photoelectron spectrum used for this calculation corresponds to a measured XUV photon spectrum with subtracted Ip of the $3p^6$ state in Ar. Thus, the calculated photoelectron spectrum is in agreement with the experimentally observed one up to the photoionization cross section of Ar, which was not taken into account in the present case. In order to perform the calculation on a single event basis, the modelled photoelectron spectrum was approximated as a sum of discrete events with 0.01 a.u. momentum step. The momentum spectrum of the resulting ensemble of photoelectrons containing 742 entries is shown in Fig. 40.

The calculation was performed for each photoelectron individually using two random value generation functions: 'random' and 'gauss' from the 'random' library in Python. These functions are returning pseudo random floating point values with a homogeneous distribution over a $[0.0, 1.0)$ range, or with a Gaussian probability distribution, respectively. They are incorporated in the calculation in order to simulate the angular momentum distribution, and the effect of a finite interaction region volume on the momentum reconstruction. For each photoelectron with momentum p_0 in the ensemble shown in Fig. 40 a set of 50 angles α between the $\overrightarrow{p_0}$ and the z-axis was prepared using the 'random' function. Then the initial photoelectron momentum components in the coordinate system O were calculated as:

$p_{0\,x}$ and $p_{0\,z}$ initial momentum component model.

$$\begin{cases} p_{0\,x} &= p_0 \cdot \sin\alpha \\ p_{0\,z} &= p_0 \cdot \cos\alpha \end{cases} \tag{126}$$

Due to cylindrical symmetry of the problem along the z-axis, the photoelectron trajectories along the x and y axes are identical. Thus, the calculation can be performed for a $\overrightarrow{p_0}$ lying in the x-z plane without loss of generality. Here the photoelectron momentum angular distribution inhomogeneity with respect to the laser polarization axis is neglected for simplicity. The resulting initial photoelectron momentum distribution in the x-z plane is shown in Fig. 41 (a). In order to simulate the effect of a finite interaction volume, the initial position $\{x_0, y_0, z_0\}$ for each photoelectron is calculated using a 'gauss' function. Since the beam diameter is estimated to be equal 100 µm, a 50 µm sigma was applied into the function.

First, the photoelectron momentum reconstruction was simulated for 710 V/m and 650 µT E and B fields. The corresponding photoelectron radial position of impact as a function of the time-of-flight is shown in Fig. 39 (a). The photoelectron trajectories were calculated according to Eq. 119. From these trajectories the impact position and the time-of-flight $\{x_T, y_T, T\}$ were determined for each photoelectron in the ensemble shown in Fig. 40, and for a zero initial momentum photoelectron $\{x_0, y_0, T_0\}$. T_{cycl} was calculated from the B field strength according to Eq. 115. Applying $\{x_0, y_0, T_0, E, T_{cycl}\}$ within the initial momentum reconstruction equations (Eq. 121 and 122), the initial photoelectron momentum distribution shown in Fig. 41 (b) was reconstructed.

In order to illustrate the effect of an error in each of the parameters $\{x_0, T_0, E, T_{cycl}\}$ on the reconstructed momentum distribution, the reconstruction was performed applying non-zero $\{dx_0, dT_0, dE, dT_{cycl}\}$. The effect of dx_0 and dy_0 is equivalent due to cylindrical symmetry of the problem. First, a $dx_0 = 2$ mm was applied within the momentum reconstruction equations, or in other words the x-axis impact position coordinate of a zero initial momentum photoelectron was overestimated by 2 mm. The resulting reconstructed photoelectron momentum distribution is shown in Fig. 41 (c). The reconstructed distribution is stretched along the I–III quadrant diagonal. For a negative dx_0, the reconstructed distribution is stretched along II–IV quadrant diagonal instead.

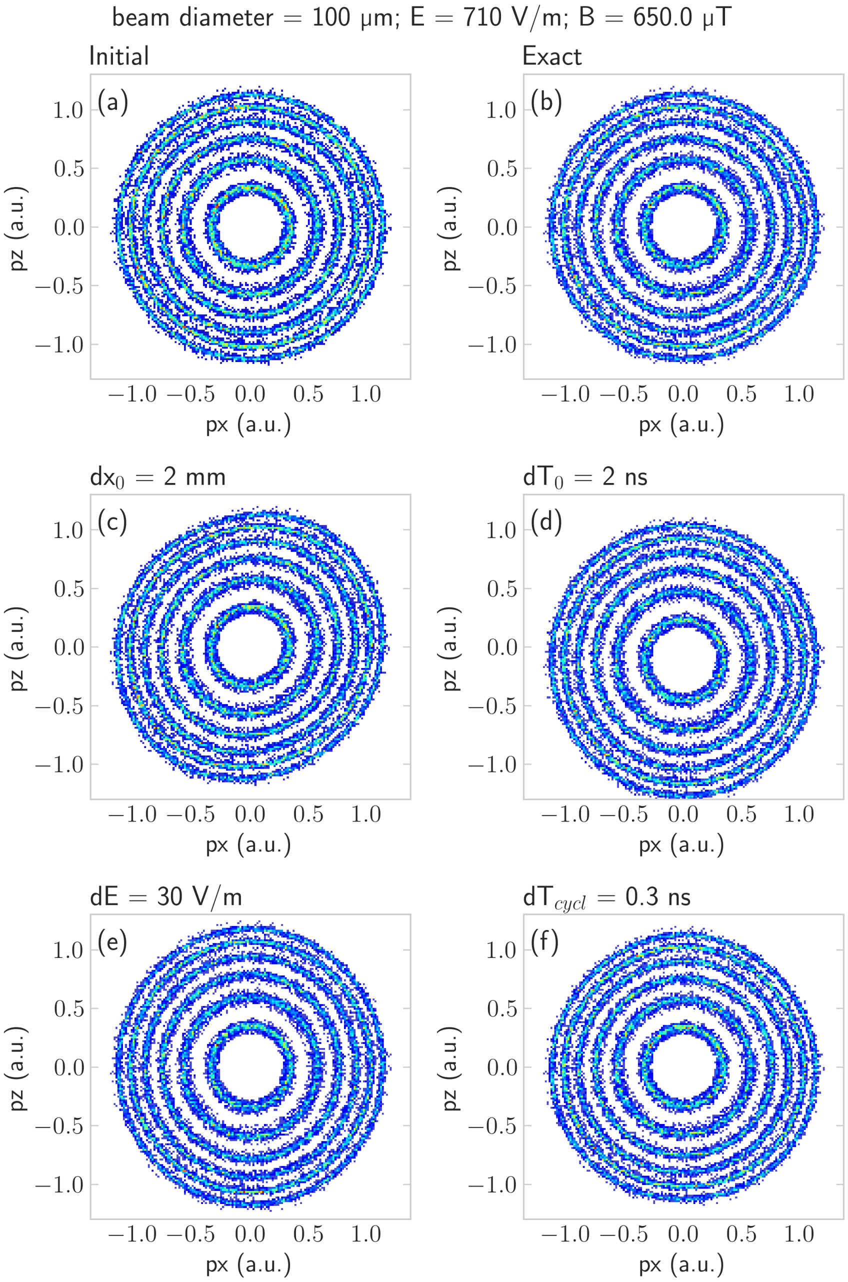

Figure 41: An x-z plane initial photoelectron momentum distribution *(a)*, a reconstructed distribution with the exact parameters *(b)*, with 2 mm error in x_0 *(c)*, with 2 ns error in T_0 *(d)*, with 30 V/m error in E *(e)* and with 0.3 ns error in T_{cycl} *(f)*. The applied E and B fields strengths are 710 V/m and 650 μT, respectively.

As a result of a non-zero dT_0, the reconstructed momentum distribution is shifted along the z-axis as shown in Fig. 41 (d). If the T_0 value is overestimated, the distribution is shifted towards negative p_z and vice versa. An error in the applied electric field strength dE stretches or squeezes the reconstructed distribution along the z-

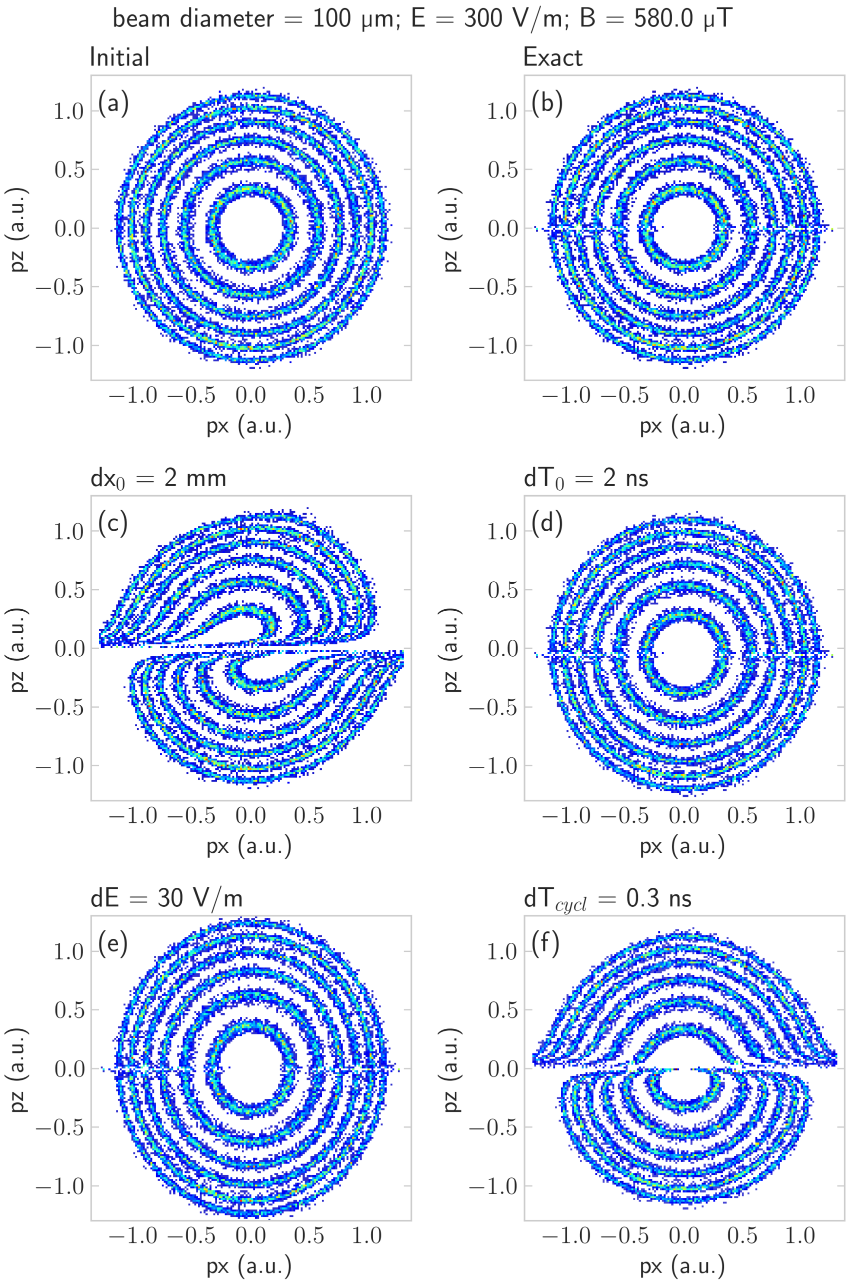

Figure 42: An x-z plane initial photoelectron momentum distribution *(a)*, a reconstructed distribution with the exact parameters *(b)*, with 2 mm error in x_0 *(c)*, with 2 ns error in T_0 *(d)*, with 30 V/m error in E *(e)* and with 0.3 ns error in T_{cycl} *(f)*. The applied E and B fields strengths are 300 V/m and 580 µT, respectively.

axis for overestimated or underestimated values of E, respectively, as shown in Fig. 41 (e). Finally, an overestimation of the cyclotron period dT_{cycl} deforms the reconstructed momentum distribution as shown in Fig. 41 (f). The initial momentum reconstruction is most sensitive to an error in T_{cycl}. In the experiments, T_{cycl} can be calculated from the value of the applied B field strength, but in general for the acquired one this way the precision is not sufficient. Thus, the final adjustments have to be performed based on the shape of the reconstructed photoelectron momentum distribution.

A similar simulation was performed for 300 V/m and 580 µT E and B fields strengths. The corresponding photoelectron radial position of impact as a function of the time-of-flight is shown in Fig. 39 (b). These conditions are close to those used for the experiments reported in the present thesis. Thus, the reconstructed photoelectron initial momentum distribution distortions shown in Fig. 42 are similar to those observed in the experiment. The information on photoelectrons with times-of-flight overlapping with a magnetic node is lost. In the momentum distribution reconstructed with the exact parameters, this corresponds to a line along the x-axis as shown in Fig. 42 (b). Close to the node the distortions induced by a non-zero dx_0 and dT_{cycl} are much more prominent. The distortions induced by a non-zero dT_0 and dE are not affected by the presence of a node.

The reported simulations are illustrating the distortions in the reconstructed photoelectron momentum distribution related to an error in different reconstruction parameters. Since the distortions related to each of the parameters are unique, their fine tuning can be performed based on the shape of the reconstructed momentum distribution, using the results shown in Figs. 41 and 42 as guidelines.

4.5.2 *Motion of a particle in noncollinear fields*

The initial photoelectron momentum reconstruction equations (Eq. 121 and 122) are derived assuming that the E and B fields applied during the experiment are exactly collinear. Thus, in case the applied $\vec{E}$ and $\vec{B}$ have a small angle between them, the reconstructed distribution is distorted. In the present section consequences of E and B fields noncollinearity on the photoelectron trajectories and initial momentum reconstruction are investigated. In order to do so, the equation of motion of a photoelectron is derived for the noncollinear E and B fields case.

In the present section the Cartesian laboratory coordinate system O defined with respect to the Reaction Microscope in Section 4.4.2 is used. The collinearity of the $\vec{E}$ and the z-axis is defined by the orientation of the electrode stack with respect to the detector plane in the ReMi. The effective $\vec{B}_{eff}$ field is defined not only by the orientation of the main magnetic field coils inducing $\vec{B}_{applied}$, but also includes a contribution of the magnetic field of the Earth $\vec{B}_{Earth}$. $\vec{B}_{Earth}$ has not only a component normal to the planets surface $B_{Earth,z}$, but also a non-zero tangential component $B_{Earth,\vec{r}}$. In Berlin the magnetic field of the Earth has a strength on the order of $B_{Earth} = 49.5\,\mu T$ at an inclination $\beta = 67°$ to the surface [149]. This corresponds to

$B_{\mathtt{Earth},z} = \sin(\beta) \cdot B_{\mathtt{Earth}} = 45.6\,\mu\mathrm{T}$ and $B_{\mathtt{Earth},\vec{r}} = \cos(\beta) \cdot B_{\mathtt{Earth}} = 19.3\,\mu\mathrm{T}$. The $B_{\mathtt{Earth},z}$ component is collinear with the applied magnetic field $\vec{B}_{\mathtt{applied}}$, so the effective B field in the experiment $B_{\mathtt{eff},z} = B_{\mathtt{Earth},z} + |\vec{B}_{\mathtt{applied}}|$. The $B_{\mathtt{Earth},\vec{r}}$ component could be compensated for using octagonal auxiliary coils (see Section 4.2.2). In case the compensatory magnetic field is not optimised, a non-zero $B_{\mathtt{eff},\vec{r}}$ component is present during the measurement.

Noncollinear E *and* B *fields*

In order to investigate the effect of a non-zero $B_{\mathtt{eff},\vec{r}}$ on the photoelectron trajectories the corresponding equation of motion has to be derived. In that case the $\vec{E}$ and $\vec{B}$ fields in the coordinate system O have a form:

$$\begin{cases} \vec{E} &= E \cdot \vec{e_z} \\ \vec{B} &= B_x \cdot \vec{e_x} + B_y \cdot \vec{e_y} + B_z \cdot \vec{e_z} \end{cases} \tag{127}$$

Coordinate system rotation angles

Let us define angles α and θ as follows:

$$\begin{cases} \sin\alpha &= \frac{B_y}{\sqrt{B_x^2+B_y^2}} \\ \cos\alpha &= \frac{B_x}{\sqrt{B_x^2+B_y^2}} \end{cases}, \quad \begin{cases} \sin\theta &= \frac{\sqrt{B_x^2+B_y^2}}{B} \\ \cos\theta &= \frac{B_z}{B} \end{cases} \tag{128}$$

Where $B = \sqrt{B_x^2 + B_y^2 + B_z^2}$ is the absolute strength of the magnetic field. The matrix R corresponding to transformation from the coordinate system O to the coordinate system O′, in which $\vec{B}$ is parallel to the z'-axis has a following form (for more details please refer to Section A.2):

$O \to O'$ *transformation*

$$\begin{aligned} R &= \begin{bmatrix} \cos\theta & 0 & -\sin\theta \\ 0 & 1 & 0 \\ \sin\theta & 0 & \cos\theta \end{bmatrix} \times \begin{bmatrix} \cos\alpha & \sin\alpha & 0 \\ -\sin\alpha & \cos\alpha & 0 \\ 0 & 0 & 1 \end{bmatrix} \\ &= \begin{bmatrix} \cos\theta\cos\alpha & \cos\theta\sin\alpha & -\sin\theta \\ -\sin\alpha & \cos\alpha & 0 \\ \sin\theta\cos\alpha & \sin\theta\sin\alpha & \cos\theta \end{bmatrix} \end{aligned} \tag{129}$$

Then the matrix R^{-1} corresponding to an inverse transformation from the coordinate system O′ to the coordinate system O has a form:

$O' \rightarrow O$ *transformation*

$$R^{-1} = \begin{bmatrix} \cos\alpha & -\sin\alpha & 0 \\ \sin\alpha & \cos\alpha & 0 \\ 0 & 0 & 1 \end{bmatrix} \times \begin{bmatrix} \cos\theta & 0 & \sin\theta \\ 0 & 1 & 0 \\ -\sin\theta & 0 & \cos\theta \end{bmatrix}$$
$$= \begin{bmatrix} \cos\theta\cos\alpha & -\sin\alpha & \sin\theta\cos\alpha \\ \cos\theta\sin\alpha & \cos\alpha & \sin\theta\sin\alpha \\ -\sin\theta & 0 & \cos\theta \end{bmatrix} = R^T \tag{130}$$

The equation describing a photoelectron trajectory in noncollinear E and B fields has a form (for an explicit derivation please refer to Section A.2):

Trajectory in noncollinear E and B fields

$$\vec{x}(t) = R^T$$
$$\times \begin{pmatrix} \frac{1}{m\omega_c}(p_{0\,x'} \cdot \sin\omega_c t - p_{0\,y'} \cdot \cos\omega_c t + p_{0\,y'}) + x'_0 + \frac{q}{m\omega_c^2} \cdot E_{x'} \cdot (1 - \cos\omega_c t) \\ \frac{1}{m\omega_c}(p_{0\,y'} \cdot \sin\omega_c t + p_{0\,x'} \cdot \cos\omega_c t - p_{0\,x'}) + y'_0 + \frac{q}{m\omega_c^2} \cdot E_{x'} \cdot (\sin\omega_c t - \omega_c t) \\ \frac{q}{2m} \cdot E_{z'} \cdot t^2 + \frac{1}{m} \cdot p_{0\,z'} \cdot t + z'_0 \end{pmatrix} \tag{131}$$

With the parameters defined as follows:

Initial conditions

$$\begin{cases} E_{x'} & = -\sin\theta \cdot E \\ E_{z'} & = \cos\theta \cdot E \end{cases} \tag{132}$$

$$\begin{pmatrix} p_{0\,x'} \\ p_{0\,y'} \\ p_{0\,z'} \end{pmatrix} = R \times \vec{p_0} = R \times \begin{pmatrix} p_{0\,x} \\ p_{0\,y} \\ p_{0\,z} \end{pmatrix} \tag{133}$$

$$\begin{pmatrix} x'_0 \\ y'_0 \\ z'_0 \end{pmatrix} = R \times \vec{x_0} = R \times \begin{pmatrix} x_0 \\ y_0 \\ z_0 \end{pmatrix} \tag{134}$$

Here $\vec{p_0}$ and $\vec{x_0}$ are the initial charged particle momentum and position in coordinate system O.

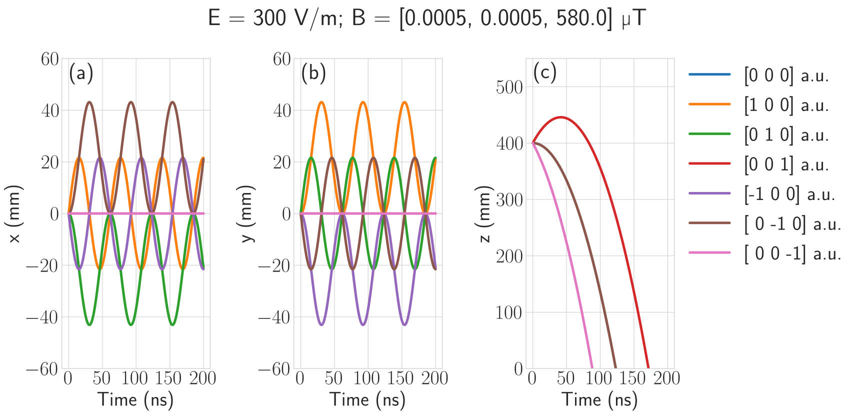

Figure 43: Photoelectron trajectories in the laboratory coordinate system O along x, y and z axes shown in *(a)*, *(b)* and *(c)*, respectively. The applied field $\vec{B} = [0.0005, 0.0005, 580]$ μT.

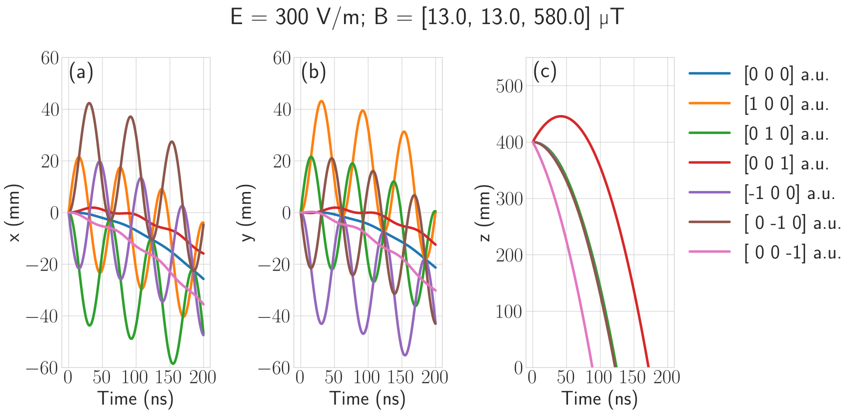

Figure 44: Photoelectron trajectories in the laboratory coordinate system O along x, y and z axes shown in *(a)*, *(b)* and *(c)*, respectively. The applied field $\vec{B} = [13, 13, 580]$ μT.

In order to illustrate the effect of E and B field noncollinearity on the photoelectron trajectories, they were calculated according to Eq. 131 for two different $\vec{B}$ fields. In Fig. 43 the resulting trajectories of photoelectrons with different initial momentum vectors $\vec{p_0}$ are shown for a case of a well-adjusted compensatory magnetic field. In other words, in this case the $B_{\vec{r}}$ component is 10^6 times smaller than the B_z component, which corresponds to almost perfectly collinear E and B fields. For the calculation the interaction region–photoelectron detector distance equal 400 mm was used. It corresponds to the dimensions of the ReMi used for the experiments reported in the present thesis. For simplicity, the photoelectron detector plane is positioned at $z = 0$. Thus, the interaction region is positioned at $(0, 0, 400)$ mm in order to preserve the orientation of the laboratory coordinate system O. The $x(t)$, $y(t)$ and $z(t)$ photoelectron trajectories are shown

p_0 (a.u.)	p reconstructed (a.u.)	error (%)
$[1, 0, 0]$	$[1.0, -4 \cdot 10^{-9}, 0.0]$	$5 \cdot 10^{-7}$
$[0, 1, 0]$	$[-4 \cdot 10^{-9}, 1.0, 0.0]$	$5 \cdot 10^{-7}$
$[0, 0, 1]$	$[5 \cdot 10^{-7}, -1 \cdot 10^{-6}, 1.0]$	0.04
$[-1, 0, 0]$	$[-1.00, 4 \cdot 10^{-10}, 0.0]$	$5 \cdot 10^{-7}$
$[0, -1, 0]$	$[4 \cdot 10^{-9}, -1.0, 0.0]$	$5 \cdot 10^{-7}$
$[0, 0, -1]$	$[8 \cdot 10^{-7}, 2 \cdot 10^{-7}, -1.0]$	0.04

Table 1: Momentum reconstruction errors for photoelectrons with different initial momentum p_0, travelling in a magnetic field $\vec{B} = [5 \cdot 10^{-4}, 5 \cdot 10^{-4}, 580]$ µT with respect to the laboratory frame coordinate system O.

p_0 (a.u.)	p reconstructed (a.u.)	error (%)
$[1, 0, 0]$	$[1.0, 0.002, 0.02]$	0.3
$[0, 1, 0]$	$[0.002, 1.0, 0.02]$	0.2
$[0, 0, 1]$	$[0.01, -0.03, 1.0]$	0.03
$[-1, 0, 0]$	$[-1.0, -0.005, -0.02]$	0.5
$[0, -1, 0]$	$[-0.005, -1.0, -0.02]$	0.6
$[0, 0, -1]$	$[0.02, 0.006, -1.0]$	0.3

Table 2: Momentum reconstruction errors for photoelectrons with different initial momentum p_0, travelling in a magnetic field $\vec{B} = [13, 13, 580]$ µT with respect to the laboratory frame coordinate system O.

in Fig. 43. From the photoelectron time-of-flight T — the time when $z(T) = 0$ in Fig. 43 (c), the impact position coordinates $x(T)$ and $y(T)$ were calculated. Then, the initial photoelectron momentum was reconstructed for each trajectory according to Eq. 164 and 170, applying the calculated time-of-flight and impact position of the $[0, 0, 0]$ a.u. initial momentum photoelectron as x_0, y_0 and T_0 parameters for the reconstruction.

A similar calculation was performed for the case of a $B_{\vec{T}}$ component equal to $B_{\mathrm{Earth}\,\vec{T}}$ in Berlin, which would correspond to a measurement performed without activating the auxiliary octagonal coils. The calculated photoelectron trajectories are shown in Fig. 44. As a result of the non-zero $B_{\vec{T}}$, the photoelectron trajectories are substantially distorted. As a first-order approximation, the photoelectron trajectories are shifted along the x- and y-axes in the direction opposite to the corresponding B field component.

The results of the initial momentum reconstruction for two different B fields are shown in Tab. 1 and 2. Without compensating for the Earth magnetic field tangential component $B_{Earth\,\vec{r}}$, even though the corresponding trajectories are significantly distorted, the errors in the photoelectron initial momentum reconstruction are below $1\,\%$.

4.5.3 *Compensatory* B *fields tuning*

In the present section practical recipes for the compensatory magnetic field tuning are discussed. The remaining $B_{\vec{r}}$ component results in a shift of the photoelectron trajectories in the x-y plane, as shown in Fig. 44. Thus, a compensated $B_{\vec{r}}$ component corresponds to photoelectron trajectories aligned along the z-axis. A suitable reference for the photoelectron trajectories determination are the magnetic nodes. In the measured photoelectron impact position distributions along x and y axes as a function of the time-of-flight the nodes are clearly visible, as shown in Fig. 45 (a). For the compensatory magnetic fields tuning it is advantageous to have as many nodes in the measured photoelectron distribution as possible. In order to achieve that, the applied E field strength should be reduced as much as possible (see Fig. 39). In the reported Reaction Microscope, the voltages applied to the spectrometer stack are constrained by the voltages applied to the MCP front of the photoelectron detector, which in the present case is on the order of $+100\,\mathrm{V}$. The voltage applied to the positive (photoelectron) side of the spectrometer stack is dictated by the geometrical properties of the ReMi, and has to be adjusted such, that the E field is homogeneous over the whole photoelectron trajectory. If this condition is violated, an electrostatic lens affecting the obtained photoelectron momentum resolution is created between the last electrode on the stack and the MCP front. The voltage applied to the negative (photoion) side of the electrode stack can be reduced down to approximately $-10\,\mathrm{V}$. The creation of an electrostatic lens on the ion detector side of the stack is prevented by a mesh installed between the last electrode and the ion detector MCP.

In order to increase the number of the magnetic nodes contained in the photoelectron TOF range, the applied main B field strength should be increased as high as possible. It is constrained only by the specs of the DC current supply for the main magnetic field coils. For the measurement shown in Fig. 45, a $0.9\,\mathrm{mT}$ B field was applied. Since relatively high magnetic fields correspond to small cyclotron periods T_{cycl} (Eq. 115), the number of nodes observed in the measured photoelectron distribution is big enough to perform a linear fit along them. If the magnetic field of the Earth tangential component $B_{\vec{r}}$ is properly

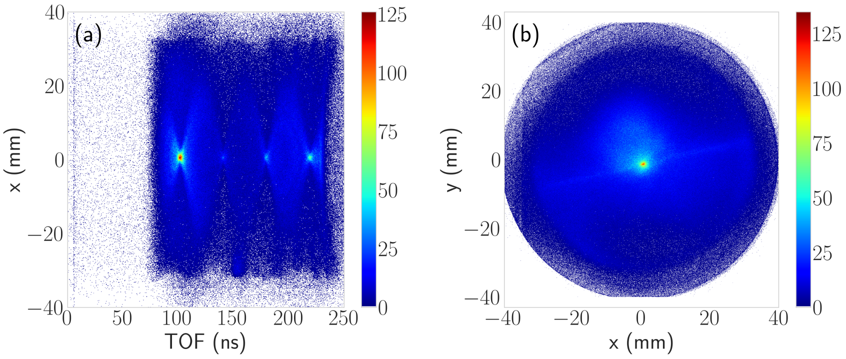

Figure 45: Example of a measured photoelectron x-axis impact position distribution as a function of the time-of-flight *(a)* and the corresponding x-y impact position coordinates *(b)*. The measurement was performed in Ar with XUV APTs. The applied fields were $E = 225\,\mathrm{V/m}$, $B = 900\,\mu\mathrm{T}$ (corresponding to $T_{cycl} = 39.5\,\mathrm{ns}$).

compensated, the fitted line should be parallel to the time-of-flight axis.

As visible from Eq. 128, the photoelectron trajectory distortions depend on the ratio between the $B_{\vec{r}}$ and B_z components. This means that the effect is stronger for lower applied $B_{applied}$ field. In order to further reduce $B_{\vec{r}}$, one has to decrease $B_{applied}$. At least one node has to be present in the measured photoelectron time-of-flight range. The E field can be slightly adjusted in order to fulfil this requirement. This node should lay on the same line as the nodes measured at higher $B_{applied}$ field. In order to acquire the required precision, measurements at high and low $B_{applied}$ field can be performed iterationally.

The main disadvantage of the suggested method for compensatory magnetic field adjustment is that it requires recording and processing of a separate dataset for each applied E and B fields strengths, which can be time consuming. A faster option is to use a photoelectron x-y impact position distribution, as shown in Fig. 45 (b), available live in COBOLD software (RoentDek). In this projection a magnetic node looks like a bright spot in the centre of the photoelectron distribution. The E and B fields can be scanned over a range in which at least one node is present in the measured photoelectron distribution. If the E and B fields are collinear, the magnetic node x-y position remains constant as a function of the applied field strength.

4.5.4 *Main B field calibration*

In the present section practical recipes for the main magnetic field calibration are discussed. In the experiments the current I applied to the main magnetic field coils is controlled. It is defining the applied B

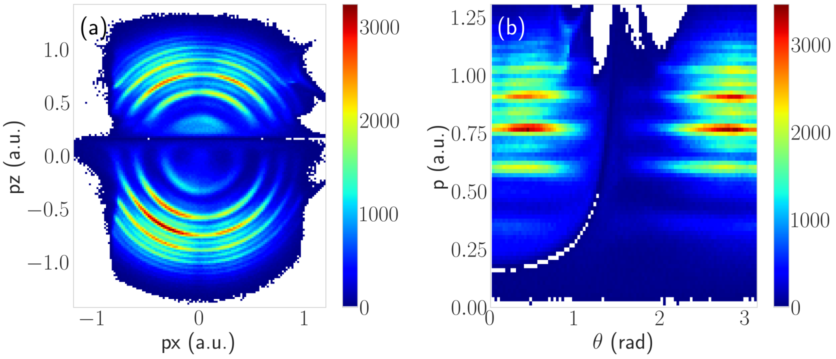

Figure 46: A slice through the measured photoelectron momentum distribution along the x-z plane in the laboratory Cartesian coordinate system, where the z-axis is parallel to the laser polarization *(a)*, and in the polar coordinate system *(b)*. The angle θ is defined with respect to the z-axis. The measurement was performed in Ar with XUV APTs.

field strength. Thus, a relation between the two has to be derived. The T_{cycl} measured as the time-of-flight difference between two adjacent magnetic nodes, as shown in Fig. 45, is directly related to the B field strength (see Eq. 115). The T_{cycl} dependence on the applied current I has a following form:

Cyclotron period as a function of the current in the coils

$$(T_{cycl}(I))^{-1} = a \cdot I + b \tag{135}$$

The linear term b corresponds to the z-axis component of the Earth magnetic field, which is $B_{Earth,z} = 45.6\,\mu T$ in Berlin pointing towards the planet surface [149]. Thus, the sign of the linear term b in Eq. 135 depends on the orientation of the applied magnetic field. In the present case $\vec{B}_{applied}$ is also pointing down towards the ion detector, so the linear term $b > 0$. In order to perform the main magnetic field calibration T_{cycl} has to be measured for a range of applied currents I. Then a linear fit has to be performed for the measured cyclotron frequencies $(T_{cycl}(I))^{-1}$ as a function of current I. In the present setup the fitting parameters in Eq. 135 are: $a = 1.35\,MHz/A$ and $b = 1.32\,MHz$.

The cyclotron period T_{cycl} is entering the initial photoelectron momentum reconstruction routine as a parameter (see Section 4.4.2). Performing a calibration of the main magnetic field using Eq. 135, the cyclotron period T_{cycl} corresponding to current I can be estimated. In order to avoid distortions in the reconstructed photoelectron momentum distribution, especially in the vicinity of magnetic nodes, T_{cycl} has to be defined with a precision up to 0.1 ns (see Section 4.5.1). Such a precision could not be obtained from the cyclotron frequencies fitting. Thus, fine tuning of T_{cycl} has to be performed based on the reconstructed photoelectron momentum distribution circularisation, as shown in Fig. 46. It is convenient to check the symmetry of the reconstructed photoelectron momentum distribution in polar coordinate system, as shown in Fig. 46 (b).

4.5.5 *Reaction Microscope momentum resolution*

The momentum resolution of the Reaction Microscope strongly depends on the applied E and B field strengths. Additionally, it is not the same for the z-axis and for the x- and y-axes. Since ion trajectories in the ReMi are not depending on the B field, more general considerations can be derived for the ion momentum resolution. On the other hand, the electron momentum resolution strongly depends on the position of the magnetic nodes with respct to the measured photoelectron distribution (see Section 4.4.1).

The ion momentum resolution for the p_z component is inversely proportional to the applied E field strength and limited by the ion detector time-of-flight resolution (see Section 4.4.3). For the electronics used in the reported setup the TOF resolution is on the order of 100 ps. Thus, from a technical perspective, in the present ReMi at $E = 300\,\mathrm{V/m}$ the ion p_z momentum component resolution could reach up to 0.003 a.u. Another contribution to the error in determination of the ion p_z comes from the z component of the initial velocity of a particle in the molecular beam prior to ionization. In the present setup the FWHM of the velocity distribution in the molecular beam along the z-axis is on the order of 50 m/s. For an N^+ fragment with approximately 14 Da mass this corresponds to $\Delta p_{z\,ion} = 0.6$ a.u.

For the ion $p_{x,y}$ components the resolution is dictated by the resolution of the impact position detector. In the present setup the resolution of the delay line anodes is on the order of 100 µm, while the detector diameter is 80 mm. At $E = 300\,\mathrm{V/m}$ for the N^+ fragments this corresponds to $\Delta p_{x,y\,ion} = 0.1$ a.u. The uncertainty originating from the velocity distribution in the molecular beam for the y-axis is similar to the z-axis, due to symmetry. On the other hand, since in the reported molecular beam the FWHM of the velocity distribution along the beam axis is on the order of 200 m/s (see Section 4.3.3), for an N^+ fragment this corresponds to $\Delta p_{x\,ion} = 2$ a.u.

Similar to ions, the electron p_z momentum component resolution is also inversely proportional to the applied E field strength (see Section 4.4.2). In the reported system at $E = 300\,\mathrm{V/m}$ the full photoelectron distribution measured in the experiment with the maximum absolute momentum $|p_{max}| = 1.25$ a.u. arrives to the detector in a 100 ns time-of-flight window. Since the electron detector TOF resolution is on the order of 100 ps, this corresponds to $\Delta p_{z\,e} = 0.003$ a.u. For photoelectrons the effect of the velocity distribution of particles in the molecular beam prior to ionization on the momentum resolution is negligible due to small electron mass.

The electron $p_{x,y}$ momentum component resolution is not the same over the full photoelectron distribution detected in the experiment. In the vicinity of a magnetic node the resolution is substantially reduced, till the information on the photoelectron initial momentum is completely lost right at the node (see Section 4.4.1). For photoelectron detection the choice of the E and B fields is a trade-off between the p_z momentum resolution and a loss of information on the $p_{x,y}$ momentum components at particular times-of-flight overlapping with magnetic nodes. For example, in the reported experiments at $E = 300\,\mathrm{V/m}$ and $B = 580\,\mu\mathrm{T}$ one magnetic node is positioned in the middle of the photoelectron TOF distribution. In the present system at optimal conditions, i.e at equal distance from the two adjacent nodes, for an electric field $E = 300\,\mathrm{V/m}$ the $\Delta p_{x,y\,e} = 0.003\,\mathrm{a.u.}$

The photoelectron momentum resolution could be further reduced if the compensatory magnetic fields are not properly adjusted, which results in modification of the photoelectron trajectories in the ReMi (see Section 4.5.2). The dominant factor limiting the photoelectron momentum resolution in attosecond experiments is a broadband spectrum of the XUV pulses. For example, the harmonics in the XUV APTs used in the reported experiments are up to $0.1\,\mathrm{a.u.}$ broad. Thus, in the measured photoelectron spectra the spectral lines with smaller energy difference could not be resolved.

Part III

EXPERIMENTAL RESULTS

In the third part of the thesis the results of an attosecond pump-probe experiment performed in N_2 are reported. The photoionization dynamics corresponding to the $C\,^2\Sigma_u^+$ state of the N_2^+ ion was studied with vibrational state resolution. The measured photoionization delays reveal a non-trivial energy dependence.

5

PHOTOIONIZATION DELAYS MEASURED IN MOLECULAR NITROGEN

Molecular nitrogen is one of the main constituents of the atmosphere on Earth and Titan, the moon of Saturn [150]. It was also observed in gas clouds in interstellar space [151]. In the ground state the N_2 molecule is inert due to a triple bond, while its ionization or fragmentation products are highly reactive (for more details on the N_2 molecule please refer to Section 2.4.6). These products are assumed to be involved in chemical reactions leading to the formation of prebiotic molecules. The interaction of XUV photons from the Sun's radiation with N_2 in the upper atmosphere of the Earth induces transitions to different ionic dissociative or non-dissociative states. In order to unravel the underlying mechanisms of these processes they have been experimentally investigated in the laboratory environment. Multiple XUV photon-induced transitions in N_2 have been studied using XUV spectroscopy with attosecond pulses [35, 37, 40, 43, 44] or synchrotron radiation [47–49]. The present work is focused on the predissociative $C\,^2\Sigma_u^+$ state of the N_2^+ ion. The predissociation of the $C\,^2\Sigma_u^+$ state has been previously theoretically investigated [88, 89], but, to the best of our knowledge, the photoinduced electron dynamics corresponding to the $X\,^1\Sigma_g^+ \rightarrow C\,^2\Sigma_u^+$ state transition has never been experimentally accessed. The measurements reported here are complementing the existing data on the XUV photon ionization of N_2 and fill the gap between already studied non-dissociative ion states, such as the X, A and B states, and dissociative highly excited states, such as the F and H states.

In the reported experiments the ultrafast photoionization dynamics associated with two-photon induced (one XUV ± one NIR) transitions from the $X\,^1\Sigma_g^+$ ground state of the neutral N_2 molecule to the predissociative $C\,^2\Sigma_u^+$ state of the N_2^+ ion was investigated with vibrational resolution. This dynamics was accessed using extreme ultraviolet (XUV)–near infrared (NIR) time-resolved pump-probe spectroscopy measurements with XUV attosecond pulse trains, i.e. the RABBIT technique (for more details please refer to Section 2.5). The 7 fs FWHM NIR laser pulses with a central wavelength around 800 nm delivered by the NOPCPA system were used for high-order harmonic generation in Kr (see Section 3.2.1). The temporal structure of the generated attosecond pulse trains is similar to those described in Section 3.3.1. In the spectral domain they cover a range from 15 to 50 eV (the lower edge corresponds to the cutoff of the 200 nm Al filter). Replicas of the NIR pulses used for HHG were utilized as probe

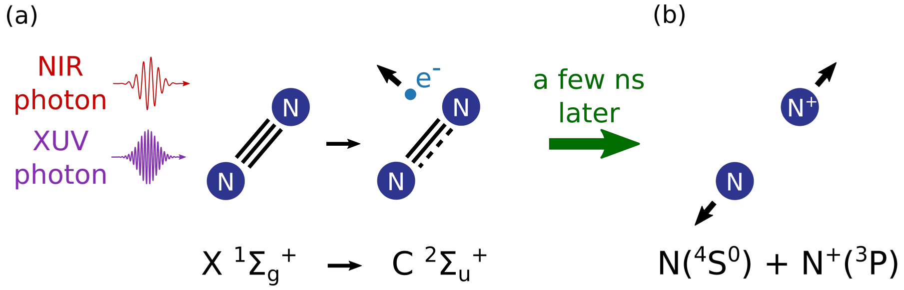

Figure 47: Schematic view of the RABBIT experiment on the $C\,^2\Sigma_u^+$ state: *(a)* the XUV ± NIR two-photon $X\,^1\Sigma_g^+ \rightarrow C\,^2\Sigma_u^+$ state transition in N_2, *(b)* a few ns later dissociation of the N_2^+ ion.

pulses for the experiments. A 200 as pump-probe delay step was chosen. Slow pump-probe delay drift occurring during the measurement was later corrected for (see Section 3.2.4).

The $C\,^2\Sigma_u^+$ state of the N_2^+ ion is a predissociative state for $v \geqslant 3$ with energies above the first dissociation limit of the N_2^+ ion at 24.31 eV [91]. The predissociative lifetime of the $C\,^2\Sigma_u^+$ state has been estimated to be on the order of 5 ns [92, 93]. In the XUV photon energy range used in the reported experiments, N^+ fragments resulting from predissociation of the $C\,^2\Sigma_u^+$ state are the dominant contribution to the measured N^+ fragment spectrum [50, 152]. Nevertheless, in the respective XUV photon energy range the probability of photoinduced transitions from the $X\,^1\Sigma_g^+$ ground state to the $C\,^2\Sigma_u^+$ state is approximately 200 times smaller than the total probability of the three dominant transitions to the non-dissociative states of N_2^+ ion: $X\,^2\Sigma_g^+$, $A\,^2\Pi_u$ and $B\,^2\Sigma_u^+$ states [50]. Thus, a high repetition rate source is required in order to obtain significant statistics on the photoinduced transition under investigation.

Due to the corresponding Franck-Condon factors, the absorption of a single XUV photon induces transitions from the $v = 0$ vibrational state of the $X\,^1\Sigma_g^+$ state to a set of vibrational states of the $C\,^2\Sigma_u^+$ state. In the measured N^+ fragment spectrum vibrational states of the $C\,^2\Sigma_u^+$ state with $v \geqslant 3$ are observed. The vibrational spacing (i.e. the energy difference between the adjacent vibrational states) between the low vibrational states $v = 3, ..., 7$ of the $C\,^2\Sigma_u^+$ state is on the order of 250 meV [91].

The suggested mechanism involved in the performed RABBIT measurements on the $C\,^2\Sigma_u^+$ state is the following (schematically shown in Fig. 47, analogous to the experiment performed in CO by J. Vos *et.al* [54, 57]):

- the XUV ± NIR two-photon transition from the $v = 0$ vibrational state of the $X\,^1\Sigma_g^+$ electronic ground state of N_2 to a set of vibrational states of the $C\,^2\Sigma_u^+$ state of the N_2^+ ion,
- (a few ns later) the N_2^+ ion in the $C\,^2\Sigma_u^+$ state predissociates.

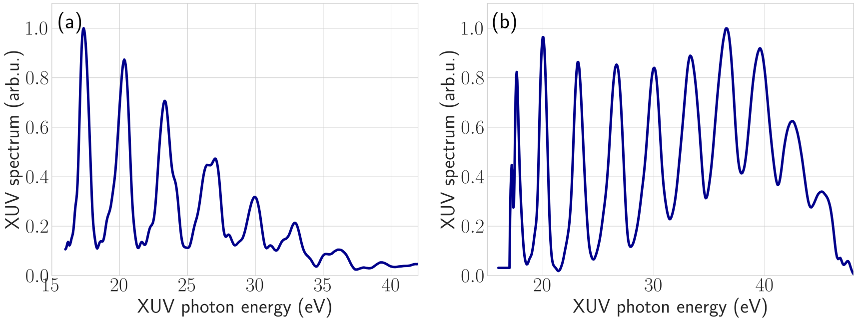

Figure 48: XUV spectra of attosecond pulse trains used for the RABBIT experiments performed in a mixture with Ar and He are shown in subplots *(a)* and *(b)* respectively. The lowest high-order harmonic in the XUV spectra shown here is HH11 due to the Al filter cutoff.

If the mechanism suggested above is correct, the sideband oscillation phases extracted from the RABBIT spectrograms constructed from photoelectrons measured in coincidence with N^+ fragments (corresponding to predissociation of the $C\,^2\Sigma_u^+$ state) contain information on Wigner-like photoionization delays τ_W — the delays corresponding to scattering of the emitted photoelectron on the potential of the $C\,^2\Sigma_u^+$ ion state (for more details please refer to Section 2.5.8).

In order to access the molecular photoionization delays using the RABBIT technique it is advantageous to have an atomic reference (see Section 2.2). Thus, two independent RABBIT measurements were performed in two different gas mixtures: a mixture of N_2 with Ar (approximately 9-to-1 ratio) and a mixture of N_2 with He (approximately 1-to-1 ratio). The XUV spectra of the attosecond pulse trains used for the two measurements are shown in Fig. 48. The XUV spectra in the two experiments are different due to slightly different performance of the NOPCPA system, and also due to different phase matching conditions in the HHG process.

Ar (ionization potential = 15.76 eV, for more details please refer to Section 2.3.3) was chosen as the admixture gas since it is well studied and has a relatively large photoionization cross section in the XUV photon energy range used. Another reason to choose Ar as the admixture gas is that in the respective photon energy range, the ionization of Ar dominantly occurs from the $3p^6$ orbital with s or d photoelectrons emitted. On the other hand, as a result of the $X\,^1\Sigma_g^+ \rightarrow C\,^2\Sigma_u^+$ parallel photoinduced transitions in N_2, also s or d photoelectrons are emitted. Since Wigner-like delays induced by scattering on a short range potential strongly depend on the angular momentum of the scattered photoelectron [69], the equality of the angular momenta of the scattered photoelectrons in atomic and molecular targets is preferable for comparison of the experimentally measured delays.

Unfortunately, there are a few complications associated with using Ar as the phase reference for a RABBIT measurement on photoinduced $X\,^1\Sigma_g^+ \rightarrow C\,^2\Sigma_u^+$ state transitions in N_2:

- a substantial difference in the asymptotic momenta of the photoelectrons resulting from ionization of Ar and N_2 by the same harmonic, due to a big difference between the ionization potential of Ar and the first dissociation limit of N_2^+ ($|D(N_2^+L_1) - Ip(Ar)| = 8.55\,\text{eV}$).
- the $3s^{-1}4p$ resonance in Ar modifies the measured sideband oscillation phases at XUV photon energies around 26.63 eV [26].

In order to avoid the extra complexity related to using Ar as an admixture gas, a second series of experiments was performed with a mixture of N_2 and He (ionization potential = 24.58 eV, for more details please refer to Section 2.3.2). An initial argument for using He as the admixture gas was the small difference between the ionization potential of He and the first dissociation limit of N_2^+ ($|D(N_2^+L_1) - Ip(He)|$ $= 0.27\,\text{eV}$). The ionization of He occurs from the $1s^2$ orbital (with a p electron emitted) and does not contain resonances in the XUV photon energy range used. This allows easier determination of the group delay of the XUV pulse trains. Unfortunately, the difference in the angular momentum of photoelectrons emitted from He and from N_2 during the $X\,^1\Sigma_g^+ \rightarrow C\,^2\Sigma_u^+$ state transition adds extra complexity to the comparison of the experimentally measured phases. Additionally, due to the approximately 5 times smaller photoionization cross section of He compared to Ar in the respective XUV photon energy range, the required concentration of He in the gas mixture was higher.

In the experiments both photoelectrons and ions were detected in coincidence using the Reaction Microscope (see Section 4.2.2). The coincidence detection capabilities were used for separating photoelectrons resulting from ionization of different species or corresponding to different photoionization channels, such as the $X\,^1\Sigma_g^+ \rightarrow C\,^2\Sigma_u^+$ photoionization channel. Then RABBIT spectrograms were constructed from photoelectrons measured in coincidence with ions selected from the ion time-of-flight (TOF) spectra. In Figs. 49 (a) and 50 (a) the ion TOF spectra corresponding to the RABBIT measurements in $N_2 + Ar$ and $N_2 + He$ mixtures are shown.

The time-of-flight T of an ion with zero initial momentum $\vec{p_0} = \vec{0}$ in the Reaction Microscope depends on the ion mass M and charge q as follows (for more details please refer to Section 4.4):

Ion time-of-flight

$$T = \sqrt{\frac{M}{q}} \cdot \sqrt{\frac{2L}{E}} \qquad (136)$$

Here L is the distance between the interaction region and the ion detector along the z-axis and E is the applied electric field strength.

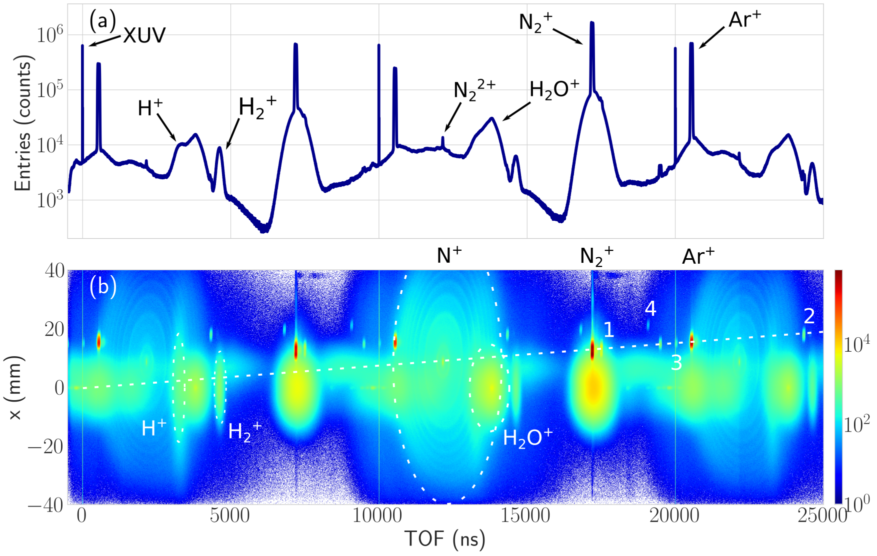

Figure 49: *(a)* Ion time-of-flight spectrum for N_2/Ar experiment shown on a logarithmic scale. *(b)* Ion impact position along the molecular beam axis as a function of the time-of-flight (with logarithmic colour scale). The labelled peaks correspond to: 1 — N_2^+ ion containing one ^{15}N isotope; 2 — organic contamination of the gas mixing station, possibly butadiene; 3 — $^{36}Ar^+$ and $^{38}Ar^+$ isotopes; 4 — Ar_2^+ dimers.

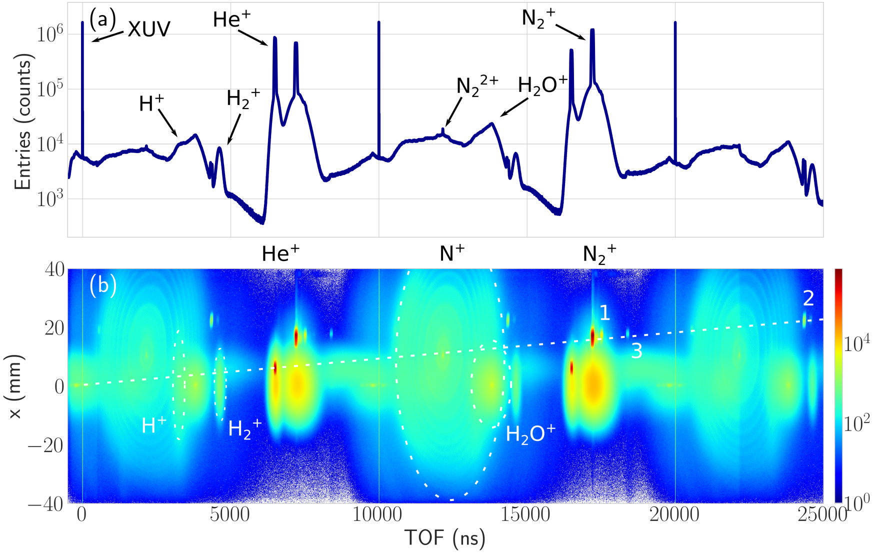

Figure 50: *(a)* Ion time-of-flight spectrum for N_2/He experiment shown on a logarithmic scale. *(b)* Ion impact position along the molecular beam axis as a function of the time-of-flight (with logarithmic colour scale). The labelled peaks correspond to: 1 — N_2^+ ion containing one ^{15}N isotope; 2 — organic contamination of the gas mixing station, possibly butadiene; 3 — HeN_2^+ complexes.

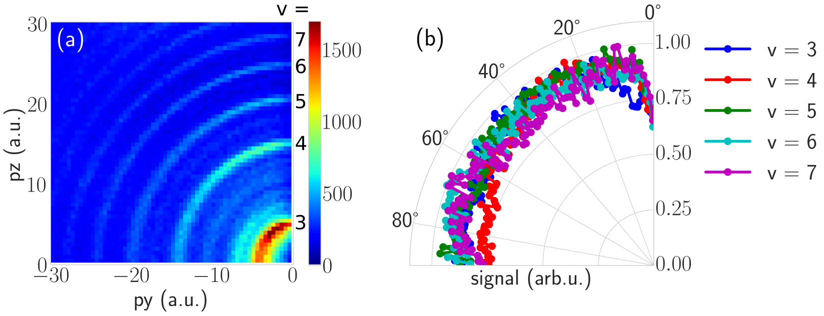

Figure 51: *(a)* A slice through the measured N^+ fragment momentum distribution (for $|p_x| < 5$ a.u.). The laser polarization is parallel to the z-axis. *(b)* Angular distribution of the N^+ fragments with respect to the laser polarization for particular vibrational states of the $C\,^2\Sigma_u^+$ state. The signal depletion along the laser polarization axis is a result of the Jacobian.

Using Eq. 136 the peaks in the ion TOF spectra can be unambiguously assigned. Since the applied data acquisition time window had a 25.5 µs duration, it effectively covered three laser pulses (for more details please refer to Section 4.2.6). Thus, a series of "ghost" peaks appeared in the ion TOF spectra.

The ratio between the signals corresponding to the "ghost" and "real" peaks is equal to the photoionization probability during the experiment. In both reported measurements it was on the order of 20 %, which corresponds to a single ionization event per 5 laser pulses. The sharp peaks appearing every 10 µs in the TOF spectra correspond to XUV photons scattered on the gas target.

Ion time-of-flight and impact position

The "real" and "ghost" peaks can be easily separated from the ion impact position along the molecular beam x-axis, as a function of the time-of-flight, as shown in Figs. 49 (b) and 50 (b). The ion impact position x is related to the time-of-flight T as follows:

$$x = \langle v \rangle T \tag{137}$$

Here $\langle v \rangle$ is the mean velocity of the gas particles in the molecular beam (see Section 4.3). Thus, the "real" peaks are appearing along the straight line shown in Figs. 49 (b) and 50 (b).

A slice through the three-dimensional N^+ fragment momentum distribution obtained in the N_2/Ar experiment is shown in Fig. 51 (a). In this figure the z-axis corresponds to the laser polarization axis, and the y-axis is parallel to the laser beam axis in the Reaction Microscope. In the measured N^+ fragment spectrum the particular vibrational states of the $C\,^2\Sigma_u^+$ electronic state (with $\nu = 3, ..., 7$ in our experiment) can be resolved. Coincidence detection in turn allows separation of the photoelectrons corresponding to each particular vibrational state. In the N_2/Ar experiment due to high concentration of

N_2 in the gas mixture (90%) the obtained statistics was sufficient for constructing separate RABBIT spectrograms for each of the $\nu = 3,4,5$ vibrational states of the $C\,^2\Sigma_u^+$ state. Unfortunately, the number of photoelectrons corresponding to the $\nu = 6,7$ vibrational states detected in this experiment was not sufficient for constructing separate RABBIT spectrograms, and thus they were integrated. The total number of detected events corresponding to individual $\nu = 3,4,5$ vibrational states in the N_2/Ar experiment is on the order of 10^6, which for a 30 hour long measurement corresponds to approximately 10 events per second (the overall photoelectron detection rate was kept on the order of 20 kHz during the measurement).

On the other hand, due to the lower concentration of N_2 in the gas mixture with He (50%) than that in the mixture with Ar, in the N_2/He experiment the obtained statistics was not sufficient for constructing separate spectrograms for each vibrational state. Thus, the photoelectrons corresponding to the $\nu = 3,4,5$ states of the $C\,^2\Sigma_u^+$ state were integrated. Unfortunately, the obtained statistics for the $\nu = 6,7$ vibrational states in this experiment was not sufficient for phase extraction. The total number of detected events integrated over the $\nu = 3,4,5$ vibrational states in the N_2/He experiment is on the order of $2 \cdot 10^6$, which for a 60 hour long measurement corresponds to approximately 5 events per second per vibrational state.

In Fig. 51 (b) the angular distributions of the measured N^+ fragments are shown in the laboratory frame for each vibrational state of the $C\,^2\Sigma_u^+$ state resolved in the experiments. The measured angular distributions of the N^+ fragments are almost spherically symmetric. This is consistent with the fact that for $\nu \leqslant 14$ vibrational states of the $C\,^2\Sigma_u^+$ state the predissociative lifetimes significantly exceed the rotational periods [49]. As a result, the measured alignment of the recoil axis is not equivalent to the alignment of the internuclear axis at the instant of photoionization. Thus, a transformation of the measured photoelectron momentum angular distributions from the laboratory frame to the molecular frame is not possible. For the construction of RABBIT spectrograms measured in the $C\,^2\Sigma_u^+$ state the photoelectrons emitted in the full 4π solid angle were integrated. As a result, the photoionization delays measured in N_2 were averaged over all emission angles with respect to the internuclear axis. In contrast, for the construction of RABBIT spectrograms measured in atomic targets only photoelectrons emitted in a $\pm 30°$ angular range with respect to the laser polarization were integrated.

In Fig. 52 (a) the kinetic energy correlation diagram (KECD) of coincident N^+ fragments and photoelectrons measured in the N_2/Ar experiment integrated over the full pump-probe delay range is shown. The kinetic energy release (KER) of the N_2^+ ion dissociation was calculated as twice the energy of the detected N^+ fragment, since the energy released in the N_2^+ ion dissociation is equally distributed be-

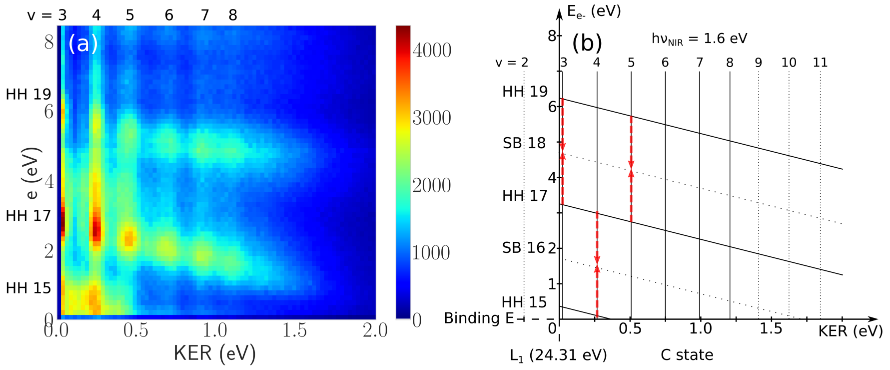

Figure 52: *(a)* Kinetic energy correlation diagram of coincident N^+ fragments and photoelectrons integrated over the full pump-probe delay range. The photoelectron energy and ion kinetic energy release are plotted along the vertical and horizontal axes, respectively. *(b)* Schematic view of the KECD shown in *(a)*. The NIR photon induced continuum photoelectron transitions occurring in the RABBIT experiment are shown as red arrows.

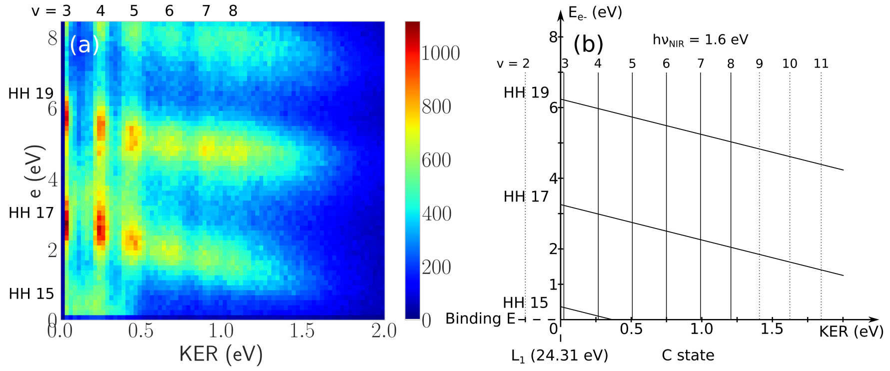

Figure 53: *(a)* Kinetic energy correlation diagram of coincident N^+ fragments and photoelectrons measured in the absence of the NIR probe (only with XUV pulses). The photoelectron energy and ion kinetic energy release are plotted along the vertical and horizontal axes, respectively. *(b)* Schematic view of the KECD shown in *(a)*.

tween the N^+ and N fragments (the N fragment is not detected in the experiment). On the diagram the vertical lines correspond to different vibrational states $\nu \geqslant 3$ of the $C\,^2\Sigma_u^+$ state. Due to energy conservation, the diagonal lines correspond to the high-order harmonics and sidebands. The discussed features in the KECD are schematically shown in Fig. 52 (b). RABBIT spectrograms corresponding to the $C\,^2\Sigma_u^+$ state were constructed from photoelectrons selected along the vertical spectral lines corresponding to particular vibrational states in the KECD. The signals were integrated over a 0.1 eV broad KER range for each vibrational state.

A similar diagram measured in absence of the NIR probe (only with XUV pulses) is shown in Fig. 53. In that case, the photoelec-

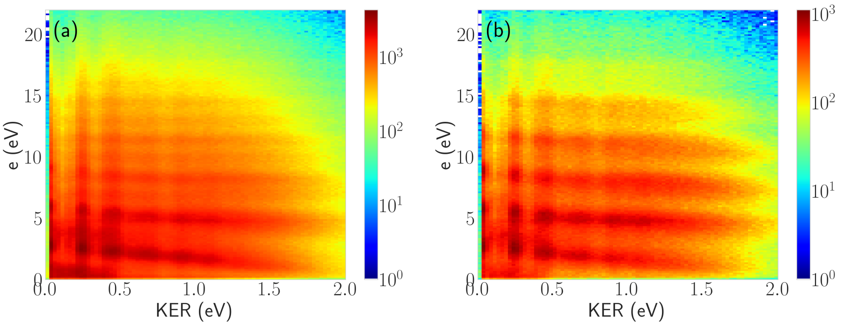

Figure 54: In *(a)* and *(b)* kinetic energy correlation diagrams of coincident N$^+$ fragments and photoelectrons integrated over the full pump-probe delay range (similar to Figure 52), and measured in the absence of the NIR probe (only with XUV pulses, similar to Figure 53) are shown, respectively. Both plots are shown with logarithmic colour scale. The photoelectron energy and ion kinetic energy release are plotted along the vertical and horizontal axes, respectively.

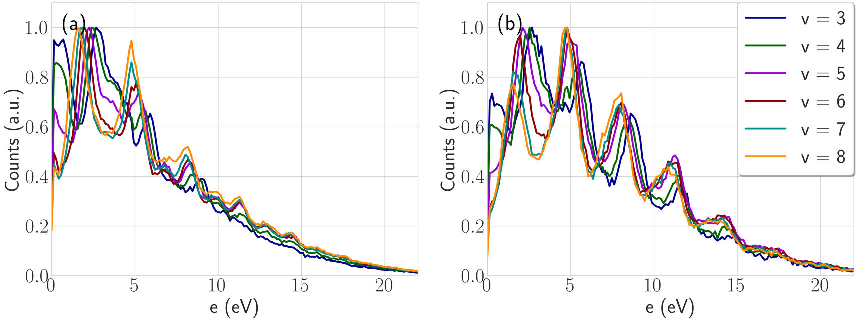

Figure 55: In *(a)* and *(b)* normalized photoelectron spectra corresponding to the $v = 3, ..., 8$ vibrational states of the C $^2\Sigma_u^+$ state integrated over the full pump-probe delay range and measured in the absence of the NIR probe (only with XUV pulses) are shown, respectively.

tron spectra corresponding to the vibrational states of the C $^2\Sigma_u^+$ state contain only the harmonic spectral lines, as schematically shown in Fig. 53 (b).

In Fig. 54 both KECDs measured with and without the NIR probe are shown on a logarithmic scale. In the presence of the NIR probe the photoelectron spectral lines in the KECD are not exactly parallel to each other and become 'tilted' at higher photoelectron energies. In the KECD measured without the NIR field this effect is not observed. In Fig. 55 (a) and (b) photoelectron spectra corresponding to the $v = 3, ..., 8$ vibrational states measured with and without the NIR probe are shown, respectively. In the presence of the NIR probe the harmonic spectral lines in the photoelectron spectra are overlapping above 10 eV photoelectron energy, which is not true for the XUV only case. Since this effect is observed only in the presence of the NIR pulse, it is attributed to an interaction of the NIR field with the potential of the N_2^+ ion. In this picture the NIR field is bending the Coulomb potential of an ion effectively reducing the photoelectron binding energy, which is manifested in an increase of the measured photoelectron kinetic energy. The suggested picture could not explain why this effect is not observed in the low photoelectron energy range, i.e. for the high harmonic 16. This phenomenon requires further investigation.

The pump-probe delay axis in all RABBIT spectrograms shown here is the delay between the XUV and NIR pulses (where positive delays correspond to the XUV pulses arriving first). For a delay axis assigned this way, the extracted oscillation phases and the corresponding photoionization delays assigned as $\tau(\omega) = \delta(\phi(\omega)_{\mathrm{scattered}} - \phi(\omega)_{\mathrm{free}})/\delta\omega$ [18] have the same sign (see Section 2.5.9). In other words, larger phases correspond to larger delays. The phases of the sideband oscillations were extracted from the measured RABBIT spectrograms using a Fast Fourier Transform (FFT) algorithm as the phases of the 2ω angular frequency component, where ω is the angular frequency of the fundamental NIR photon. For all RABBIT spectrograms shown here the photoelectron kinetic energy axis binning was chosen to be 300 meV. The phases of the 2ω component were extracted for each energy individually, and then averaged over each sideband spectral line, which are approximately 1.5 eV broad for the XUV APTs used.

In Fig. 56 a RABBIT spectrogram measured in Ar is shown. Subplot (a) shows the original experimentally acquired dataset. In order to enhance the contrast of the oscillating signals, a linear fit was performed over the full pump-probe delay range for each energy, and then the non-oscillatory part was subtracted from the measured spectrograms, thus isolating the time-varying part. The difference plot resulting from such a baseline subtraction is shown in subplot (b), with the colour scale representing the difference between the instantaneous yield and the baseline in % of the baseline signal. Subplot (c) shows the square root of the Fourier Transform Power Spectrum (FTPS = $|F(\omega)|^2$) of the original RABBIT spectrogram shown in subplot (a). In the square root of the FTPS, $1, 2, 3$ and 4ω components are present (labelled on the plots). The significant 4ω component reflects multiple NIR photon-induced transitions involved in the photoionization process. This is an indication of a higher probe NIR field intensity applied during the measurement, compared with the NIR intensities used in conventional RABBIT experiments. In this experiment the NIR probe intensity was estimated to be on the order of $2 \cdot 10^{11}$ W/cm^2. The relatively high NIR intensity explains the shape of the oscillating signals in the measured RABBIT spectrogram in Ar (for more details please refer to Section 2.5.9). Odd frequency components are present in the FTPS of the measured RABBIT spectrograms

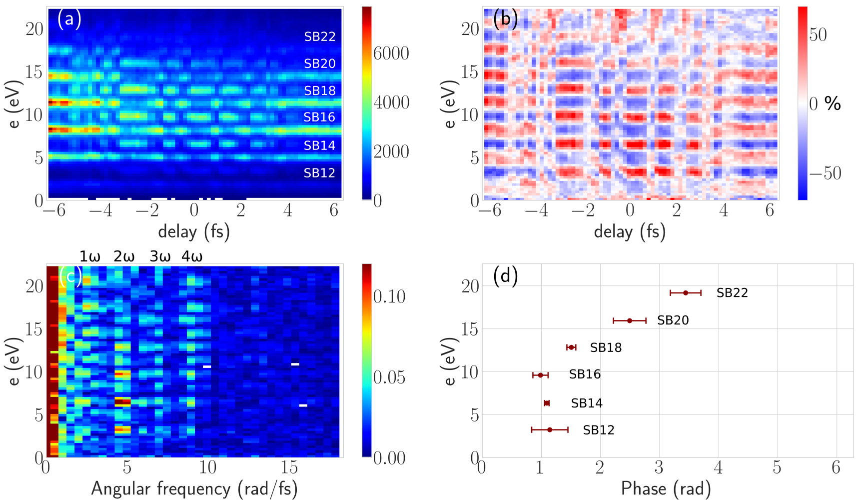

Figure 56: Measured RABBIT spectrogram in Ar *(a)* with corresponding difference plot *(b)* showing the difference between the signal measured at a particular pump-probe delay and the average signal over the full delay range for each photoelectron energy (in % of the average signal). Subplot *(c)* shows the square root of the Fourier Transform Power Spectrum of the measured RABBIT spectrogram shown in *(a)*. In *(d)* the phases of the 2ω component in the Fourier Transform are shown for sidebands 12–22. The error bars represent a $\pm 1\sigma$ confidence range.

since the APTs used were relatively short (compared with conventional APTs used for RABBIT experiments with a FWHM on the order of tens of fs). The phases of the 2ω component (approximately 4.7 rad/fs for an 800 nm central wavelength) were extracted for each sideband and are plotted as a function of photoelectron energy in subplot (d). In the XUV photon energy range above approximately 25 eV the XUV APTs used for the RABBIT measurement in N_2 mixture with Ar can be approximated as having a positive group delay dispersion (GDD) on the order of $0.03\,\mathrm{fs}^2$ (1 eV photon energy corresponds to approximately 1.52 rad/fs angular frequency). The measured group delay dispersion is on the same order of magnitude as the GDDs of APTs generated at different NIR intensities in different gases reported in [80]. The group delay dispersion was determined from a linear fit of the extracted phases for sidebands 16–22. We assume that the non-linear energy dependence of the phases for sidebands 12 and 14 is an indication of a third-order phase of the APTs.

In Figs. 57–60 RABBIT spectrograms corresponding to the $\nu = 3, 4, 5$ vibrational states and an average spectrogram over the $\nu = 6, 7$ states of the $C\,^2\Sigma_u^+$ state are shown, respectively. The contrast in the RABBIT spectrograms measured in N_2 is significantly lower than that in the simultaneously measured spectrogram in Ar. This effect is attributed to the background ionization of N_2 in the ReMi resulting in N^+ fragments. These fragments are then arriving to the ion detector within a 5 µs ion time-of-flight window, that is set for selecting the N^+ fragments originating from the molecular beam (see Figs. 49, 50). As a result, the corresponding electrons are included into the RABBIT spectrograms, effectively increasing the background signal. The background ionization does not affect non-dissociative channels, such as the Ar^+ or He^+ channels, since the duration of corresponding ion TOF windows was set on the order of 100 ns. In the TOF spectra the Ar^+ or He^+ ions originating from the background are forming pedestals around the sharp peaks corresponding to the molecular beam ionization (see Figs. 49, 50). Thus, background ions with corresponding photoelectrons are not included in the spectrograms.

In order to access the oscillating signal phases, the Fourier Transform was performed not on the original RABBIT spectrograms shown in Figs. 57–60 in subplots (a), but on the difference plots acquired analogous to the Ar measurement shown in subplots (b). In subplots (c) the square root of the resulting FTPS is shown. In the molecular case the 4ω component in the Fourier domain is weaker compared to the atomic case. This is also visible from the shape of the oscillating signals in the measured RABBIT spectrograms shown in subplots (a). The simple harmonic shape indicates that a lower number of NIR photons were involved in the photoionization process under investigation in the molecular case than in the atomic case, even though the experimentally applied NIR probe intensity was exactly the same due to the simultaneous measurement. One of the possible explanations of this effect is that it results from the NIR field interaction with the N_2^+ ion potential, effectively reducing the number of NIR photons inducing continuum photoelectron transitions. The phases of the 2ω component were extracted for each sideband spectral line and plotted as a function of the photoelectron energy in subplots (d).Within the error bars, no vibrational state dependency is observed in the extracted sideband oscillation phases for the $\nu = 3, ..., 7$ vibrational states of the $C\,^2\Sigma_u^+$ state.

In all RABBIT spectrograms measured in the $C\,^2\Sigma_u^+$ state a nonlinear energy dependence of the sideband phases is clearly visible above approximately 10 eV photoelectron energy. Unfortunately, the corresponding XUV photon energy range was not resolved in the RABBIT spectrogram simultaneously measured in Ar due to relatively small photoionization cross section. Assuming that the forth- and higher-order phases of the APTs used are small, the sideband phases measured in Ar could be linearly extrapolated to the respective XUV photon energy range and compared to those measured in the $C\,^2\Sigma_u^+$ state. The resulting discrepancy above approximately 35 eV XUV photon energy indicates a contribution of Wigner-like short range potential-induced photoionization delays to the observed effect.

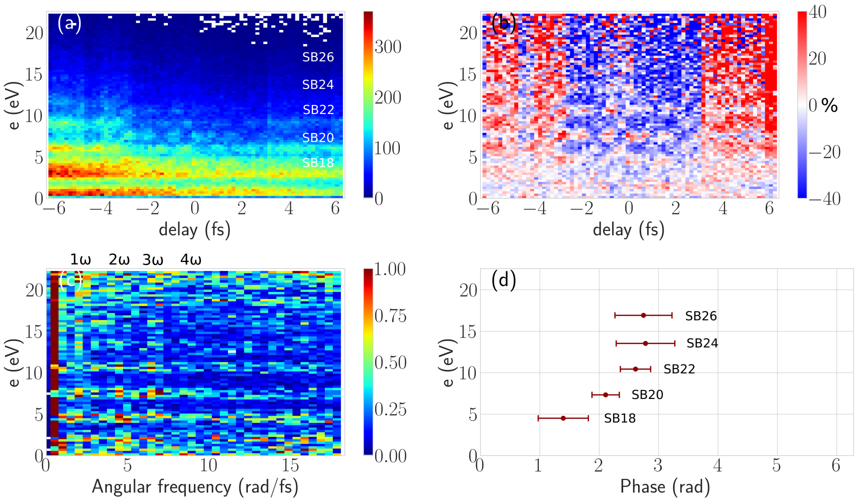

Figure 57: Measured RABBIT spectrogram in combination with the formation of C $^2\Sigma_u^+$ $\nu = 3$ state *(a)* with corresponding difference plot *(b)* showing the difference between the signal measured at a particular pump-probe delay and the average signal over the full delay range for each photoelectron energy (in % of the average signal). Subplot *(c)* shows the square root of the Fourier Transform Power Spectrum of the difference plot shown in *(b)*. In *(d)* the phases of the 2ω component in the Fourier Transform are shown for sidebands 18–26. The error bars represent a $\pm 1\sigma$ confidence range.

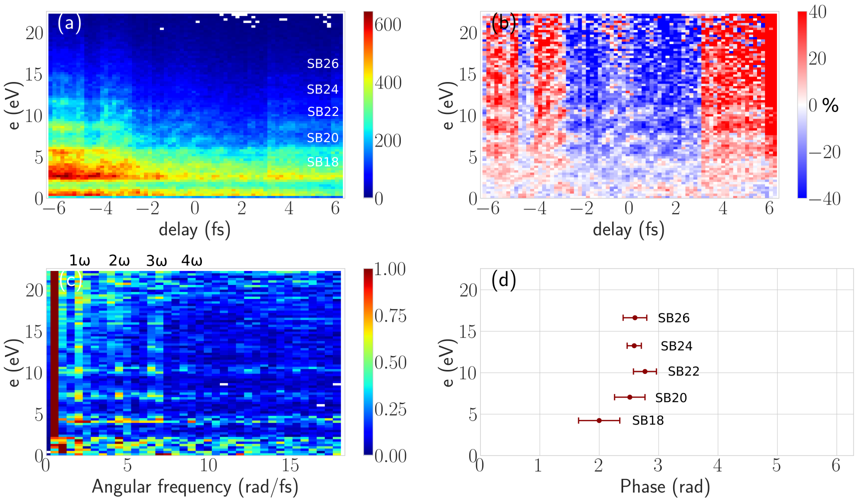

Figure 58: Measured RABBIT spectrogram in combination with the formation of C $^2\Sigma_u^+$ $\nu = 4$ state *(a)* with corresponding difference plot *(b)*, square root of the Fourier Transform Power Spectrum *(c)* and phases of the 2ω component in the Fourier Transform *(d)*. Analogous to Figure 57.

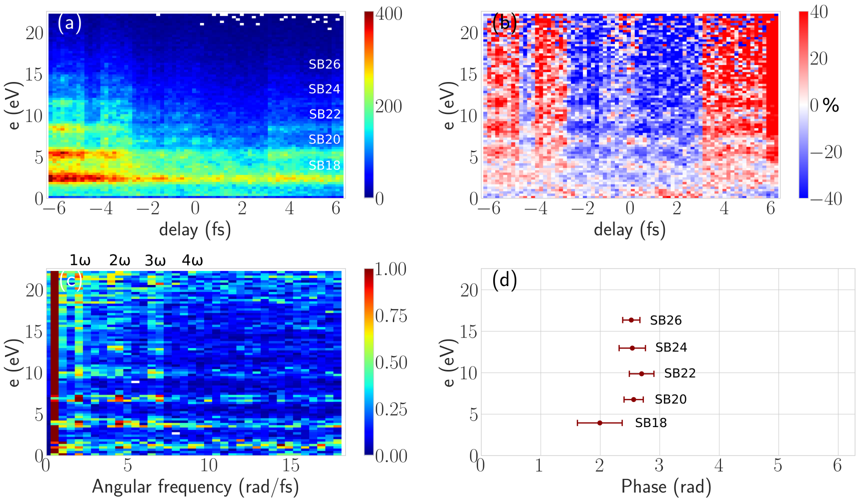

Figure 59: Measured RABBIT spectrogram in combination with the formation of $C\,^2\Sigma_u^+$ $\nu = 5$ state *(a)* with corresponding difference plot *(b)*, square root of the Fourier Transform Power Spectrum *(c)* and phases of the 2ω component in the Fourier Transform *(d)*. Analogous to Figure 57.

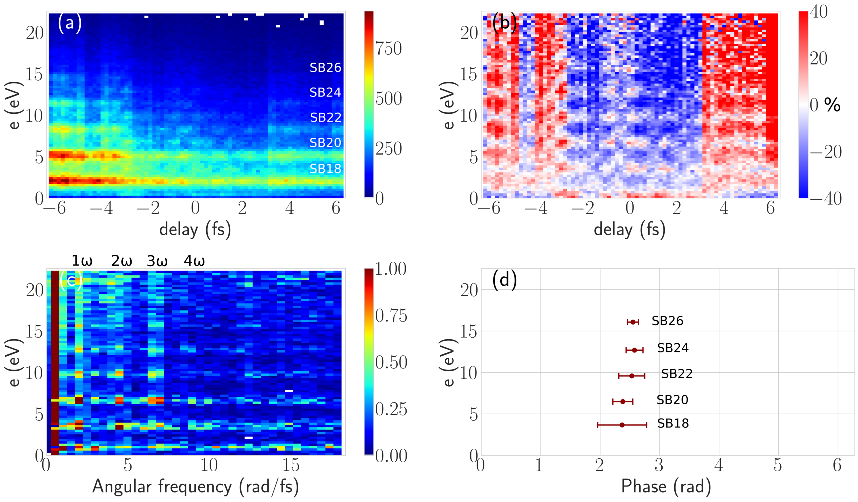

Figure 60: Measured RABBIT spectrogram in combination with the formation of $C\,^2\Sigma_u^+$ $\nu = 6,7$ states *(a)* with corresponding difference plot *(b)*, square root of the Fourier Transform Power Spectrum *(c)* and phases of the 2ω component in the Fourier Transform *(d)*. Analogous to Figure 57.

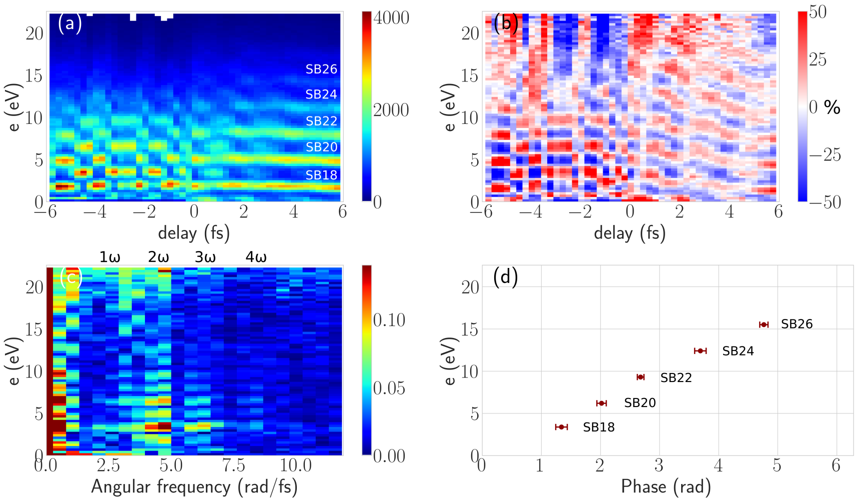

Figure 61: Measured RABBIT spectrogram in He *(a)* with corresponding difference plot *(b)* showing the difference between the signal measured at a particular pump-probe delay and the average signal over the full delay range for each photoelectron energy (in % of the average signal). Subplot *(c)* shows the square root of the Fourier Transform Power Spectrum of the measured RABBIT spectrogram shown in *(a)*. In *(d)* the phases of the 2ω component in the Fourier Transform are shown for sidebands 18–26. The error bars represent a $\pm 1\sigma$ confidence range.

An analogous analysis was performed for the RABBIT spectrograms measured in the N_2 and He gas mixture. In Fig. 61 the RABBIT spectrogram measured in He is shown. In this experiment the NIR probe intensity was estimated to be on the order of $1 \cdot 10^{11}\,\mathrm{W/cm^2}$. Again, in the atomic case the phases of the 2ω component were extracted from a Fourier Transform of the measured RABBIT spectrogram shown in Fig. 61 (a). The XUV APTs used for the RABBIT measurement in N_2 mixture with He had a positive group delay dispersion on the order of $0.04\,\mathrm{fs}^2$. Analogous to the measurement in Ar, the group delay dispersion was determined from a linear fit of the extracted phases of sidebands 18–26. The measured GDD of the APTs in this experiment is on the same order of magnitude as those reported in [80]. The ratio between the APT GDDs in the two experiments indicates that in the N_2/Ar measurement the NIR field intensity used for the HHG was higher than that in the N_2/He measurement. In the reported setup the NIR probe intensity in the experiment strongly depends on the spatial overlap of the XUV and NIR foci. Thus, in each experiment the ratio between the NIR intensities in the experiment and used for HHG is slightly different due to different alignment of XUV and NIR beams.

Due to the lower concentration of N_2 in the N_2/He gas mixture than that in the N_2/Ar mixture, and since no vibrational state

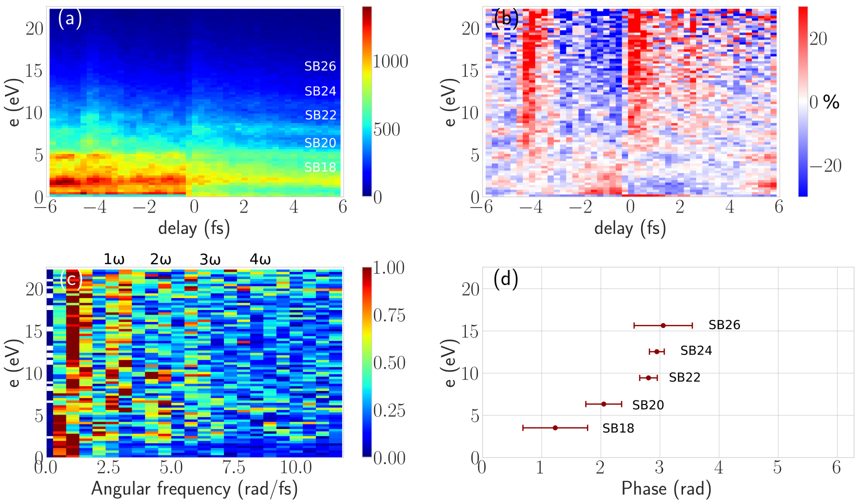

Figure 62: Measured RABBIT spectrogram in combination with the formation of $C\,^2\Sigma_u^+$ averaged over $v = 3,4,5$ states obtained in the N_2/He experiment *(a)* with corresponding difference plot *(b)* showing the difference between the signal measured at a particular pump-probe delay and the average signal over the full delay range for each photoelectron energy (in % of the average signal). Subplot *(c)* shows the square root of the Fourier Transform Power Spectrum of the difference plot shown in *(b)*. In *(d)* the phases of the 2ω component in the Fourier Transform are shown for sidebands 18–26. The error bars represent a $\pm 1\sigma$ confidence range.

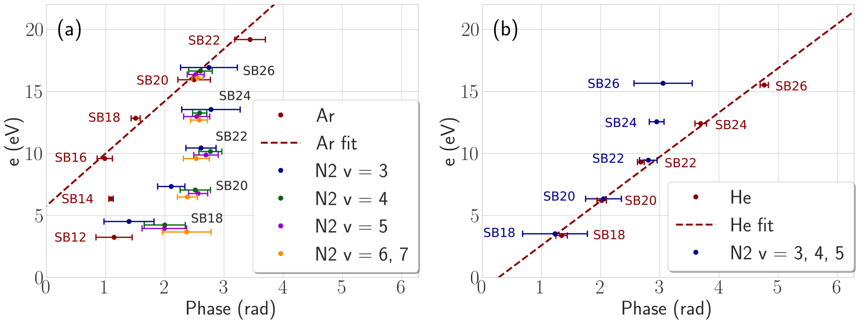

Figure 63: Comparison of sideband phases measured in the N_2 mixture with Ar *(a)* and in the N_2 mixture with He *(b)*. The dots show the experimentally measured sideband phases with error bars representing a $\pm 1\sigma$ confidence range. The dashed lines show linear fits to the sideband phases measured in Ar and He.

dependency of the extracted sideband oscillation phases was observed, in this experiment the photoelectrons corresponding to $v = 3,4,5$ states of the $C\,^2\Sigma_u^+$ state were integrated. The resulting RABBIT spectrogram is shown in Fig. 62 (a). Analogous to the N_2/Ar case the sideband oscillation phases shown in Fig. 62 (d) were extracted as 2ω contribution phases in the FTPS of the difference plot, shown in subplots (c) and (b), respectively. The sideband energies in the two RABBIT measurements performed in the two gas mixtures are slightly different due to different performance of the NOPCPA system resulting in a small variation of the central wavelength.

In Fig. 63 the sideband oscillation phases extracted from the measured RABBIT spectrograms in both experiments are plotted together for comparison. Both measurements show similar sideband phase behaviour for the $\nu = 3, ..., 7$ vibrational states of the $C\,^2\Sigma_u^+$ state as a function of the photoelectron energy, taking into account the group delay difference between the XUV APTs used. Starting from approximately 10 eV above the first dissociation limit of the N_2^+ ion (34 eV photon energy), photoelectrons ionized from the N_2 molecule are accelerated with respect to the atomic reference (the corresponding sideband phases are smaller in the molecular case than in the atomic case, for more details please refer to Section 2.5.9). Around 15 eV above the first dissociation limit (39 eV photon energy) the observed delay reaches its minimum on the order of -400 ± 100 as. For the measurement in the mixture with He the photoionization delays were compared directly, while for the measurement in Ar the photoionization delays were linearly extrapolated to the corresponding XUV photon energy range as shown in Fig. 63 (a). Unfortunately, due to the spectral shape of the APTs used, photoelectrons with higher energies were not observed in the performed experiments.

Non-trivial photoionization delay energy dependencies observed in different states of small molecules, such as the $X\,^2\Sigma_g^+$ ground state of the N_2^+ ion [43, 44], the X and A states of the N_2O^+ ion [41] and the $B\,^2\Sigma_u^+$ state of the CO_2^+ ion [42], were explained by the presence of shape resonances. At the shape resonance, right after the ionization the photoelectron is occupying a quasibound state with a lifetime typically on the order of a few hundreds of attoseconds. Thus, the shape resonance is manifested in retardation of the photoelectron, since it gets effectively trapped in the potential barrier [153]. To the best of our knowledge, the acceleration of the photoelectron observed in the $C\,^2\Sigma_u^+$ state could not be explained by a presence of a shape resonance. As an alternative mechanism we suggest a channel opening around approximately 10 eV above the first dissociation limit of the N_2^+ ion (approximately 34 eV photon energy). This mechanism can be explained as follows: due to the high photon energy, an XUV photon interaction with a molecule induces a big number of transitions simultaneously. As soon as the XUV photon energy becomes sufficient to induce transitions to the next higher energy ionic state, i.e. a new channel is open, all dipole transition matrix elements of the transitions to lower energy states become modified. This is manifested in the XUV photon energy dependence of the partial-channel photoionization cross sections of these states. In the time domain this results in the energy dependence of the photoionization delays. As a potential candidate for channel opening in the present case the $F\,^2\Sigma_g^+$ state of the N_2^+ ion is suggested. $F\,^2\Sigma_g^+$ state is a dissociative ionic state with approximately 28.5 eV ionization potential and $2\sigma_u^{*-1} 1\pi_u^{-1} 1\pi_g^{*+1}$ dominant configuration [36]. Around 35 eV the $X\,^1\Sigma_g^+ \rightarrow F\,^2\Sigma_g^+$ transition becomes a dominant dissociative channel due to a relatively big partial-channel photoionization cross section (approximately 0.8 Mb). The suggested hypothesis is supported by a previously made observation that around 35 eV XUV photon energy the photoionization cross section of the $C\,^2\Sigma_u^+$ state is decreasing, while the cross section of the $F\,^2\Sigma_g^+$ state is simultaneously increasing [50, 154].

Unfortunately, due to the complex multielectron nature of the $X\,^1\Sigma_g^+ \rightarrow C\,^2\Sigma_u^+$ state transition a theoretical calculation is required in order to determine the exact mechanism explaining the observed non-trivial energy dependence of the photoionization delays. The two electrons involved in the respective transition (one excited and one ionized, see Section 2.4.6) significantly increases the complexity of such a calculation. Apart from the non-trivial photoionization delay energy dependence, another question is raised by the observed difference in the sideband strength in the photoionization of N_2 and the atomic targets at equal NIR probe intensities. Also the observed 'tilt' of the photoelectron spectral lines in the KECDs measured in the presence of a NIR probe requires further investigation. In order to answer these questions a collaboration with the group of Prof. Fernando Martin at Universidad Autónoma de Madrid was established. Hopefully, a theoretical investigation of the studied process would help to find an explanation of these three effects.

6

CONCLUSION

In recent years the development of new laser pulse sources has guided the advances in the field of attosecond spectroscopy. Time resolved experiments performed at high XUV photon fluxes and detection rates allowed access to photoionization dynamics in different targets with overall increasing complexity. Even in the simplest possible case of homonuclear diatomic molecules it is often complicated to obtain information on the XUV photon induced dynamics state-selectively, due to the large number of available transitions in the corresponding photon energy range. Thus, in order to resolve particular photoionization channels, such as dissociative channels in molecules, the detection of photoelectrons and ions in coincidence is preferable.

In the present work a new beamline combining a 100 kHz tabletop HHG-based XUV laser pulse source with a Reaction Microscope was developed and commissioned. The reported beamline is designed for XUV–NIR attosecond pump-probe spectroscopy experiments. The setup is equipped with an active pump-probe delay stabilization system allowing for measurements with overall duration exceeding multiple tens of hours, which is crucial for coincidence detection experiments. Both XUV attosecond pulse trains and isolated attosecond pulses available for the experiments were characterized employing RABBIT and attosecond streaking techniques, respectively. Due to the high repetition rate and coincidence detection capabilities the reported beamline can be used for studying correlated photoelectron and ion dynamics. It also allows access to dissociative photoionization channels with low relative probability, which is advantageous for studying photoionization dynamics in molecules.

With the reported beamline photoionization dynamics corresponding to XUV photon-induced transitions from the ground $X\,^1\Sigma_g^+$ state of the N_2 molecule to the predissociative $C\,^2\Sigma_u^+$ state of the N_2^+ ion was studied using the RABBIT technique. The coincidence detection capabilities allowed separation of photoelectrons corresponding to particular vibrational states of the $C\,^2\Sigma_u^+$ state. From the resulting RABBIT spectrograms photoionization delays were extracted for each vibrational state individually and compared with an atomic reference. The obtained photoionization delay energy dependence is similar within the error bars for the vibrational states $\nu = 3, ..., 7$. It shows a non-trivial behaviour in the XUV photon energy range around 39 eV. In that energy range photoelectrons emitted from the molecular nitrogen are accelerated with respect to the atomic reference, reaching a minimum delay on the order of -400 ± 100 as. This effect could be attributed to multiple electrons involved in the XUV-induced process under investigation. In order to unravel the exact mechanisms responsible, a theoretical simulation is required.

The present work further extends the frontiers of attosecond spectroscopy in molecules overcoming the limitations induced by the lack of sufficient statistics for particular photoionization channels with low relative probability. This is achieved by increasing the repetition rate of the laser pulse source, while keeping the XUV photon flux sufficiently high, which requires high overall laser power. The described approach allowed access to attosecond electron dynamics corresponding to a particular predissociative state of molecular nitrogen with vibrational resolution. The experimental study of this dynamics would not be possible at lower detection rates due to the low relative probability of the corresponding XUV photon induced transitions.

In the last few decades our understanding of the molecular mechanisms in different living organisms has been rapidly developing. Photoinduced electron dynamics and charge transfer in biomolecules are of particular interest, since they are governing such fundamental processes as photosynthesis and vision. Unfortunately, investigation of ultrafast dynamics in organic molecules is incredibly complicated due to their size and overall complexity. The results reported in the present thesis are manifesting one step further towards attosecond spectroscopy of large bio-relevant molecules with coincidence detection using table-top HHG based sources.

PUBLICATIONS

The following publications are included in the thesis:

- M. Osolodkov, F. J. Furch, F. Schell, P. Šušnjar, F. Cavalcante, C. S. Menoni, C. P. Schulz, T. Witting and M. J. J. Vrakking. "Generation and characterisation of few-pulse attosecond pulse trains at 100 kHz repetition rate." In: *J. Phys. B: At. Mol. Opt. Phys.* 53 (2020), p. 194003.
- T. Witting, M. Osolodkov, F. Schell, F. Morales, S. Patchkovskii, P. Šušnjar, F. H. M. Cavalcante, C. S. Menoni, C. P. Schulz, F. J. Furch and M. J. J. Vrakking. "Generation and characterization of isolated attosecond pulses at 100 kHz repetition rate." In: *Optica* 9.2 (2022), p. 145.

The following publications are not included in the thesis:

- T. Witting, F. J. Furch, O. Kornilov, M. Osolodkov, C. P. Schulz and M. J. J. Vrakking. "Retrieval of attosecond pulse ensembles from streaking experiments using mixed state time-domain ptychography." In: *J. Phys. B: At. Mol. Opt. Phys.* 53 (2020), p. 194001.

Part IV

APPENDIX

Appendix contains an explicit derivation of the equations describing charged particle trajectories in the Reaction Microscope, discussed in the main text.

ATOMIC UNITS

Since atomic units are frequently used in the present work, here, for convenience, we put a table of constants (Table 3) and a table of unit conversion from atomic units to conventional units for different physical quantities (Table 4).

CONSTANT	SYMB.	A.U.	VALUE
Reduced Planck constant	$\hbar$	1	$1.055 \cdot 10^{-34}$ J·s
Electron charge	e	1	$1.602 \cdot 10^{-19}$ C
Electron mass	m_e	1	$9.109 \cdot 10^{-31}$ kg
Speed of light in vacuum	c	137.036	$2.998 \cdot 10^{8}$ m/s
Vacuum dielectric permittivity	ϵ_0	$1/4\pi$	$8.854 \cdot 10^{-12}$ F/m

Table 3: A table of constants in atomic units and SI units.

QUANTITY	EXPR.	REFERENCE	VALUE
Length	a_0	Bohr radius	$5.29 \cdot 10^{-11}$ m = 0.529 Å
Energy	E_h	Hartree = $2 \times Ip^H$	$4.36 \cdot 10^{-18}$ J = 27.21 eV
Time	$\hbar/E_h$		$2.42 \cdot 10^{-17}$ s = 24.2 as
Velocity	$a_0 E_h/\hbar$		$2.188 \cdot 10^{6}$ m/s
Electric field	$E = e/a_0^2$		$5.14 \cdot 10^{11}$ V/m
Laser intensity	$\frac{1}{2}\epsilon_0 c E^2$	↔ peak E = 1 a.u.	$3.51 \cdot 10^{16}$ W/cm^2
Momentum	$\hbar/a_0$		$1.993 \cdot 10^{-24}$ kg·m/s

Table 4: A table of unit conversion from atomic units to other conventional units.

APPENDIX A

A.1 CHARGED PARTICLE TRAJECTORIES IN HOMOGENEOUS E AND B FIELDS

In the appendix an explicit derivation of charged particle equation of motion in the Reaction Microscope is given. A case of collinear E and B fields described in cylindrical and Cartesian coordinate systems is covered in Section A.1.1 and Section A.1.2, respectively. A case of noncollinear E and B fields is discussed in Section A.2.

A.1.1 *Motion of a charged particle in cylindrical coordinate system*

In the present section an equation of motion of a charged particle in the Reaction Microscope in the cylindrical coordinate system is derived. Let us define a cylindrical coordinate system O_{cyl} with respect to the Reaction Microscope as follows (similar to Section 4.4.1):

- z-axis: spectrometer axis towards the ion detector parallel to $\vec{E}$ and $\vec{B}$,
- $\vec{r}$: radial coordinate of a particle in the detector plane with $r = 0$ corresponding to the projection of an interaction region on the detector along the z-axis,
- the origin $(0, 0)$ is fixed to an interaction region.

In the Reaction Microscope a particle with charge q and mass m is exposed to collinear homogeneous E and B fields. The corresponding equation of motion in the coordinate system O_{cyl} has a form (here $\times$ stands for vector multiplication):

$$\begin{cases} m\ddot{z}(t) & = q \cdot E \\ m\ddot{\vec{r}}(t) & = q \cdot \dot{\vec{r}}(t) \times \vec{B} \end{cases} \tag{138}$$

A schematic view of the corresponding trajectory in the detector plane is shown in Fig. 38. Let us define a radius of the charged particle orbit in the detector plane as R. Then an equation describing a centrifugal force can be applied into the equation of motion of a particle in the detector plane:

$$m|\ddot{\vec{r}}| = m\frac{|\dot{\vec{r}}|^2}{R} = |\dot{\vec{r}}| \cdot |qB| \tag{139}$$

Integrating Eq. 138 over t, and using Eq. 139, the equation of motion of a charged particle can be written in the following form:

$$\begin{cases} m\dot{z}(t) & = p_z(t) = q \cdot E \cdot t + p_{0\,z} \\ m|\vec{r}| & = |\vec{p}_{0\,\vec{r}}| = R \cdot |qB| \end{cases} \tag{140}$$

Here $p_{0\,z}$ and $\vec{p}_{0\,\vec{r}}$ are the particle z and $\vec{r}$ initial momentum components, respectively. Let us define a cyclotron period T_{cycl} — a period of a charged particle movement on a circular orbit induced by a magnetic field. From the definition of T_{cycl} the following equation can be derived:

$$2\pi \cdot R = |\vec{r}| \cdot T_{cycl} = \frac{R \cdot |qB|}{m} \cdot T_{cycl} \tag{141}$$

Which is equivalent to:

$$T_{cycl} = 2\pi \frac{m}{|qB|} \tag{142}$$

For particles with the same charge to mass ration the T_{cycl} depends only on the magnetic field strength B, while it does not depend on the initial particle momentum. Thus, T_{cycl} is universal for all photoelectrons detected in the experiment. Since all photoelectrons start their trajectories in the interaction region, at $t = T_{cycl}$ the projections of their trajectories on the detector plane overlap with each other creating a nod. Thus, in the nod all information on the initial momentum component $\vec{p}_{0\,\vec{r}}$ is lost.

In order to derive an equation for the $|\vec{r}(t)|$ we are going to use a geometrical argument as shown in Fig. 38:

$$|\vec{r}(t)| = \sqrt{2 \cdot R \cdot (1 - \cos(\alpha(t)))} = \sqrt{2 \cdot \frac{|\vec{p}_{0\,\vec{r}}|}{|qB|} \cdot \left(1 - \cos\left(2\pi \frac{t}{T_{cycl}}\right)\right)} \tag{143}$$

Integrating Eq. 140 over t, and applying Eq. 142 into Eq. 143 one an equation of motion of a charged particle in the cylindrical coordinate system O_{cyl} is derived:

$$\begin{cases} z(t) & = \frac{qE}{2m} \cdot t^2 + \frac{p_{0\,z}}{m} \cdot t \\ |\vec{r}(t)| & = \sqrt{2 \cdot \frac{|\vec{p}_{0\,\vec{r}}|}{|qB|} \cdot \left(1 - \cos\left(\frac{|qB| \cdot t}{m}\right)\right)} \end{cases} \tag{144}$$

A.1.2 *Motion of a charged particle in Cartesian coordinate system*

In the present section an equation of motion of a charged particle in the Reaction Microscope in the Cartesian coordinate system is derived. Then, from this equation, and equation for the initial momentum reconstruction is derived.

Let us define a laboratory frame Cartesian coordinate system O with respect to the Reaction Microscope as follows:

- x-axis: molecular beam axis parallel to $\langle \vec{v} \rangle$,
- y-axis: laser beam axis parallel to laser photon $\vec{k}$,
- z-axis: spectrometer axis towards the ion detector parallel to $\vec{E}$ and $\vec{B}$.

A classical equation of motion of a particle with charge q and mass m in homogeneous collinear E and B fields has a following form (here $\times$ stands for vector multiplication):

$$m\ddot{\vec{x}} = q(\vec{E} + \dot{\vec{x}} \times \vec{B}) \tag{145}$$

Here $\vec{x}$ is a three dimensional position vector. Then, in the coordinate system O:

$$\begin{cases} \vec{E} & = E \cdot \vec{e_z} \\ \vec{B} & = B \cdot \vec{e_z} \end{cases} \tag{146}$$

Here $\vec{e_z}$ is a Cartesian basis vector. Let us assign the initial coordinates of a charged particle right after ionization, which corresponds to $t = 0$, in the position and momentum space as follows:

$$\begin{cases} \vec{x}(0) & = \vec{x_0} = \begin{pmatrix} x_0 \\ y_0 \\ z_0 \end{pmatrix} \\ \dot{\vec{x}}(0) & = \frac{\vec{p_0}}{m} = \frac{1}{m} \begin{pmatrix} p_{0\,x} \\ p_{0\,y} \\ p_{0\,z} \end{pmatrix} \end{cases} \tag{147}$$

In the coordinate system O the equation of motion (Eq. 145) has a following form (here and further in the present section × stands for matrix multiplication):

$$m \begin{pmatrix} \ddot{x}(t) \\ \ddot{y}(t) \\ \ddot{z}(t) \end{pmatrix} = q \begin{pmatrix} 0 \\ 0 \\ E \end{pmatrix} + q \begin{pmatrix} \dot{x}(t) \\ \dot{y}(t) \\ \dot{z}(t) \end{pmatrix} \times \begin{pmatrix} 0 \\ 0 \\ B \end{pmatrix} \tag{148}$$

Which is equivalent to:

$$\begin{cases} m\ddot{x}(t) & = q \cdot \dot{y}(t) \cdot B \\ m\ddot{y}(t) & = -q \cdot \dot{x}(t) \cdot B \\ m\ddot{z}(t) & = q \cdot E \end{cases} \tag{149}$$

Integrating this equation over t an equation for the particle momentum components are acquired:

$$\begin{cases} p_x(t) & = m\dot{x}(t) = q \cdot (y(t) - y_0) \cdot B + p_{0\,x} \\ p_y(t) & = m\dot{y}(t) = -q \cdot (x(t) - x_0) \cdot B + p_{0\,y} \\ p_z(t) & = m\dot{z}(t) = q \cdot E \cdot t + p_{0\,z} \end{cases} \tag{150}$$

In order to simplify this equation a cyclotron angular frequency ω_c is used as a parameter. It is defined as:

$$\omega_c = \frac{2\pi}{T_{cycl}} = \frac{qB}{m} \tag{151}$$

Here T_{cycl} is a cyclotron period — a period of a charged particle movement on a circular orbit induced by a magnetic field defined in Eq. 115.

Integrating the equation for $p_z(t)$ (Eq. 150) over t the equation of motion along the z-axis is obtained:

$$z(t) = \frac{q}{2m} \cdot E \cdot t^2 + \frac{1}{m} \cdot p_{0\,z} \cdot t + z_0 \tag{152}$$

In order to derive an equation of motion along x- and y-axes, the following differential equation obtained combining Eq. 149 with Eq. 150 has to be solved:

$$\begin{cases} \ddot{x}(t) + \omega_c^2 x(t) & = \frac{\omega_c}{m} \cdot p_{0\,y} + \omega_c^2 \cdot x_0 \\ \ddot{y}(t) + \omega_c^2 y(t) & = -\frac{\omega_c}{m} \cdot p_{0\,x} + \omega_c^2 \cdot y_0 \end{cases} \tag{153}$$

The solution of the differential equation for $x(t)$ and the first derivative of this solution have the following form:

$$\begin{cases} x(t) & = C_1 e^{i\omega_c t} + C_2 e^{-i\omega_c t} + \frac{1}{m\omega_c} \cdot p_{0\,y} + x_0 \\ \dot{x}(t) & = i\omega_c C_1 e^{i\omega_c t} - i\omega_c C_2 e^{-i\omega_c t} \end{cases} \tag{154}$$

Here $C_{1,2}$ are constants. At $t = 0$ Eq. 154 has a form:

$$\begin{cases} x_0 & = C_1 + C_2 + \frac{1}{m\omega_c} \cdot p_{0\,y} + x_0 \\ \frac{1}{m} \cdot p_{0\,x} & = i\omega_c C_1 - i\omega_c C_2 \end{cases} \tag{155}$$

Then the constants $C_{1,2}$ are:

$$\begin{cases} C_1 & = \frac{1}{2im\omega_c} \cdot p_{0\,x} - \frac{1}{2m\omega_c} \cdot p_{0\,y} \\ C_2 & = -\frac{1}{2im\omega_c} \cdot p_{0\,x} - \frac{1}{2m\omega_c} \cdot p_{0\,y} \end{cases} \tag{156}$$

The resulting equation of motion along the x-axis $x(t)$ has the following form:

$$x(t) = \frac{1}{m\omega_c}(p_{0\,x} \cdot \sin\omega_c t - p_{0\,y} \cdot \cos\omega_c t + p_{0\,y}) + x_0 \tag{157}$$

The same procedure has to be repeated for the y-axis. For $y(t)$ the solution of the differential equation (Eq. 153) and the first derivative of this solution have the following form:

$$\begin{cases} y(t) & = C_1 e^{i\omega_c t} + C_2 e^{-i\omega_c t} - \frac{1}{m\omega_c} \cdot p_{0\,x} + y_0 \\ \dot{y}(t) & = i\omega_c C_1 e^{i\omega_c t} - i\omega_c C_2 e^{-i\omega_c t} \end{cases} \tag{158}$$

Here $C_{1,2}$ are constants. At $t = 0$ Eq. 158 has a form:

$$\begin{cases} y_0 & = C_1 + C_2 - \frac{1}{m\omega_c} \cdot p_{0\,x} + y_0 \\ \frac{1}{m} \cdot p_{0\,y} & = i\omega_c C_1 - i\omega_c C_2 \end{cases} \tag{159}$$

Then the constants $C_{1,2}$ are:

$$\begin{cases} C_1 & = \frac{1}{2im\omega_c} \cdot p_{0\,y} + \frac{1}{2m\omega_c} \cdot p_{0\,x} \\ C_2 & = -\frac{1}{2im\omega_c} \cdot p_{0\,y} + \frac{1}{2m\omega_c} \cdot p_{0\,x} \end{cases} \tag{160}$$

The resulting equation of motion along the y-axis $y(t)$ has the following form:

$$y(t) = \frac{1}{m\omega_c}(p_{0\,y} \cdot \sin\omega_c t + p_{0\,x} \cdot \cos\omega_c t - p_{0\,x}) + y_0 \tag{161}$$

The complete equation of motion of a charged particle in the coordinate system O is:

$$\vec{x}(t) = \begin{pmatrix} x(t) \\ y(t) \\ z(t) \end{pmatrix} = \begin{pmatrix} \frac{1}{m\omega_c}(p_{0\,x} \cdot \sin\omega_c t - p_{0\,y} \cdot \cos\omega_c t + p_{0\,y}) + x_0 \\ \frac{1}{m\omega_c}(p_{0\,y} \cdot \sin\omega_c t + p_{0\,x} \cdot \cos\omega_c t - p_{0\,x}) + y_0 \\ \frac{q}{2m}E \cdot t^2 + \frac{1}{m}p_{0\,z} \cdot t + z_0 \end{pmatrix} \tag{162}$$

The initial momentum $p_{0\,x}$, $p_{0\,y}$ and $p_{0\,z}$ can be reconstructed from the measured time-of-flight and position of impact on the detector $\{T$, x_T and $y_T\}$. The $z(T)$ is the coordinate of the detector plane in the coordinate system O. Let us have a look at a special case of a charged particle with zero initial momentum $\vec{p_0} = \vec{0}$. For such particle:

$$\begin{cases} x(t) & = x_0 \\ y(t) & = y_0 \\ z(t) & = \frac{q}{2m}E \cdot t^2 + z_0 \end{cases} \tag{163}$$

The time-of-flight of a zero initial momentum particle is assigned as T_0. Since $z(T) - z_0 = L$ — the distance from the interaction region to the detector plane, it is universal for all particles. Thus, for two similar particles with zero and non-zero initial momenta, respectively the following equation can be derived:

$$\frac{q}{2m}E \cdot T_0^2 = \frac{q}{2m}E \cdot T^2 + \frac{1}{m}p_{0\,z} \cdot T \tag{164}$$

Then the equation for the initial momentum z component reconstruction is:

$$p_{0\,z} = \frac{qE}{2}\frac{T_0^2 - T^2}{T} \tag{165}$$

At the time-of-flight T the equations of motion along x and y axes has a form:

$$\begin{cases} m\omega_c(x(T) - x_0) & = p_{0\,x} \cdot \sin\omega_c T + p_{0\,y}(1 - \cos\omega_c T) \\ m\omega_c(y(T) - y_0) & = p_{0\,y} \cdot \sin\omega_c T - p_{0\,x}(1 - \cos\omega_c T) \end{cases} \tag{166}$$

Here $x(T)$ and $y(T)$ are the particle impact position on the detector. Using the trigonometric identities it can be rewritten in the following form:

$$\begin{cases} m\omega_c(x(T)-x_0) & = 2p_{0\,x}\cdot\sin\frac{\omega_c T}{2}\cos\frac{\omega_c T}{2} + 2p_{0\,y}\cdot\sin^2\frac{\omega_c T}{2} \\ m\omega_c(y(T)-y_0) & = 2p_{0\,y}\cdot\sin\frac{\omega_c T}{2}\cos\frac{\omega_c T}{2} - 2p_{0\,x}\cdot\sin^2\frac{\omega_c T}{2} \end{cases} \tag{167}$$

Dividing both sides of Eq. 167 by $2\sin\frac{\omega_c T}{2}$ on gets:

$$\begin{cases} \frac{m\omega_c}{2\sin\frac{\omega_c T}{2}}(x(T)-x_0) & = p_{0\,x}\cdot\cos\frac{\omega_c T}{2} + p_{0\,y}\cdot\sin\frac{\omega_c T}{2} \\ \frac{m\omega_c}{2\sin\frac{\omega_c T}{2}}(y(T)-y_0) & = p_{0\,y}\cdot\cos\frac{\omega_c T}{2} - p_{0\,x}\cdot\sin\frac{\omega_c T}{2} \end{cases} \tag{168}$$

Which is equivalent to:

$$\frac{m\omega_c}{2\sin\frac{\omega_c T}{2}}\begin{pmatrix}(x(T)-x_0)\\(y(T)-y_0)\end{pmatrix} = \begin{bmatrix}\cos\frac{\omega_c T}{2} & \sin\frac{\omega_c T}{2}\\ -\sin\frac{\omega_c T}{2} & \cos\frac{\omega_c T}{2}\end{bmatrix}\times\begin{pmatrix}p_{0\,x}\\p_{0\,y}\end{pmatrix} = A\times\begin{pmatrix}p_{0\,x}\\p_{0\,y}\end{pmatrix} \tag{169}$$

Taking a transposed matrix A^T ($A^T = A^{-1}$) and multiplying both sides of Eq. 169 by A^T, the equation for the initial x and y momentum components reconstruction is derived:

$$\begin{pmatrix}p_{0\,x}\\p_{0\,y}\end{pmatrix} = \frac{m\omega_c}{2\sin\frac{\omega_c T}{2}}\begin{bmatrix}\cos\frac{\omega_c T}{2} & -\sin\frac{\omega_c T}{2}\\ \sin\frac{\omega_c T}{2} & \cos\frac{\omega_c T}{2}\end{bmatrix}\times\begin{pmatrix}(x(T)-x_0)\\(y(T)-y_0)\end{pmatrix} \tag{170}$$

A.2 MOTION OF A CHARGED PARTICLE IN NONCOLLINEAR E AND B FIELDS

In the present section an equation describing photoelectron trajectories in noncollinear E and B fields in the Reaction Microscope is derived. The problem is described in the Cartesian coordinate system O defined in Section A.1.2.

Let us assume that the $\vec{E}$ is parallel to the z-axis, while the $\vec{B}$ is not. Then $\vec{E}$ and $\vec{B}$ in the coordinate system O are defined as:

$$\begin{cases} \vec{E} &= E \cdot \vec{e_z} \\ \vec{B} &= B_x \cdot \vec{e_x} + B_y \cdot \vec{e_y} + B_z \cdot \vec{e_z} \end{cases} \tag{171}$$

The equation of motion of a photoelectron with charge q and mass m in the E and B fields has a form:

$$m\ddot{\vec{x}} = q(\vec{E} + \dot{\vec{x}} \times \vec{B}) \tag{172}$$

The photoelectron initial coordinate and momentum are defined as:

$$\begin{cases} \vec{x}(0) &= \vec{x_0} = \begin{pmatrix} x_0 \\ y_0 \\ z_0 \end{pmatrix} \\ \dot{\vec{x}}(0) &= \frac{\vec{p_0}}{m} = \frac{1}{m} \begin{pmatrix} p_{0\,x} \\ p_{0\,y} \\ p_{0\,z} \end{pmatrix} \end{cases} \tag{173}$$

Then the photoelectron equation of motion in the E and B fields defined as shown in Eq. 171 has a form:

$$m \begin{pmatrix} \ddot{x}(t) \\ \ddot{y}(t) \\ \ddot{z}(t) \end{pmatrix} = q \begin{pmatrix} 0 \\ 0 \\ E \end{pmatrix} + q \begin{pmatrix} \dot{x}(t) \\ \dot{y}(t) \\ \dot{z}(t) \end{pmatrix} \times \begin{pmatrix} B_x \\ B_y \\ B_z \end{pmatrix} \tag{174}$$

Which is equivalent to:

$$\begin{cases} m\ddot{x}(t) &= q \cdot (\dot{y}(t)B_z - \dot{z}(t)B_y) \\ m\ddot{y}(t) &= q \cdot (\dot{z}(t)B_x - \dot{x}(t)B_z) \\ m\ddot{z}(t) &= q \cdot (E + \dot{x}(t)B_y - \dot{y}(t)B_x) \end{cases} \tag{175}$$

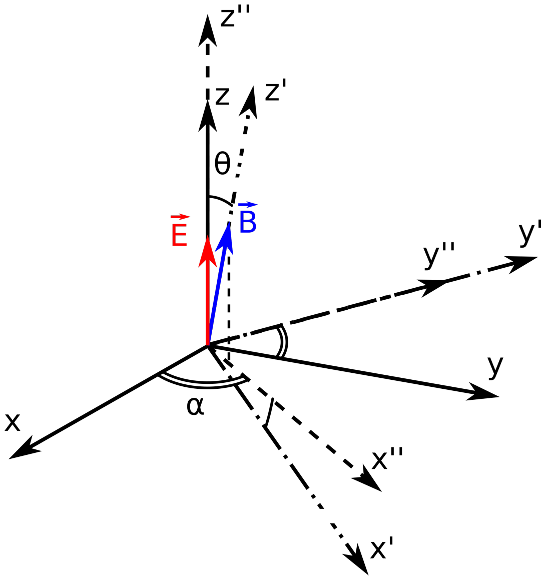

Figure 64: The relative orientation of the Cartesian coordinate systems O, O′ and intermediate coordinate system O″. Angles θ and α are labelled with single and double lines, respectively.

Integrating Eq. 175 over t and applying the initial conditions, the equation for photoelectron momentum components is derived:

$$\begin{cases} p_x(t) &= m\dot{x}(t) = q\cdot\left((y(t)-y_0)\cdot B_z-(z(t)-z_0)\cdot B_y\right)+p_{0\,x} \\ p_y(t) &= m\dot{y}(t) = q\cdot\left((z(t)-z_0)\cdot B_x-(x(t)-x_0)\cdot B_z\right)+p_{0\,y} \\ p_z(t) &= m\dot{z}(t) = q\cdot\left(E_z\cdot t+(x(t)-x_0)\cdot B_y-(y(t)-y_0)\cdot B_x\right)+p_{0\,z} \end{cases} \tag{176}$$

The photoelectron equation of motion can be simplified describing the problem with respect to another Cartesian coordinate system O′ defined such, that the z'-axis is parallel to the $\vec{B}$. The orientation of x' and y' axes can be chosen arbitrary. Let us assign the angle between the $\vec{E}$ and $\vec{B}$ as θ (see Fig. 64). It is advantageous to orient the O′ coordinate system such, that the transformation from O to O′ can be performed by two sequential basic rotations through an intermediate coordinate system O″: a rotation on angle α around the z-axis followed by a rotation on angle θ around the y''-axis.

The respective angles are defined as follows:

$$\begin{cases} \sin\alpha &= \frac{B_y}{\sqrt{B_x^2+B_y^2}} \\ \cos\alpha &= \frac{B_x}{\sqrt{B_x^2+B_y^2}} \end{cases}, \quad \begin{cases} \sin\theta &= \frac{\sqrt{B_x^2+B_y^2}}{B} \\ \cos\theta &= \frac{B_z}{B} \end{cases} \tag{177}$$

Here $B = \sqrt{B_x^2+B_y^2+B_z^2}$ is the absolute strength of the magnetic field. The transformation from the coordinate system O to the coordinate system O′ through an intermediate system O″ can be performed by multiplication on matrix R:

$$\begin{aligned} R &= \begin{bmatrix} \cos\theta & 0 & -\sin\theta \\ 0 & 1 & 0 \\ \sin\theta & 0 & \cos\theta \end{bmatrix} \times \begin{bmatrix} \cos\alpha & \sin\alpha & 0 \\ -\sin\alpha & \cos\alpha & 0 \\ 0 & 0 & 1 \end{bmatrix} \\ &= \begin{bmatrix} \cos\theta\cos\alpha & \cos\theta\sin\alpha & -\sin\theta \\ -\sin\alpha & \cos\alpha & 0 \\ \sin\theta\cos\alpha & \sin\theta\sin\alpha & \cos\theta \end{bmatrix} \end{aligned} \tag{178}$$

For example, the transformation of a $\vec{B}$ from O to O′ is performed as follows:

$$\begin{aligned} \vec{B}_{O'} &= \begin{pmatrix} B_{x'} \\ B_{y'} \\ B_{z'} \end{pmatrix} = R \times \vec{B}_O \\ &= \begin{bmatrix} \cos\theta\cos\alpha & \cos\theta\sin\alpha & -\sin\theta \\ -\sin\alpha & \cos\alpha & 0 \\ \sin\theta\cos\alpha & \sin\theta\sin\alpha & \cos\theta \end{bmatrix} \times \begin{pmatrix} B_x \\ B_y \\ B_z \end{pmatrix} = \begin{pmatrix} 0 \\ 0 \\ B \end{pmatrix} \end{aligned} \tag{179}$$

Then the $\vec{E}$ in the coordinate system O′ has a form:

$$\vec{E}_{O'} = \begin{pmatrix} E_{x'} \\ E_{y'} \\ E_{z'} \end{pmatrix} = R \times \vec{E}_O = \begin{pmatrix} -\sin\theta \cdot E \\ 0 \\ \cos\theta \cdot E \end{pmatrix} \tag{180}$$

The initial photoelectron position $\overrightarrow{x_0'}$ and momentum $\overrightarrow{p_0'}$ in the coordinate system O′ have a form:

$$\vec{x}'(0) = \overrightarrow{x_0'} = \begin{pmatrix} x_0' \\ y_0' \\ z_0' \end{pmatrix} = R \times \begin{pmatrix} x_0 \\ y_0 \\ z_0 \end{pmatrix} \tag{181}$$

$$\dot{\vec{x}}'(0) = \frac{\vec{p}'}{m} = \frac{1}{m} \begin{pmatrix} p_{0\,x'} \\ p_{0\,y'} \\ p_{0\,z'} \end{pmatrix} = \frac{1}{m} \cdot R \times \begin{pmatrix} p_{0\,x} \\ p_{0\,y} \\ p_{0\,z} \end{pmatrix} \tag{182}$$

Then, the photoelectron equation of motion in coordinate system O' has a form:

$$m \begin{pmatrix} \ddot{x}'(t) \\ \ddot{y}'(t) \\ \ddot{z}'(t) \end{pmatrix} = q \begin{pmatrix} E_{x'} \\ 0 \\ E_{z'} \end{pmatrix} + q \begin{pmatrix} \dot{x}'(t) \\ \dot{y}'(t) \\ \dot{z}'(t) \end{pmatrix} \times \begin{pmatrix} 0 \\ 0 \\ B \end{pmatrix} \tag{183}$$

Which is equivalent to:

$$\begin{cases} m\ddot{x}'(t) & = q \cdot (E_{x'} + \dot{y}'(t) \cdot B) \\ m\ddot{y}'(t) & = q \cdot (-\dot{x}'(t) \cdot B) \\ m\ddot{z}'(t) & = q \cdot (E_{z'}) \end{cases} \tag{184}$$

Integrating Eq. 184 over t and applying the initial conditions, the equation for the photoelectron momentum components in the coordinate system O' is derived:

$$\begin{cases} p_{x'}(t) & = m \cdot \dot{x}'(t) = q \cdot (E_{x'} \cdot t + (y'(t) - y'_0) \cdot B) + p_{0\,x'} \\ p_{y'}(t) & = m \cdot \dot{y}'(t) = -q \cdot (x'(t) - x'_0) \cdot B + p_{0\,y'} \\ p_{z'}(t) & = m \cdot \dot{z}'(t) = q \cdot E_{z'} \cdot t + p_{0\,z'} \end{cases} \tag{185}$$

Integrating this equation over t, the equation of motion along the z'-axis is obtained by:

$$z'(t) = \frac{q}{2m} \cdot E_{z'} \cdot t^2 + \frac{1}{m} \cdot p_{0\,z'} \cdot t + z'_0 \tag{186}$$

The equations of motion along x' and y' axes can be separated as follows:

$$\begin{cases} \ddot{x}'(t) + \omega_c^2 x'(t) & = \frac{\omega_c}{m} \cdot p_{0\,y'} + \frac{q}{m} \cdot E_{x'} + \omega_c^2 \cdot x'_0 \\ \ddot{y}'(t) + \omega_c^2 y'(t) & = -\frac{\omega_c}{m} \cdot p_{0\,x'} - \frac{\omega_c q}{m} \cdot E_{x'} \cdot t + \omega_c^2 \cdot y'_0 \end{cases} \tag{187}$$

Here ω_c is the cyclotron frequency defined in Eq. 151. Eq. 187 is analogous to Eq. 153 up to a non-zero $E_{x'}$ term. The solution of this differential equation for the $x'(t)$ and the first derivative of this solution have a form:

$$\begin{cases} x'(t) & = C_1 e^{i\omega_c t} + C_2 e^{-i\omega_c t} + \frac{1}{m\omega_c} \cdot p_{0\,y'} + \frac{q}{m\omega_c^2} \cdot E_{x'} + x'_0 \\ \dot{x}'(t) & = i\omega_c C_1 e^{i\omega_c t} - i\omega_c C_2 e^{-i\omega_c t} \end{cases} \tag{188}$$

At $t = 0$ Eq. 188 has a form:

$$\begin{cases} x'_0 & = C_1 + C_2 + \frac{1}{m\omega_c} \cdot p_{0\,y'} + \frac{q}{m\omega_c^2} \cdot E_{x'} + x'_0 \\ \frac{1}{m} \cdot p_{0\,x'} & = i\omega_c C_1 - i\omega_c C_2 \end{cases} \tag{189}$$

Then the constants $C_{1,2}$ are:

$$\begin{cases} C_1 & = \frac{1}{2im\omega_c} \cdot p_{0\,x'} - \frac{1}{2m\omega_c} \cdot p_{0\,y'} - \frac{q}{2m\omega_c^2} \cdot E_{x'} \\ C_2 & = -\frac{1}{2im\omega_c} \cdot p_{0\,x'} - \frac{1}{2m\omega_c} \cdot p_{0\,y'} - \frac{q}{2m\omega_c^2} \cdot E_{x'} \end{cases} \tag{190}$$

The resulting equation for $x'(t)$ has a form:

$$\begin{aligned} x'(t) = & \frac{1}{m\omega_c}(p_{0\,x'} \cdot \sin\omega_c t - p_{0\,y'} \cdot \cos\omega_c t + p_{0\,y'}) + x'_0 \\ & + \frac{q}{m\omega_c^2} \cdot E_{x'} \cdot (1 - \cos\omega_c t) \end{aligned} \tag{191}$$

Eq. 191 is analogous to Eq. 157 up to an additional $q/m\omega_c^2 \cdot E_{x'} \cdot (1 - \cos\omega_c t)$ term. Since $E_{x'} = -\sin\theta \cdot E = -E \cdot \sqrt{B_x^2 + B_y^2}/B$, this term linearly depends on the ratio between the z and $\vec{r}$ B field components in the coordinate system O.

The solution for the y' component of a photoelectron motion is analogous to the x' component. For the $y'(t)$ the solution of the differential equation 187 and the first derivative of this solution have a form:

$$\begin{cases} y'(t) & = C_1 e^{i\omega_c t} + C_2 e^{-i\omega_c t} - \frac{1}{m\omega_c} \cdot p_{0\,x'} - \frac{q}{m\omega_c} \cdot E_{x'} \cdot t + y'_0 \\ \dot{y}'(t) & = i\omega_c C_1 e^{i\omega_c t} - i\omega_c C_2 e^{-i\omega_c t} - \frac{q}{m\omega_c} \cdot E_{x'} \end{cases} \tag{192}$$

At $t = 0$ Eq. 192 has a form:

$$\begin{cases} y'_0 & = C_1 + C_2 - \frac{1}{m\omega_c} \cdot p_{0\,x'} + y'_0 \\ \frac{1}{m} \cdot p_{y'} & = i\omega_c C_1 - i\omega_c C_2 - \frac{q}{m\omega_c} \cdot E_{x'} \end{cases} \tag{193}$$

Then the constants $C_{1,2}$ are:

$$\begin{cases} C_1 & = \frac{1}{2im\omega_c} \cdot p_{0\,y'} + \frac{1}{2m\omega_c} \cdot p_{0\,x'} + \frac{q}{2im\omega_c^2} \cdot E_{x'} \\ C_2 & = -\frac{1}{2im\omega_c} \cdot p_{0\,y'} + \frac{1}{2m\omega_c} \cdot p_{0\,x'} - \frac{q}{2im\omega_c^2} \cdot E_{x'} \end{cases} \tag{194}$$

The resulting equation for $y'(t)$ has a form:

$$\begin{aligned} y'(t) = {} & \frac{1}{m\omega_c}(p_{0\,y'}\cdot\sin\omega_c t + p_{0\,x'}\cdot\cos\omega_c t - p_{0\,x'}) + y'_0 \\ & + \frac{q}{m\omega_c^2}\cdot E_{x'}\cdot(\sin\omega_c t - \omega_c t) \end{aligned} \tag{195}$$

Eq. 195 is analogous to Eq. 161 up to an additional $q/m\omega_c^2 \cdot E_{x'} \cdot (\sin\omega_c t - \omega_c t)$ term. Since $E_{x'} = -\sin\theta\cdot E = -E\cdot\sqrt{B_x^2+B_y^2}/B$, this term linearly depends on the ratio between the z and $\vec{r}$ B field components in the coordinate system O similar to the x'-axis case (see Eq. 191).

The complete photoelectron equation of motion in the coordinate system O' is:

$$\vec{x}'(t) = \begin{pmatrix} \frac{1}{m\omega_c}(p_{0\,x'}\cdot\sin\omega_c t - p_{0\,y'}\cdot\cos\omega_c t + p_{0\,y'}) + x'_0 + \frac{q}{m\omega_c^2}\cdot E_{x'}\cdot(1-\cos\omega_c t) \\ \frac{1}{m\omega_c}(p_{0\,y'}\cdot\sin\omega_c t + p_{0\,x'}\cdot\cos\omega_c t - p_{0\,x'}) + y'_0 + \frac{q}{m\omega_c^2}\cdot E_{x'}\cdot(\sin\omega_c t - \omega_c t) \\ \frac{q}{2m}\cdot E_{z'}\cdot t^2 + \frac{1}{m}\cdot p_{0\,z'}\cdot t + z'_0 \end{pmatrix} \tag{196}$$

In order to project the corresponding photoelectron trajectory onto the original laboratory coordinate system O, the $\vec{x}'(t)$ should be multiplied by a matrix R^{-1}:

$$\begin{aligned} R^{-1} &= \begin{bmatrix} \cos\alpha & -\sin\alpha & 0 \\ \sin\alpha & \cos\alpha & 0 \\ 0 & 0 & 1 \end{bmatrix} \times \begin{bmatrix} \cos\theta & 0 & \sin\theta \\ 0 & 1 & 0 \\ -\sin\theta & 0 & \cos\theta \end{bmatrix} \\ &= \begin{bmatrix} \cos\theta\cos\alpha & -\sin\alpha & \sin\theta\cos\alpha \\ \cos\theta\sin\alpha & \cos\alpha & \sin\theta\sin\alpha \\ -\sin\theta & 0 & \cos\theta \end{bmatrix} = R^T \end{aligned} \tag{197}$$

The photoelectron equation of motion in the coordinate system O has a form:

$$\begin{aligned} \vec{x}(t) = {} & R^T \\ & \times \begin{pmatrix} \frac{1}{m\omega_c}(p_{0\,x'}\cdot\sin\omega_c t - p_{0\,y'}\cdot\cos\omega_c t + p_{0\,y'}) + x'_0 + \frac{q}{m\omega_c^2}\cdot E_{x'}\cdot(1-\cos\omega_c t) \\ \frac{1}{m\omega_c}(p_{0\,y'}\cdot\sin\omega_c t + p_{0\,x'}\cdot\cos\omega_c t - p_{0\,x'}) + y'_0 + \frac{q}{m\omega_c^2}\cdot E_{x'}\cdot(\sin\omega_c t - \omega_c t) \\ \frac{q}{2m}\cdot E_{z'}\cdot t^2 + \frac{1}{m}\cdot p_{0\,z'}\cdot t + z'_0 \end{pmatrix} \end{aligned} \tag{198}$$

Where:

$$\begin{cases} E_{x'} &= -\sin\theta \cdot E \\ E_{z'} &= \cos\theta \cdot E \end{cases} \tag{199}$$

$$\begin{pmatrix} p_{0\,x'} \\ p_{0\,y'} \\ p_{0\,z'} \end{pmatrix} = R \times \begin{pmatrix} p_{0\,x} \\ p_{0\,y} \\ p_{0\,z} \end{pmatrix} \tag{200}$$

$$\begin{pmatrix} x'_0 \\ y'_0 \\ z'_0 \end{pmatrix} = R \times \begin{pmatrix} x_0 \\ y_0 \\ z_0 \end{pmatrix} \tag{201}$$

And:

$$\begin{cases} \sin\alpha &= \frac{B_y}{\sqrt{B_x^2+B_y^2}} \\ \cos\alpha &= \frac{B_x}{\sqrt{B_x^2+B_y^2}} \end{cases}, \quad \begin{cases} \sin\theta &= \frac{\sqrt{B_x^2+B_y^2}}{B} \\ \cos\theta &= \frac{B_z}{B} \end{cases} \tag{202}$$

BIBLIOGRAPHY

[1] H. Hertz. "Über einen Einfluß des ultravioletten Lichtes auf die elektrische Entladung." In: *Ann. Phys.* 17 (1887), p. 983.

[2] A. Einstein. "Über einen Erzeugung und Verwandlung des Lichtes betreffenden heuristischen Gesichtspunkt." In: *Ann. Phys.* 322 (1905), p. 132.

[3] D. Greenberger, K. Hentschel, and F. Weinert, eds. *Compendium of quantum physics*. Springer, 2009.

[4] M. Niaz et al. "Reconstruction of the history of the photoelectric effect and its implications for general physics textbooks." In: *Sci. Educ.* 94.5 (2010), p. 903.

[5] J. L. Bromberg. *The laser in America, 1950-1970*. The MIT Press, 1991.

[6] V. S. Letokhov. *Laser photoionization spectroscopy*. Academic Press, 1987.

[7] D. W. Pratt. "High resolution spectroscopy in the gas phase: even large molecules have well-defined shapes." In: *Annu. Rev. Phys. Chem.* 49 (1998), p. 481.

[8] S. Mukamel. "Femtosecond optical spectroscopy: a direct look at elementary chemical events." In: *Annu. Rev. Phys. Chem.* 41 (1990), p. 647.

[9] A. H. Zewail. "Femtochemistry: atomic-scale dynamics of the chemical bond." In: *J. Phys. Chem. A* 104.24 (2000), p. 5660.

[10] A. McPherson et al. "Studies of multiphoton production of vacuum-ultraviolet radiation in the rare gases." In: *J. Opt. Soc. Am. B* 4.4 (1987), p. 595.

[11] M. Ferray et al. "Multiple-harmonic conversion of 1064 nm radiation in rare gases." In: *J. Phys. B: At. Mol. Opt. Phys.* 21 (1988), p. 31.

[12] P. M. Paul et al. "Observation of a train of attosecond pulses from high harmonic generation." In: *Sci. Rep.* 292.5522 (2001), p. 1689.

[13] M. Hentschel et al. "Attosecond metrology." In: *Nature* 414 (2001), p. 509.

[14] M. Drescher et al. "Time-resolved atomic inner-shell spectroscopy." In: *Nature* 419 (2002), p. 803.

[15] H. G. Muller. "Reconstruction of attosecond harmonic beating by interference of two-photon transitions." In: *Appl. Phys. B* 74 (2002), p. 17.

[16] L. Cattaneo et al. “Comparison of attosecond streaking and RABBITT.” In: *Opt. Express* 24.25 (2016), p. 29060.

[17] L. Gallmann et al. “Photoemission and photoionization time delays and rates.” In: *Struct. Dyn.* 4 (2017), p. 061502.

[18] E. P. Wigner. “Lower limit for the energy derivative of the scattering phase shift.” In: *Phys. Rev.* 98.1 (1955), p. 145.

[19] R. Hofstadter. “Electron scattering and nuclear structure.” In: *Rev. Mod. Phys.* 28.3 (1956), p. 214.

[20] N. F. Mott and H. S. W. Massey. *The theory of atomic collisions*. Ed. by N. F. Mott amd E. C. Bullard and D. H. Wilkinson. Oxford at the Clarendon Press, 1965.

[21] A. Maquet, J. Caillat, and R. Taïeb. “Attosecond delays in photoionization: time and quantum mechanics.” In: *J. Phys. B: At. Mol. Opt. Phys.* 47 (2014), p. 204004.

[22] M. Schultze et al. “Delay in photoemission.” In: *Sci. Res.* 328. 5986 (2010), p. 1658.

[23] K. Klünder et al. “Probing single-photon ionization on the attosecond time scale.” In: *Phys. Rev. Lett.* 106 (2011), p. 143002.

[24] C. Palatchi et al. “Atomic delay in helium, neon, argon and krypton.” In: *J. Phys. B: At. Mol. Opt. Phys.* 47 (2014), p. 245003.

[25] M. Swoboda et al. “Phase measurement of resonant two-photon ionization in helium.” In: *Phys. Rev. Lett.* 104 (2010), p. 103003.

[26] M. Kotur et al. “Spectral phase measurement of a Fano resonance using tunable attosecond pulses.” In: *Nat. Commun.* 7 (2016), p. 10566.

[27] C. Alexandridi et al. “Attosecond photoionization dynamics in the vicinity of the Cooper minima in argon.” In: *Phys. Rev. Res.* 3 (2021), p. 012012.

[28] S. Heuser et al. “Angular dependence of photoemission time delay in helium.” In: *Phys. Rev. A* 94 (2016), p. 063409.

[29] C. Cirelli et al. “Anisotropic photoemission time delays close to a Fano resonance.” In: *Nat. Commun.* 9 (2018), p. 955.

[30] J. Joseph et al. “Angle-resolved studies of XUV-IR two-photon ionization in the RABBITT scheme.” In: *J. Phys. B: At. Mol. Opt. Phys.* 53 (2020), p. 184007.

[31] D. Busto et al. “Fano’s propensity rule in angle-resolved attosecond pump-probe photoionization.” In: *Phys. Rev. Lett.* 123 (2019), p. 133201.

[32] F. Calegari et al. “Ultrafast electron dynamics in phenylalanine initiated by attosecond pulses.” In: *Sci. Res.* 346.6207 (2014), p. 336.

[33] E. Perfetto et al. "Ultrafast quantum interference in the charge migration of tryptophan." In: *J. Phys. Chem. Lett.* 11.3 (2020), p. 891.

[34] F. Kelkensberg et al. "Molecular dissociative ionization and wave-packet dynamics studied using two-color XUV and IR pump-probe spectroscopy." In: *Phys. Rev. Lett.* 103 (2009), p. 123005.

[35] M. Lucchini et al. "Autoionization and ultrafast relaxation dynamics of highly excited states in N2." In: *Phys. Rev. A* 86 (2012), p. 043404.

[36] M. Eckstein. "Investigation of ultrafast electronic and nuclear dynamics in molecular nitrogen using an XUV time delay compensating monochromator." PhD thesis. Freie Universität Berlin, 2015.

[37] M. Eckstein et al. "Dynamics of N2 dissociation upon innervalence ionization by wavelength-selected XUV pulses." In: *Phys. Chem. Lett.* 6.3 (2015), p. 419.

[38] S. Haessler et al. "Phase-resolved attosecond near-threshold photoionization of molecular nitrogen." In: *Phys. Rev. A* 80 (2009), p. 011404.

[39] G. Sansone et al. "Electron localization following attosecond molecular photoionization." In: *Nature* 465 (2010), p. 763.

[40] A. Trabattoni et al. "Mapping the dissociative ionization dynamics of molecular nitrogen with attosecond time resolution." In: *Phys. Rev. X* 5 (2015), p. 041053.

[41] M. Huppert et al. "Attosecond delays in molecular photoionization." In: *Phys. Rev. Lett.* 117 (2016), p. 093001.

[42] A. Kamalov et al. "Electron correlation effects in attosecond photoionization of CO2." In: *Phys. Rev. A* 102 (2020), p. 023118.

[43] S. Nandi et al. "Attosecond timing of electron emission from a molecular shape resonance." In: *Sci. Adv.* 6.31 (2020).

[44] V. Loriot et al. "High harmonic generation-2ω attosecond stereo-photoionization interferometry in N2." In: *J. Phys. Photonics* 2 (2020), p. 024003.

[45] S. Fukahori et al. "Ultrafast electron-nuclear wavepacket in O2+ generated and probed with attosecond pulse trains." In: *J. Phys. B: At. Mol. Opt. Phys.* 53 (2020), p. 164001.

[46] M. S. Schöffler et al. "Ultrafast probing of core hole localization in N2." In: *Sci. Rep.* 320.5878 (2008), p. 920.

[47] C. Nicolas et al. "Dissociative photoionization of N2 in the 24-32 eV photon energy range." In: *J. Phys. B: At. Mol. Opt. Phys.* 36 (2003), p. 2239.

[48] T. Aoto et al. “Inner-valence states of N2+ and the dissociation dynamics studied by threshold photoelectron spectroscopy and configuration interaction calculation.” In: *J. Chem. Phys.* 124 (2006), p. 234306.

[49] T. Ayari et al. “State-to-state dissociative photoionization of molecular nitrogen: the full story.” In: *Adv. Phys.: X* 5.1 (2020), p. 1831955.

[50] J. Joseph. “Spectral and temporal resolution of photoionization dynamics in atoms and molecules.” PhD thesis. l’Université Paris-Sacley, 2021.

[51] J. Rist et al. “Measuring the photoelectron emission delay in the molecular frame.” In: *Nat. Commun.* 12 (2021), p. 6657.

[52] S. Grundmann et al. “Zeptosecond birth time delay in molecular photoionization.” In: *Sci. Res.* 370.6514 (2020), p. 339.

[53] L. Cattaneo et al. “Attosecond coupled electron and nuclear dynamics in dissociative ionization of H2.” In: *Nat. Phys.* 14 (2018), p. 733.

[54] J. Vos et al. “Orientation-dependent stereo Wigner time delay and electron localization in a small molecule.” In: *Sci. Res.* 360.6395 (2018), p. 1326.

[55] P. Hockett et al. “Time delay in molecular photoionization.” In: *J. Phys. B: At. Mol. Opt. Phys.* 49 (2016), p. 095602.

[56] M. Sabbar et al. “Combining attosecond XUV pulses with coincidence spectroscopy.” In: *Rev. Sci. Instrum.* 85 (2014), p. 103113.

[57] J. Vos. “Attosecond photoionization dynamics in small molecules.” PhD thesis. ETH Zurich, 2018.

[58] H. Ahmadi et al. “Collinear setup for delay control in two-color attosecondmeasurements.” In: *J. Phys. Photonics* 2 (2020), p. 024006.

[59] S. Mikaelsson et al. “A high-repetition rate attosecond light source for time-resolved coincidence spectroscopy.” In: *Nanophotonics* 10.1 (2021), p. 117.

[60] F. Shobeiry. “Attosecond electron-nuclear dynamics in photodissociation of H2 and D2.” PhD thesis. Heidelberg University, 2021.

[61] H. Srinivas et al. “High-repetition rate attosecond beamline formulti-particle coincidence experiments.” In: *Opt. Express* 30.8 (2022), p. 13630.

[62] H. Teng et al. “Attosecond laser station.” In: *Chin. Phys. B* 27.7 (2018), p. 074203.

[63] J. Lei et al. “Experimental platform of atomic and molecular photophysics based on xuv laser and reaction microscope.” In: *Nucl. Phys. Rev.* 37.2 (2020), p. 225.

[64] F. J. Furch et al. "CEP-stable few-cycle pulses with more than 190 µJ of energy at 100 kHz from a noncollinear optical parametric amplifier." In: *Opt. Lett.* 42.13 (2017), p. 2495.

[65] Francesca Calegari et al. "Advances in attosecond science." In: *J. Phys. B: At. Mol. Opt. Phys.* 49 (2016), p. 062001.

[66] J. Biegert et al. "Attosecond technology(ies) and science." In: *J. Phys. B: At. Mol. Opt. Phys.* 54 (2021), p. 070201.

[67] M. Nisoli et al. "Attosecond electron dynamics in molecules." In: *Chem. Rev.* 117.16 (2017), p. 10760.

[68] J.-C. Diels and W. Rudolph. *Ultrashort laser pulse phenomena*. Ed. by Paul Liao and Paul Kelley. Elsevier, 2006.

[69] J. M. Dahlström, A. L'Huillier, and A. Maquet. "Introduction to attosecond delays in photoionization." In: *J. Phys. B: At. Mol. Opt. Phys.* 45 (2012), p. 183001.

[70] M. Nisoli, S. De Silvestri, and O. Svelto. "Generation of high energy 10 fs pulses by a new pulse compression technique." In: *Appl. Phys. Lett.* 68.20 (1996), p. 2793.

[71] S. Hadrich et al. "Energetic sub-2-cycle laser with 216 W average power." In: *Opt. Lett.* 41.18 (2016), p. 4332.

[72] F. Böhle et al. "Compression of CEP-stable multi-mJ laser pulses down to 4 fs in long hollow fibers." In: *Laser Phys. Lett.* 11 (2014), p. 095401.

[73] T. Nagy et al. "Femtosecond multi-10-mJ pulses at 2 µm wavelength by compression in a hollow-core fiber." In: *Opt. Lett.* 46.13 (2021), p. 3033.

[74] A. Suda et al. "Generation of sub-10-fs, 5-mJ optical pulses using a hollow fiber with a pressure gradient." In: *Appl. Phys. Lett.* 96.11 (2005), p. 111116.

[75] T. T. Luu et al. "Extreme-ultraviolet high-harmonic generation in liquids." In: *Nat. Commun.* 9 (2018), p. 3723.

[76] S. Ghimire and D. A. Reis. "High-harmonic generation from solids." In: *Nat. Phys.* 15 (2019), p. 10.

[77] P. B. Corkum. "Plasma perspective on strong-field multiphoton ionization." In: *Phys. Rev. Lett.* 71.13 (1993), p. 1994.

[78] K. J. Schafer et al. "Above threshold ionization beyond the high harmonic cutoff." In: *Phys. Rev. Lett.* 70.11 (1993), p. 1599.

[79] F. Krausz and M. Ivanov. "Attosecond physics." In: *Rev. Mod. Phys.* 81 (2009), p. 163.

[80] Y. Mairesse et al. "Attosecond synchronization of high-harmonic soft X-rays." In: *Sci. Rep.* 302.5650 (2003), p. 1540.

[81] G. J. Schulz. "Resonances in electron impact on atoms and diatomic molecules." In: *Rev. Mod. Phys.* 45.3 (1973), p. 378.

[82] M. J. Seaton. “Quantum defect theory.” In: *Rep. Prog. Phys.* 46 (1983), p. 167.

[83] I. V. Hertel and C. P. Schulz. *Atoms, molecules and optical physics*. Springer, 2015.

[84] *National Institute of Standards and Technology*. `https://webbook.nist.gov`.

[85] J. A. R. Samson and W. C. Stolte. “Precision measurements of the total photoionization cross-sections.” In: *J. Electron Spectrosc. Relat. Phenom.* 123 (2002), p. 265.

[86] U. Fano. “Propensity rules: an analytical approach.” In: *Phys. Rev. A* 32.1 (1985), p. 617.

[87] P. F. Bernath. *Spectra of atoms and molecules*. Oxford University Press, 2005.

[88] A. L. Roche and J. Tellinghuisen. “Predissociation and perturbations in the C2u+ state of N2+ from interaction with the B2u+ state.” In: *Mol. Phys.* 38.1 (1979), p. 129.

[89] B. Paulus, J. F. Pérez-Torres, and C. Stemmle. “Time-dependent description of the predissociation of N2+ in the C2u+ state.” In: *Phys. Rev. A* 94 (2016), p. 053423.

[90] S. R. Langhoff and C. W. Bauschlicher. “Theoretical study of the first and second negative systems of N2+.” In: *J. Chem. Phys.* 88 (1987), p. 329.

[91] P. Baltzer et al. “Inner-valence states of N2+ studied by uv photoelectron spectroscopy and configuration-interaction calculations.” In: *Phys. Rev. A* 46.9 (1992), p. 5545.

[92] P. Erman. “Direct measurement of the N2+ C state predissociation probability.” In: *Phys. Scr.* 14 (1976), p. 51.

[93] P. Fournier et al. “Collision-induced dissociation of 10 keV N2+ ions: evidence for predissocioation of the C state.” In: *Chem. Phys. Lett.* 9.5 (1971), p. 426.

[94] F. Quéré, Y. Mairesse, and J. Itatani. “Temporal characterization of attosecond XUV fields.” In: *J. Mod. Opt.* 52.2-3 (2005), p. 339.

[95] R. Zimmermann and L. Hanley. *Photoionization and photo-induced processes in mass spectrometry: fundamentals and applications*. Wiley, 2020.

[96] G. L. Yudin et al. “Attosecond photoelectron interference in the separable Coulomb-Volkov continuum.” In: *J. Phys. B: At. Mol. Opt. Phys.* 40 (2007), p. 93.

[97] D. J. Kane and R. Trebino. “Characterization of arbitrary femtosecond pulses using frequency-resolved optical gating.” In: *IEEE J. Quantum Electron.* 29.2 (1993), p. 571.

[98] D. J. Kane. “Real-time measurement of ultrashort laser pulses using principal component generalized projections.” In: *IEEE J. Sel. Top. Quantum Electron.* 4.2 (1998), p. 278.

[99] Y. Mairesse and F. Quéré. “Frequency-resolved optical gating for complete reconstruction of attosecond bursts.” In: *Phys. Rev. A* 71 (2005), p. 011401.

[100] J. M. Dahlström et al. “Theory of attosecond delays in laser-assisted photoionization.” In: *Chem. Phys.* 414 (2013), p. 53.

[101] M. Osolodkov et al. “Generation and characterisation of few-pulse attosecond pulse trains at 100 kHz repetition rate.” In: *J. Phys. B: At. Mol. Opt. Phys.* 53 (2020), p. 194003.

[102] H. R. Telle et al. “Carrier-envelope offset phase control: a novel concept for absolute optical frequency measurement and ultrashort pulse generation.” In: *Appl. Phys. B* 69 (1999), p. 327.

[103] S. A. Akhmanov et al. “Observation of parametric amplification in the optical range.” In: *JETP Lett.* 2 (1965), p. 191.

[104] P. Di Trapani et al. “Efficient conversion of femtosecond blue pulses by travelling-wave parametric generation in non-collinear phase matching.” In: *Opt. Commun.* 119 (1995), p. 327.

[105] D. Strickland and G. Mourou. “Compression of amlified chirped optical pulses.” In: *Opt. Commun.* 55.6 (1985), p. 447.

[106] F. Kelkensberg. “Capturing atomic and electronic motion with high harmonic generation light pulses.” PhD thesis. Radboud University Nijmegen, 2011.

[107] M. Schultze et al. “Multi-μJ, CEP-stabilized, two-cycle pulses from an OPCPA system with up to 500 kHz repetition rate.” In: *Opt. Express* 18.26 (2010), p. 27291.

[108] J. Matyschok et al. “Temporal and spatial effects inside a compact and CEP stabilized, few-cycle OPCPA system at high repetition rates.” In: *Opt. Express* 21.24 (2013), p. 29656.

[109] S. Hrisafov et al. “High-power few-cycle near-infrared OPCPA for soft X-ray generation at 100 kHz.” In: *Opt. Express* 28.26 (2020), p. 40145.

[110] M. Mero et al. “43 W, 1.55 μm and 12.5 W, 3.1 μm dual-beam, sub-10 cycle, 100 kHz optical parametric chirped pulse amplifier.” In: *Opt. Lett.* 43.21 (2018), p. 5246.

[111] N. Bigler et al. “High-power OPCPA generating 1.7 cycle pulses at 2.5 μm.” In: *Opt. Express* 26.20 (2018), p. 26750.

[112] G. Cerullo and S. De Silvestri. “Ultrafast optical parametric amplifiers.” In: *Rev. Sci. Instrum.* 74.1 (2003).

[113] I. N. Ross et al. “Analysis and optimization of optical parametric chirped pulse amplification.” In: *J. Opt. Soc. Am. B* 19.12 (2002), p. 2945.

[114] Dominik Hoff et al. "Continuous every-single-shot carrier-envelope phase measurement and control at 100 kHz." In: *Opt. Lett.* 43.16 (2018), p. 3850.

[115] T. Witting et al. "Characterization of high-intensity sub-4-fs laser pulses using spatially encoded spectral shearing interferometry." In: *Opt. Lett.* 36.9 (2011), p. 1680.

[116] F. Schell. "Sub-femtosecond processes in molecules studied by coincidence spectroscopy." PhD thesis. Frei Universität Berlin, 2020.

[117] V. Stert et al. "Ultrafast photoelectron spectroscopy: femtosecond pump-probe coincidence detection of ammonia cluster ions and electrons." In: *Eur. Phys. J. D* 5 (1999), p. 97.

[118] A. E. Boguslavskiy et al. "The multielectron ionization dynamics underlying attosecond strong-field spectroscopies." In: *Sci. Rep.* 335.6074 (2012), p. 1336.

[119] R. Locher et al. "Versatile attosecond beamline in a two-foci configuration for simultaneous time-resolved measurements." In: *Rev. Sci. Instrum.* 85 (2014), p. 013113.

[120] M. Chini et al. "Delay control in attosecond pump-probe experiments." In: *Opt. Express* 17.24 (2009), p. 21459.

[121] A. Zaïr et al. "Ultrastable collinear delay control setup for attosecond IR-XUV pump-probe experiment." In: *J. Opt. Soc. Am. B* 35.5 (2018), p. 110.

[122] V. Dribinski et al. "Reconstruction of Abel-transformable images: the Gaussian basis-set expansion Abel transform method." In: *Rev. Sci. Instrum.* 73.7 (2002), p. 2634.

[123] D. Spangenberg et al. "Time-domain ptychography." In: *Phys. Rev. A* 91 (2015), p. 021803.

[124] M. Lucchini et al. "Ptychographic reconstruction of attosecond pulses." In: *Opt. Express* 23.23 (2015), p. 248675.

[125] T. Witting et al. "Time-domain ptychography of over-octave-spanning laser pulses in the single-cycle regime." In: *Opt. Lett.* 41.18 (2016), p. 4218.

[126] T. Witting et al. "Retrieval of attosecond pulse ensembles from streaking experiments using mixed state time-domain ptychography." In: *J. Phys. B: At. Mol. Opt. Phys.* 53 (2020), p. 194001.

[127] J. Mauritsson, M. B. Gaarde, and K. J. Schafer. "Accessing properties of electron wave packets generated by attosecond pulse trains through time-dependent calculations." In: *Phys. Rev. A* 72 (2005), p. 013401.

[128] T. Witting et al. "Generation and characterization of isolated attosecond pulses at 100 kHz repetition rate." In: *Optica* 9.2 (2022), p. 145.

[129] M. Ryazanov. "Development and implementation of methods for sliced velocity map imaging. Studies of overtone-induced dissociation and isomerization dynamics of hydroxymethyl radical (CH2OH and CD2OH)." PhD thesis. University of Southern California, 2012.

[130] P. D. Keathley et al. "Volkov transform generalized projection algorithm for attosecond pulse characterization." In: *New J. Phys.* 18 (2016), p. 073009.

[131] C. Dorrer and I. A. Walmsley. "Accuracy criterion for ultrashort pulse characterization techniques: application to spectral phase interferometry for direct electric field reconstruction." In: *J. Opt. Soc. Am. B* 19.5 (2002), p. 1019.

[132] D. W. Chandler and P. L. Houston. "Two-dimensional imaging of state-selected photodissociation products detected by multiphoton ionization." In: *J. Chem. Phys.* 87 (1987), p. 1445.

[133] A. T. J. B. Eppink and D. H. Parker. "Velocity map imaging of ions and electrons using electrostatic lenses: application in photoelectron and photofragment ion imaging of molecular oxygen." In: *Rev. Sci. Instrum.* 68.9 (1997), p. 3477.

[134] M. Ryazanov and H. Reisler. "Improved sliced velocity map imaging apparatus optimized for H photofragments." In: *J. Chem. Phys.* 138 (2013), p. 144201.

[135] G. Gademann et al. "Velocity map imaging using an in-vacuum pixel detector." In: *Rev. Sci. Instrum.* 80 (2009), p. 103105.

[136] P. C. Samartzis et al. "State-resolved differential cross-section measurement of Cl + C2H6 -> HCl + C2H5 reaction using single-beam velocity mapping." In: *Chem. Phys. Lett.* 324.5-6 (2000), p. 337.

[137] R. L. Toomesa and T. N. Kitsopoulos. "Rotationally resolved reaction product imaging using crossed molecular beams." In: *Phys. Chem. Chem. Phys.* 5 (2003), p. 2481.

[138] O. Ghafur et al. "A velocity map imaging detector with an integrated gas injection system." In: *Rev. Sci. Instrum.* 80 (2009), p. 033110.

[139] M. J. J. Vrakking. "An iterative procedure for the inversion of two-dimensional ion/photoelectron imaging experiments." In: *Rev. Sci. Instrum.* 72.11 (2001), p. 4084.

[140] J. Ullrich and H. Schmidt-Böcking. "Time-of-flight spectrometer for the determination of microradian projectile scattering angles in atomic collisions." In: *Phys. Lett. A* 125.4 (1987), p. 193.

[141] R. Moshammer et al. “Low-energy electrons and their dynamical correlation with recoil ions for single ionization of helium by fast, heavy-ion impact.” In: *Phys. Rev. Lett.* 73.25 (1994), p. 3371.

[142] J. Ullrich et al. “Recoil-ion and electron momentum spectroscopy: reaction-microscopes.” In: *Rep. Prog. Phys.* 66 (2003), p. 1463.

[143] S. Birkner. “Strong field ionization of atoms and molecules: electron-ion coincidence measurements at high repetition rate.” PhD thesis. Freie Universität Berlin, 2015.

[144] F. J. Furch et al. “Carrier-envelope phase stable few-cycle pulses at 400 kHz for electron-ion coincidence experiments.” In: *Opt. Express* 21.19 (2013), p. 22671.

[145] F. Schell et al. “Molecular orbital imprint in laser-driven electron recollision.” In: *Sci. Adv.* 4.5 (2018).

[146] O. Jagutzki et al. “Multiple hit readout of a microchannel plate detector with a three-layer delay-line anode.” In: *IEEE Trans. Nucl. Sci.* 49.5 (2002), p. 2477.

[147] L. Pedemonte, G. Bracco, and R. Tatarek. “Theoretical and experimental study of He free-jet expansions.” In: *Phys. Rev. A* 59.4 (1998), p. 3084.

[148] G. Scoles. *Atomic and molecular beam methods*. Oxford University Press, 1988.

[149] *National Metrology Institute of Germany*. `https://www.ptb.de`.

[150] M. L. Cable et al. “Titan tholins: simulating Titan organic chemistry in the Cassini-Huygens era.” In: *Chem. Rev.* 112 (2012), p. 1882.

[151] T. P. Snow. “Molecular nitrogen in space.” In: *Nature* 429 (2004), p. 615.

[152] G. A. Garcia et al. “A multipurpose double imaging particle coincidence spectrometer for gas phase vacuum ultraviolet photodynamics studies.” In: *Rev. Sci. Instrum.* 84 (2013), p. 053112.

[153] Felix Brauße. “Shape resonances as a probe of an evolving nuclear and electronic structure in molecules.” PhD thesis. Freie Universität Berlin, 2018.

[154] P. W. Langhoff et al. “Theoretical studies of inner-valence-shell photoionization cross sections in N2 and CO.” In: *Chem. Phys.* 58 (1981), p. 71.

COLOPHON

This document was typeset using the typographical look-and-feel `classicthesis` developed by André Miede. The style was inspired by Robert Bringhurst's seminal book on typography "*The Elements of Typographic Style*". `classicthesis` is available for both LaTeX and LyX:

`https://bitbucket.org/amiede/classicthesis/`